MANCHESTER 1824
The University of Manchester

Computational Modelling of Turbulent Magnetohydrodynamic Flows

A thesis
submitted to The University of Manchester
for the degree of
doctor of philosophy (PhD)
in the faculty of Engineering and Physical Sciences

Dean Robert Wilson

School of Mechanical, Aerospace and Civil Engineering
2016

CONTENTS

Final word count: 53987

LIST OF FIGURES

LIST OF TABLES

LIST OF PUBLICATIONS

Wilson, D. R., Craft, T J, and Iacovides, H. (2013). "Application of URANS turbulence closure models to complex flows subjected to electromagnetic and other body forces". In: 8th International Symposium on Turbulent Shear Flow Phenomena. Poitiers, France.

Wilson, D. R., Craft, T. J., and Iacovides, H. (2014a). "Application of RANS turbulence closure models to flows subjected to electromagnetic and buoyancy forces". *International Journal of Heat and Fluid Flow*. 8th Symposium on Turbulence & Shear Flow Phenomena (TSFP8) 49, pp. 80–90.

Wilson, D. R., Craft, T. J., and Iacovides, H. (2014b). "On the development of URANS turbulence closure modes: Flows subjected to electromagnetic and other body forces". In: 10th Int. ERCOFTAC Symposium on Engineering Turbulence Modelling and Measurements ETMM10. Marbella, Spain.

Wilson, D. R., Craft, T. J., and Iacovides, H. (2015). "Application of Reynolds stress transport turbulence closure models to flows affected by Lorentz and buoyancy forces". *International Journal of Heat and Fluid Flow*. Special Issue devoted to the 10th Int. Symposium on Engineering Turbulence Modelling and Measurements (ETMM10) held in Marbella, Spain on September 17-19, 2014 55, pp. 180–197.

ABSTRACT

COMPUTATIONAL MODELLING OF TURBULENT MAGNETOHYDRODYNAMIC FLOWS

The study of magnetohydrodynamics unifies the fields of fluid mechanics and electrodynamics to describe the interactions between magnetic fields and electrically conducting fluids. Flows described by magnetohydrodynamics form a significant aspect in a wide range of engineering applications, from the liquid metal blankets designed to surround and remove heat from nuclear fusion reactors, to the delivery and guidance of nanoparticles in magnetic targeted drug delivery. The ability to optimize these, and other, processes is increasingly reliant on the accuracy and stability of the numerical models used to predict such flows. This thesis addresses this by providing a detailed assessment on the performance of two electromagnetically extended Reynolds-averaged Navier-Stokes models through computations of a number of electromagnetically influenced simple channel and Rayleigh-Bènard convective flows.

The models tested were the low-Re $k-\varepsilon$ linear eddy-viscosity model of Launder and Sharma (1974), with electromagnetic modifications as proposed by Kenjereš and Hanjalić (2000), and the low-Re stress-transport model of Hanjalić and Jakirlić (1993), with electromagnetic modifications as proposed by Kenjereš and Hanjalić (2004). First, a one-dimensional fully-developed turbulent channel flow was considered over a range of Reynolds and Hartmann numbers with a magnetic field applied in both wall-normal and streamwise directions. Results showed that contributions from the electromagnetic modifications were modest and, whilst both models inherently captured some of the reduction in mean strain that a wall-normal field imposed, results from the stress-transport model were consistently superior for both magnetic field directions. Then, three-dimensional time-dependent Rayleigh-Bènard convection was considered for two different Prandtl numbers, two different magnetic field directions and over a range of Hartmann numbers. Results revealed that, at sufficiently high magnetic field strengths, a dramatic reorganization of the flow structure is predicted to occur. The vertical magnetic field led to a larger number of thinner, more cylindrical plumes whilst the horizontal magnetic field caused a striking realignment of the roll cells' axes with the magnetic field lines. This was in agreement with both existing numerical simulations and physical intuition.

The superior performance of the modified stress-transport model in both flows was attributed to both its ability to provide better representation of stress generation and other processes, and its ability to accommodate the electromagnetic modifications in a more natural, and exact, fashion. The results demonstrate the capabilities of the stress-transport approach in modelling MHD flows that are relevant to industry and offer potential for those wishing to control flow structure or levels of turbulence without recourse to mechanical means.

Dean Robert Wilson
DOCTOR OF PHILOSOPHY (PHD)
2016
THE UNIVERSITY OF MANCHESTER

DECLARATION

The University of Manchester
PhD by traditional thesis Candidate Declaration

Candidate Name: Dean Robert Wilson

Faculty: Engineering and Physical Sciences

Thesis Title: Computational Modelling of Turbulent Magnetohydrodynamic Flows

Declaration to be completed by the candidate:

I declare that no portion of this work referred to in this thesis has been submitted in support of an application for another degree or qualification of this or any other university or other institute of learning.

Signed: Date: September 6, 2016

COPYRIGHT

ACKNOWLEDGEMENTS

I would like to express my sincere graditude to my supervisor Tim Craft. He truely has patience, knowledge and wisdom one can only aspire to emulate. Thanks also to Hector Iacovides, Robert Prosser, Adel Nasser, Iain Dupere, Christine Jinks, Paul Wakins, Dave Golding, Dave Jones, Alistair Revell and all other members of MACE staff who have looked out for me during my time here.

Thanks to Mark, Penny, Jack, Shelley, Rachel, Fitz and all my other friends "down south" for their support and for having to deal with my enless *"but I've got work to do"* and *"I've got no money"* excuses. They probably won't stop.

Thanks to Mariam, for being there for me and for making life fun. Thanks to Khalil, for the enless late nights spent discussing my work, and for telling me when I was spouting nonsense. Thanks to Huw, Craig, Tom and the rest of the George Begg crew over the years (there's been a few iterations; I've been here a long time...).

Thanks to my parents for their love, support and belief. Without you both, this thesis would simply not be possible.

I dedicate this work to my late mother, Angela Wilson. This one's for you.

Quos valde amas numquam vere moriuntur

NOMENCLATURE

A	Lumley's two-component stress ('flatness') parameter, $A = 1 - \frac{9}{8}(A_2 - A_3)$
A_2	second invariant of stress anisotropy, $A_2 = a_{ij}a_{ji}$
A_3	third invariant of stress anisotropy, $A_3 = a_{ij}a_{jk}a_{ki}$
A_{ij}	mean velocity gradient tensor, $A_{ij} = \partial U_i/\partial x_j$
a_{ij}	Reynolds-stress anisotropy tensor, $a_{ij} = \overline{u_i u_j}/k - \frac{2}{3}\delta_{ij}$
B_0	characteristic magnetic flux density
B_i, $\mathbf{B}$	magnetic flux density
c	speed of light
c_μ	coefficient in eddy-viscosity formula
$\mathcal{D}_k$	total diffusion of k
$\mathcal{D}_{ij}$	total diffusion of $\overline{u_i u_j}$
$\mathcal{D}^\nu_{ij}$	molecular diffusion of $\overline{u_i u_j}$
$\mathcal{D}^p_{ij}$	turbulent diffusion of $\overline{u_i u_j}$ by pressure fluctuations
$\mathcal{D}^t_{ij}$	turbulent diffusion of $\overline{u_i u_j}$ by velocity fluctuations
E	integration constant in log-law
E	two-component-limit parameter for dissipation tensor, $E = 1 - \frac{9}{8}(E_2 - E_3)$
E_2	second invariant of e_{ij}, $E_2 = e_{ij}e_{ji}$
E_3	third invariant of e_{ij}, $E_3 = e_{ij}e_{jk}e_{ki}$
E_i, $\mathbf{E}$	electric field

e_i	fluctuating electric field
e_{ij}	stress dissipation-rate anisotropy tensor, $e_{ij} = \varepsilon_{ij}/\varepsilon - \frac{2}{3}\delta_{ij}$
$\tilde{F}_i,\ F_i,\ f_i$	instantaneous, mean and fluctuating body force in index notation
$\mathcal{F}_k$	production of k due to all body forces
$\mathcal{F}_{ij}$	production of $\overline{u_i u_j}$ from all body forces
$\mathcal{F}_{ij}^b$	direct buoyant contribution to $\overline{u_i u_j}$ budget
f_μ	near-wall damping term in eddy-viscosity formula
f_w	wall damping function
g	acceleration due to gravity
$g_i,\ \mathbf{g}$	gravitational vector
I	electric current
$J_i,\ \mathbf{J}$	electric current density
k	turbulent kinetic energy, $k = \frac{1}{2}\overline{u_i u_i}$
k_α	thermal conductivity
L	characteristic length scale
$n_i,\ \mathbf{n}$	wall-normal unit vector
$\tilde{P}_i,\ P_i,\ p_i$	instantaneous, mean and fluctuating pressure
$\mathcal{P}_k$	production of k due to mean velocity gradients
$\mathcal{P}_{ij}$	stress production due to mean strain
Q	Q-criterion of Hunt et al. (1988), $Q = \frac{1}{2}\left(\Omega_{ij}\Omega_{ij} - S_{ij}S_{ij}\right)$
Q	charge (only in Chapter 3)
S_{ij}	mean rate of strain tensor, $S_{ij} = \frac{1}{2}\left(\partial U_i/\partial x_j + \partial U_j/\partial x_i\right)$
$\mathbf{S}$	surface area vector
t	time
U,V,W	Cartesian components of mean velocity
$\tilde{U}_i,\ U_i,\ u_i$	instantaneous, mean and fluctuating velocity vector in index notation

$\mathbf{U}$	velocity vector
U^*	mean velocity in log-law, $U^* = \rho U \sqrt{k}/\tau_w$
U^+	mean velocity non-dimensionalized with friction velocity, $U^+ = U/U_\tau$
U_0	characteristic velocity scale
U_τ	friction velocity, $\sqrt{\tau_w/\rho}$
U_b	bulk velocity
$\overline{u_i u_j}$	Reynolds stress tensor
$\overline{u_i \theta}$	turbulent heat flux
$\mathbf{V}$	volume
W_b	buoyant velocity scale, $W_b = \sqrt{g\beta\Delta\Theta L}$
x, y, z	cartesian coordinates
x_i, $\mathbf{x}$	cartesian coordinates in index and vector notation
y	wall distance
y^+	non-dimensionalized wall distance, $y^+ = U_\tau y/\nu$
y_ν^+	non-dimensional thickness of viscous sub-layer
α	thermal diffusivity
β	volumetric thermal expansion coefficient
Γ	generic diffusivity of general variable
δ	channel half-width
δ_{ij}	Kronecker delta unit symbol
ε	dissipation rate of the turbulent kinetic energy, k
$\tilde{\varepsilon}$	'quasi-homogeneous' dissipation rate of k
ε_{ij}	stress dissipation rate tensor
ε_{ijk}	Levi-Civita third rank alternating
ϵ_0	permittivity of free space

η	magnetic diffusivity, $\eta = (\mu_0 \sigma)^{-1}$
$\tilde{\Theta}$, Θ, θ	instantaneous, mean and fluctuating temperature
Θ_0	reference or characteristic temperature
κ	von Karman constant in log-law, $\kappa \approx 0.41$
μ	molecular viscosity
μ_t	turbulent (eddy) viscosity
μ_0	permeability of free space, defined as $\mu_0 = 4\pi \times 10^{-7}\,\mathrm{N\,A^{-2}}$
ν	kinematic molecular viscosity
ρ	fluid density
ρ_0	reference fluid density
ρ_q	charge density
Φ_{ij}	pressure-strain correlation in the $\overline{u_i u_j}$ equation
σ	electrical conductivity
σ_k	turbulent Prandtl number
τ_w	wall shear stress
τ_{ij}	viscous stress tensor
$\tilde{\phi}$, ϕ, ϕ'	instantaneous, mean and fluctuating electric potential
Φ_g	gravitational potential
$\tilde{\psi}$, Ψ, ψ	general variable: instantaneous, mean and fluctuation
Ω_{ij}	mean rate of rotation tensor, $\Omega_{ij} = \frac{1}{2}\left(\partial U_i/\partial x_j - \partial U_j/\partial x_i\right)$

Acronymns

CDS	Central Differencing Scheme
CFD	Computational fluid dynamics
DNS	Direct Numerical Simulation
EMF	Electromotive force
FVM	Finite Volume Method
GGDH	Generalized Gradient Diffusion Hypothesis
IP	Isotropization of Production
LES	Large Eddy Simulation
LEVM	Linear Eddy Viscosity model
MHD	Magnetohydrodyanmics
QUICK	Quadratic Upstream Interpolation for Convection Kinematics
RANS	Reynolds-averaged Navier-Stokes
RSM	Reynolds stress model
SIMPLE	Semi-Implicit Method for Pressure-Linkage Equations
UMIST	Upstream Monotonic Interpolation for Scalar

Dimensionless Numbers

Ha	Hartmann number	$Ha = B_0 L\sqrt{\frac{\sigma}{\mu}}$
N	Interaction parameter	$N = \frac{\sigma B_0^2 L}{\rho U_0}$
Pr	Prandtl number	$Pr = \frac{\nu}{\alpha}$
Ra	Rayleigh number	$Ra = \frac{g\beta\Delta\Theta L^3}{\nu\alpha}$
Re	Reynolds number	$Re = \frac{\rho U_0 L}{\mu}$
Re_m	magnetic Reynolds number	$Re_m = \frac{U_0 L}{\eta}$
Re_τ	Reynolds number based on friction velocity	$Re_\tau = \frac{U_\tau L}{\nu}$

CHAPTER

ONE

INTRODUCTION

Magnetohydrodynamics (MHD) is the study of the dynamics between electrically conducting fluids and magnetic fields. It unifies the fields of electrodynamics and fluid mechanics to describe the concurrent effects of both the magnetic field on the fluid flow, and the fluid flow on the magnetic field. These flows form a significant aspect in many engineering applications, from large scale astrophysical and geophysical processes, including, for example, the generation of the Earth's magnetic field through turbulent motions in its core, to energy generation, where magnetic plasma confinement is hoped to lead to controlled nuclear fusion. This chapter begins in Section 1.1 by providing a brief history of the topic alongside an introduction to some of the basic phenomena of MHD flows in Section 1.2. Following this, Section 1.3 introduces the modelling approach employed in this thesis and the range of cases to which it has been applied. Finally, Section 1.4 states the main objectives of the current work and Section 1.5 closes the chapter by providing an outline for the rest of the thesis.

1.1 A brief history

Magnetohydrodynamics arguably has its roots in the early 19th century, when Michael Faraday (1832) noted an electrically conducting material experienced an electromotive force (EMF) when it moved in the presence of a magnetic field. Noting that seawater is weakly conductive, he supposed that the motion of a large body of water through the Earths magnetic field should generate a measurable electric current. Unfortunately, his efforts to measure this, which included running a length of copper wire across the River Thames at Waterloo bridge, were not successful, but he remarked that a larger body of water, like the English Channel, should provide a more measurable effect. Fortunately for Faraday, gratification came via a conversation with C. Wollaston in 1851, who had asked Faraday to explain why he measured an EMF, in phase with tidal movements, in a submarine cable across the English Channel. Wollaston recalled Faraday's excitement (Wollaston, 1881) when, after showing his data, Faraday exclaimed "Oh beautiful, beautiful" and promptly showed Wollaston the book predicting its effect 20 years earlier.

Despite these early advances by Faraday, it was not until the late 1930's and early 1940's that interest in MHD began to significantly progress. Julius Hartmann, a Danish engineer, invented the electromagnetic pump in 1918 but could not explain why it was so inefficient. He later undertook some of the first systematic theoretical and experimental studies of how the flow of mercury was affected by the presence of a magnetic field (Hartmann and Lazarus, 1937). He termed this the study of "Hg-dynamics"; a name that evidently did not stick, but his work endowed engineers with both the first real insights into how magnetic fields would affect velocity distributions and the first detailed sets of experimental data.

Perhaps the most prominent landmark in MHD, however, was the suggestion by Hannes Alfvén in a 1942 Nature publication that the interplay between electromagnetic fields and an electrically conducting plasma would lead to "electromagnetic-hydromagnetic" or, as he would later call them, "magnetohydrodynamic" waves. These waves, subsequently confirmed by experiments and which now bear his name, led to periods of intense research into the effects of magnetic fields in plasma physics and astrophysics. Efforts to harness nuclear fusion as a means of power production then began after World War II and designs centered on utilizing magnetic fields to control and confine plasma within a toroidal shaped vessel (known as a Tokamak). The intense heat which was expected to be generated by fusion reactions generated further engineering challenges for MHD. Liquid lithium is a primary candidate for use as a coolant, since it can function to both remove heat and breed tritium (a fuel component), but the motion of this, as an electrically conducting fluid, within the vicinity of the reactor would be heavy influenced by the intense magnetic field required for plasma confinement. Research into these concepts and issues has only intensified since.

It was not long until other areas picked up on the intriguing effects that a magnetic field could bring. The 1980's saw magnetic fields beginning to be used in the processing of metals. Indeed, materials processing still today forms one of the main engineering applications of MHD. Metallic materials are regularly stirred, levitated and heated using magnetic fields as metallurgists seek ways to increase purity, improve properties and inflate commercial revenues (Davidson, 1999). The mere ability to control conducting flows via non-mechanical means, whether it be to induce a flow that was not present prior or to damp a flow which is present but not desired, offers great potential across a wide range of engineering devices and concepts. Research today focuses not just on the optimization of existing techniques and improvement of prediction tools, but also in more novel application areas, including targeted drug delivery and electromagnetic flow control.

1.2 Some basic MHD principles

Before delving into the thesis proper it will be prudent to highlight some of the interactions which form the backbone of engineering MHD. As Faraday has already highlighted above, basic MHD phenomena arises from the relative motion, spatial or temporal, between an electrically conducting fluid and a magnetic field. Once this is established, then an electromotive force is generated which, provided a suitable path exists, will cause a flow of electric current. Once there is a flow of current, there are two observable consequences;

I An additional magnetic field appears, associated with the induced currents, which serves to perturb the original (or source) magnetic field.

II An electromagnetic force appears (the Lorentz force), which results from an interaction between the induced currents and the total magnetic field (original plus induced). This serves to perturb the original motion which generated the currents.

Thus, there is clearly some mutual interaction between the fluid velocity and the electromagnetic field. The motion of the fluid affects the magnetic field (through I) and the magnetic field affects the motion of the fluid (through II). The first effect will be familiar to those who attempted to measure the magnetic field generated by a current carrying wire in school; charges in motion will produce a magnetic field. The second is a consequence of the fact that a charged particle which moves with respect to an electromagnetic field experiences a force. This force is directed perpendicular to both the motion and the direction of the magnetic field. To help illustrate the interplay between these two fields, consider the following example adapted from Roberts (1967a).

The mechanism depicted in Figure 1.1 is called a homopolar dynamo and was originally conceived by Faraday. It comprises a solid conducting disk which is free to rotate about

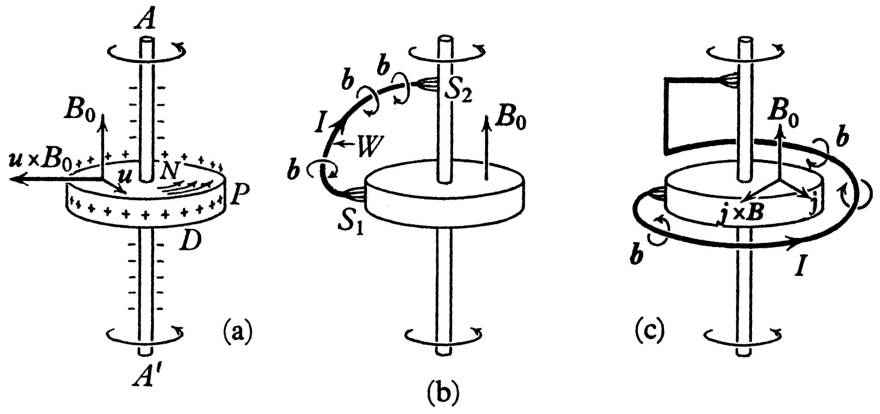

Figure 1.1: The homopolar dynamo. From Roberts (1967a).

an axle (AA'). A magnetic field $\boldsymbol{B}_0$ is applied such that it cuts the plane of the disk everywhere. If a torque is applied to the axle, such that the disk moves with an angular velocity $\boldsymbol{\Omega}$, then free charges will move with the disk, with velocity $\boldsymbol{u}$ in a direction as shown in Figure 1.1a. Since they are moving with respect to a stationary magnetic field, they experience the Lorentz force. This is given by $\boldsymbol{u} \times \boldsymbol{B}_0$ and is directed towards the periphery of the disk P. Positive charges will thus begin to accumulate around the periphery of the disk, negative charges will accumulate at N (and along the axle AA'), and the result is the existence of a potential difference.

If the circuit is completed by adding a stationary wire connected to the disk and axle via sliding brushes, as in Figure 1.1b, then the potential difference will cause an electric current I to flow. This current will, in accordance with Ampere's law, produce its own magnetic field in a direction given by the right hand screw rule. This is indicated by $\boldsymbol{b}$. If the wire is then rearranged such that it forms a loop about the disk, like in Figure 1.1c, the direction of the magnetic field $\boldsymbol{b}$ is such that the total magnetic field cutting the plane of the disk is now $\boldsymbol{B} = \boldsymbol{B}_0 + \boldsymbol{b}$. Thus the motion $\boldsymbol{u}$ has caused an additional magnetic field $\boldsymbol{b}$ to appear which perturbed our original magnetic field $\boldsymbol{B}_0$. Evidently the magnitude of the generated magnetic field will depend on the magnitude of the current, which will depend on the angular velocity of the disc. This was the first of the two observable consequences highlighted earlier.

The second observable consequence, the effect of the field $\boldsymbol{B}$ on the motion $\boldsymbol{u}$, is seen by noting that within the disk, the flow of current is directed radially away from the axis of rotation. This current, denoted by the current density $\boldsymbol{j}$ in Figure 1.1c, will also interact with the (total) magnetic field $\boldsymbol{B}$ to create a Lorentz force. The direction of this, given by the cross product between $\boldsymbol{j}$ and $\boldsymbol{B}$, is clearly in opposition to the motion of the disk $\boldsymbol{u}$. Thus the magnetic field has perturbed the original motion and, in this case, a torque must be applied to operate the disk.

Admittedly, the homopolar dynamo can only go so far in providing true insight into the kinds of MHD flows which are commonly encountered in engineering applications. This

is largely since its 'fluid' is a solid disk with only one degree of freedom. It does, however, provide a hint at the kind of complexity that can arise from relatively simple motion. Here, by just connecting the right sections of a metal disc rotating in a magnetic field, both an additional magnetic field and a force which modified the original motion applied to the disk, were generated. For it to be a true example of an MHD flow, one needs to replace the solid disk with an electrically conducting fluid. This change brings with it all the challenges of describing just the fluid flow; phenomena such as buoyancy and turbulence for example. How one can incorporate all these interactions together and provide means to supply useful engineering information is the main subject of this thesis.

1.3 Computational fluid dynamics

The study of fluid dynamics, and magnetohydrodynamics by extension, usually takes one of three approaches; physical experiments, analytical solutions, or numerical methods. It is important to state outright that these methods are (or should be) synergistic; ideally, one approach alone should not suffice.

Experimental methods, as perhaps the foundation of the scientific method, are undoubtedly invaluable. The nature of the fluids involved in MHD however, places unfortunate constraints on our ability to experiment with them. The most obvious electrically conducting fluids are liquid metals but these are either opaque, making internal visualizations difficult, or hostile to humans or other materials (mercury and sodium come to mind). Salt solutions do possess some level of electrical conductivity but it is usually so small that magnet systems become prohibitively expensive. These hurdles are in addition to the usual ones associated with undertaking experiments; the procurement and maintenance of equipment can be difficult and expensive. This is not to say experimental activity in MHD is non-existent and Chapter 2 will provide some insight into those which hold relevance to this thesis.

The other two approaches both begin with consideration of the mathematical equations that govern the problem at hand. Owing to the non-linear nature of the Navier-Stokes equations, the use of analytical methods to provide core engineering information, such as velocity or temperature distributions is, unfortunately, limited to only a few very simple types of flows. Most flows of industrial or environmental significance are invariably turbulent, involve further interactions from various body forces and usually present themselves in irregular and complex geometries. As a result, the use of numerical methods has significantly grown in popularity since their development during the 1950's and 1960's.

Computational Fluid Dynamics (CFD) offers, in principle, many advantages over experimental methods. Applied correctly, they can provide flexibility, are relatively cheap to

perform, provide access to the complete flow field, and allow one to easily undertake parametric studies, where the influence of flow or geometrical parameters can be varied systematically. Indeed this flexibility means, for some flow problems at least, that CFD may be the *only* realistic means by which they can be investigated. In addition, the exponential advancement in computational power over the last 50 years has helped accelerate and broaden the use of CFD. General purpose CFD codes are thus now very accessible[1] and a wealth of open-source and commercial packages are available.

There are a variety of modelling approaches which have been developed in CFD. A more detailed discussion on their merits will be saved for Section 4.2, but the most common modelling approach used in industry, and the approach taken in this thesis, is the Reynolds-averaged Navier-Stokes (RANS) approach. This solves an averaged form of the governing equations and uses mathematical models to incorporate the effects of turbulence on the mean flow. A hierarchy of modelling strategies are available (see, for example, Wilcox, 1998, and Hanjalic and Launder, 2011, for a detailed survey) and those under consideration in this thesis, the linear eddy-viscosity and stress-transport approaches, are discussed further in Chapter 4.

To include effects of an electromagnetic nature, such as those highlighted earlier in Section 1.2, these approaches are extended by the inclusion of additional terms. This thesis will address the ability and performance of these extended models by applying them to a series of test cases. The test cases are selected in order to cover a wide variety of physical phenomena and as wide range of flow parameters as possible. The first set of cases concerns the turbulent flow of an electrically conducting fluid down a channel bound by electrically insulating walls of infinite length. A uniform magnetic field is applied in a direction both parallel, and perpendicular, to the flow. The simplicity of the geometry and wealth of literature on ordinary fully-developed channel flows provides a means to measure the performance of models in relative isolation from other, less understood, flow phenomena.

The second set of cases investigate the effect of a magnetic field on three-dimensional, time-dependent, turbulent Rayleigh-Bènard convection. This represents a significant increase in complexity over the previous cases and aims to address how the models respond to the mutual effects of the buoyant and electromagnetic forces. Such a flow configuration may be found in materials processing, where metallic materials are subjected to both heat transfer and magnetic fields.

1.4 Objectives

The fundamental aim of this research is to explore the extent to which the Reynolds-averaged Navier-Stokes approach can reproduce the reported effects of buoyant and elec-

[1] In that you can download Code_Saturne or OpenFOAM readily from the internet. Being able to actually use the codes to produce something useful is, of course, a whole different matter!

tromagnetic forces on a series of increasingly complex test cases. The results, and subsequent analysis, should contribute to the general understanding of complex turbulence multiphysics flows and provide recommendations on how best to incorporate the effects of these body forces. Specific objectives for the thesis are set out below:

- To introduce and implement electromagnetic modifications to existing engineering type turbulence models, as identified in the literature, into the in-house finite-volume code STREAM.
- To apply these models to two classes of flow as described in Section 1.3. Qualitative and quantitative comparisons will be made with existing results where available.
- To identify the strengths and weaknesses of the tested models and identify areas for potential model development.

1.5 Outline of thesis

Chapter 2 begins with a survey of the current state of the art in MHD. It aims to provide both a better understanding of the physical phenomena surrounding MHD flows and a review of works which are relevant to the cases under consideration in this thesis. Chapter 3 details the equations which govern the evolution of MHD flows and addresses any simplifications which have been applied in this work. Chapter 4 looks at turbulence and provides details on the modelling approaches and specific models which have been applied. The extensions of these models to account for electromagnetic and buoyant forces is also provided. In Chapter 5 the numerical methods employed in this thesis are introduced and details are provided on the specific numerical code which was used. Modifications to the code, to account for the effects investigated here, are also provided. Chapter 6 presents the results of the first series of test cases which comprise one-dimensional and two-dimensional fully developed channel flows which are subjected to magnetic fields of different strengths and orientations. Then, Chapter 7 discusses the results of time-dependent simulations of magnetic Rayleigh-Bènard convection. Finally, Chapter 8 concludes the thesis and provides suggestions for further study.

CHAPTER

TWO

LITERATURE REVIEW

The objective of this chapter is to give an overview of the current state of the art in Magnetohydrodynamics and provide a summary of the phenomenology that can be observed in the flows considered in this thesis. Some attention is also paid to flows that, whilst not the main focus of this thesis, do provide valuable insight into the kinds of interactions and engineering applications that the presence of a magnetic field can bring. After a brief introduction in Section 2.1, Section 2.2 looks at both one-dimensional and two-dimensional fully developed channel flows and uses these to highlight some of the key MHD effects which feature throughout this thesis. Then, Section 2.3 first gives a brief survey of works on non-magnetic Rayleigh-Bènard convection before looking at literature dealing with the effects of both a vertical and horizontal magnetic field. Following this, Section 2.4 looks at a few examples of other electromagnetically influenced convective flows whilst Section 2.5 looks at some specific engineering applications, including magnetic dynamos, targeted drug delivery and materials processing. Finally, Section 2.6 provides some remarks that conclude the chapter.

2.1 Introduction

As highlighted in Chapter 1, the range of flows which are covered by MHD is large. It is just as readily applied to the interactions between the solar wind and the Earth's magnetic field as it is to the magnetic realignment of grain boundaries in crystal growth applications. For these two examples in particular, not only are the characteristic length and velocity scales vastly different, there is likely to be great difference in electric conductivity and characteristic magnetic field strength as well. Much like in regular hydrodynamics however, the value of certain dimensionless quantities helps classify the behaviour of these systems. One of these, which will better allow us to classify MHD flows in particular, is the magnetic Reynolds number;

$$Re_m = \frac{U_0 L}{\eta} = \mu_0 \sigma U_0 L \tag{2.1.1}$$

where $\eta = (\mu_0 \sigma)^{-1}$ is the magnetic diffusivity, μ_0 is the permeability of free space, σ is the electrical conductivity, and U_0 and L represent characteristic velocity and length scales respectively. A more mathematical derivation is provided later in Chapter 3 but, physically, it represents the ratio between advection and diffusion of the magnetic field. This, in effect, provides a measure of the relative importance of the two observable effects discussed in Section 1.2.

For a situation in which $Re_m \gg 1$ (as $\eta \to 0$) then diffusion becomes insignificant over the length scale L and the magnetic field lines will advect with the flow; that is, since they do not diffuse, they appear to be frozen into the fluid as the fluid moves. This is usually the case in astrophysics, where the length scales involved are enormous. Here, the effect of the fluid motion on the magnetic field far outweighs the effect of the magnetic field back onto the fluid (effect I) . The opposite of this, when the magnetic field influences the fluid velocity but the fluid velocity does not significantly perturb the magnetic field (effect II), is obtained when $Re_m \ll 1$. Most laboratory experiments or industrial processes fall into this category. For example, if a flow of mercury was placed in a channel with a characteristic length of $L \sim 0.1\,\mathrm{m}$ and a velocity such that $0.01\,\mathrm{m\,s^{-1}} < U < 1\,\mathrm{m\,s^{-1}}$, then given that mercury has a conductivity of $\sigma \approx 10^6\,\Omega^{-1}\mathrm{m}^{-1}$ (and hence a magnetic diffusivity of $\eta \approx 1\,\mathrm{m^2\,s^{-1}}$, given that the permeability of free space is defined as $\mu_0 = 4\pi \times 10^{-7}\,\mathrm{N\,A^{-2}}$), the magnetic Reynolds number would be $0.001 < Re_m < 0.1$.

The literature in MHD is broadly split into two, following the above two flow regimes. For this thesis, the main focus will be on the latter regime ($Re_m \ll 1$) since it is more applicable to engineering and industrial type applications. In addition, restricting attention to this class of flows allows some simplification of the governing equations to be made. These will be formalized in Chapter 3.

2.2 Closed channel flow

As far as choosing a flow configuration to begin an investigation into the fundamental phenomena of magnetohydrodynamics, a flow of conducting fluid down a channel is fairly ideal. Electromagnetic influence can be investigated through the imposition of magnetic fields and the large wealth of knowledge accumulated for flows of non-conducting fluid, combined with their geometric simplicity, will help to expose the various electromagnetic effects. As with ordinary hydrodynamic channel flows, the non-dimensional Reynolds number quantifies the relative importance of inertial forces and viscous forces;

$$Re = \frac{\rho U_0 L}{\mu} \tag{2.2.1}$$

where ρ and μ are the fluid density and viscosity respectively, U_0 is a characteristic velocity scale and L represents a characteristic length scale. If the characteristic velocity is instead chosen to be the friction velocity U_τ, which is related to the wall shear stress τ_w by $U_\tau = \sqrt{\tau_w/\rho}$, then one arrives at another commonly used form of the Reynolds number;

$$Re_\tau = \frac{U_\tau L}{\nu} \tag{2.2.2}$$

If the fluid is electrically conducting, the addition of a magnetic field will introduce the Lorentz force. Two non-dimensional parameters are typically used in the literature to describe the relative importance of this to the viscous forces and the inertial forces; the Hartmann number, Ha, and interaction parameter[1], N, respectively;

$$Ha = B_0 L\sqrt{\frac{\sigma}{\mu}}, \qquad N = \frac{\sigma B_0^2 L}{\rho U_0} = \frac{Ha^2}{Re} \tag{2.2.3}$$

where σ is the electrical conductivity, and B_0 is the characteristic magnetic field strength. Some sources prefer to use the Chandrasekhar number, Q, which is simply the square of the Hartmann number; $Q = Ha^2$. For consistency, the Hartmann number is used throughout this thesis.

2.2.1 Uniform magnetic fields

To begin, consider a steady laminar flow of an electrically conductive fluid through an infinitely long rectangular duct such as the one shown in Figure 2.1. Here, the flow is driven by a streamwise pressure gradient and a magnetic field of strength B_0 has also been imposed in the y direction. If the side walls (coloured grey in the figure) are placed sufficiently far apart ($b \gg a$), then their viscous effects will not extend to the centre of the channel and the flow reduces to one-dimensional Poiseuille flow. In the hydromagnetic

[1] Some texts refer to this as the Stuart number.

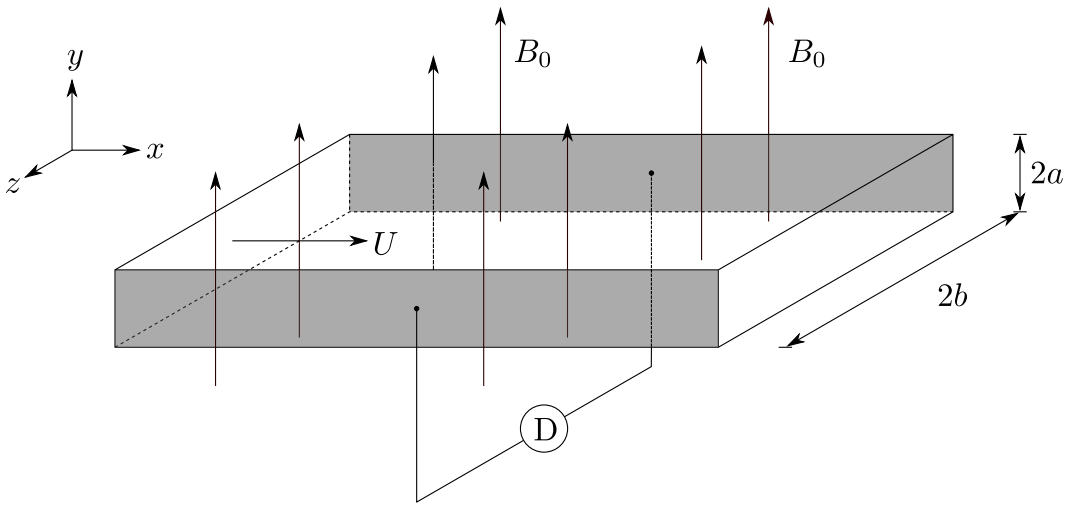

Figure 2.1: Duct flow of electrically conducting fluid through an imposed magnetic field, B_0.

case ($B_0 = 0$), the solution of the problem produces the well-known parabolic velocity distribution in the y direction and the bulk velocity will be proportional to the applied pressure gradient.

When $B_0 > 0$, we arrive at the magnetohydrodynamic equivalent of Poiseuille flow: Hartmann flow. Although, as with Poiseuille flow, the stipulation that $b \gg a$ ensures the side walls do not influence the flow in a hydrodynamic sense, as shall become clear below, their electromagnetic influence is not, in general, negligible and will depend on their electrical properties and whether or not they are connected by any external electrical circuit.

Hartmann flow

The name "Hartmann flow" resulted from the extensive analytical and experimental investigations carried out by Hartmann (1937) and Hartmann and Lazarus (1937). This sparked a wealth of literature on the subject (see, for example, Davidson (2001), Roberts (1967a), Shercliff (1965) or Branover (1978) for a review) and, as a result, the qualitative behaviour of these flows, in the laminar regime at least, is relatively well understood.

In this flow, the motion of the conducting fluid across the magnetic field lines induces a current in the z direction (much like it did with the Homopolar dynamo example in Section 1.2). This then interacts with the magnetic field to create a Lorentz force, directed in opposition to the flow. This Lorentz force is linear in U, and thus tends to homogenize the velocity profile. The problem was first solved analytically by Hartmann (1937) and the resulting velocity profiles, scaled by bulk velocity, are reproduced in Figure 2.2a for varying magnetic field strengths (Ha). The Lorentz force can be seen to cause both a

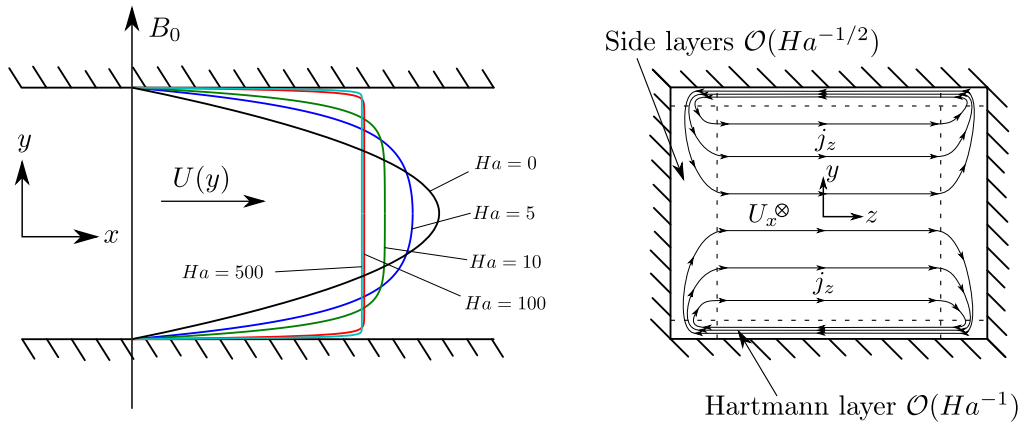

(a) (b)

Figure 2.2: Schematic representation of Hartmann flow with (a) velocity profiles superimposed, given analytically in Hartmann (1937), for a series of Hartmann numbers to scale and (b) the current closure paths in a channel of rectangular cross-section.

reduction in centreline velocity and boundary layer thickness. These thin boundary layers are known as Hartmann layers. They form along walls normal to the magnetic field, which are thus typically called Hartmann walls, and their thickness scales as $\mathcal{O}(Ha^{-1})$. The development and stability of these layers has been extensively researched (see, for example, Lingwood and Alboussière (1999), Krasnov et al. (2004), Moreau et al. (2007) and Roberts (1967b)).

The balance of forces in the channel however, is not as transparent as it might seem. Hartmann flow, as an idealization of a steady two-dimensional flow, is realized from the stipulation that $b \gg a$. Note though, that the direction of the induced current is in the z direction. What happens to this current then, will depend on the electrical properties of the side walls and the existence of any external electrical circuit. The two extremes, having walls either perfectly insulating or perfectly conducting[1], will both be considered in turn.

If the side walls are perfectly insulating, then the conservation of charge means the net current carried across the duct must be zero. The only option is for the current to form closed loops within the fluid. Indeed, as the current moves charges across the flow (in the $+z$ direction), the resulting charge separation created between the side walls sets up an electric field, E_0 say, which turns them back towards the other wall. These return currents, taking the path of least resistance, will travel in the Hartmann layers, where the flow velocity (and hence induced current) falls to zero. These current loops are shown schematically in Figure 2.2b. In the Hartmann layers then, the current flows in the *negative* z direction and the Lorentz force actually *accelerates* the flow. Additionally, since the net current in a given duct cross section must be zero, the net Lorentz force acting on

[1]That is, their conductivity is infinite.

the flow must also be zero. Thus, for an insulating duct in which the mass flow rate is kept constant, the Lorentz force can only modify the pressure gradient indirectly, by acting to increase the viscous forces in the boundary layer.

If the side walls are perfectly conducting, then the current distribution will be determined by the state of any electrical circuit which exists between the side walls (represented by the device "D" in Figure 2.1). If the device consists of a wire with zero resistance, then the currents return through this and no electric field E_0 will be created between the side walls. In the fluid, the current flows, unopposed, entirely in the positive z direction and the net current, and hence net Lorentz force, across the duct cross section is no longer zero[1]. In addition, the current density across the flow will be higher[2] (since it is unopposed) and this leads to a stronger Lorentz force which now opposes the velocity across the entire channel. The Hartmann layers still form, since continuity of the velocity ensures it must increase in the near-wall region to compensate the decelerating effect of the Lorentz force in the channel centre. The pressure gradient now balances both the Lorentz force and the viscous forces.

Actually, it should be noted that in both of the above cases, for a given Ha, the shape of the velocity profile (given in Figure 2.2a) is identical. The existence of an electric field E_0 in the spanwise direction, which depends on electrical configuration of the side walls and external circuit, only serves to change the relationship between the mean velocity and the pressure gradient[3]. Thus, one can modify the mass flow rate in the channel simply by changing the electric field across the duct. This is exploited in a range of simple MHD devices. If the device supplies electric current to the fluid (enough to overcome that which is induced by the flow) then it can create bulk Lorentz forces which accelerate the flow and the device represents a pump. If the device consumes electrical energy, then the Lorentz force opposing the flow increases and an increase in pressure gradient is required to maintain a constant mass flow rate and power the device. A third option, is to simply connect a voltmeter between the side walls and measure the electric field which is induced; the mean velocity will be proportional to the electric field and the device functions as a flow meter. A more extensive overview of such devices is provided by Sutton and Sherman (2006).

Ducts of finite aspect ratio

In the previous section it was noted that although the viscous effects of the side walls could be ignored if $b \gg a$, some consideration needed to be paid to their electromagnetic effects. Here, ducts where $b \sim a$ are considered and the effect of the magnetic field on

[1] The integral of the current around the entire path (fluid and external device) is still zero of course.
[2] If compared with insulating walls for the same mass flow rate.
[3] Proof of this is provided in Subsection 6.3.1.

the velocity profiles in the spanwise direction is investigated. As one might envisage, the relative conductivities of the four walls will influence the current paths and the distribution of the Lorentz force.

In a fully insulated duct, it was observed previously that the electric current is turned along these walls and travels back across the duct in the Hartmann layers. Along these side walls then, the current must have a non-zero component in the y direction. Since this is parallel to the magnetic field, the Lorentz force is not as active and, as Shercliff (1953) showed, the boundary layers along these walls are thicker and scale as $\mathcal{O}(Ha^{-1/2})$. They are termed Shercliff layers and are shown schematically in Figure 2.2b.

Solutions in a fully conducting duct have been obtained by Chang and Lundgren (1961). Here the conducting walls provide the return path for the current and the situation is much like in the previous section when the perfectly conducting side walls were connected with a wire of zero resistance. The Lorentz force is much stronger than in the case with insulated walls but, since it does not change the shape of the velocity profile in the y direction, it only serves to modify the pressure gradient. In the z direction, normal to the side walls, both Hunt and Stewartson (1965) and Lundgren et al. (1961) noted that for high Hartmann numbers there was a small velocity peak which occurred towards the walls. This is of the same order as the velocity in the core and results from some slight curvature in the current paths as they enter the wall. Since here the current returns through the Hartmann walls, rather than some idealized external circuit, the current must turn to travel down through the side walls. This turning extends slightly into the fluid, resulting in a slight decrease in Lorentz force and a corresponding increase in velocity.

The final combination of wall conductivities which is worth mentioning, is that obtained when the Hartmann walls are perfectly conducting and the side walls are perfectly insulating. This case was also investigated by Hunt (1965) and Hunt and Stewartson (1965) and leads to an intriguing velocity distribution in the direction normal to the side walls (z). Since the side walls are perfectly insulating, the current generated in the centre of the channel turns as it reaches the side walls and travels towards, and into, the Hartmann walls. Since the Hartmann walls provide the path of least (well, exactly zero) resistance, no current will travel back across the channel in the Hartmann layers. There are two consequences of this. The first, is that since the current turns along the side walls, towards a direction parallel with the magnetic field, the Lorentz force vanishes in the side layers. The second, is due to the path of the currents being in the Hartmann walls rather than the Hartmann layers. As a result, the net current within the fluid is not zero, and the Lorentz force in the core of the channel is much stronger than in the case when the Hartmann walls are insulating. This leads to the formation of the so-called M-shaped velocity profiles where two large velocity peaks, of order $\mathcal{O}(Ha)$, are produced in the side layers.

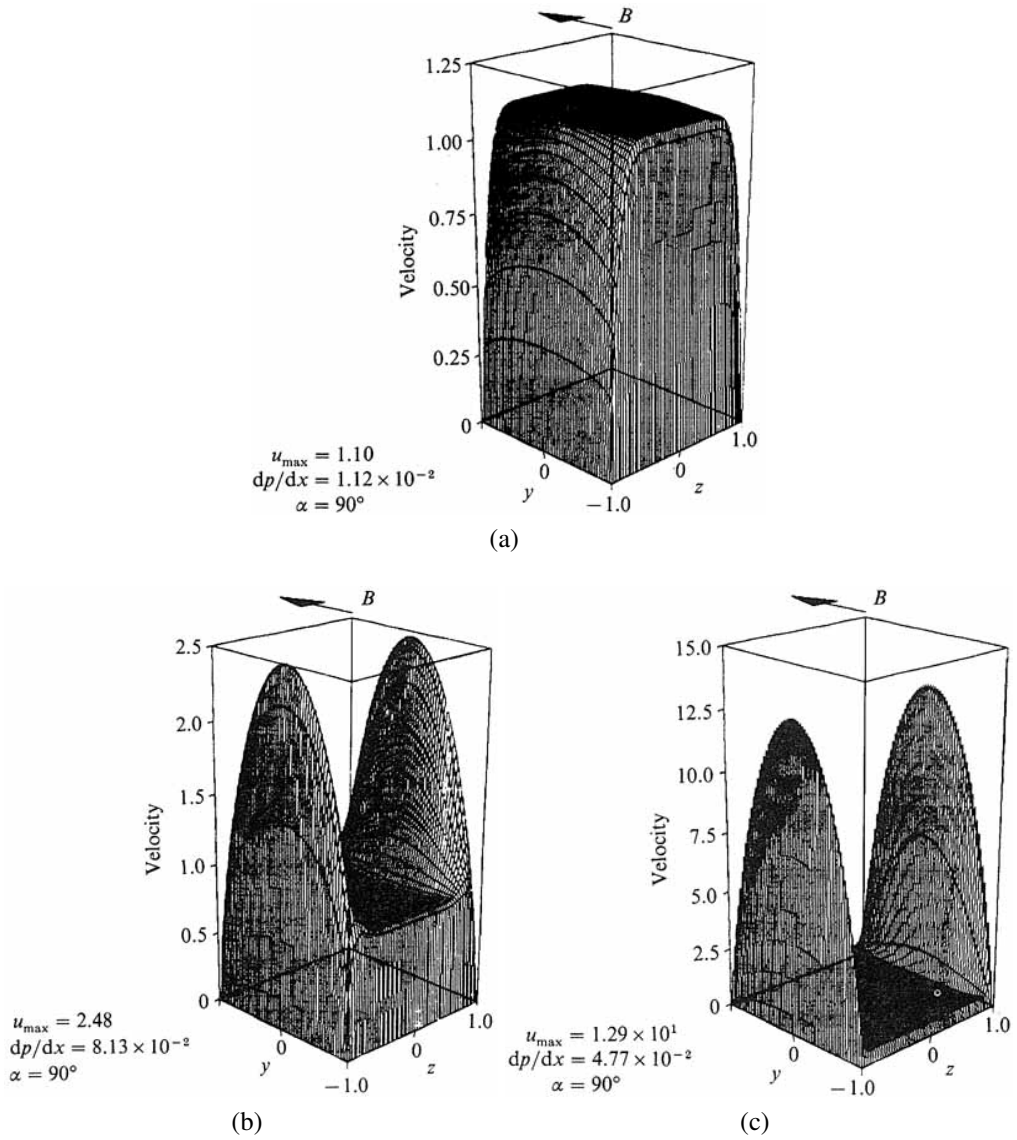

Figure 2.3: Velocity profiles obtained by Sterl (1990) for the fully-developed two-dimensional flow of conducting fluid down a duct of square cross-section with different wall conductivities: (a) all walls insulating at $Ha = 100$ (b) conducting Hartmann walls with insulating side walls at $Ha = 100$, and (c) the same but at $Ha = 1000$.

Numerical results for a selection of the flows described above, at Hartmann numbers up to 1000, have been obtained by Sterl (1990). Velocity profiles are presented in Figure 2.3 in the form of a three-dimensional surface above the cross-section of the duct. When all the walls are fully insulating, Figure 2.3(a) demonstrates the flattening of the velocity profile in the core and both the Hartmann and side layers are readily identified. For the case where the Hartmann walls are conducting and the side walls are insulating Figures 2.3(b) and 2.3(c) show the quite striking formation of the side wall jets. As the Hartmann number increases the magnitude of the peaks increases at the expense of the velocity in the core.

The preceding discussion has focused on MHD flows in the laminar regime, with the intention of highlighting the variety of ways in which the Lorentz force can transform the flow. Now the effect of the magnetic field on the turbulence will be considered in more detail.

Magnetic damping

Returning to the investigations of Hartmann and Lazarus (1937), one of the other major observations was that an applied magnetic field could reduce turbulence levels within a turbulent flow, even to the extent that the flow would relaminarize. Hartmann determined the state of the flow by measuring the pressure drop across the test section and comparing the result with theoretical values for purely laminar flow. What he found was that as the magnetic field strength was increased over a turbulent flow, the pressure gradient across the flow initially decreased before then rapidly rising after the flow transitioned to a laminar regime. He thus reasoned that the initial decrease was due to the damping effect of the magnetic field on the turbulent fluctuations, whilst the latter increase was due to the effect of the bulk Lorentz force, which served to brake the flow. This suggests that the magnetic field can modify the turbulence directly, by damping velocity fluctuations, and somewhat indirectly, by changing the mean velocity profiles. Hartmann noted however, that separating these effects was not trivial.

Later experiments by Murgatroyd (1953) largely confirmed the above results and further showed that it was possible to obtain laminar flow at Reynolds numbers up to $Re = 10^5$ so long as the Hartmann number was such that $Re/Ha < 900$. Reed and Lykoudis (1978) obtained experimental measurements of the turbulent shear stress in a flow of mercury through a wall-normal magnetic field. They noted that the magnetic field tends to suppress the turbulent shear stress more effectively than the individual velocity fluctuations that comprise it.

Given the general tendency for the magnetic field to damp and oppose fluid motion in the examples discussed so far, the observation that it can directly damp out turbulent fluctuations is not particularly surprising. In the absence of magnetic fields, turbulent energy is eventually dissipated as heat by molecular action. The addition of the magnetic field invites a further dissipation mechanism which is termed Ohmic or Joule dissipation (Davidson, 2001). Physically, this arises from the presence of electric currents in the flow which cause Ohmic heating.

Several theoretical and experimental studies have addressed the implications of Joule dissipation on the structure of the turbulence. Moffatt (1967) examined the decay of initially isotropic turbulence in a strong magnetic field and found that the turbulence became increasingly two-dimensional in the sense that it was independent of the direction parallel to the magnetic field[1]. This was confirmed to some extent by the experiments of Kolesnikov and Tsinober (1974) and Alemany et al. (1979) which looked at the decay of grid generated turbulence in the presence of a magnetic field. More detailed numerical studies of

[1] That is, the velocity fluctuations were found to not vary, or vary slowly, in the direction of the magnetic field.

the same (Hossain, 1991; Schumann, 1976; Zikanov and Thess, 1998) agreed with these findings but noted that a purely two-dimensional state was generally not achieved.

Explanations for this transition were provided by Sommeria and Moreau (1982), who argued that an electromagnetic diffusion-like process caused vorticity to diffuse in a direction parallel to the magnetic field, leading to turbulent eddies which are elongated in that direction. Davidson (1995, 1997), however, provided a more rigorous explanation. He argued that the propagation of vorticity along the magnetic field lines was a direct consequence of the need for the fluid to conserve angular momentum despite a continual decline in kinetic energy, courtesy of Joule dissipation. Since the details provide useful insight into the more general evolution of vortices in MHD flows, they are offered here.

Consider an inviscid fluid which is vigorously stirred before being left to itself in a large electrically insulated sphere. The radius of the sphere is taken such that it is much larger than any integral length scale associated with the flow[1] and a uniform magnetic field is applied. Clearly the velocity fluctuations associated with the isotropic turbulence will interact with the magnetic field to induce currents. The resulting Joule dissipation will ensure that the kinetic energy of the flow decreases monotonically. Note also, that since the sphere is electrically insulating, the net current within the sphere will be zero since the current paths must necessarily form closed loops. If the net current is zero, the net Lorentz force must also be zero and, since this is confined to the plane normal to the magnetic field, it cannot provide any net torque to the fluid in that direction. Consequently, the component of angular momentum parallel to the magnetic field must be conserved.

This presents somewhat of a conundrum. Conservation of angular momentum implies the flow cannot come to rest. Yet so long as Joule dissipation is finite, the kinetic energy of the fluid must continue to fall. The only way to satisfy these requirements is for the flow to evolve in such as way as to reduce the current density, and hence Joule dissipation, to zero. Davidson (1995) shows that this occurs when the velocity becomes independent of the direction parallel to the magnetic field. It follows then, that the flow must evolve into one which is strictly two-dimensional and which contains vortices elongated and stretched along the direction of the magnetic field lines. Obviously any real flow is viscous and this stretching will thus be accompanied by viscous dissipation.

Since the above argument can also be applied to isolated vortices, which are such fundamental structures in fluid flows, it can be used to provide guidance on how many different types of MHD flows will evolve. Indeed, this point will be revisited in Section 2.3 as it serves to explain phenomena which arise when magnetic fields are applied to convective flows. To now close this subsection on channel flows with uniform magnetic fields, a brief summary of more recent numerical works is provided.

[1] large enough that the timescale of any viscous effects from the boundary is much larger than any timescale associated with processes in the flow.

Numerical simulations of fully turbulent MHD channel flows

In the time since Hartmann, computational power has improved vastly and a number of numerical studies have tackled the problem of fully turbulent MHD channel flow. Lee and Choi (2001) presented a DNS study of a turbulent MHD channel flow ($Re = 4000$) in which a moderate magnetic field ($17 \leq Ha \leq 42$) was applied in each of the orthogonal directions and the walls were electrically insulating. They found that in the case of a wall-normal or spanwise magnetic field all turbulent intensities decreased significantly and that in all cases the turbulent structures were elongated in the direction of the applied field. They additionally showed that this elongation is associated with a rapid decrease of Joule dissipation. This was in agreement with a later study by Krasnov et al. (2008), who also noted reductions in skin friction except when a wall-normal magnetic field exceeded a certain value. Here, as also reported by Satake et al. (2002) and Chaudhary et al. (2010) in similar studies, the increase in drag due to the thinning Hartmann layers (i.e. the Lorentz force) exceeded the drag reduction due to turbulence suppression.

A recent DNS study by Krasnov et al. (2012) for flow down an insulated rectangular duct was reported for $Re = 10^5$ and $0 \leq Ha \leq 300$. A snapshot of the instantaneous velocity field is reproduced in Figure 2.4 which clearly demonstrates the laminarization effect of the magnetic field. At $Ha = 100$ the core develops a sizeable laminar region, which extends into the Hartmann layers (top and bottom walls) at $Ha = 200$. At $Ha = 300$ the turbulent side layers become much thinner and further analysis revealed two distinct zones. Very close to the side walls was a layer dominated by small-scale structures without any observed anisotropy. In between the laminar core and this small layer, however, was a zone dominated by large vortices with axes approximately aligned with the magnetic field. Generally, the average velocity fluctuations are reduced for all Hartmann numbers considered. An exception was noted near the Hartmann walls for $Ha = 100$, where stronger mean shear increased turbulent production. Excluding this exception, the findings corroborate those of earlier studies and show excellent agreement with an LES study in the same parameter range by Kobayashi (2008).

A selection of further DNS studies, which provide data useful for model validation, can also be found in the literature. The DNS database of Noguchi et al. (2004) openly provides results for a variety of low-Re one-dimensional channel flows including those with an applied wall-normal and longitudinal magnetic field. Data from this database will be used to provide comparisons in Chapter 6. Data at higher Reynolds numbers ($1120 \leq Re_\tau \leq 1194$) and higher magnetic fields ($0 \leq Ha \leq 32.5$) has been obtained in a study by Satake et al. (2006), who investigated the effect of a wall-normal magnetic field on turbulent Hartmann flow. They found that large scale turbulent structures were reduced in the centre of the channel.

It is evident thus far that the applications of a magnetic field can induce significant anisotropy in the turbulent stresses. Whilst approaches such as DNS, which resolve the

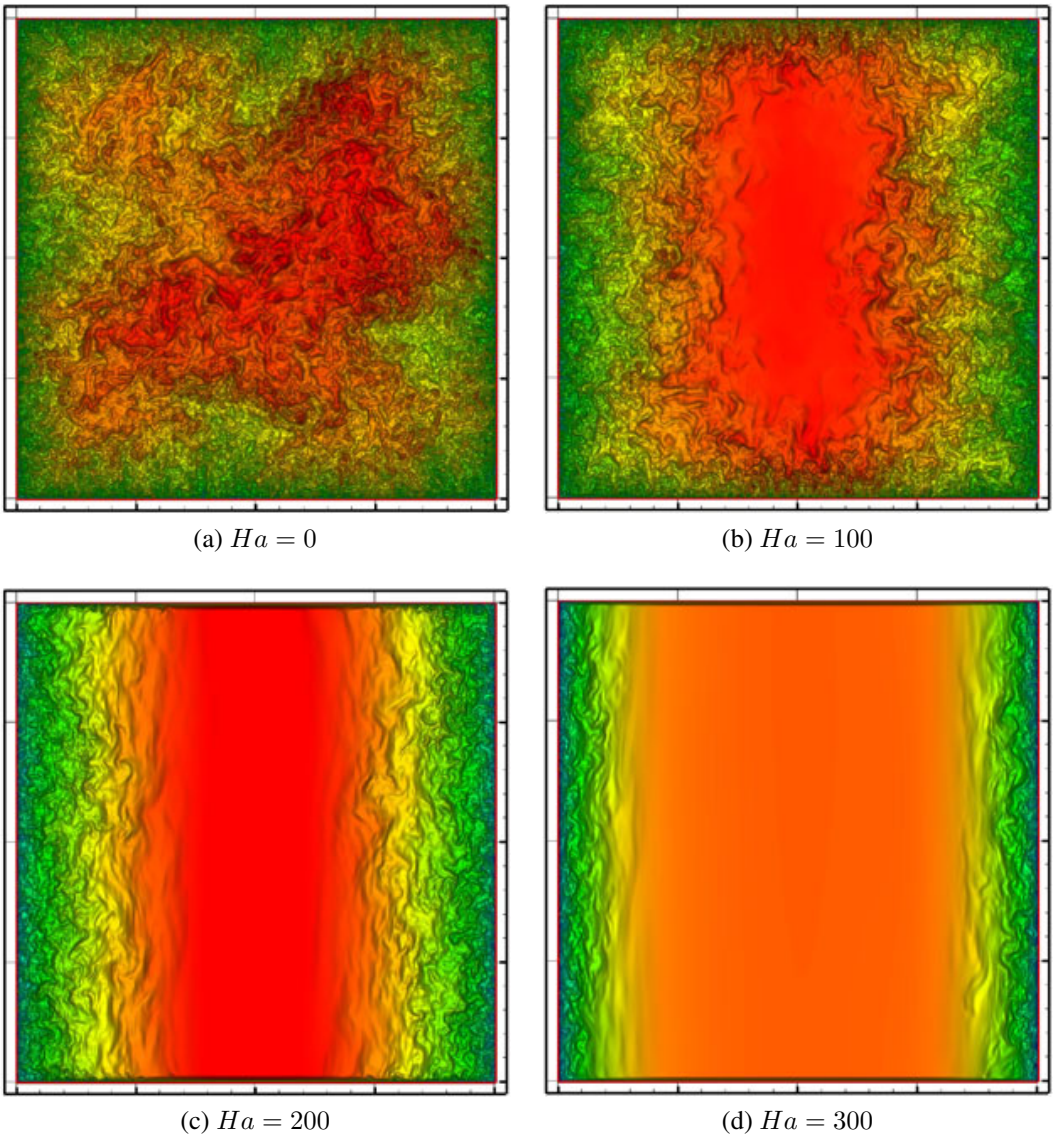

(a) $Ha = 0$ (b) $Ha = 100$

(c) $Ha = 200$ (d) $Ha = 300$

Figure 2.4: Instantaneous distributions of streamwise velocity plotted on a cross-section through an insulating channel and subjected to a uniform vertical magnetic field; $Re = 10^5$. Contour levels are the same in all plots ranging from 0 (blue) to 1.25 (red). The very sharp velocity gradients at the walls render the boundary layers almost invisible. From Krasnov et al. (2012).

full spectrum of length scales, will inherently capture this, the linear eddy-viscosity class of model within the RANS approach will not directly[1]. Despite this, Ji and Gardner (1997) showed that inclusion of additional electromagnetic sink terms in the equations for turbulent kinetic energy, and its dissipation, could qualitatively reproduce the damping effect of a magnetic field on turbulent pipe flow. The additional terms, however, made use of a bulk parameter (the interaction parameter, N) to correctly scale the damping; a practice not common or desirable in turbulence modelling because of the difficulty in evaluating such a parameter in a more general flow configuration. Kenjereš and Hanjalić (2000) removed this limitation by making use of a local interaction parameters, defined using

[1] the reasons for this will be further explored in Chapter 4.

the local turbulent timescale. A priori testing of the model against the DNS database of Noguchi et al. (2004) showed considerable improvement over the model by Ji and Gardner (1997). Further, full, numerical simulations of a high-Re channel flow showed good agreement with experimental data. The latter case considered the effects of the fluid entering and leaving a region with a magnetic field; something which will be discussed further in the next section.

The second-moment approach to closure within the RANS framework does provide means to account for anisotropic effects, but the literature on their use in electromagnetic flows is limited. Widlund et al. (1998) transported an additional scalar parameter which contained information on the dimensionality and anisotropy of the turbulence that was affected specifically by electromagnetic effects. Application of the model to a case of decaying turbulence in the presence of a magnetic field showed good agreement with DNS data. Kenjereš et al. (2004) extended the RANS second-moment approach to account for the effects of magnetic fields in analogy with general practices for modelling effects of body forces. The model was tested against a series of magnetic channel flows and showed good agreement with experimental and LES data. Thus the approaches tested as part of this thesis, described later in Chapter 4, are based on these forms.

Away from simple channels, the implications of magnetic fields have also been investigated in other classically studied flows, including expanding channels (Walker et al., 1971, 1972; Walker and Ludford, 1974a,b, 1975), backwards facing steps (Abbassi and Ben Nassrallah, 2007) and impinging jets (Lee et al., 2005).

2.2.2 Non-uniform magnetic fields

Although the flows reported in the previous section offer great insight, they are not entirely realistic of many applications. Most MHD flows in engineering applications will be subject to magnetic field gradients, mainly due to physical restraints on the size of magnets. Here attention is paid first to flows that enter through the fringe regions of uniform magnetic fields and second to flows past localized highly non-uniform fields, which draw similarities with bluff bodies. As shall become clear, these magnetic "fringe" regions can have a dramatic effect on the development of the flow.

Fringing magnetic fields

Fringing magnetic fields, areas where the magnetic field strength increases over a short distance, are common in industrial settings. Magnet systems are usually limited in size, either by their sheer mass or by their cost, and this means that fluids will inevitably have to pass into and out of regions where the magnetic field strength is non-zero. In addition,

any real magnetic field is necessarily three-dimensional and thus a supposed “uniform“ magnetic field within the magnet system can only be idealised.

To illustrate the implications this has for the development of the flow, consider a two-dimensional channel flow which is subjected to a uniform magnetic field over only part of its length. The walls are assumed to be electrically insulated. As the flow enters the magnetic field region, the magnetic field strength obviously must rise from zero far upstream of the magnet to some finite characteristic value within the centre of the magnet over some distance. If this distance is small enough compared with the channel height, then a stepwise change in magnetic field strength can be assumed. This is shown schematically in Figure 2.5 where the magnet region is shaded grey. The magnetic field here is in the positive z direction, or out of the page.

As the fluid passes into the magnetized region, the motion of the fluid will interact with the magnetic field in the usual fashion to generate an electric current in the negative y direction. Since the current must form closed loops, it closes *outside* of the magnetic region where, although there is no EMF (since $B = 0$), there must exist an electric field to drive the currents back across the channel. In the magnetic region, this current combines with the magnetic field to induce a Lorentz force which strongly opposes the motion in the centre of the channel, as illustrated in Figure 2.5. At the top and bottom of the current loop the current flows parallel to the flow direction, but, since this is still perpendicular to the magnetic field, Lorentz forces appear which are directed towards the centre of the channel. This arrangement of the Lorentz force will lead to the generation of vorticity in the top and bottom half of the channel, of opposing sign, as the flow passes into the magnetized region. The result of all this is the formation of an M-shaped velocity profile, with strong deceleration in the core and corresponding acceleration towards the walls.

After the flow has passed this region, the currents it generates are balanced by the electric field since there is no path of lower resistance for them to traverse back across the channel (unlike in the Hartmann flow case, where this was through the Hartmann layers). The Lorentz force is thus inactive across the bulk of the magnetized region and viscous forces begin to transform the flow back into its pre-magnetic state. As the flow then leaves the magnetized section, current loops form in a similar fashion to that at the entrance but loop in the opposite sense. The flow experiences the same arrangement of Lorentz forces and is similarly distorted. If the length of the magnetized section is short, such that viscous forces have not fully smeared out the original disturbances in the velocity profile, then the effect will multiply and the magnitude of the wall jets increases.

The development of the velocity profile throughout the channel is shown schematically in Figure 2.5. The effect starts noticeably forming for interactions parameters around $N = 0.2$ and increases steadily with N. Velocity distributions in the plane parallel to the magnetic field ($x - z$) are Hartmann like, becoming increasingly flatter as N increases (Branover, 1978).

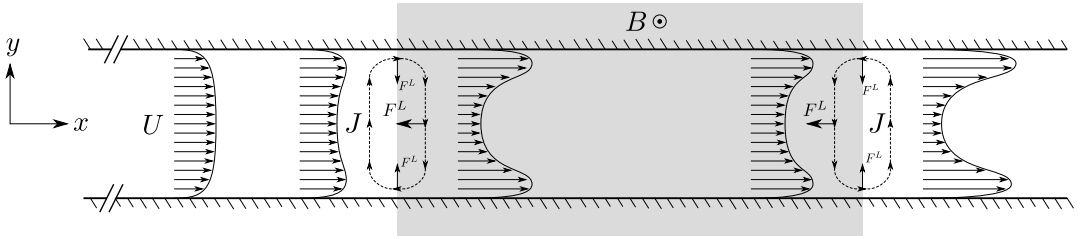

Figure 2.5: Schematic diagram of a flow of conducting fluid through a region of non-zero magnetic field strength. Note the formation of current loops at the entrance and exit to the magnetized region, which generate strong decelerating Lorentz forces.

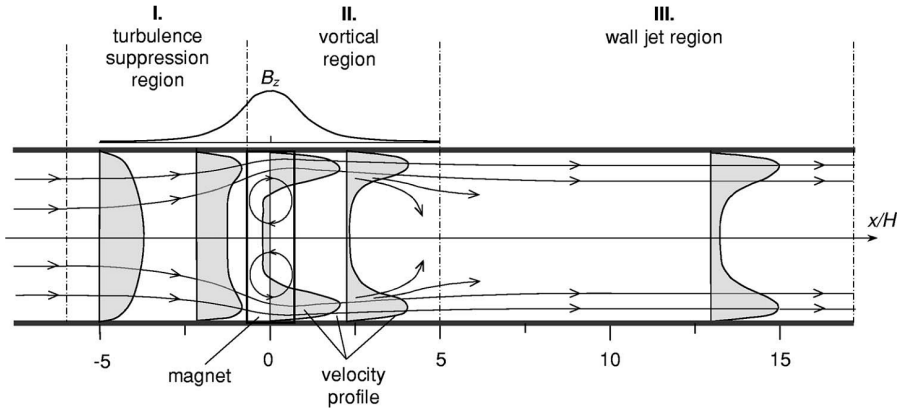

Figure 2.6: Conceptual structure of a flow of liquid metal through a small magnetized region. Three distinct regions are identified. From Andreev et al. (2007).

The above flow pattern has been demonstrated in numerous experimental studies (Andreev et al., 2007; Bocheninskii et al., 1971; Sukoriansky et al., 1986). In the study by Andreev et al. (2007) flow of a gallium based eutectic alloy was placed in an insulating channel with only part of its length subjected to a uniform magnetic field. For a range of Reynolds numbers $(5 \times 10^2 \leq Re \leq 1.6 \times 10^4)$ and fixed Hartmann number $(Ha = 400)$ they report three distinct regions in the complex flow structure, reproduced in Figure 2.6. In the first region, the turbulent suppression region, the intensity of velocity fluctuations was reduced by 8-10 times that of the initial flow. In the second region, the vortical region, the sharp increase in magnetic field strength deforms the velocity profile into an M-shape with large wall jets flanking a stagnant central region. After the flow has left the magnetic field, the velocity in the central region increases but the flow remains dominated by the wall-jets which grow in width as the recovering turbulent fluctuations destabilise the flow. This behaviour is in clear agreement with that described earlier in Figure 2.5.

Complementary 3D numerical simulations by Votyakov and Zienicke (2007) with the same interaction parameters, though laminar, found excellent agreement with the results by Andreev et al. (2007) adding that a swirling flow in the duct corners was responsible for the redistribution of the velocity profile back into a parabolic one. Numerical simulations in the turbulent realm $(Re = 2 \times 10^5, Ha = 700)$ were carried out by Kenjereš and

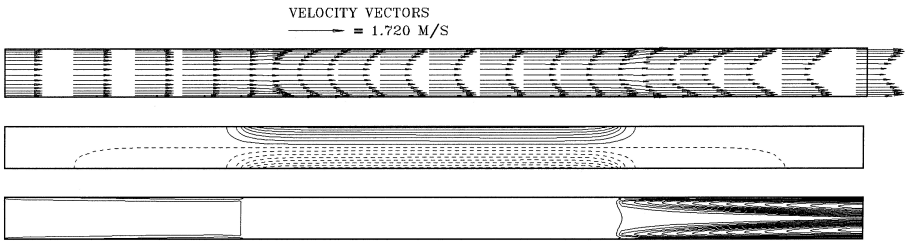

Figure 2.7: Velocity vectors, electric potential and turbulent viscosity distribution for the flow of liquid metal through a rectangular duct with part of its length subjected to a uniform magnetic field. From Kenjereš and Hanjalić (2000).

Hanjalić (2000) who used an electromagnetically modified $k-\varepsilon$ model. Their results, reproduced in Figure 2.7, showed successful reproduction of the M-shaped velocity profile and offered improvements over an earlier model by Ji and Gardner (1997).

Magnetic Obstacles

It was seen in the previous section that the fringe regions at the entrance and exit to a magnetized section of a channel flow caused substantial modifications to the flow structure. By reducing the magnetized section to a small localized area of the flow, this retardation is spatially confined and can be better described as an obstruction or magnetic obstacle (Cuevas et al., 2006b).

The idea of an obstruction in the flow naturally draws similarities with that of solid obstacles. As one of the classical fluid dynamics cases, the latter has a long history of intense investigation and the results are qualitatively well understood (see, for example, Williamson, 1996). Whereas these flows are governed solely by the Reynolds number, the additional parameter provided by the magnetic field allows for a far richer variety of flow regimes. Votyakov et al. (2007) showed, through both 3D laminar numerical simulations and complementary experiments, that the flow undergoes two bifurcations. The first occurs when the interaction parameter exceeds some critical value and leads to the formation of a vortex pair inside the magnetic obstacle. The second, which has a greater dependence on the Reynolds number, results in the formation of co-rotating attached vortices, analogous to those trailing solid obstacles. This co-rotating nature ensures that a third pair of interconnecting vortices are established and hence a complex six vortex pattern emerges as illustrated in Figure 2.8.

Earlier 2D numerical results by Cuevas et al. (2006a,b) failed to predict this six-vortex pattern, instead observing the unsteady generation of a single vortex pair which was eventually shed by inertially driven shear layers. This point was explored in detail in a series of papers by Votyakov and Kassinos (2010) and Votyakov et al. (2008). Their 3D numerical simulations, initially in the same parameter range as Cuevas et al., showed that the vortex

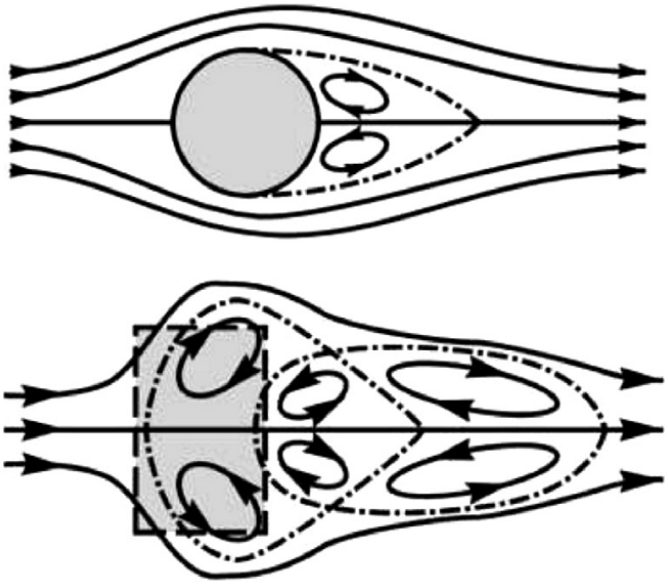

Figure 2.8: Diagram demonstrating the similarity concepts between flow around a solid obstacle (top) and a magnetic obstacle (bottom). Note the complex wake pattern trailing the magnetic obstacle, formed of three vortex pairs. Originally from Votyakov et al. (2008), adapted by Kenjereš et al. (2011).

structures were helical in nature and it was this secondary flow which stabilized the vortices and allowed development of the six-vortex pattern. Upon increasing the Reynolds number $(Re = 900, Ha = 90)$ Votyakov and Kassinos (2009) observed the shedding of the trailing vortices, leaving a four vortex pattern which was stabilized by Hartmann layers present on the top and bottom walls.

Little work has been done to determine the nature of this unique structure when the flow enters the turbulent domain. Votyakov and Kassinos (2010) postulate that at high Hartmann number, turbulence surrounding the core could destabilise the six-vortex structure. A 3D numerical study by Kenjereš et al. (2011) at $Re = 900$, which demonstrated good agreement with those earlier reported studies by Votyakov et al., reported turbulent bursts in the wake of the flow. Although the turbulence was not sustained, the distribution of turbulent stress was substantially altered as N increased.

2.3 Rayleigh-Bènard convection

The previous section aimed to elucidate some of the basic physical phenomena which arise when an electrically conducting fluid interacts with a magnetic field. Now that this understanding is hopefully in place, this section aims to provide a review and discussion on another major class of flow considered in this thesis; Rayleigh-Bènard convection.

Buoyant flows in general, and convective flows in particular, can exhibit quite complex behaviour even when present in relatively simple geometries. A layer of fluid heated from below will acquire an unstable density distribution due to the thermal expansion of fluid at the base. If the fluid is subject to a gravitational field then these differences in density will lead to buoyant forces. Hot, less dense, fluid rises whilst cool, denser, fluid falls. If the fluid layer is confined between two horizontal plates, then these 'plumes' will impinge upon the opposing surface and induce horizontal motions. The end result is the establishment of one or more convective cells and, depending on the strength of the buoyant forces, these plumes can form quite complex, time-dependent, patterns.

This particular convective arrangement (when the fluid is heated from below) is termed Rayleigh-Bènard convection after Rayleigh (1916), who studied the stability of such flows. For motion to occur, the buoyant force must be sufficient to overcome the two mechanisms which oppose it; viscous dissipation and thermal diffusion. This is embodied and quantified by the non-dimensional Rayleigh number;

$$Ra = \frac{g\beta\Delta\Theta L^3}{\nu\alpha} \tag{2.3.1}$$

where g is acceleration due to gravity, α is the thermal diffusivity, β is the volumetric thermal expansion coefficient, L is the depth of the fluid layer and $\Delta\Theta$ is the temperature difference between the top and bottom of the fluid.

Rayleigh (1916) calculated that for a fluid layer between two infinite horizontal parallel plates, the critical Rayleigh number is $Ra_c = 1073$. After this is exceeded, motion begins and convective cells are established. From here, a very diverse array of flow structures can develop. Convective cells may form into quite ordered, or less ordered, patterns and the flow in general may be steady state, exhibit oscillation, or become fully turbulent. The specific regime that a flow will enter is determined, to a first approximation, by both the Rayleigh number and the Prandtl number (Getling, 1998). The latter is given by;

$$Pr = \frac{\nu}{\alpha} \tag{2.3.2}$$

Physically, the Prandtl number determines the relative sizes of the viscous and thermal boundary layers close to the horizontal walls. The magnitudes of both these parameters will contribute to the state of the system. Krishnamurti (1973) collated experimental

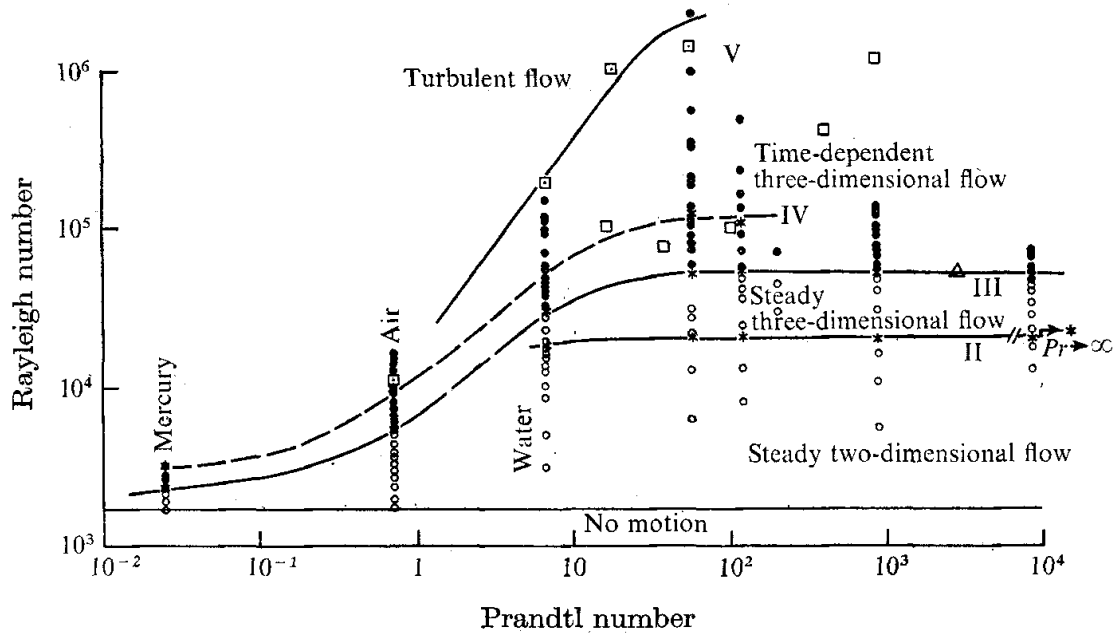

Figure 2.9: Regime diagram for Rayleigh-Bènard convection in the $Ra - Pr$ parameter space from Krishnamurti (1973). Experimental observations are represented by symbols and solid lines mark the boundaries between identifiable regimes.

observations available at the time into a regime diagram, reproduced here in Figure 2.9. For water ($Pr \approx 7$), it can be seen that an increase in Ra above the critical value leads to steady two-dimensional flow before transitioning to steady three-dimensional, time-dependent three-dimensional and, finally, fully turbulent flow. A reduction in Prandtl number tends to reduce the Rayleigh number at which these transitions occur. This has implications for MHD type convection since the fluids involved are typically liquid metals with Prandtl numbers of $\mathcal{O}(10^{-2})$.

There is considerable literature on non-magnetic Rayleigh-Bènard convection. For a recent review of progress see, for example, Bodenschatz et al. (2000), Manneville (2006) or Ahlers et al. (2009). Here, attention is paid to those studies which specifically investigate the addition of magnetic fields.

2.3.1 Vertical magnetic field

From early theoretical (Chandrasekhar, 1952, 1954a) and experimental (Lehnert and Little, 1957; Nakagawa, 1955) works it is known that, in general, the introduction of a sufficiently strong vertical magnetic field[1] delays the onset of convective motion. In particular Chandrasekhar (1952) concluded that the critical Rayleigh numbers increases as $Ra_c \sim \pi^2 Ha^2$.

[1]Here, the vertical direction is taken to mean the direction aligned with the gravitation vector.

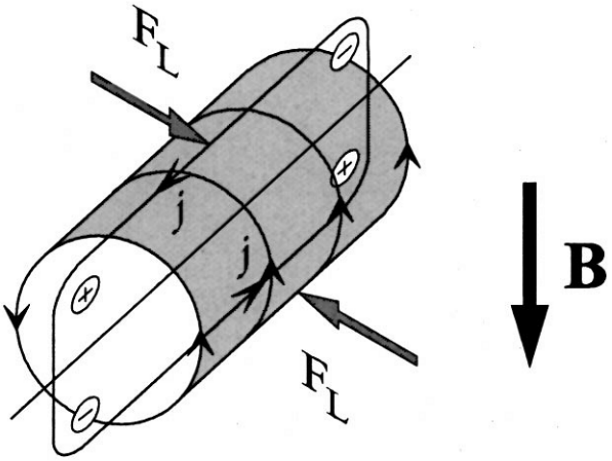

Figure 2.10: Magnetic damping of a convective roll cell by Lorentz forces $\mathbf{F}_L$, resulting from the interaction between a vertical magnetic field $\mathbf{B}$ and the current density $\mathbf{j}$. From Burr and Müller (2001).

The increase in critical Rayleigh number afforded by the magnetic field is readily explained. Figure 2.10 shows a schematic representation of a convective cell within a magnetic field. As the cell rotates, the horizontal motion across the magnetic field lines will generate a current perpendicular to both. Since this motion is obviously in different directions at the top and bottom of the cell, the currents form a loop along the length of the cell as shown. The Lorentz force then acts to oppose this horizontal motion. Since a convective cell cannot exist without recirculation, this stabilizes the fluid and increases the critical Rayleigh number. The buoyant driving force must now overcome the combined effects of viscous dissipation, thermal diffusion and Joule dissipation.

In fact, for an incompressible, inviscid, fluid of zero resistivity which is impressed with a magnetic field in the direction of gravity, Chandrasekhar (1961) determined that velocity gradients in the direction of the magnetic field are zero. This is exactly what was concluded earlier (in Subsection 2.2.1) for the case of freely decaying isotropic turbulence in a uniform magnetic field. There, it was noted that the result should also apply for an isolated vortex. Since convection cells are, by definition, vortices it is not particularly surprising that this particular phenomena is also prevalent in convective flows. The absence of velocity gradients in the direction of the magnetic field is analogous to the Taylor-Proudman theorem for rotating flows. This states that for a fluid which rotates steadily with a sufficiently high angular velocity, velocity gradients parallel to the rotation axis vanish.

As was noted in Section 1.3, the types of fluids which are typically electrically conducting present several experimental difficulties. The most significant is the opaqueness of liquid metals, which makes visualization of the internal motions difficult. This is particularly problematic for convective flows, since often one of the main objectives is to determine the

structure and patterns which form in the flow. Despite this, there are a few experimental studies of note.

Cioni et al. (2000) applied a vertical magnetic field to a mercury layer confined in a vertical cylinder for high Rayleigh numbers ($Ra \leq 3 \times 10^9$) and strong magnetic fields ($Ha < 2000$). Their results demonstrated excellent agreement with the $Ra_c \sim \pi^2 Ha^2$ scaling law presented by Chandrasekhar (1952) and highlighted the development of a stably stratified interior with a significant reduction in heat transfer as the magnetic field strength was increased. Similar results were obtained by Burr and Müller (2001) who used a four-element temperature probe to provide measurements in an eutectic sodium-potassium alloy (for $10^3 < Ra < 10^5$ and $0 < Ha < 2500$). They found that for constant Rayleigh number an increase in the strength of the vertical magnetic field inhibited convective motions, diminished heat transfer, and reduced the horizontal length scale associated with the convective cells.

On the numerical side, it has been demonstrated that the RANS approach, run in unsteady mode, can reproduce the large scale flow patterns and typical convective structures associated with ordinary Rayleigh-Bènard convection (Ammour et al., 2013; Kenjereš and Hanjalić, 1999b). The literature on numerical studies with an applied magnetic field is, however, a little more limited. Hanjalić and Kenjereš (2000, 2001, 2006) modelled unresolved motion using a $k - \varepsilon - \theta^2$ eddy-viscosity based closure model. They considered the application of both a strong ($Ha = 100$) and weak ($Ha = 20$) vertical magnetic field to Rayleigh-Bènard convection at $Ra = 10^7$. They successfully reproduced the major structural features of the flow and obtained good agreement with Cioni et al. (2000) despite differences in geometry. The magnetic field was shown to suppress both mean and fluctuating horizontal motion and, for $Ha = 100$, to cause plume structures to become more cylindrical and elongated in the direction of the magnetic field. In a separate paper using the same approach, Kenjereš and Hanjalić (2004) increased the parameter range to $10^7 \leq Ra \leq 10^9$ and $0 \leq Ha \leq 500$ and found a vertical field greatly reduced the heat transfer.

2.3.2 Horizontal magnetic field

Whilst the vertical magnetic field was seen to delay the onset of primary convective motion, a horizontal magnetic field does not. Fauve et al. (1981, 1984) showed that in this case the convective pattern takes the form of stationary rolls aligned parallel to the magnetic field lines. Thus the critical Rayleigh number remains unchanged and the effect of the field is to inhibit secondary, oscillatory, behaviour.

It is difficult to investigate this particular setup experimentally since the walls which bound the fluid become influential and the solution of the problem will depend on their

electrical properties. With a vertical magnetic field, the currents were seen to form tightly closed loops within the convective cell itself. Here, since the convective rolls become aligned with the magnetic field, downward motion between two counter-rotating cells will produce a current which is directed towards the centre of the cell. In between the adjacent counter-rotating cells, upward motion will produce a current also directed toward the same centre (since the motion, and hence the current direction, is reversed). The only way for these currents to close is to turn parallel to the magnetic field direction and travel towards the Hartmann walls. Figure 2.11, from Burr and Müller (2002), illustrates this schematically. As this current reaches the walls, it loops through the boundary layers and back across the channel. For this reason, these walls are termed Hartmann walls since they play a similar role to those in the channel flows considered in Section 2.2.

In the experimental study by Burr and Müller (2002) it was noted that the presence of these Hartmann walls alters the dynamics of the flow (compared to the analyses by Fauve et al. (1981, 1984) above) since they generated Lorentz forces within the boundary layers at the side which generated larger viscous forces. That said, the transformation of the flow from a three-dimensional convective pattern into a quasi-two-dimensional flow pattern where the convective cells became increasingly aligned with the magnetic field lines was shown. They also found a range of magnetic field intensities where enhanced heat transfer was observed.

Andreev et al. (2003), who used a novel superconducting magnet setup to achieve similar Hartmann numbers with less conductive but transparent electrolytes, confirmed the experimental results of Burr and Müller (2002) and showed that the increase in heat transfer was due to the two-dimensionality of the flow.

A later experimental study by Yanagisawa et al. (2010) used ultrasonic velocimetry to provide visualization of the flow patterns and suppression processes in a rectangular box of Gallium subjected to an abrupt increase in the strength of a horizontal magnetic field $(0 < Ra < 3.5 \times 10^5,\ 0 < Ha < 44)$. The oscillatory motion of the two-dimensional roll structures was suppressed and accompanied by a reduction in temperature fluctuations as shown in Figure 2.12.

Contrary to the above findings, numerical simulations by Kenjereš and Hanjalić (2004) showed a horizontal magnetic field increasing in strength reduced heat transfer up until the flow structure re-organized into a two-dimensional state. After this, it was unaffected. Unfortunately there is a distinct lack of high quality DNS data for electromagnetically influenced Rayleigh-Bènard convective flows and this prevents proper quantitative validation of these, and other, results.

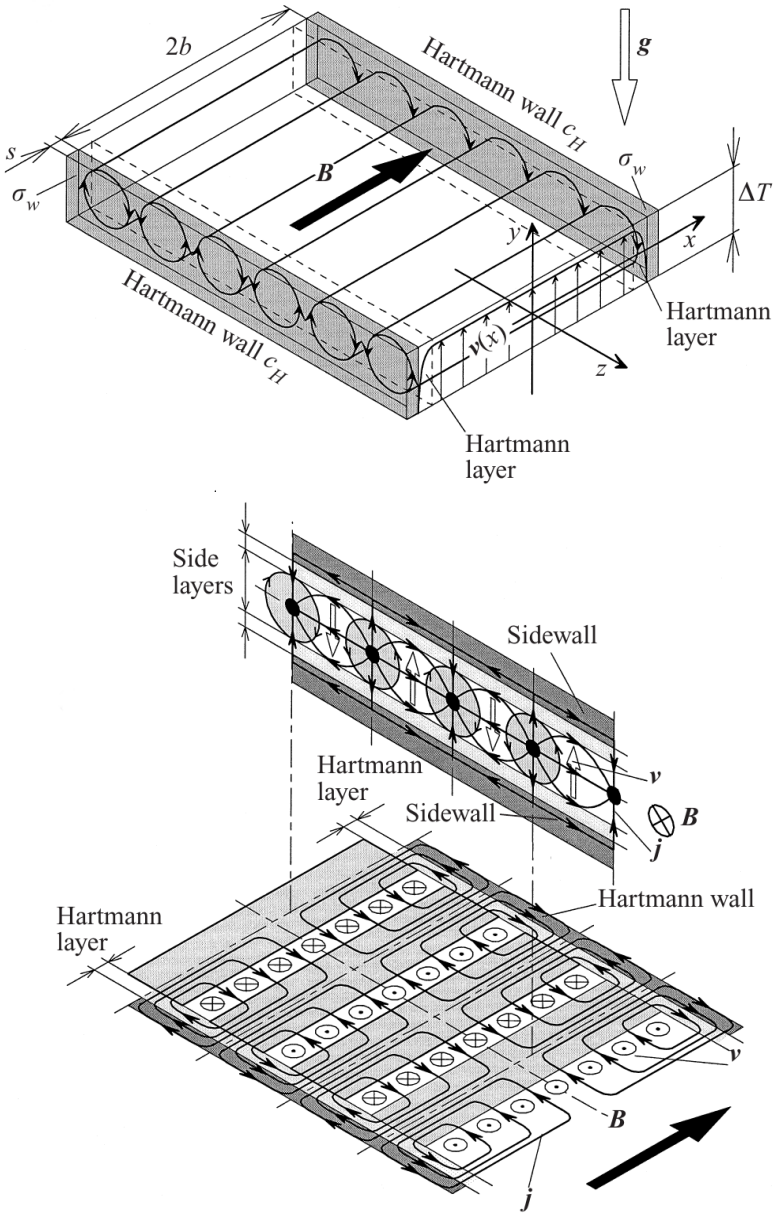

Figure 2.11: Schematic of two-dimensional structures which form when a horizontal magnetic field is applied to Rayleigh-Bènard convection. Left, geometry and flow pattern of the cells and right, closure paths of the electric current. Adapted from Burr and Müller (2001).

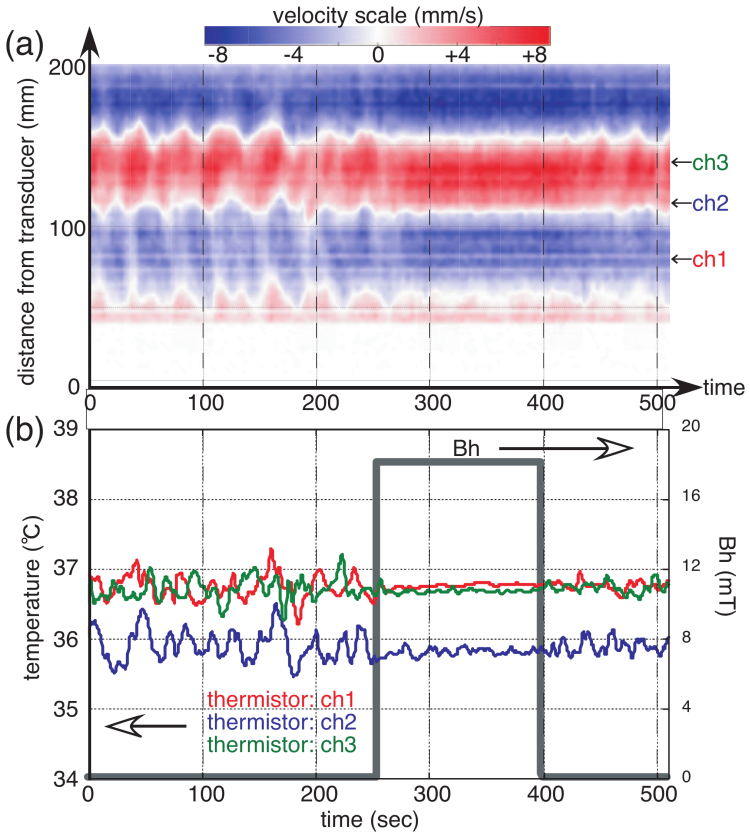

Figure 2.12: A layer of Gallium heated from below is abruptly subjected to a horizontal magnetic field: (a) time series of velocity as measured by ultrasonic Doppler velocimetry and (b) temperature measurements from three thermistors. The white streaks in (a) represent the boundaries between convective rolls. When the field strength is increased, as indicated by (b), both oscillatory motions and temperature fluctuations are suppressed. With subsequent removal of the field the oscillations begin to return. From Yanagisawa et al. (2010).

2.4 Convection in other configurations

Many actual processes involve more than just the Rayleigh-Bènard convective arrangement discussed in the previous section. In this section, attention is given to some other configurations, and force fields, which typically arise. First the implications of adding system rotation, in addition to a magnetic field, are summarised before a brief look at the effect of magnetic fields on cases where the applied heat flux is perpendicular to gravity is provided.

2.4.1 Subject to a magnetic field and rotation

It was seen in the previous section that the Lorentz force tended to either inhibit primary convective motion (a vertical magnetic field) or inhibit secondary oscillations (a horizontal magnetic field). When the whole system undergoes rotation the Coriolis force becomes active and the simultaneous actions of this with the Lorentz force can yield some intriguing results. This particular configuration has relevance to materials processing and geophysical flows.

Investigations into the stability of such a system by Chandrasekhar (1954b, 1956) demonstrated extremely complex and unexpected behaviour. Experimental work by Aurnou and Olson (2001) measured heat transfer for a layer of liquid gallium ($Pr = 0.023$) heated from below ($Ra \leq 3 \times 10^4$) in a tank subject to both a vertical magnetic field ($Ha = 25,\ 34.78$), and system rotation. Their results indicate that the simultaneous action of both forces does tend to inhibit convective motions.

A Numerical study by Varshney and Baig (2008b) looked at Rayleigh-Bènard convection in an 8:8:1 electrically insulated rectangular cavity with an applied horizontal magnetic field. Results, reproduced in Figure 2.13, without rotation showed good agreement with Aurnou and Olson (2001) and reproduced the expected alignment of the two-dimensional structures with the magnetic field. When rotation was added, the structures were initially skewed before being broken up at higher angular velocities. Applying the same approach but with a vertical field, Varshney and Baig (2008a) found that in general the velocity fluctuations were reduced with increased Ha regardless of the rate of rotation. At the highest rotation rate, an increase in Ha led to an increase in heat transfer.

2.4.2 Convection with a horizontal temperature gradient

In one crystal growth method, known as the Bridgman-Stockbarger technique, the melt is contained within a crucible which is withdrawn horizontally from a furnace. This subjects

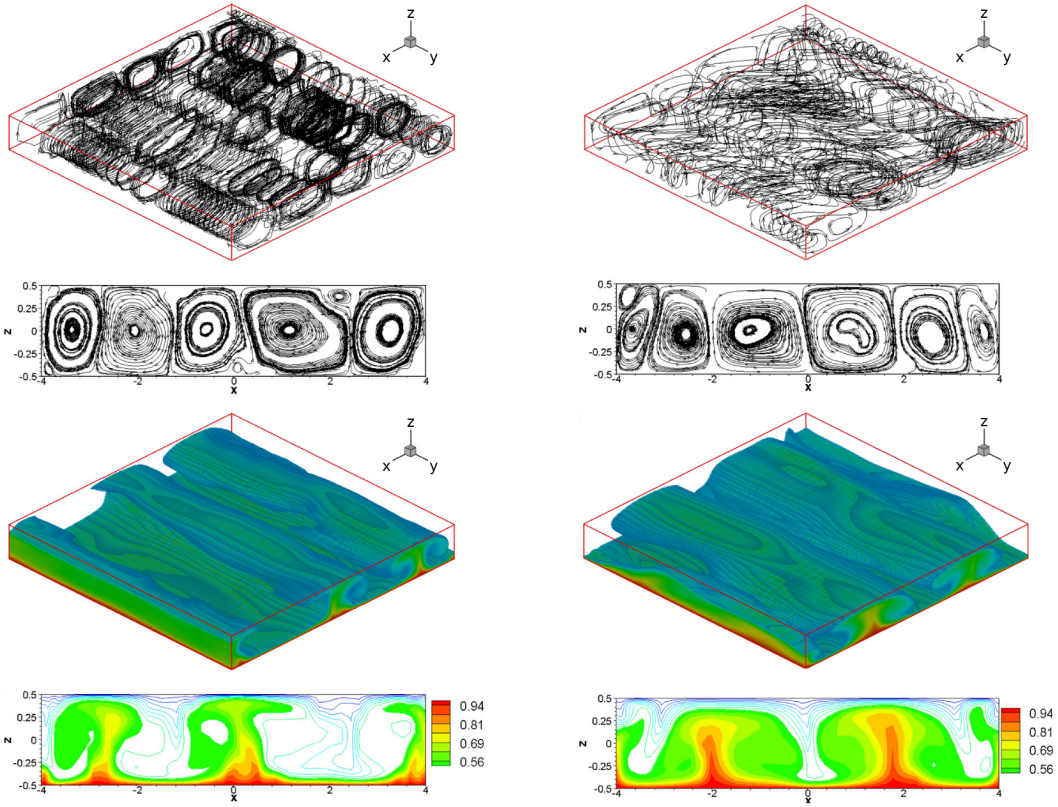

(a) $Ha = 1100, Ta = 0$ (b) $Ha = 1100, Ta = 2.5 \times 10^7$

Figure 2.13: 3D and 2D visualizations of rotating magnetic Rayleigh-Bènard convection subject to a magnetic field B_y, angular velocity Ω_z and gravitational field $-g_z$. From top to bottom respectively: 3D flow structures, 2D flow structures in central xz plane, isotherms showing 3D thermal structure and 2D thermal flow structures in central xz plane. From Varshney and Baig (2008b).

the melt, and solidification front, to a horizontal temperature gradient which drives end wall convection. The growth interface, whose stability is crucial in minimizing defects, can be highly distorted by convection even though the maximum melt velocity may be relatively low (Lan, n.d.). These distortions, which manifest as oscillations superimposed upon the steady convective motions, are known to cause unwanted striations within the crystal and early experiments by Hurle (1966) and Utech and Flemings (1966) showed that they could be eliminated by the application of a magnetic field.

The growing demand for improved crystal quality by the semi-conductor industry, combined with a more fundamental interest in these types of flows, has spurred a number of further experimental and numerical studies, which focus on eliminating the unwanted oscillatory convection. Ozoe and Okada (1989) present a numerical study in which they applied a magnetic field in the three orthogonal directions to molten silicon $(Pr = 0.054)$ in a cubical cavity with differentially heated walls. They showed that the magnetic field had a damping effect in all three directions but was most effective when applied parallel to the direction of heat flux. As the field strength was increased, the magnitude of the main circulation dramatically decreased and at the strongest field simulated, $Ha = 500$, es-

sentially stopped altogether. These results were later reinforced by an experimental study with liquid gallium ($Pr = 0.024$) where they state that a magnetic field parallel to either gravity or the direction of heat flux was almost 10 times as effective in suppressing heat transfer (Okada and Ozoe, 1992) as a field applied in the other directions.

An experimental study by Hof et al. (2003) investigated the damping effect for different orientations of magnetic field at a relatively low Rayleigh number of $Ra \sim 722$. For a vertical field they found the steady convection decayed exponentially with Ha, and that heat transport was almost purely by conduction at $Ha \approx 50$. For a magnetic field transverse to the flow, their results indicated it provided greater damping than that of a longitudinal field, contradicting earlier results by Ozoe and Okada (1989). By way of an explanation, they note that the aspect ratio of the container may be critical in determining the current paths, and hence the spatial distribution of the Lorentz force (a conclusion noted also in Subsection 2.3.2). A later paper by Hof et al. (2005) adds that the onset of oscillations can be postponed using magnetic fields of approximately one order of magnitude below that necessary to significantly damp the steady flow. Later studies (Battira and Bessaïh, 2008; Kolsi et al., 2007; Xu et al., 2006) have confirmed this general picture.

In contrast to the wealth of literature in the laminar regime, relatively little has been done numerically in the fully turbulent regime. Kenjereš and Hanjalić (2004) present a numerical study of side-heated transitional convection ($Ra = 10^6$) in a cubical cavity subjected to magnetic fields in all three orthogonal directions using the same T-RANS approach as Hanjalić and Kenjereš (2001) (a $k - \varepsilon - \theta^2$ model). Additional modelling to account for molecular dissipation of heat flux was also included to bring preliminary ordinary hydrodynamic results in line with prior DNS by Kerr and Herring (2000). In agreement with Ozoe and Okada (1989) and Okada and Ozoe (1992) they observed a magnetic field parallel to the heat flux was most effective at reducing convective heat transfer. Interestingly, they also applied magnetic fields locally confined to only the boundary layers of the thermally active walls where a strong reduction was again observed for the field parallel to the heat flux and, over the range $0 \leq Ha \leq 140$, was even more effective than a field applied in the vertical direction over the whole domain.

2.5 Selected further applications

As well as providing valuable insight into complex fluid mechanical interactions, magnetohydrodynamics has also found some more novel applications. The aim of many of these studies is to probe the feasibility of new techniques utilizing MHD. This section reports some of those studies in four areas, namely the magnetic dynamo, targeted drug delivery, materials processing and electromagnetic flow control.

2.5.1 The magnetic dynamo

It is estimated that without a mechanism to constantly generate a celestial magnetic field, the electromagnetic decay time of the Earth's primordial field would only be 10^5 years[1] (Roberts, 1967a). Since this is evidently not the case, the field must be continuously replenished. As the most widely accepted theory, the magnetic dynamo describes the process by which the kinetic energy of fluid motion is converted to magnetic energy. This occurs when the magnetic Reynolds number reaches some critical value; the motion $\mathbf{U}$ has a strong influence on the magnetic field $\mathbf{B}$ and the induced magnetic field $\mathbf{b}$ can no longer be ignored as it was for the flows considered previously.

Early experiments focused on the use of rotation to induce a self-sustaining magnetic field (Lowes and Wilkinson, 1963, 1968; Wilkinson, 1984). The principle was demonstrated first using simple rotating cylinders, which produced both steady and oscillating magnetic fields, before more complex geometry actually produced magnetic fields which reversed polarity; something which the Earth's magnetic field is known to do. Attempts at numerical modelling initially suffered from a dearth of experimental validation data but this changed in 1999 when two major experimental facilities were set up; one in Riga, Latvia, and the other in Karlsruhe, Germany. The Riga dynamo (Figure 2.14), for example, consists of three concentric tubes of approximately $3\,\mathrm{m}$ length. In the innermost tube, a propeller drives a helical flow of liquid sodium towards the base. It then returns straight back up through a coaxial tube and stays at rest in the third outermost tube. Once the critical magnetic Reynolds number was reached (calculated at $Re_m = 17.7$) two regimes were identified: a kinematic regime, which is associated with exponential growth of the magnetic field, and a dynamic or saturation regime, in which growth falls to zero as the increasing Lorentz forces deform the velocity field. For a review of the history and results of both of these experiments see Gailitis et al. (2008, 2000, 2001a, 2002a, 2001b, 2002b,c, 2003, 2004), Müller and Stieglitz (2002), Müller et al. (2004, 2006), Sarkar and Tilgner (2005), and Stieglitz and Müller (2001)

[1] A timescale for this can be estimated using $\tau_\eta = L^2/\eta$. The Earth's outer core is estimated to have a radius of $2300\,\mathrm{km}$ and a conductivity of $\sigma \approx 6 \times 10^5\,\Omega^{-1}\,\mathrm{m}^{-1}$ (Merrill et al., 1998), then $\eta \approx 1.33\,\mathrm{m}^2\,\mathrm{s}^{-1}$ and it follows that $\tau_\eta = 3.988 \times 10^{12}\,\mathrm{s} = 1.263 \times 10^5\,\mathrm{yrs}$.

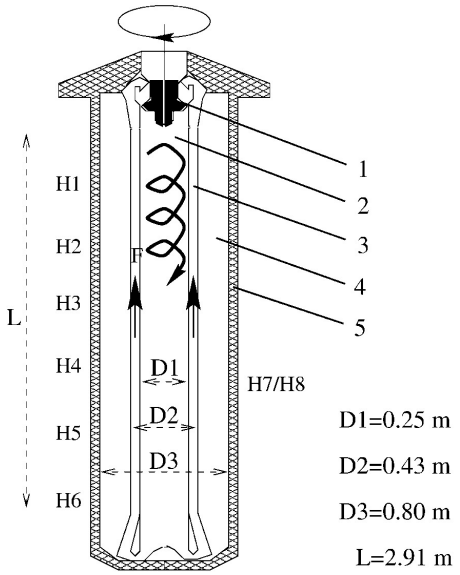

Figure 2.14: Cross section of the Riga dynamo facility; (1) Propeller, (2) Helical flow region, (3) back-flow region, (4) sodium at rest and (5) thermal insulation. H1,...,H8 represent Hall sensors. From Gailitis et al. (2001a)

Numerically modelling of the Riga dynamo is, with a Reynolds number of $Re \approx 3.5 \times 10^6$, presently outside the capabilities of DNS. Accordingly, attempts using a RANS approach have been presented by Kenjereš et al. (2006). Due to difficulties in defining magnetic boundary conditions for non-spherical geometries, they opted for a segregated approach where a RANS model was used for the hydrodynamics and a finite-difference model was used for the magnetic field. Preliminary simulations demonstrated good agreement with existing experimental data and concluded that a $k-\varepsilon$ turbulence model would suffice. The results from full scale simulations showed the model improved prediction of magnetic field growth rate and frequency over prior 1D and 2D models (Gailitis et al., 2004) but they report the level of information it could provide, especially on the dynamics of the self-excitation process, was restricted by the segregated implementation.

Later, Kenjereš and Hanjalić (2007) reported results from a hybrid approach where the fluid flow and magnetic field variables are solved for simultaneously, but using RANS and DNS methods respectively. Using the same extended $k-\varepsilon$ model previously used to simulate magnetic Rayleigh-Bènard convection results, reproduced in Figure 2.15, demonstrate they correctly reproduced both the helical fluid flow structure in the central tube and the characteristic double-helix spatial distribution of the magnetic field. Magnetic field distributions during both the self-excitation and saturation regimes demonstrated good agreement with experimental data. Plots of the magnetic field strength show the amplitude of oscillations are also well captured but the frequency was slightly under predicted. Suggestions for further work included a full Reynolds stress model to account for the known anisotropy the magnetic field induces.

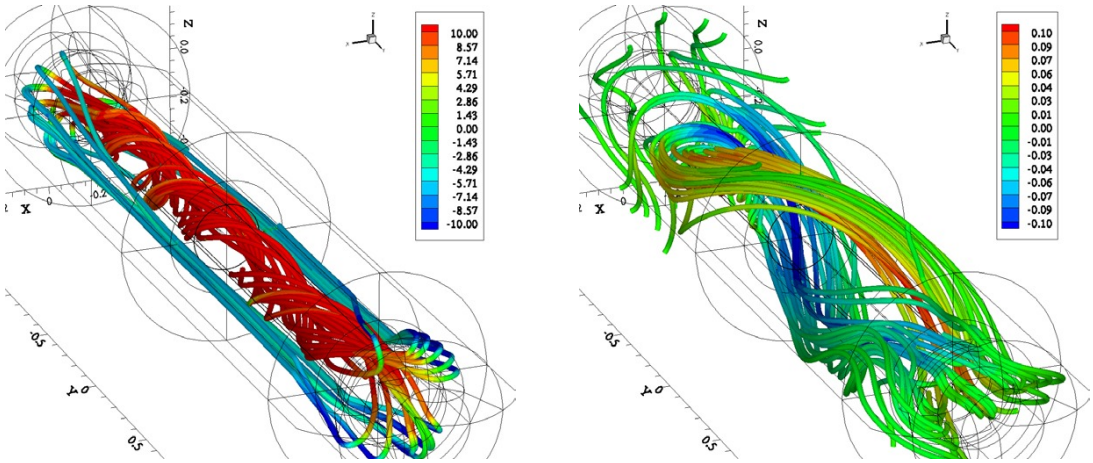

(a) (b)

Figure 2.15: 3D snapshots of the typical swirling flow pattern inside the Riga dynamo experiment from numerical simulations by Kenjereš and Hanjalić (2007): (a) Streamlines coloured by axial velocity (ms^{-1}) and (b) magnetic flux lines coloured by the axial magnetic field strength (T).

2.5.2 Targeted drug delivery

The more traditional drug delivery methods, such as intravenous or oral administration, result in the drug entering the blood stream as a molecule. This non-specific systemic distribution is naturally very inefficient in the treatment of a wide range of diseases. In the case of cancerous tumours, this results in the well-known side effects of chemotherapy as the toxic drugs cannot differentiate between cancerous and healthy cells. One promising method to overcome these issues is a form of targeted drug delivery in which the drug is bound to a biocompatible magnetic nanoparticle before injection. Introduction of an external magnetic field not only allows the particles to be directed to the site of interest but, through magnetic excitation, can facilitate an active release mechanism. Beginning life as contrast agents for MRI investigations, the use of magnetic nanoparticles in animal studies has shown promising results. Several animal studies using this delivery method, as highlighted by Jurgons et al. (2006) and Kenjereš (2008), demonstrated complete remission in tumour-bearing rabbits whilst using only 20% of the regular dosage (Alexiou et al., 2005, 2006). This short section briefly details some studies relating to the CFD modelling of biofluids containing such particles. For more in-depth reviews, see Arruebo et al. (2007), Dobson (2006), and Pankhurst et al. (2003).

Generating a mathematical model of a bio-fluid such as blood has inherent difficulties owing to its dynamic composition and containment within elastic arteries (Ikbal et al., 2009). For example, not only is blood known to exhibit non-Newtonian behaviour at low shear rates (due to the agglutination of the red blood cells, Ku, 1997) but the application of a magnetic field also increases its apparent viscosity (Haik et al., 2001). The electrical conductivity and magnetic susceptibility (which measures the degree to which a material responds to a magnetic field) similarly vary with both oxygenation and flow rate.

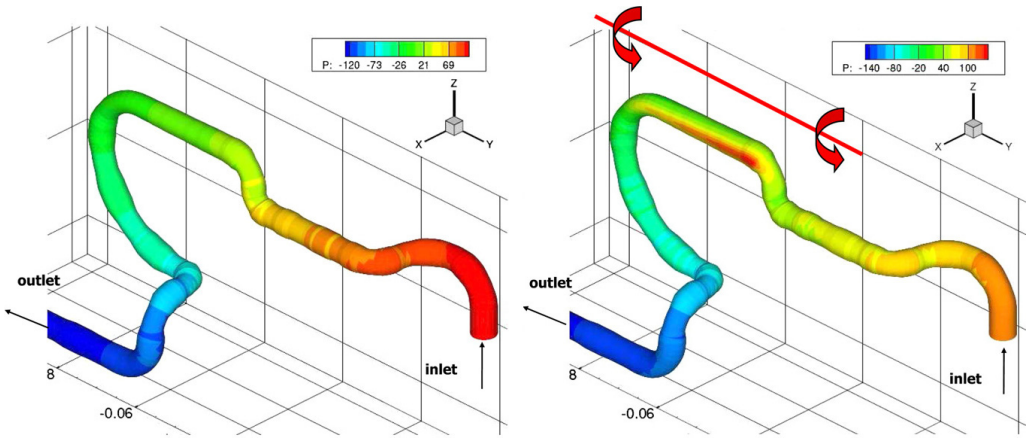

Figure 2.16: Contours of the local pressure distribution along the wall of a realistic right-coronary artery. Left is without and right is with a magnetic field originating from a wire source 2 cm away from the artery, $|B_0| = 10\mathrm{T}$. Adapted from Kenjereš (2008).

A numerical study by Kenjereš (2008) looked at the effect of non-uniform magnetic fields in realistic (i.e. based on patient data) stenotic arteries. Their simplified laminar model regarded blood as a homogeneous, Newtonian substance and included effects of both the Lorentz force and magnetization force as source terms in the momentum equation. Maxwell's equations were handled through solving a single equation for the electric potential, and a non-uniform magnetic field was included by using the laws of Biot-Savart and Ampére to obtain the field distribution around a series of infinitely long wires. As highlighted by Figure 2.16, they demonstrated that the magnetic field induces significant changes in both the local pressure distribution and secondary flow patterns. With the latter, the appearance of additional vortical structures close to the arterial wall downstream of the stenosis was linked to the action of the magnetization force. Several other numerical studies have similarly shown that a magnetic field can dramatically alter the flow rate in both healthy and stenosed arteries (Grief and Richardson, 2005; Ikbal et al., 2009; Sankar et al., 2011; Wang et al., 2008)

Magnetically targeted nanoparticles have also been proposed as a method to induce cell apoptosis via localised hyperthermia. Since a sustained temperature of above $42\,^{\circ}\mathrm{C}$ will cause cell death, an alternating magnetic field could be used to actively heat nanoparticles through the induced currents (Joule dissipation). A number of studies have investigated this use (see the review by Moroz et al., 2002 for example) but most are medical based, and to the author's best knowledge, no CFD studies have been reported to date.

2.5.3 Material processing

An increasing demand for homogeneous metals in the aerospace industry fuelled a surge in new electromagnetic based processing techniques during the late 1900's. Since then,

and apart from their use in crystal growth (briefly discussed in Subsection 2.4.2), magnetic fields have been routinely used to manipulate materials via stirring or damping and through levitation or separation (Davidson, 1999). From a fluid dynamics perspective, the modelling of these flows introduces significant difficulties. They involve solidification fronts, free-surfaces, heat transfer (of all types) at low Prandtl number and are almost invariably turbulent. Couple these features with a magnetic field, and they are then also subject to Lorentz forces whose spatial distribution can be rather complex. In spite of this the potential for improving materials' characteristics has prompted many authors to tackle these flows, and a short summary of relevant works is provided here. For a more detailed overview, see Part B of Davidson (2001) and the review by Davidson (1999).

Defects in continuously cast steel slabs, both internal and external, are known to be closely related to the flow of the molten steel in the mold. The cause of defects is usually unwanted turbulence from the submerged entry nozzle which continuously feeds the mold. This turbulence disturbs the free surface allowing debris and gas bubbles to become trapped (Davidson, 2001; Gillon, 2000). Since any motion of electrically conducting fluid across magnetic field lines will induce an opposing Lorentz force, an imposed static magnetic field can be used to effectively damp the unwanted motion. This technique, called electromagnetic braking (EMBR), was demonstrated by several authors to be very successful. Idogawa et al. (1993) presented RANS based numerical simulations in which turbulence was accounted for by use of a $k - \varepsilon$ model. Their results show that the magnetic field dramatically reduces the velocity of the flow striking the faces of the mould. Experiments with a mercury model demonstrated good agreement with the numerical simulations, and subsequent inclusion of the technology at a working plant suggested that the magnetic field reduced turbulent fluctuations to an extent which prevented the entrapment of slag. Later studies, including a similar RANS based numerical study (Ha et al., 2003) and LES study (Chaudhary et al., 2012), show good agreement.

Other uses of magnetic fields in the casting process include electromagnetic stirring. This is achieved by applying a rotating magnetic field, generated much like that of an induction motor. As highlighted by Toh and Takeuchi (2002), this has proved effective at suppressing both the formation of CO bubbles and subsurface inclusions by homogenizing the temperature and flow velocity in the vicinity of the meniscus. Away from casting, the use of magnetic fields has also shown promise in areas such as magnetic separation (Mohanty et al., 2011; Svoboda and Fujita, 2003), magnetic levitation (Tournier et al., 2001) and in controlling diffusion flames (Gillon, 2000).

2.5.4 Electromagnetic flow control

The prospect of manipulating electrically conducting fluid by non-physical means has led some efforts to develop control techniques for flows over hydrofoils and bluff bodies.

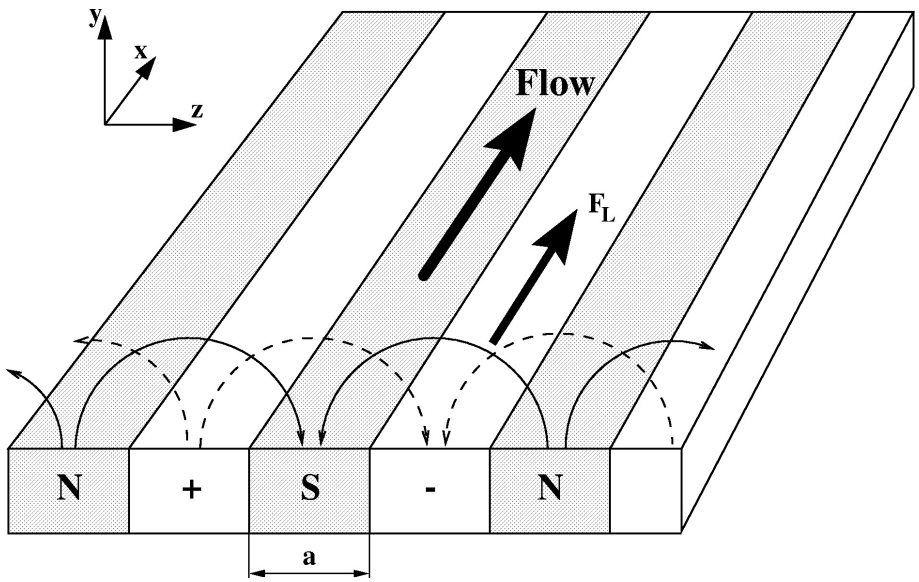

Figure 2.17: 3D schematic of an actuator generating a streamwise Lorentz force. Note the alternating arrangement of magnet poles and electrodes. From Posdziech and Grundmann (2001).

Many of the techniques are aimed at minimizing flow separation and improving lift or drag characteristics. One example comprises an alternating arrangement of opposing magnet poles with opposing electrodes, as depicted in Figure 2.17, which generates a Lorentz force in the streamwise direction.

Unlike ordinary MHD, where the Lorentz force is induced from the movement of the fluid relative to a magnetic field, the induced currents here are negligible. Instead, the electrodes are externally powered and provide the ability to induce Lorentz forces which either accelerate or decelerate the flow in the region adjacent to the electrodes. This application of MHD is usually termed electro-magnetohydrodynamics (EMHD) or electromagnetic flow control (EMFC).

Studies on hydrofoils and circular cylinders using the above type of arrangement have demonstrated that this kind of control is indeed possible. Results from a numerical study by Mutschke et al. (2006), reproduced in Figure 2.18, indicate that a sufficiently strong steady Lorentz force is capable of completely preventing flow separation on a hydrofoil. With oscillatory control, they also point out improved lift characteristics when the frequency was in the region of the natural shedding frequency. These results are in agreement with those investigating circular cylinders (Kim and Lee, 2000; Posdziech and Grundmann, 2001) who show that the Lorentz force prevents development of an inflectional velocity profile through accelerating the fluid in the near-wall region and thus stabilizing the flow. With postponement of flow separation a favourable pressure gradient is maintained and pressure drag is reduced, but at the expense of increased frictional drag from greater near-wall acceleration. Overall, the effect is a global reduction in drag but this depends on the profile of the Lorentz force which is in turn determined by the specific actuator arrangement. A further interesting result detailed by Kim and Lee (2000), and separately

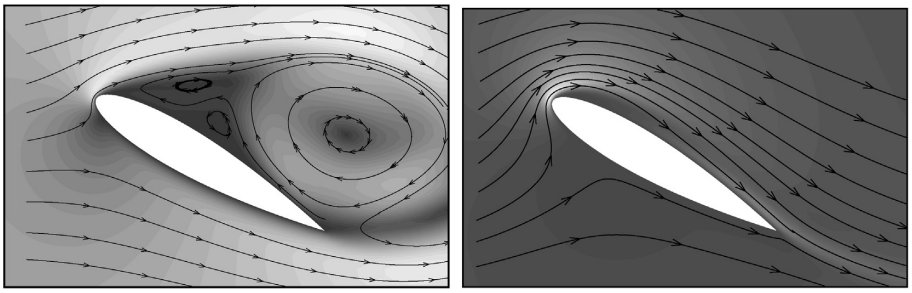

Figure 2.18: Snapshots of the flow around a PTL-4 hydrofoil at $\alpha = 30°$, $Re = 500$ showing streamtraces and contours of u_x. Left side is without any control and right side is with control. From Mutschke et al. (2006).

by Zhi-Hua et al. (2006), is the suppression of the well documented von Kármán vortex street with a Lorentz force of sufficient magnitude. The latter study also numerically demonstrated both open and closed loop control systems targeted at both manipulating the wake field and achieving a total drag coefficient of zero.

Significant attention has also been paid to turbulent wall bounded flows where existing control strategies are mainly passive, e.g. the use of riblets or large-eddy-break-up devices. These work by preventing the formation of coherent turbulent structures which are known to contain the majority of the turbulent energy. Choi et al. (1994) used direct numerical simulation to investigate the possibility of using an active control system to modify and suppress these large coherent structures in a fully developed turbulent channel flow ($Re = 1800$). Drag reductions of up to 25% were reported for control mechanisms which actively counteracted velocity fluctuations in directions transverse to the wall. A more realistic approach, where the feedback sensors were located on the wall rather than the more optimal position of near-wall, yielded only a 6% reduction. The overall picture however is still unclear. Direct numerical simulations by O'Sullivan and Biringen (1998) report only a very modest reduction in mean drag of around 1% with localised reductions of 11%, whilst application of an oscillating spanwise Lorentz force by Berger et al. (2000) gave a reduction in skin friction of around 40%. Experimental work by Breuer et al. (2004) failed to reproduce the values of drag reduction achieved by Berger et al., reporting only a 10% reduction, but did note excellent agreement on the velocity profiles induced by the actuators.

Although the application of Lorentz force actuators has been shown to have desirable effects on fluid flow, many of the studies mentioned above report very low levels of electrical to mechanical efficiency, with values in the region of 10^{-3} to 10^{-4}. Since the magnets used are of fixed strength, the magnitude of the Lorentz force can only be increased through increased current density. The low conductivity of working fluids such as seawater make this very expensive. Improvements to actuator designs, which concentrate on the inefficient spatial distribution of the Lorentz force, have reduced the total energy expenditure by around 12% but no set-up currently offers true power savings (Spong et al., 2005).

2.6 Concluding remarks

Although less attention has been paid in the literature to MHD cases when compared with their hydrodynamical counterparts, there evidently is still a wide range of areas which has been covered, from a number of more fundamental studies in channel and convective flows to more specific, application based, studies which look at optimizing existing engineering processes (drug delivery and materials processing).

It was seen that, generally, the imposition of a magnetic field over a flow of electrically conducting fluid leads to the creation of Lorentz forces directed in opposition to the motion which caused them. These reduce velocity gradients parallel to the magnetic field and suppress turbulence levels. In a simple one-dimensional channel flow arrangement, where the magnetic field is directed normal to the channel walls, this leads to both reduced centreline velocities, smaller boundary layers and, for initially turbulent flows and a magnetic field of sufficient strength, relaminarization. In two-dimensional duct flows, the electrical properties of the walls are influential and, for one particular configuration, it was seen to be possible to generate an 'M-shaped' velocity profile.

In Rayleigh-Bènard type convective flows, a magnetic field was seen to instigate quite different changes in the convective flow structures depending on the direction in which it was applied. A magnetic field applied in the vertical direction initially delayed the onset of convection (by restricting horizontal motion), but at higher Rayleigh numbers produced thinner roll cell structures which appeared elongated in the direction of the magnetic field. With a horizontal magnetic field, the fundamental effect was the same (i.e. elongation of roll cells in the direction of the magnetic field) but, since the magnetic field was now directed perpendicular to the buoyant force, the resulting convective pattern consisted of a series of long parallel roll cells whose axes were aligned with the magnetic field lines.

In addition to the two main classes of flow mentioned above there were other arrangements which were discussed, including convective flows with different heating arrangements and flows which were also subject to rotation. However, because of the fundamental nature of the former cases, and their ability to test the performance of models in a range of MHD interactions, whilst only requiring relatively simple geometry, they are the flow types studied in most detail in this thesis.

CHAPTER

THREE

GOVERNING EQUATIONS

This chapter aims to provide a mathematical description of magnetohydrodynamic flow within the framework of the Reynolds Averaged Navier-Stokes approach. First, a review of the equations governing ordinary fluid flow and heat transfer is presented in Section 3.1, which includes the terms describing the only non-magnetic body force considered in this research, buoyancy. Second, Section 3.2 introduces the equations of electrodynamics, including the set of Maxwell's equations with relevant simplifications, a version of Ohm's law applicable to moving media and the continuum version of the Lorentz force. Finally the coupling between the fluid velocity and the electromagnetic field is detailed in Section 3.3. Within this, consideration is given to simplifications applicable for the particular class of flow considered in this research.

As is common in fluid dynamics, index tensor notion and the Einstein summation convention is generally used, where a lone subscript, usually i, denotes one of the three orthogonal directions and a repeated index, usually j, indicates summation over all values of that index. This convention is briefly broken in the section on electromagnetism where it is customary, and move convenient, to use vector notation.

3.1 Hydrodynamics and heat transfer

The governing equations of incompressible fluid flow arise from the application of mass conservation and momentum conservation (Newton's second law) to an infinitesimal control volume containing fluid of constant density ρ. This yields the equations of continuity and momentum respectively, given here in terms of the instantaneous velocity $\tilde{U}_i$;

$$\frac{\partial \tilde{U}_i}{\partial x_i} = 0 \tag{3.1.1}$$

$$\rho\left(\frac{\partial \tilde{U}_i}{\partial t} + \tilde{U}_j\frac{\partial \tilde{U}_i}{\partial x_j}\right) = -\frac{\partial \tilde{P}}{\partial x_i} + \frac{\partial \tilde{\tau}_{ij}}{\partial x_j} + \tilde{F}_i \tag{3.1.2}$$

where $\tilde{F}_i$ represents any additional body forces, $\tilde{P}$ is the fluid pressure, $\tilde{\tau}_{ij}$ is the viscous stress tensor and those quantities with a tilde are instantaneous. Equation (3.1.2) expresses a balance between fluid momentum and the forces which can affect it. The forces, on the RHS, arise due to changes in pressure, viscous stresses, and any other body forces (such as buoyancy).

In incompressible flows, the conservation of energy can be expressed via a scalar transport equation for the instantaneous temperature $\tilde{\Theta}$;

$$\frac{\partial \tilde{\Theta}}{\partial t} + \tilde{U}_j\frac{\partial \tilde{\Theta}}{\partial x_j} = \frac{\partial}{\partial x_j}\left[\alpha\frac{\partial \tilde{\Theta}}{\partial x_j}\right] \tag{3.1.3}$$

where α is the thermal diffusivity.

3.1.1 Navier-Stokes equation

By providing a relationship between the viscous stress tensor, $\tilde{\tau}_{ij}$, and the rate of increase of strain in the fluid, the generalised momentum equation becomes the Navier-Stokes equation. For a Newtonian fluid of viscosity μ, the relationship is;

$$\tilde{\tau}_{ij} = \mu\left(\frac{\partial \tilde{U}_i}{\partial x_j} + \frac{\partial \tilde{U}_j}{\partial x_i}\right) \tag{3.1.4}$$

Substitution of Equation (3.1.4) into Equation (3.1.2) gives the Navier-Stokes equation;

$$\rho\left(\frac{\partial \tilde{U}_i}{\partial t} + \tilde{U}_j\frac{\partial \tilde{U}_i}{\partial x_j}\right) = -\frac{\partial \tilde{P}}{\partial x_i} + \frac{\partial}{\partial x_j}\left[\mu\left(\frac{\partial \tilde{U}_i}{\partial x_j} + \frac{\partial \tilde{U}_j}{\partial x_i}\right)\right] + \tilde{F}_i \tag{3.1.5}$$

3.1.2 Reynolds averaging

Reynolds averaging is a concept introduced by Osborne Reynolds to aid mathematical description of the random fluctuations exhibited by quantities in turbulent motion. It recognises that any instantaneous variable, $\tilde{\Phi}(x_i, t)$, can be expressed as the sum of an average or mean value, $\Phi(x_i)$, and fluctuation around that mean, $\phi(x_i, t)$;

$$\tilde{\Phi}(x_i, t) = \Phi(x_i) + \phi(x_i, t) \tag{3.1.6}$$

To obtain the mean value an averaging process is applied. The three most common types are the time average, the phase average and the ensemble average (Wilcox, 1998). The time average, for example, which is appropriate for statistically stationary turbulence, is defined as;

$$\overline{\tilde{\Phi}}(x_i, t) = \Phi(x_i) = \lim_{\Delta t \to \infty} \frac{1}{\Delta t} \int_t^{t+\Delta t} \tilde{\Phi}(x_i, t)\, \mathrm{d}t \tag{3.1.7}$$

where the overbar denotes a Reynolds averaged quantity and Δt is a time interval larger than the time scale associated with the slowest variations of $\tilde{\Phi}$.

The ensemble average, the most general type of average (appropriate for time and space dependant turbulence), can be understood as an average over N independent realizations of the same event. Mathematically, this is written as;

$$\overline{\tilde{\Phi}}(x_i, t) = \Phi(x_i) = \lim_{N \to \infty} \frac{1}{N} \sum_{n=1}^{N} \tilde{\Phi}_n(x_i, t) \tag{3.1.8}$$

where $\tilde{\Phi}_n(x_i, t)$ is the value of $\tilde{\Phi}(x_i, t)$ on the nth repetition.

By definition, the average of the fluctuation about the mean is $\overline{\phi}(x_i, t) = 0$. The average of the product between two fluctuating quantities (such as, say, $\overline{uv}$) need not be zero however, since the fluctuations in the quantities may be correlated. Hence, for two general instantaneous signals $\tilde{\Phi}$ and $\tilde{\Psi}$, their averaged product becomes;

$$\overline{\tilde{\Phi}\tilde{\Psi}} = \overline{(\Phi + \phi)(\Psi + \psi)} = \overline{\Phi\Psi} + \overline{\Phi\psi} + \overline{\phi\Psi} + \overline{\phi\psi} = \Phi\Psi + \overline{\phi\psi} \tag{3.1.9}$$

Performing the decomposition on the instantaneous quantities in the continuity equation (3.1.1) and Navier-Stokes equation (3.1.5), and then averaging, results in a set of equations governing the mean velocity and pressure field known as the Reynolds-averaged Navier-Stokes (RANS) equations;

$$\frac{\partial U_i}{\partial x_i} = 0 \tag{3.1.10}$$

$$\rho\left(\frac{\partial U_i}{\partial t} + U_j \frac{\partial U_i}{\partial x_j}\right) = -\frac{\partial P}{\partial x_i} + \frac{\partial}{\partial x_j}\left[\mu\left(\frac{\partial U_i}{\partial x_j} + \frac{\partial U_j}{\partial x_i}\right) - \rho\overline{u_i u_j}\right] + F_i \tag{3.1.11}$$

Similarly, the transport equation for the instantaneous temperature $\tilde{\Theta}$, Equation (3.1.3), transforms to;

$$\frac{\partial \Theta}{\partial t} + U_j \frac{\partial \Theta}{\partial x_j} = \frac{\partial}{\partial x_j}\left[\alpha \frac{\partial \Theta}{\partial x_j} - \overline{u_j \theta}\right] \tag{3.1.12}$$

The Reynolds averaging process has introduced an extra term, $\rho\overline{u_i u_j}$, into Equation (3.1.11) for the mean momentum, called the Reynolds stress tensor, and a similar term, $\overline{u_j\theta}$, into the transport equation for the mean temperature, Equation (3.1.12), often called the turbulent heat flux. These terms describe the effect of the turbulence on the mean flow and must be defined in order to close the equations. Different closure methods for these terms are discussed in Chapter 4.

3.1.3 Buoyancy

Buoyancy is a body force which arises when variations of density in a fluid are subject to gravitational acceleration. The gravity field exerts a body force, ρg_i, per unit volume. The density variations are most commonly caused by thermal expansion of heated fluid.

When there are only modest variations in temperature, so that density variations may be at most only 1%, the Boussinesq approximation may be used. In this it is assumed that differences in density are small enough to be neglected in the inertial terms and only become significant when multiplied by the gravitational acceleration. Density variations can then be incorporated by assuming a linear dependence with temperature. Let $\Delta\tilde{\Theta} = \tilde{\Theta} - \Theta_0$ and taking a Taylor series expansion;

$$\rho(\Theta_0 + \Delta\tilde{\Theta}) = \rho(\Theta_0) + \frac{\partial \rho}{\partial \tilde{\Theta}}(\Delta\tilde{\Theta}) + \frac{1}{2!}\frac{\partial^2 \rho}{\partial \tilde{\Theta}^2}(\Delta\tilde{\Theta})^2 + \ldots \tag{3.1.13}$$

where Θ_0 is a suitably chosen reference temperature and $\rho(\Theta_0) = \rho_0$ is the density at that reference temperature. By neglecting quadratic terms and introducing the volumetric expansion coefficient, β;

$$\beta = -\frac{1}{\rho_0}\frac{\partial \rho}{\partial \tilde{\Theta}} \tag{3.1.14}$$

Equation (3.1.13) can be written as;

$$\rho = \rho_0 - \rho_0 \beta(\tilde{\Theta} - \Theta_0) \tag{3.1.15}$$

The instantaneous buoyant body force, $\tilde{F}_i^b$, can then be written as;

$$\tilde{F}_i^b = \rho g_i = \rho_0 g_i - \rho_0 g_i \beta(\tilde{\Theta} - \Theta_0) \tag{3.1.16}$$

For uniform gravitational fields the term $g_i\rho_0$, which results from the constant reference

density, can be re-written in terms of a gravitational potential Φ_g;

$$\rho_0 g_i = -\rho_0 \frac{\partial \Phi_g}{\partial x_i} \tag{3.1.17}$$

This can then be readily absorbed into the pressure gradient through use of a modified pressure;

$$P^* = P + \Phi_g \tag{3.1.18}$$

which aids computational stability by reducing the size of source terms.

Performing a Reynolds decomposition on Equation (3.1.16) and averaging results in the mean part of the buoyancy force;

$$F_i^b = -\rho_0 \frac{\partial \Phi_g}{\partial x_i} - g_i \beta \rho_0 \left(\Theta - \Theta_0\right) \tag{3.1.19}$$

and the fluctuating part of the buoyancy force;

$$f_i^b = -\rho_0 g_i \beta \theta \tag{3.1.20}$$

3.2 Electromagnetism

Classical electromagnetism is concerned with the interactions between charged particles and the electromagnetic field. For the purposes of magnetohydrodynamics, the equations of concern are Maxwell's equations, the Lorentz force law and Ohm's law. Attention here is restricted to conducting, non-magnetic materials for which the electrical conductivity is isotropic. For a more detailed treatment and derivation, the reader is directed to one of many text books devoted to the subject, e.g. Griffiths (1999).

3.2.1 Maxwell's equations

In 1873 James Clark Maxwell unified all previously unrelated observations in the fields of electrodynamics and magnetism into a single set of partial differential equations. These describe electric charges and electric currents as the sources of the electric and magnetic fields respectively and provide a means to evaluated how they evolve in space and time.

Charge conservation

For applications involving continuous media, it is convenient to introduce the charge density, ρ_q, and the current density, $\mathbf{J}$. For a distribution of discrete charges, q_n, in an arbitrary volume V, the charge density is defined as;

$$\int_V \rho_q \ \mathrm{dV} = \sum_n q_n = Q \quad \rightarrow \quad \rho_q = \frac{dQ}{d\mathrm{V}} \tag{3.2.1}$$

where Q is the total charge present within the volume V. The current density $\mathbf{J}$ is defined as the current flow per unit cross-sectional area. Thus, if the total current through a surface S is I, then;

$$I = \int_S \mathbf{J} \cdot \ \mathrm{d}\mathbf{S} \tag{3.2.2}$$

where $\mathbf{S}$ is the area vector which has magnitude S and is positive in the direction of the outward facing normal. Since charge is conserved, the net flow of current into a volume element must produce an increase in the total charge within the volume. Thus;

$$-\int_S \mathbf{J} \cdot \ \mathrm{d}\mathbf{S} = \frac{\partial}{\partial t} \int_\mathrm{V} \rho_q \ \mathrm{dV} = \int_\mathrm{V} \frac{\partial \rho_q}{\partial t} \ \mathrm{dV} \tag{3.2.3}$$

Using the divergence theorem;

$$-\int_S \mathbf{J} \cdot \ \mathrm{d}\mathbf{S} = -\int_\mathrm{V} \boldsymbol{\nabla} \cdot \mathbf{J} \ \mathrm{dV} \tag{3.2.4}$$

so that Equation (3.2.3) becomes;

$$\int_{\mathrm{V}} \left(\boldsymbol{\nabla} \cdot \mathbf{J} + \frac{\partial \rho_q}{\partial t} \right) \, \mathrm{dV} = 0 \tag{3.2.5}$$

Since the integrand must hold for any arbitrary volume V, the conservation of charge can be expressed as;

$$\frac{\partial \rho_q}{\partial t} + \boldsymbol{\nabla} \cdot \mathbf{J} = 0 \tag{3.2.6}$$

Maxwell-Faraday law

Michael Faraday concluded, from his experiments in the period 1831-32, that the electromagnetic force (EMF) induced in a closed circuit was equal to the rate of change of magnetic flux which penetrates any closed surface spanning that circuit. Maxwell formalised this into a relationship between the magnetic field, $\mathbf{B}$, and the electric field, $\mathbf{E}$, recited here in differential form;

$$\boldsymbol{\nabla} \times \mathbf{E} = -\frac{\partial \mathbf{B}}{\partial t} \tag{3.2.7}$$

Maxwell-Ampère law

The Maxwell-Ampère law relates the magnetic field to moving charges and time-varying electric fields;

$$\boldsymbol{\nabla} \times \mathbf{B} = \mu_0 \left[\mathbf{J} + \epsilon_0 \frac{\partial \mathbf{E}}{\partial t} \right] \tag{3.2.8}$$

where μ_0 is the permeability of free space and ϵ_0 is the permittivity of free space.

Gauss's law

Gauss's law relates the distribution of electric charge to the resulting electric field $\mathbf{E}$;

$$\boldsymbol{\nabla} \cdot \mathbf{E} = \frac{\rho_q}{\epsilon_0} \tag{3.2.9}$$

Divergence of $\mathbf{B}$

Taking the divergence of Equation (3.2.7), it becomes apparent that;

$$\frac{\partial}{\partial t} \left(\boldsymbol{\nabla} \cdot \mathbf{B} \right) = 0 \quad \rightarrow \quad \boldsymbol{\nabla} \cdot \mathbf{B} = const. \tag{3.2.10}$$

The divergence of the magnetic field is therefore constant. If it is assumed that the constant is zero, then the magnetic field $\mathbf{B}$ becomes solenoidal; a picture that is consistent with observation. If, in fact, $\boldsymbol{\nabla} \cdot \mathbf{B} \neq 0$ then the resulting equation would take a form equivalent to Gauss's law for electric fields (Equation (3.2.9)). This would imply the existence of a magnetic charge density, which would lead to the idea the magnetic field arising from a bar magnet, for example, was actually the result of two isolated poles which carried opposing magnetic charges. Since magnetic monopoles have thus far eluded detection[1], it is reasonable to conclude that, in fact[2];

$$\boldsymbol{\nabla} \cdot \mathbf{B} = 0 \tag{3.2.11}$$

3.2.2 Ohm's law

Maxwell's Equations (3.2.6) – (3.2.9) and Equation (3.2.11) provide nine constraints for ten unknowns (in three dimensions). To close the system, a constitutive relationship is employed which relates the electric field to the current density. This is Ohm's law and the generalised form, for a conductor of isotropic conductivity σ moving with a velocity $\mathbf{U}$ relative to a magnetic field $\mathbf{B}$, is;

$$\mathbf{J} = \sigma \left(\mathbf{E} + \mathbf{U} \times \mathbf{B} \right) \tag{3.2.12}$$

3.2.3 Lorentz force

A charged particle placed within an electromagnetic field experiences a force. This is known as the Lorentz force, named after the dutch physicist Hendrik Lorentz[3]. It arises from three fundamental interactions: that with the static electric field, that with a time varying magnetic field, and that with the relative movement of a charge with respect to a magnetic field. For a particle with charge q, the discrete Lorentz force, $\mathbf{f}^L$, is given by;

$$\mathbf{f}^L = \underbrace{q\mathbf{E}_s}_{\text{Coloumb force}} + \underbrace{q\mathbf{E}_i}_{\text{induced electric field}} + \underbrace{q\mathbf{U} \times \mathbf{B}}_{\text{magnetic force}} \tag{3.2.13}$$

where the induced electric field arises from a time varying magnetic field via Faraday's law (3.2.7). It is common to combine the two electric fields such that;

$$\mathbf{f}^L = q \left(\mathbf{E} + \mathbf{U} \times \mathbf{B} \right) \tag{3.2.14}$$

[1] See Milton, 2006.

[2] That the base unit of a magnetic field appears to be a dipole, seems to emphasise the idea that the source of the magnetic field is actually the *movement* of electric charge (as described by Amperés law), rather than some additional intrinsic property of matter.

[3] Although named after Lorentz, it was actually first derived by Oliver Heaviside.

For applications involving continuous media, it is beneficial to re-formulate the law in terms of the charge density ρ_q. A small amount of charge δQ will experience a small force $\delta \mathbf{f}^L$ such that;

$$\delta \mathbf{f}^L = \delta Q \left(\mathbf{E} + \mathbf{U} \times \mathbf{B} \right) \tag{3.2.15}$$

Dividing by a small volume $\delta \mathrm{V}$, and taking the limit as $\delta \mathrm{V} \to 0$;

$$\lim_{\delta \mathrm{V} \to 0} \frac{\delta \mathbf{f}^L}{\delta \mathrm{V}} = \frac{d\mathbf{f}^L}{d\mathrm{V}} = \frac{dQ}{d\mathrm{V}} \left(\mathbf{E} + \mathbf{U} \times \mathbf{B} \right) \tag{3.2.16}$$

Since $d\mathbf{f}^L/d\mathrm{V}$ is simply the force per unit volume, $\mathbf{F}^L$, and $dQ/d\mathrm{V}$ is the charge density ρ_q (via Equation (3.2.1)), Equation (3.2.16) becomes;

$$\mathbf{F}^L = \rho_q \mathbf{E} + \rho_q \left(\mathbf{U} \times \mathbf{B} \right) \tag{3.2.17}$$

Finally, since a charge density in motion is just a form of current, the second term on the RHS of Equation (3.2.17) can be related to the current density as follows. Consider a charge density ρ_q which sweeps out a differential area δA as it travels with velocity U. In a time δt, the total charge that passes is equal to the total charge contained in the volume, $U \delta t \delta A$. Hence;

$$\delta Q = \rho_q U \delta A \delta t \quad \to \quad \frac{\delta Q}{\delta t} = \rho_q U \delta A \tag{3.2.18}$$

In the limit as $\delta t \to 0$ and $\delta A \to 0$;

$$\frac{dQ}{dt} = \int_A \rho_q U \ \mathrm{d}A \tag{3.2.19}$$

In three-dimensions, this simply becomes;

$$\frac{dQ}{dt} = \int_A \rho_q \mathbf{U} \cdot \mathrm{d}\mathbf{A} = \int_A \mathbf{J} \cdot \mathrm{d}\mathbf{A} = I \tag{3.2.20}$$

where through the use of Equation (3.2.2) it becomes apparent that $\mathbf{J} = \rho_q \mathbf{U}$. Hence the Lorentz force law becomes;

$$\mathbf{F}^L = \rho_q \mathbf{E} + \mathbf{J} \times \mathbf{B} \tag{3.2.21}$$

3.2.4 Relativistic considerations

This research is only concerned with non-relativistic phenomena, that is, when the characteristic velocity of the materials concerned is much less than the speed of light. With this in mind, several terms in the preceding set of equations can be neglected through an order of magnitude analysis (Roberts, 1967a; Shercliff, 1965).

If a variation in the flow has a time-scale denoted by τ and a length scale denoted by L,

then from Faraday's law (3.2.7);

$$\frac{\mathcal{O}(\boldsymbol{\nabla}\times\mathbf{E})}{\mathcal{O}(\partial\mathbf{B}/\partial t)}=\mathcal{O}(1)\quad\rightarrow\quad\frac{\mathcal{O}(\mathbf{E})}{\mathcal{O}(\mathbf{B})}=\frac{L}{\tau}\tag{3.2.22}$$

which gives a relationship between the magnitudes of the electric and magnetic fields. Now, taking the ratio between the LHS and the 2nd term on the RHS in Ampére's law (3.2.8);

$$\frac{\mathcal{O}(\epsilon_0\mu_0\partial\mathbf{E}/\partial t)}{\mathcal{O}(\nabla\times\mathbf{B})}=\epsilon_0\mu_0\frac{\mathcal{O}(\mathbf{E})/\tau}{\mathcal{O}(\mathbf{B})/L}\approx\frac{1}{c^2}\left(\frac{L}{\tau}\right)^2=\frac{U_0^2}{c^2}\ll 1\tag{3.2.23}$$

where $U_0 = L/\tau$ is a typical velocity scale and $c = 1/\sqrt{\epsilon_0\mu_O}$ is the speed of light. Thus the final term in the Maxwell-Ampère law, which Maxwell called the displacement current, is negligible, and the form of the Maxwell-Ampere law (3.2.8) suitable for non-relativistic MHD is;

$$\boldsymbol{\nabla}\times\mathbf{B}=\mu_0\mathbf{J}\tag{3.2.24}$$

which was the form originally presented by Ampère. The omission of the displacement current term also implies that the time dependent part of Equation (3.2.6) must also be neglected, since taking the divergence of Equation (3.2.24);

$$\boldsymbol{\nabla}\cdot(\boldsymbol{\nabla}\times\mathbf{B})=\boldsymbol{\nabla}\cdot\mu_o\mathbf{J}=0\quad\rightarrow\quad\boldsymbol{\nabla}\cdot\mathbf{J}=0\tag{3.2.25}$$

This condition on the current density, which is just a mathematical statement of Kirchoff's first law, ensures that any current in a conducting medium, bound by fully insulated surfaces, must form closed loops.

A similar analysis can be applied to the constituent terms of the Lorentz force. Firstly by substituting in Equations (3.2.24) and (3.2.9) it is noted that the ratio of the terms on the RHS of Equation (3.2.21) becomes;

$$\frac{\rho_e\mathbf{E}}{\mathbf{J}\times\mathbf{B}}=\frac{\varepsilon_0(\boldsymbol{\nabla}\cdot\mathbf{E})\mathbf{E}}{\boldsymbol{\nabla}\times\mathbf{B}/\mu_0\times\mathbf{B}}\tag{3.2.26}$$

Then by considering the order of magnitude;

$$\frac{\mathcal{O}(\varepsilon_0(\boldsymbol{\nabla}\cdot\mathbf{E})\mathbf{E})}{\mathcal{O}(\boldsymbol{\nabla}\times\mathbf{B}/\mu_0\times\mathbf{B})}=\epsilon_0\mu_0\frac{\mathcal{O}(\mathbf{E}^2)}{\mathcal{O}(\mathbf{B}^2)}=\frac{1}{c^2}\left(\frac{L}{\tau}\right)^2=\frac{U^2}{c^2}\ll 1\tag{3.2.27}$$

Hence the electrostatic term in Equation (3.2.21) is insignificant when the velocities under consideration are much less than the speed of light. The form of the Lorentz force applicable in this research is thus;

$$\mathbf{F}^L=\mathbf{J}\times\mathbf{B}\tag{3.2.28}$$

3.2.5 Summary

Taking into account the simplifications introduced in the previous section, a summary of the equations of electromagnetism relevant to MHD is presented below.

$$\text{Charge conservation,} \quad \boldsymbol{\nabla} \cdot \mathbf{J} = 0 \tag{3.2.29a}$$

$$\text{Ampère's law,} \quad \boldsymbol{\nabla} \times \mathbf{B} = \mu_0 \mathbf{J} \tag{3.2.29b}$$

$$\text{Faraday's law,} \quad \boldsymbol{\nabla} \times \mathbf{E} = -\frac{\partial \mathbf{B}}{\partial t} \tag{3.2.29c}$$

$$\text{Solenoidal nature of } \mathbf{B}, \quad \boldsymbol{\nabla} \cdot \mathbf{B} = 0 \tag{3.2.29d}$$

$$\text{Ohm's law,} \quad \mathbf{J} = \sigma \left(\mathbf{E} + \mathbf{U} \times \mathbf{B} \right) \tag{3.2.29e}$$

$$\text{Lorentz force,} \quad \mathbf{F}^L = \mathbf{J} \times \mathbf{B} \tag{3.2.29f}$$

3.3 Magnetohydrodynamics

The previous two sections provide all the information required to build a mathematical description of magnetohydrodynamic fluid flow. In essence, it is simply the coupling between the Navier-Stokes equations and Maxwell's equations. This is mathematically described in the next few sections.

3.3.1 Transport equation for $\mathbf{B}$

An equation governing the evolution of an instantaneous magnetic field $\mathbf{B}$ can be found by first substituting Ampère's law (3.2.29b) into Ohm's law (3.2.29e);

$$\frac{\boldsymbol{\nabla} \times \mathbf{B}}{\mu_0 \sigma} = \mathbf{E} + \mathbf{U} \times \mathbf{B} \tag{3.3.1}$$

Taking the curl and substituting Faraday's law (3.2.29c);

$$\frac{\boldsymbol{\nabla}(\boldsymbol{\nabla} \cdot \mathbf{B}) - \nabla^2 \mathbf{B}}{\mu_0 \sigma} = -\frac{\partial \mathbf{B}}{\partial t} + \boldsymbol{\nabla} \times (\mathbf{U} \times \mathbf{B}) \tag{3.3.2}$$

where the general vector relationship $\boldsymbol{\nabla} \times (\boldsymbol{\nabla} \times \mathbf{A}) = \boldsymbol{\nabla} (\boldsymbol{\nabla} \cdot \mathbf{A}) - \nabla^2 \mathbf{A}$ has been used. Then upon rearranging, and using the solenoidal nature of $\mathbf{B}$;

$$\frac{\partial \mathbf{B}}{\partial t} = \boldsymbol{\nabla} \times (\mathbf{U} \times \mathbf{B}) + \frac{1}{\mu_0 \sigma} \nabla^2 \mathbf{B} \tag{3.3.3}$$

This takes the form of a typical transport equation, where the final term on the RHS is recognized as a diffusion type term and $\eta = (\mu_0 \sigma)^{-1}$ is the magnetic diffusivity. Taking the ratio of the terms on the right hand side;

$$\frac{\mathcal{O}\left(\boldsymbol{\nabla} \times (\mathbf{U} \times \mathbf{B})\right)}{\mathcal{O}\left(\eta \nabla^2 \mathbf{B}\right)} = \frac{UL}{\eta} = Re_m \tag{3.3.4}$$

where Re_m is the magnetic Reynolds number. As explained in Section 2.1, the magnetic Reynolds number measures the relative importance of advection to diffusion of the magnetic field.

Given a velocity field $\mathbf{U}$, Equation (3.3.3) evidently governs the evolution of the magnetic field $\mathbf{B}$ in time and space. One approach to couple the hydrodynamic and electromagnetic equations would therefore be to solve Equation (3.3.3) (a vector equation) and use Ampère's law (3.2.29b) to compute the corresponding current density $\mathbf{J}$. The Lorentz force term in the momentum equation, $\mathbf{J} \times \mathbf{B}$, is then fully defined. This requires, in 3D, an extra three transport equations to be solved.

This thesis is only concerned with cases where $Re_m \ll 1$, however, as they constitute the majority of MHD flows of engineering interest. As will become clear in the next section, restricting attention to this class of flows allows some significant simplifications to the governing equations.

3.3.2 Low Re_m approximation

Frequently referred to as the *inductionless* approximation, the low Re_m approximation is applicable for flows in which $Re_m \ll 1$. Physically, this amounts to stating the magnetic field associated with the induced currents is negligible in comparison to any externally applied or imposed magnetic field. This is usually the case when a flow is induced by some external means and directed through a static magnetic field. It also applies in situations where the magnetic field travels or rotates uniformly and slowly, since through a suitable change of reference frame (to that of the travelling magnetic field) the magnetic field becomes static.

To obtain the simplifications afforded by the approximation, following Davidson (2001), consider a case where Re_m is low and an imposed magnetic field is steady. Let $\mathbf{E}_0$, $\mathbf{J}_0$ and $\mathbf{B}_0$ represent the fields would would exist if, at some point, $\mathbf{U} = 0$. If $\mathbf{e}$, $\mathbf{j}$ and $\mathbf{b}$ are perturbations in those quantities as a result of a vanishingly small velocity field $\mathbf{U}$ then, from the expressions in Equation (3.2.29);

$$\boldsymbol{\nabla} \times \mathbf{E}_0 = -\frac{\partial \mathbf{B}_0}{\partial t} = 0 \tag{3.3.5a}$$

$$\boldsymbol{\nabla} \times \mathbf{e} = -\frac{\partial \mathbf{b}}{\partial t} \tag{3.3.5b}$$

$$\mathbf{J}_0 = \sigma \mathbf{E}_0 \tag{3.3.5c}$$

$$\mathbf{j} = \sigma \left(\mathbf{e} + \mathbf{U} \times \mathbf{B}_0 \right) \tag{3.3.5d}$$

where the second order term $\mathbf{u} \times \mathbf{b}$ has been neglected from Equation (3.3.5d). Since, from the earlier order of magnitude analysis in Equation (3.2.22), $\mathbf{e} \sim \mathrm{U}\mathbf{b}$, the induced electric field $\mathbf{e}$ can also be neglected in Equation (3.3.5d). Ohm's law becomes;

$$\mathbf{J} = \mathbf{J}_0 + \mathbf{j} = \sigma \left(\mathbf{E}_0 + \mathbf{U} \times \mathbf{B}_0 \right) \tag{3.3.6}$$

From Equation (3.3.5a), $\mathbf{E}_0$ is irrotational and so it may be written as the gradient of a scalar, $-\nabla\phi$, where ϕ is the electrostatic potential. Ohm's law (3.3.6) then finally becomes;

$$\mathbf{J} = \sigma \left(-\nabla\phi + \mathbf{U} \times \mathbf{B}_0 \right) \tag{3.3.7}$$

The leading order term in the Lorentz force is;

$$\mathbf{F}^L = \mathbf{J} \times \mathbf{B}_0 \tag{3.3.8}$$

To eliminate the current density, simply substituting Ohm's law gives;

$$\mathbf{F}^L = \sigma\left(-\nabla\phi + \mathbf{U}\times\mathbf{B}_0\right)\times\mathbf{B}_0 \tag{3.3.9}$$

Provided therefore that a (steady) magnetic field is imposed the only unknown in Equation (3.3.9) is the electrostatic potential. Fortunately, the divergence free condition imposed on the current density (see Equation (3.2.25)) means that by taking the divergence of Equation (3.3.7);

$$\begin{aligned}\boldsymbol{\nabla}\cdot\mathbf{J} &= \boldsymbol{\nabla}\cdot\sigma\left(-\nabla\phi + \mathbf{U}\times\mathbf{B}_0\right) = 0\\ \nabla^2\phi &= \boldsymbol{\nabla}\cdot\left(\mathbf{U}\times\mathbf{B}_0\right)\end{aligned} \tag{3.3.10}$$

one arrives at a Poisson type equation for ϕ involving the flow velocity and the magnetic field, both known quantities. With this in mind, the solution of an MHD problem within the low-Re_m approximation requires only the specification of the imposed magnetic field, the solution of one extra Poisson type equation and inclusion of the Lorentz force term into the mean momentum equations.

To finish, the additional equations are expressed in the tensor index notion more common to fluid dynamics. Taking the quantities in their instantaneous form and dropping the 0 subscript on the magnetic field vector, Equation (3.3.9) becomes;

$$\tilde{F}_i^L = \sigma\left(-\varepsilon_{ijk}\tilde{B}_k\frac{\partial\tilde{\phi}}{\partial x_j} + \tilde{U}_j\tilde{B}_i\tilde{B}_j - \tilde{U}_i\tilde{B}_j\tilde{B}_j\right) \tag{3.3.11}$$

and Equation (3.3.10) becomes;

$$\frac{\partial^2\tilde{\phi}}{\partial x_i^2} = \frac{\partial}{\partial x_i}\left(\varepsilon_{ijk}\tilde{U}_j\tilde{B}_k\right) \tag{3.3.12}$$

where ε_{ijk} is the third rank Levi-Civita alternating tensor. Since the magnetic field is now assumed fixed and constant, its turbulent fluctuations are zero by definition. A Reynolds decomposition of both Equation (3.3.11) and Equation (3.3.12) therefore yields no fluctuating second moments and, after averaging, the mean contribution is achieved by simply dropping the tildes. The fluctuating part of Equation (3.3.11) becomes;

$$f_i^L = \sigma\left(-\varepsilon_{ijk}B_k\frac{\partial\phi'}{\partial x_j} + u_jB_iB_j - u_iB_jB_j\right) \tag{3.3.13}$$

where, in this case, the prime on ϕ indicates it is a fluctuating quantity.

3.3.3 Statement of equations

The complete system of equations governing non-relativistic MHD flow under the low-Re_m approximation, subject to buoyancy and within the RANS framework consist of;

the continuity equation;

$$\frac{\partial U_i}{\partial x_i} = 0 \tag{3.3.14}$$

the RANS equation, with the Lorentz and buoyancy force terms;

$$\begin{aligned}\frac{\partial U_i}{\partial t} + U_j \frac{\partial U_i}{\partial x_j} = &- \frac{1}{\rho}\frac{\partial P^*}{\partial x_i} + \frac{\partial}{\partial x_j}\left[\nu\left(\frac{\partial U_i}{\partial x_j} + \frac{\partial U_j}{\partial x_i}\right) - \rho\overline{u_i u_j}\right] - g_i\beta\left(\Theta - \Theta_0\right) \\ &+ \frac{\sigma}{\rho}\left(-\varepsilon_{ijk}B_k\frac{\partial \phi}{\partial x_j} + U_j B_i B_j - U_i B_j B_j\right)\end{aligned} \tag{3.3.15}$$

where the pressure has been redefined as $P^* = P + \Phi_g$;

the reduced energy equation for scalar temperature Θ;

$$\frac{\partial \Theta}{\partial t} + U_j\frac{\partial \Theta}{\partial x_j} = \frac{\partial}{\partial x_j}\left[\alpha\frac{\partial \Theta}{\partial x_j} - \overline{u_j\theta}\right] \tag{3.3.16}$$

and the Poisson equation for the electrostatic potential;

$$\frac{\partial^2 \phi}{\partial x_i^2} = \frac{\partial}{\partial x_i}\left(\varepsilon_{ijk}U_j B_k\right) \tag{3.3.17}$$

There are still two terms which remain to be addressed: $\rho\overline{u_i u_j}$ and $\overline{u_i\theta}$. These are discussed in the next chapter.

CHAPTER

FOUR

TURBULENCE MODELLING

"I am an old man now, and when I die and go to heaven there are two matters on which I hope for enlightenment. One is quantum electrodynamics, and the other is the turbulent motion of fluids. And about the former I am rather optimistic"
Horace Lamb, 1932

Turbulence is a ubiquitous feature in fluid flow. Being able to properly account for it in CFD simulations is thus an important challenge in engineering. This chapter opens in Section 4.1 with a brief overview of turbulence as a phenomenon and includes the ways in which it can be modified by a magnetic field. Section 4.2 then provides an overview of the most common solution strategies employed within CFD. In perhaps unconventional fashion, the more elaborate stress-transport approach is introduced first in Section 4.3 since it provides a deeper understanding of the various processes by which turbulent stresses are transported, diffused and dissipated. The more common eddy-viscosity approach then naturally follows as a simplification in Section 4.4. Finally, Section 4.5 details some approaches commonly used to model flows within the vicinity of a wall.

4.1 Characteristics of turbulent flows

The majority of flows of engineering and environmental significance are turbulent. They are characterized by fluid motions which, in both space and time, exhibit chaotic and irregular behaviour. Mathematically, it is mainly the interactions between the non-linear inertial terms and the viscous terms in the Navier-Stokes equations which cause the flow to become unstable. Thus, the transition of a flow from laminar to turbulent flow is governed largely by the Reynolds number. Osborne Reynolds famously demonstrated that a laminar pipe flow would transition to turbulence somewhere in the range $2000 < Re < 4000$, but other factors, such as pipe roughness, the uniformity of the inlet flow and even the ambient noise in the room of the experiment, were also influential.

Once a flow is turbulent, one of the most prominently observed features is increased mixing. In contrast to laminar flows, where fluid tends to flow in a smooth, orderly, fashion, the presence of large, swirling, eddying motions in turbulent flow leads to intense and vigorous mixing. Aside from having implications for transported quantities, such as heat or concentration, the turbulence also mixes the momentum of the fluid itself, manifesting as an apparent stress (the Reynolds stresses). It is this "eddying motion" which tends to most visibly characterize turbulent flows. These eddies are observed to cover a wide range of time and length scales, from the largest, which are governed by the geometry of the flow, to the smallest, which, as shall be discussed below, are responsible for the eventual dissipation of turbulent energy.

4.1.1 Spectral view of turbulence and the energy cascade

The turbulent eddies within a flow serve to distribute energy across the range of length scales that are found. The most widely accepted mechanism, originally put forward by Richardson (1922), is that turbulent energy is captured from the mean flow through engulfment by large-scale eddies. These eddies are then progressively broken down to smaller eddies (taking a proportion of the captured energy with them) through a process of inertially driven eddy stretching and distortion. This occurs until the scales of motion are so small, and the velocity gradients so large, that the energy is dissipated as heat by viscous action. The eddies that lie between the largest (responsible for energy capture) and the smallest (responsible for energy dissipation) serve as energy carriers, transferring energy down the spectrum of scales in a "cascading" fashion.

To quantify this cascading process somewhat, take k to be the turbulent kinetic energy which is transferred and carried by the eddies throughout the cascade and ε to be the rate at which k is dissipated due to the action of viscosity at the smallest scales. If the turbulence is statistically steady, then ε must also equal the rate at which k is fed to the

turbulence from the mean flow, otherwise there would be a net gain or loss in energy (and a build up of eddies of a particular size). This led Kolmogorov (1941) to suppose that the motion at the smallest scales, therefore, should only be dependant on the rate at which they receive energy from the mean flow, ε, and ν, the viscosity. Dimensional arguments then lead to the following velocity (v), length (η) and time (τ) scales;

$$v = (\nu\varepsilon)^{1/4}, \quad \eta = \left(\frac{\nu^3}{\varepsilon}\right)^{1/4}, \quad \tau = \left(\frac{\nu}{\varepsilon}\right)^{1/2} \tag{4.1.1}$$

which are known as the *Kolmogorov microscales* and represent turbulent motion at the finest scales.

Despite generally being associated with the fine-scale motion, ε is primarily determined by the motion of the large scale eddies, since it is these which determine the rate at which k is captured from the mean flow. If U and ℓ are velocity and length scales associated with the large eddies, then these eddies will have energy of order U^2 and a timescale of $\tau_\ell = \ell/U$. The rate of energy transfer from the mean flow, therefore, can be expected to scale as;

$$\varepsilon \sim U^2/\tau_\ell = U^3/\ell \tag{4.1.2}$$

Viscosity can be expected to play little part in the energy cascade, since a Reynolds number formed from U and ℓ will be much greater than unity (for high bulk Reynolds numbers at least). Once captured by the turbulence then, turbulent kinetic energy will transfer down the cascade, unimpeded by viscosity, until the length scale of the motion becomes small enough that viscous forces do become significant i.e. when the Reynolds number associated with the turbulent motions becomes of order one. The energy is then dissipated to heat by the viscous forces. Since ε is fixed by the large scale motion, the size of the small scales adjusts so as to ensure turbulent energy is dissipated at a rate that balances the rate it is transferred from the mean flow (Hanjalic and Launder, 2011).

The range of scales within a particular flow can be estimated by combining Equation (4.1.1) and Equation (4.1.2) to give

$$\frac{v}{U} \sim Re^{-1/4}, \quad \frac{\eta}{\ell} \sim Re^{-3/4}, \quad \frac{\tau}{\tau_\ell} \sim Re^{-1/2} \tag{4.1.3}$$

where the Reynolds number is based on the large scale eddies $Re = U\ell/\nu$. Evidently, as Re increases, the scales of the finest motion become smaller compared with those of the largest eddies. Kolmogorov argued that, because of this, at sufficiently high Reynolds number the small scale motions are statistically isotropic. Anisotropy which is induced at large scales by boundary conditions or body forces is lost as energy is transferred down the spectrum.

The view of turbulence above as advanced by Kolmogorov (1941) and Richardson (1922), amongst others, largely underpins a lot of the turbulence modelling approaches which are

used within the RANS framework. As the next section shall discuss, the application of a magnetic field, as something which is known to induce anisotropy, will clearly serve to disrupt this view somewhat.

4.1.2 MHD turbulence

It was seen in Chapter 2 that the application of a magnetic field to initially isotropic freely decaying turbulence resulted in a kind of transformation towards a two-dimensional, and hence highly anisotropic, state. Clearly this has some implications for one of Kolmogorov's hypotheses introduced in the previous section, which was that turbulence exhibits local (small scale) isotropy at high Reynolds numbers. Davidson (1997) argued that this transformation towards a two-dimensional state is a result of the need for the flow to conserve angular momentum despite a continual reduction in kinetic energy due to Joule dissipation. To provide more rigor to this, the problem is revisited here in more mathematical detail.

Consider again a large electrically insulated sphere of radius R and volume V. The sphere contains an electrically conducting fluid of constant viscosity and it sits in a uniform imposed magnetic field $\mathbf{B}$. The instantaneous equation governing the motion of the fluid is, from Equation (3.1.5), in vector notation;

$$\rho\frac{D\mathbf{U}}{Dt} = -\nabla P + \mu\nabla^2\mathbf{U} + \mathbf{J}\times\mathbf{B} \tag{4.1.4}$$

where the final term on the RHS is recognized as the Lorentz force. Taking the dot product of Equation (4.1.4) with $\mathbf{U}$ yields;

$$\frac{D}{Dt}\left[\frac{1}{2}\rho\mathbf{U}^2\right] = -\boldsymbol{\nabla}\cdot(P\mathbf{U}) + \mu\nabla^2\mathbf{U}\cdot\mathbf{U} + (\mathbf{J}\times\mathbf{B})\cdot\mathbf{U} \tag{4.1.5}$$

which governs the evolution of the fluid's kinetic energy, $1/2\rho U^2$, in the system. The first term on the RHS represents work done by pressure gradients. The remaining terms on the RHS will be addressed in turn to help elicit some physical meaning. From Ohm's law, Equation (3.3.7);

$$\mathbf{U}\times\mathbf{B} = -\frac{1}{\sigma}\mathbf{J} + \nabla\phi \tag{4.1.6}$$

and the rate of working of the Lorentz force, the final term on the RHS of Equation (4.1.5), can be rewritten as;

$$(\mathbf{J}\times\mathbf{B})\cdot\mathbf{U} = \mathbf{J}\cdot(\mathbf{B}\times\mathbf{U}) = -\mathbf{J}\cdot(\mathbf{U}\times\mathbf{B}) = -\frac{1}{\sigma}\mathbf{J}^2 - \boldsymbol{\nabla}\cdot(\phi\mathbf{J}) \tag{4.1.7}$$

With the help of the vector identity $\boldsymbol{\nabla}\times(\boldsymbol{\nabla}\times\mathbf{A}) = \nabla(\boldsymbol{\nabla}\cdot\mathbf{A}) - \nabla^2\mathbf{A}$, the viscous term in Equation (4.1.4) can be rewritten as;

$$\mu\nabla^2\mathbf{U} = -\mu\boldsymbol{\nabla}\times(\boldsymbol{\nabla}\times\mathbf{U}) = -\mu\boldsymbol{\nabla}\times\boldsymbol{\omega} \tag{4.1.8}$$

where the continuity condition, $\boldsymbol{\nabla} \cdot \mathbf{U} = 0$, has been used and $\boldsymbol{\omega} = \boldsymbol{\nabla} \times \mathbf{U}$ is the vorticity. The corresponding viscous term in Equation (4.1.5) now becomes, with the vector identity $\boldsymbol{\nabla} \cdot (\mathbf{A} \times \mathbf{B}) = \mathbf{B} \cdot (\boldsymbol{\nabla} \times \mathbf{A}) - \mathbf{A} \cdot (\boldsymbol{\nabla} \times \mathbf{B})$ and some manipulation;

$$\mu \boldsymbol{\nabla}^2 \mathbf{U} \cdot \mathbf{U} = -\mu \mathbf{U} \cdot (\boldsymbol{\nabla} \times \boldsymbol{\omega}) = \mu \boldsymbol{\nabla} \cdot (\mathbf{U} \times \boldsymbol{\omega}) - \mu \boldsymbol{\omega}^2 \tag{4.1.9}$$

Collecting the terms, Equation (4.1.5) becomes;

$$\frac{D}{Dt}\left[\frac{1}{2}\rho \mathbf{U}^2\right] = -\boldsymbol{\nabla} \cdot (P\mathbf{U}) + \mu \boldsymbol{\nabla} \cdot (\mathbf{U} \times \boldsymbol{\omega}) - \boldsymbol{\nabla} \cdot (\phi \mathbf{J}) - \mu \boldsymbol{\omega}^2 - \frac{1}{\sigma}\mathbf{J}^2 \tag{4.1.10}$$

The advective part of the total derivative can be rewritten;

$$\mathbf{U} \cdot \boldsymbol{\nabla}\left[\frac{1}{2}\rho \mathbf{U}^2\right] = \boldsymbol{\nabla} \cdot \left[\left(\frac{1}{2}\rho \mathbf{U}^2\right)\mathbf{U}\right] \tag{4.1.11}$$

Taking this to the RHS and gathering all the divergence terms together;

$$\frac{\partial}{\partial t}\left[\frac{1}{2}\rho \mathbf{U}^2\right] = \boldsymbol{\nabla} \cdot \left[-\left(P + \frac{1}{2}\rho \mathbf{U}^2\right)\mathbf{U} + \mu\left(\mathbf{U} \times \boldsymbol{\omega}\right) - \phi \mathbf{J}\right] - \mu \boldsymbol{\omega}^2 - \frac{1}{\sigma}\mathbf{J}^2 \tag{4.1.12}$$

By integrating this over the volume of the sphere, and with help from the divergence theorem and the impermeability $(\mathbf{U} \cdot \mathrm{d}\mathbf{S} = 0)$ and insulating conditions $(\mathbf{J} \cdot \mathrm{d}\mathbf{S} = 0)$ imposed at the boundary of the sphere (S), the divergence term vanishes. Equation (4.1.12) then becomes;

$$\frac{\partial}{\partial t}\int_{\mathrm{V}}\left(\frac{1}{2}\rho \mathbf{U}^2\right)\,\mathrm{dV} = -\mu\int_{\mathrm{V}}\boldsymbol{\omega}^2\,\mathrm{dV} - \frac{1}{\sigma}\int_{\mathrm{V}}\mathbf{J}^2\,\mathrm{dV} \tag{4.1.13}$$

which can be seen to govern the evolution of the total kinetic energy within the system. The dissipative mechanisms within the system now become clear. Since both terms inside the integrands on the RHS are positive, they demonstrate that the kinetic energy of the flow will fall monotonically in time if either $\boldsymbol{\omega}$ or $\mathbf{J}$ are non-zero. Physically, the term involving $\boldsymbol{\omega}^2$ represents viscous dissipation and the term involving $\mathbf{J}^2$ represents Joule dissipation.

Now, suppose that the fluid in the sphere is vigorously stirred, such that the turbulence which is created is statistically homogeneous and isotropic, and then left to itself. In the absence of magnetic fields, the current vanishes and the turbulence will be expected to eventually decay (and the fluid come to rest) courtesy of the viscous dissipation term.

To better expose the effects of the magnetic field, take the fluid to be inviscid. Equation (4.1.13) becomes;

$$\frac{\partial}{\partial t}\int_{\mathrm{V}}\left(\frac{1}{2}\rho \mathbf{U}^2\right)\,\mathrm{dV} = -\frac{1}{\sigma}\int_{\mathrm{V}}\mathbf{J}^2\,\mathrm{dV} \tag{4.1.14}$$

Clearly, if the flow is initially turbulent, the fluctuating motions across the magnetic field lines will induce a current $\mathbf{J}$ and this would be expected to lead to a continual decline in

kinetic energy. However, as Davidson (1995) shows, one component of angular momentum is conserved during this decay. To see why, take $\boldsymbol{\tau}^L$ to be the torque induced by the Lorentz force $\mathbf{J} \times \mathbf{B}$;

$$\boldsymbol{\tau}^L = \mathbf{x} \times (\mathbf{J} \times \mathbf{B}) \tag{4.1.15}$$

where $\mathbf{x}$ is the displacement vector between the point at which the force acts and the point where the torque is measured. Consider the component of torque parallel to $\mathbf{B}$, given by;

$$\boldsymbol{\tau}^L \cdot \mathbf{B} = [(\mathbf{x} \cdot \mathbf{B})\,\mathbf{J} - (\mathbf{x} \cdot \mathbf{J})\,\mathbf{B}] \cdot \mathbf{B} \tag{4.1.16}$$

For the purposes of computing the torque, one only needs to consider the distance vector perpendicular to the magnetic field, $\mathbf{x}_\perp$. Thus, Equation (4.1.16) becomes;

$$[(\mathbf{x}_\perp \cdot \mathbf{B})\,\mathbf{J} - (\mathbf{x}_\perp \cdot \mathbf{J})\,\mathbf{B}] \cdot \mathbf{B} = -B^2\,(\mathbf{x}_\perp \cdot \mathbf{J}_\perp) \tag{4.1.17}$$

since, also, only the component of $\mathbf{J}$ parallel to $\mathbf{x}_\perp$ will contribute. The RHS can be transformed by using $J_i = \boldsymbol{\nabla} \cdot (x_i \mathbf{J})$ such that;

$$x_i J_i = x_i \boldsymbol{\nabla} \cdot (x_i \mathbf{J}) = \boldsymbol{\nabla} \cdot \left(x_i^2 \mathbf{J}\right) - x_i J_i$$

$$\rightarrow x_\perp J_\perp = \frac{1}{2} \boldsymbol{\nabla} \cdot \left(x_\perp^2 \mathbf{J}\right) \tag{4.1.18}$$

Substituting this into Equation (4.1.17), the component of torque parallel to the magnetic $\mathbf{B}$ is given by;

$$\boldsymbol{\tau}^L \cdot \mathbf{B} = -\frac{B^2}{2} \boldsymbol{\nabla} \cdot \left(x_\perp^2 \mathbf{J}\right) \tag{4.1.19}$$

Integrating this over the sphere;

$$-\frac{B^2}{2} \int_{\mathrm{V}} \boldsymbol{\nabla} \cdot \left(x_\perp^2 \mathbf{J}\right)\, \mathrm{dV} = -\frac{B^2}{2} \int_S x_\perp^2 \mathbf{J} \cdot\, \mathrm{d}\mathbf{S} = 0 \tag{4.1.20}$$

since, as before, the insulating condition at the boundary ensures $\mathbf{J} \cdot\, \mathrm{d}\mathbf{S} = 0$. The global torque, caused by the Lorentz force, parallel to $\mathbf{B}$ is thus zero. Since there are no viscous forces, the component of angular momentum parallel to $\mathbf{B}$;

$$\mathbf{H}_\parallel = \int_{\mathrm{V}} (\mathbf{x} \times \mathbf{U})\, \mathrm{dV} \tag{4.1.21}$$

must be conserved as the flow evolves. This presents a bit of a problem. If the flow possesses some finite amount of $\mathbf{H}_\parallel$, then it cannot come to rest. The energy equation (4.1.14), however, states that so long as the flow is moving, and generating a finite amount of current, its kinetic energy must continue to fall. Consequently, it appears as though the flow must somehow evolve to eliminate Joule dissipation whilst maintaining its angular momentum. The generation of current is explicitly linked to the flow velocity by Ohm's

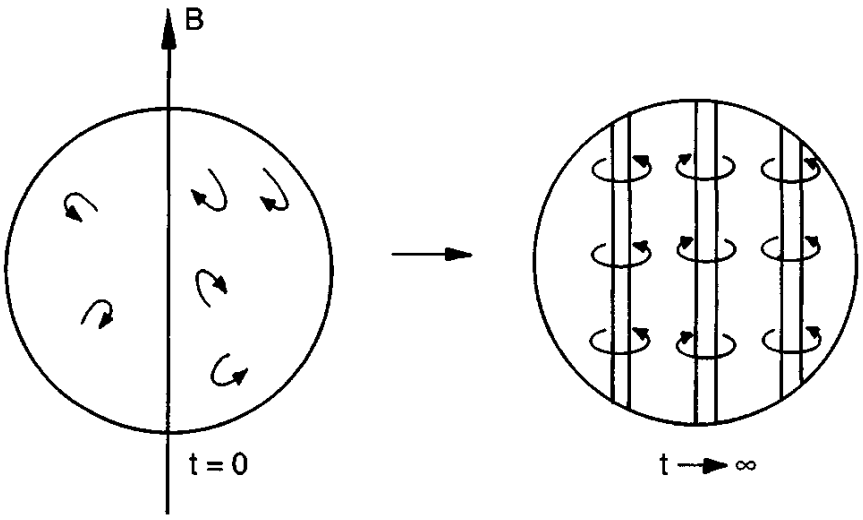

Figure 4.1: Initially homogeneous and isotropic turbulence (left) evolves into a two-dimensional state (right) where vortices become aligned and stretched in the direction of the magnetic field Davidson (2001).

law, in Equation (3.3.7). Taking the curl of this;

$$\boldsymbol{\nabla} \times \mathbf{J} = \sigma \left(-\nabla\phi + \mathbf{U} \times \mathbf{B} \right) = \sigma \boldsymbol{\nabla} \times \left(\mathbf{U} \times \mathbf{B} \right) \tag{4.1.22}$$

This can be simplified with the vector identity;

$$\boldsymbol{\nabla} \times \left(\mathbf{U} \times \mathbf{B} \right) = \mathbf{U} \left(\boldsymbol{\nabla} \cdot \mathbf{B} \right) - \mathbf{U} \left(\boldsymbol{\nabla} \cdot \mathbf{U} \right) + \left(\mathbf{B} \cdot \boldsymbol{\nabla} \right) \mathbf{U} - \left(\mathbf{U} \cdot \boldsymbol{\nabla} \right) \mathbf{B} \tag{4.1.23}$$

where since $\boldsymbol{\nabla} \cdot \mathbf{B} = 0$, $\boldsymbol{\nabla} \cdot \mathbf{U} = 0$ and the magnetic field $\mathbf{B}$ does not vary in space, Equation (4.1.22) becomes;

$$\boldsymbol{\nabla} \times \mathbf{J} = \left(\mathbf{B} \cdot \boldsymbol{\nabla} \right) \mathbf{U} \tag{4.1.24}$$

This, along with $\boldsymbol{\nabla} \cdot \mathbf{J} = 0$, uniquely defines the vector field $\mathbf{J}$. The interesting point about Equation (4.1.24), and one which reveals how the flow evolves, is that the term on the RHS vanishes if $\mathbf{U}$ exhibits no variation in the direction of the magnetic field $\mathbf{B}$. Since there are no external sources of current, one way for the flow to evolve into a state where $\mathbf{J} = 0$, as the preceding argument suggests it must, is for it to rearrange into a strictly two-dimensional state independent of the direction of the magnetic field. The turbulent eddies become elongated in the direction of the magnetic field and stretch out to become column like. Figure 4.1 provides a schematic representation. As this transformation occurs, the magnitude of the current, and hence Joule dissipation, decreases.

Contrary to Kolmogorov's picture for non-MHD turbulence, the presence of a magnetic field actually drives the flow towards a highly anisotropic state, stretching the eddies along the magnetic field lines. Of course, in any real flow, the fluid will not be inviscid and thus the stretching process will be accompanied by viscous dissipation, eventually coming to rest.

4.2 Overview of solution strategies

There are three broad strategies employed to numerically simulate fluid flows and they have all received at least a mention thus far: Direct Numerical Simulation (DNS), Large Eddy Simulation (LES) and solution of the Reynolds-averaged Navier-Stokes (RANS) equation. Whatever approach one takes, the governing equations of the problem first need to be discretized, over a mesh or grid of discrete points, before they can be subject to numerical treatment. The size and resolution of this mesh will determine the range of length scales which it becomes possible to reproduce. Any motion on a lengthscale smaller than the smallest cell will not be captured and, similarly, the time step used in the solution process must also be small enough to capture the fastest fluctuations in the flow. The strategies discussed here are broadly split according to the range of length scales which they attempt to resolve.

4.2.1 Direct Numerical Simulation

If one wishes to resolve the entire spectrum of length and time scales, then as a minimum the mesh must be composed of cells whose size is smaller than the Kolmogorov length scale and use a time step smaller than the Kolmogorov time scale for the flow in question. If these constraints are satisfied then the solution can be considered a *Direct Numerical Simulation*. The approach does not involve any modelling and, if done correctly, will resolve the entirety of the energy spectrum. Solutions obtained this way provide a degree of accuracy and a level of detail far beyond that which experimental methods can currently provide but they are, however, very computationally expensive. So much so in fact[1] that, whilst DNS is useful for fundamental research, it is not generally suitable for use on routine industrial (or even routine academic) computations.

4.2.2 Large Eddy Simulation

Large Eddy Simulation aims to reduce the large computational expenditure of DNS by only attempting to resolve part of the energy spectrum. It achieves this by applying a "filter" over the Navier-Stokes equations which removes motion on the smallest, unresolvable, scales. The large scale motion is fully resolved and the unresolved motion is accounted for by a so called sub-grid-scale model. Since some proportion of the energy spectrum is resolved, the sub-grid-scale models used are less crucial to the computed behaviour of the flow than in RANS and they can thus afford to be simpler in nature. Despite the reduction in computational cost, however, LES still falls outside of the realm of most industrial calculations.

[1] As an estimate, the number of mesh nodes required to resolve the complete spectrum increases as $N^3 \sim 4.4 Re_t^{9/4}$ (Pope, 2000).

4.2.3 Solution of the Reynolds-averaged Navier-Stokes equation

The final strategy, as already detailed in Chapter 3, solves the RANS form of the Navier-Stokes equation. Since the equations are averaged, they can only provide the averaged turbulent properties (such as the turbulent kinetic energy, k) at a point in space with no information about how that energy is distributed across the spectrum. All of the effects of the turbulent fluctuations are provided by the model through the Reynolds stress tensor $\overline{u_i u_j}$, which appears in the RANS equation. The challenge for the RANS approach then, is to provide an accurate means of computing $\overline{u_i u_j}$.

There are two main approaches to this. The first supposes that a relationship exists between the turbulent stresses and the mean strains through a turbulent or eddy-viscosity. The eddy-viscosity itself is supplied by solving one or more equations for what essentially are representative time and length scales for the present turbulence. The second, and more elaborate, approach solves transport equations for each component of $\overline{u_i u_j}$ (the second-moments). These are thus often referred to as stress-transport or Reynolds stress models (RSM). The attraction of this over eddy-viscosity based approaches is that the terms describing stress production as a result of mean straining are exact and require no modelling. The task is then to provide suitable models for those terms in the $\overline{u_i u_j}$ transport equation that are unclosed. Closures for other transported quantities, such as temperature, can often be achieved in an analogous fashion. The RANS approach is the form of modelling employed in this research and both the eddy-viscosity and stress-transport approaches discussed here have been used. The next few sections provide the rationale and mathematical details behind the models used.

4.3 Stress-transport models

In the stress-transport class of model, a transport equation for each component of the Reynolds stresses $\overline{u_i u_j}$ is solved. Since the equations are for the second moments, this approach is often referred to as second-moment closure. These can be derived by subtracting the RANS equation (3.1.11) from the instantaneous Navier-Stokes equations (3.1.5) to obtain a transport equation for the fluctuating velocity u_i. Then;

$$\frac{D\overline{u_i u_j}}{Dt} = \overline{u_i \frac{Du_j}{Dt}} + \overline{u_j \frac{Du_i}{Dt}} \tag{4.3.1}$$

where the overbar indicates a Reynolds averaging operation and D/Dt represents the material or Lagrangian derivative;

$$\frac{D\overline{u_i u_j}}{Dt} = \frac{\partial \overline{u_i u_j}}{\partial t} + U_k \frac{\partial \overline{u_i u_j}}{\partial x_k} \tag{4.3.2}$$

Following this, one arrives at the Reynolds stress transport equation, written here in symbolic form;

$$\frac{D\overline{u_i u_j}}{Dt} = \mathcal{P}_{ij} - \varepsilon_{ij} + \Phi_{ij} - \mathcal{D}_{ij} + \mathcal{F}_{ij} \tag{4.3.3}$$

where;

$$\mathcal{P}_{ij} = -\left(\overline{u_j u_k} \frac{\partial U_i}{\partial x_k} + \overline{u_i u_k} \frac{\partial U_j}{\partial x_k} \right) \tag{4.3.4}$$

$$\varepsilon_{ij} = 2\nu \overline{\frac{\partial u_i}{\partial x_k} \frac{\partial u_j}{\partial x_k}} \tag{4.3.5}$$

$$\Phi_{ij} = \overline{\frac{p}{\rho} \left(\frac{\partial u_j}{\partial x_i} + \frac{\partial u_i}{\partial x_j} \right)} \tag{4.3.6}$$

$$\mathcal{D}_{ij} = \underbrace{\frac{\partial}{\partial x_k} \left[\overline{u_i u_j u_k} + \overline{\frac{p}{\rho} \left(u_j \delta_{ik} + u_i \delta_{jk} \right)} - \nu \frac{\partial}{\partial x_k} \left(\overline{u_i u_j} \right) \right]}_{\mathcal{D}^t_{ij} + \mathcal{D}^p_{ij} + \mathcal{D}^\nu_{ij}} \tag{4.3.7}$$

$$\mathcal{F}_{ij} = \frac{1}{\rho} \sum_n \left(\overline{f_i^n u_j + f_j^n u_i} \right) \tag{4.3.8}$$

The $\mathcal{P}_{ij}$ term represents the production of $\overline{u_i u_j}$ by the action of mean strain. Since it only contains contributions from the Reynolds stresses and the mean velocity gradients it is exact and does not require modelling.

The $\mathcal{F}_{ij}$ term represents the sum of contributions to the $\overline{u_i u_j}$ budget from n fluctuating body forces denoted by f_i^n. For buoyancy, substitution of the fluctuating buoyancy force, Equation (3.1.20), into Equation (4.3.8) gives;

$$\mathcal{F}^b_{ij} = -\rho\beta \left(\overline{u_i \theta} g_j + \overline{u_j \theta} g_i \right) \tag{4.3.9}$$

A model for the unknown correlation between the fluctuating velocity and the fluctuating temperature, $\overline{u_i\theta}$, is already required since it appeared in the equation for the mean temperature (Equation (3.1.12)).

For electromagnetic interactions, the fluctuating Lorentz force is recalled from Equation (3.3.13);

$$f_i^L = \sigma\left(-\varepsilon_{ikl}B_l\frac{\partial\phi'}{\partial x_k} + u_lB_iB_l - u_iB_lB_l\right) \tag{4.3.10}$$

The contribution to $\mathcal{F}_{ij}$ becomes;

$$\mathcal{F}_{ij}^L = \frac{\sigma}{\rho}\left(\underbrace{-\varepsilon_{ikl}B_l\overline{u_j\frac{\partial\phi'}{\partial x_k}} - \varepsilon_{jkl}B_l\overline{u_i\frac{\partial\phi'}{\partial x_k}}}_{\mathcal{F}_{ij}^{L1}} + \underbrace{B_iB_k\overline{u_ju_k} + B_jB_k\overline{u_iu_k} - 2B_k^2\overline{u_iu_j}}_{\mathcal{F}_{ij}^{L2}}\right) \tag{4.3.11}$$

The second part of this term, $\mathcal{F}_{ij}^{L2}$, is exact and requires no additional effort. The $\mathcal{F}_{ij}^{L1}$ term, however, contains the correlation between the fluctuating velocity and the fluctuating gradient of the electrostatic potential and requires modelling. This is discussed later in Subsection 4.3.2.

All of the other terms in the stress transport equation require modelling. The group of terms represented by $\mathcal{D}_{ij}$ are diffusive in character and contain contributions from the triple moments of velocity, $\mathcal{D}_{ij}^t$, pressure-velocity correlations, $\mathcal{D}_{ij}^p$, and viscous effects, $\mathcal{D}_{ij}^\nu$. The latter would be expected to generally be negligible over most of a flow, except perhaps within the viscous sublayer next to a solid wall. The Φ_{ij} term contains the correlation between the fluctuating pressure and fluctuating strain. Because of this, it is usually called the pressure-strain or pressure-scrambling term. The importance of this term becomes clear when one considers its contribution to the turbulent kinetic energy, k. A transport equation for k can be formed by simply taking half the trace of Equation (4.3.3), since, by definition, $k = \overline{u_ku_k}/2$. Thus, taking half the trace of Equation (4.3.6);

$$\frac{1}{2}\Phi_{kk} = \overline{\frac{p}{\rho}\frac{\partial u_k}{\partial x_k}} \tag{4.3.12}$$

For incompressible flow, this is zero by continuity. Thus the Φ_{ij} term makes no contribution to the overall level of turbulent kinetic energy, and instead serves to redistribute energy among the normal stress components. Much attention has been paid to the modelling of Φ_{ij} since it represents a physical process absent from those turbulence models which rely heavily on a transport equation for k. Approaches to modelling this term are considered in greater detail below.

Finally, the ε_{ij} term represents the destruction of $\overline{u_i u_j}$ by viscous action. Although evidently describing effects molecular in origin, the term cannot in general be neglected. In a simple shear flow (one in which U_1 is a function of x_2 and $U_2 = U_3 = 0$), the production term represents the continual extraction of turbulent energy from the mean flow. Since, as described above, the Φ_{ij} term does not change the overall level of turbulent kinetic energy and diffusion only leads to a spatial reorganization of the energy, the only mechanism left which can reduce the level of turbulent energy is dissipation.

Modelling the pressure-strain term

A Poisson equation for the fluctuating pressure can be obtained by taking the divergence of the Navier-Stokes equation (3.1.5) and subtracting its mean part, Equation (3.1.11), to give;

$$\frac{1}{\rho}\frac{\partial^2 p}{\partial x_l^2} = -2\frac{\partial U_l}{\partial x_m}\frac{\partial u_m}{\partial x_l} + \frac{\partial^2}{\partial x_l \partial x_m}\left(\rho\overline{u_l u_m} - u_l u_m\right) + \frac{\partial f_l}{\partial x_l} \tag{4.3.13}$$

where f_l is a fluctuating body force. This can be formally integrated with the help of a Green's function to produce an expression for the fluctuating pressure, p. Multiplying that by $(\partial u_i/\partial x_j + \partial u_j/\partial x_i)$ results in an expression for Φ_{ij}, although solution of the resulting integrals is difficult. Instead, most researchers have opted for a slightly more heuristic approach. This begins with noting that Equation (4.3.13) suggests three distinct types of interactions which will affect the pressure fluctuations: those involving the mean rate of strain, those involving purely fluctuating quantities, and those associated with body forces. Reflecting this, a suitable model for Φ_{ij} would be;

$$\Phi_{ij} = \Phi_{ij}^{(1)} + \Phi_{ij}^{(2)} + \Phi_{ij}^{(f)} + \Phi_{ij}^{(w)} \tag{4.3.14}$$

where the $\Phi_{ij}^{(1)}$ part is known as the *slow* pressure-strain term, representing interactions which only depend on fluctuating quantities (the middle term on the RHS of Equation (4.3.13)) and tend to return the stress field to an isotropic state. $\Phi_{ij}^{(2)}$, which corresponds to the first term on the RHS of Equation (4.3.13), is known as the *fast* or *rapid* pressure-strain term. The term so called because the presence of the mean velocity gradient ensures it will respond immediately to a change in strain. It can be viewed as generally acting to return the production tensor, $\mathcal{P}_{ij}$, to isotropy (Hanjalic and Launder, 2011). $\Phi_{ij}^{(3)}$, the third term on the RHS of Equation (4.3.13) acts in a similar fashion to $\Phi_{ij}^{(2)}$ but reduces the anisotropy in the stresses induced by applied body forces. Finally, the $\Phi_{ij}^{(w)}$ term, which does not correspond to a particular process immediately identifiable in Equation (4.3.13), is often called the wall-echo or *wall-reflection* term. This provides the necessary corrections to Φ_{ij} to account for the presence of a wall or free-surface.

Specific closure routes are now considered below, beginning with the 'basic' model of Gibson and Launder (1978). Extensions to those models to account for low-Re and elec-

tromagnetic effects are provided by the Hanjalić and Jakirlić model, which is detailed after.

4.3.1 Basic second-moment closure

The basic second-moment closure model is formed from contributions by Rotta (1951), Launder and Sharma (1974), Launder et al. (1975), Launder (1975) and Gibson and Launder (1978). The model constants used here are those presented by Gibson and Launder (1978). The slow pressure-strain term is modelled following Rotta (1951) as;

$$\Phi_{ij}^{(1)} = -c_1 \frac{\varepsilon}{k} \left(\overline{u_i u_j} - \frac{1}{3} \delta_{ij} \overline{u_k u_k} \right) \tag{4.3.15}$$

where $c_1 = 1.8$. The term will act as a source or sink of $\overline{u_i u_j}$ directly in proportion to its deviation from the isotropic state scaled by a turbulent time scale. It is based on the notion that freely decaying anisotropic turbulence becomes more isotropic as it decays.

The rapid pressure-strain term follows the *isotropization-of-production* (IP) model of Naot et al. (1970). This, in an analogous fashion to Rotta's model of the slow term, tends to redistribute the effects of an imposed mean strain by reducing the anisotropy of the production tensor. It is given by;

$$\Phi_{ij}^{(2)} = -c_2 \left(\mathcal{P}_{ij} - \frac{1}{3} \delta_{ij} \mathcal{P}_{kk} \right) \tag{4.3.16}$$

where the value c_2 is taken as 0.6.

Contributions from the fluctuating buoyancy force, should it exist, are included by adopting the IP strategy employed above (Launder, 1975);

$$\Phi_{ij}^{(b)} = -c_3^b \left(\mathcal{F}_{ij}^b - \frac{1}{3} \delta_{ij} \mathcal{F}_{kk}^b \right) \tag{4.3.17}$$

where the constant $c_3^b = 0.6$.

For the wall-reflection term, it is known from experiments that the main effect of a wall on $\overline{u_i u_j}$ is to dampen the level of the stress component normal to the wall (Hanjalic and Launder, 2011). Physically, this arises due to the "blocking" effect of the wall; velocity fluctuations must diminish more quickly in the wall-normal direction, partly because of the continuity constraint. As such, and in contrast to the other terms within Φ_{ij}, the wall tends to preferentially promote anisotropy in $\overline{u_i u_j}$. The $\Phi_{ij}^{(w)}$ term is split into three parts: one associated with the slow part, one associated with the fast part and one associated with the body-force induced part of the pressure-strain term;

$$\Phi_{ij}^{(w)} = \Phi_{ij}^{(w,1)} + \Phi_{ij}^{(w,2)} + \Phi_{ij}^{(w,f)} \tag{4.3.18}$$

A model for $\Phi_{ij}^{(w,1)}$ was developed by Shir (1973);

$$\Phi_{ij}^{(w,1)} = c_1^w \frac{\varepsilon}{k}\left(\overline{u_k u_l} n_l n_k \delta_{ij} - \frac{3}{2}\overline{u_i u_k} n_j n_k - \frac{3}{2}\overline{u_j u_k} n_i n_k\right) f_w \tag{4.3.19}$$

where n_i is the ith component of the wall-normal vector, $c_1^w = 0.5$ and f_w is an empirical function that varies from unity at the wall to zero far enough away;

$$f_w = \frac{k^{3/2}}{2.5\varepsilon y} \tag{4.3.20}$$

where y is the distance normal from the wall. The second part to the wall correction is modelled as per Gibson and Launder (1978);

$$\Phi_{ij}^{(w,2)} = c_2^w \left(\Phi_{kl}^{(2)} n_l n_k \delta_{ij} - \frac{3}{2}\Phi_{ik}^{(2)} n_j n_k - \frac{3}{2}\Phi_{jk}^{(2)} n_i n_k\right) f_w \tag{4.3.21}$$

As noted above, it was necessary to include a wall-reflection correction when using the IP model of Naot et al. (1970) to ensure that the stress component normal to the wall was sufficiently damped. For buoyancy however, this correction is not generally applied to $\Phi_{ij}^{(b)}$ in the literature. Hanjalic and Launder (2011) suggests that this is purely due to better agreement being achieved without it. A correction has been applied, however, for the contribution to the pressure-strain term from electromagnetic interactions. This is detailed later in Subsection 4.3.2.

The approach taken for the dissipation rate tensor, ε_{ij}, begins by noting that dissipation occurs at the smallest scales of motion, since this is where fluctuating velocity gradients are steepest. As such, and invoking the local isotropy hypothesis of Kolmogorov (1941) as discussed in Section 4.1, the contributions to ε_{ij} are assumed to be isotropic. The natural approach, therefore, is to express ε_{ij} as proportional to its contraction;

$$\varepsilon_{ij} = \frac{2}{3}\varepsilon\delta_{ij} \tag{4.3.22}$$

where ε is the scalar dissipation rate;

$$\varepsilon = \nu\overline{\frac{\partial u_i}{\partial x_j}\frac{\partial u_i}{\partial x_j}} \tag{4.3.23}$$

The assumption that the dissipation is isotropic is generally valid for high-Re flows. The scalar dissipation rate is obtained via a transport equation very similar in form to that used in the two-equation eddy-viscosity models considered later. The main difference is in the utilization of the full second-moment forms of the production terms, $\mathcal{P}_{ij}$.

$$\frac{D\varepsilon}{Dt} = \frac{\partial}{\partial x_k}\left[\left(\nu\delta_{kl} + c_\varepsilon\frac{k}{\varepsilon}\overline{u_k u_l}\right)\frac{\partial\varepsilon}{\partial x_l}\right] + \frac{1}{2}c_{\varepsilon 1}\frac{\varepsilon}{k}\mathcal{P}_{kk} - c_{\varepsilon 2}\frac{\varepsilon^2}{k} + \mathcal{F}_\varepsilon \tag{4.3.24}$$

where the constants are given as $c_\varepsilon = 0.18$, $c_{\varepsilon 1} = 1.44$ and $c_{\varepsilon 2} = 1.92$, and $\mathcal{F}_\varepsilon^L$ contains contributions from body forces.

For the diffusion terms, there are three parts to consider: the triple-moments, the pressure-velocity correlations and the viscous contribution. For the triple-moments, the *generalized gradient diffusion hypothesis* (GGDH) of Daly and Harlow (1970) is used, where the flux of some quantity ψ is approximated as;

$$\overline{u_k \psi} \propto -\frac{k}{\varepsilon} \overline{u_k u_l} \frac{\partial \psi}{\partial x_l} \tag{4.3.25}$$

Setting $\psi = \overline{u_i u_j}$ gives;

$$\overline{u_i u_j u_k} = -c_s \frac{k}{\varepsilon} \overline{u_k u_l} \frac{\partial \overline{u_i u_j}}{\partial x_l} \tag{4.3.26}$$

The constant c_s is taken as 0.2. The pressure part of the diffusion term is often assumed to be negligible and the viscous part does not require modelling. Thus the inclusion of Equation (4.3.26) completes the model.

4.3.2 Hanjalić and Jakirlić low-Re model

The Hanjalić and Jakirlić model aims to extend the applicability of the basic second-moment closure to those flows with significant low-Re and wall-proximity effects. It was proposed in a series of papers by Hanjalić and Jakirlić (1993), Hanjalić et al. (1994) and Jakirlić and Hanjalić (1995).

The model introduces a low-Re number version of the ε transport equation and makes the various coefficients in the $\overline{u_i u_j}$ equation functions of $Re_t = k^2/\nu\varepsilon$, the turbulent Reynolds number, and the invariants of the stress and dissipation rate tensors. This, in principle, allows the effects of anisotropy on the stress bearing and dissipative scales to be accounted for separately.

The linear pressure-strain terms of the basic model are adopted for the slow, rapid and wall reflection terms, Equations (4.3.15), (4.3.16), (4.3.19) and (4.3.21) respectively, where the coefficients are defined as;

$$\begin{gathered}
c_1 = C + A^{0.5} E^2 \,, \qquad C = 2.5 A f_A^{0.25} f_{Re_t} \,, \qquad f_A = \min\left[A_2, 0.6\right] \\
f_{Re_t} = \min\left[\left(\frac{Re_t}{150}\right)^{1.5}, 1\right] \,, \qquad f_w = \min\left[\frac{k^{1.5}}{2.5\varepsilon y_n}, 1.4\right] \\
c_2 = 0.8 A^{0.5} \,, \qquad c_1^w = \max\left[1 - 0.7C, 0.3\right] \,, \qquad c_2^w = \min\left[A, 0.3\right]
\end{gathered} \tag{4.3.27}$$

where;

$$A \equiv 1 - \frac{9}{8}\left(A_2 - A_3\right) \ , \qquad E \equiv 1 - \frac{9}{8}\left(E_2 - E_3\right) \tag{4.3.28}$$

$$A_2 \equiv a_{ij}a_{ij} \ , \qquad A_3 \equiv a_{ij}a_{jk}a_{ki} \ , \qquad E_2 \equiv e_{ij}e_{ij} \ , \qquad E_3 \equiv e_{ij}e_{jk}e_{ki} \tag{4.3.29}$$

and;

$$a_{ij} = \frac{\overline{u_i u_j}}{k} - \frac{2}{3}\delta_{ij} \ , \qquad e_{ij} = \frac{\varepsilon_{ij}}{\varepsilon} - \frac{2}{3}\delta_{ij} \tag{4.3.30}$$

The model for ε_{ij} is given by;

$$\varepsilon_{ij} = f_s \varepsilon^*_{ij} + \left(1 - f_s\right)\frac{2}{3}\delta_{ij}\varepsilon \tag{4.3.31}$$

where;

$$\varepsilon^*_{ij} = \frac{\varepsilon}{k}\frac{\overline{u_i u_j} + \left(\overline{u_i u_k}n_j n_k + \overline{u_j u_k}n_i n_k + \overline{u_k u_l}n_k n_l n_i n_j\right) f_d}{1 + \frac{3}{2}\frac{\overline{u_p u_q}}{k}n_p n_q f_d} \tag{4.3.32}$$

and;

$$f_s = 1 - A^{0.5}E^2 \ , \qquad f_d = \left(1 + 0.1Re_t\right)^{-1} \tag{4.3.33}$$

The transport equation for the rate of dissipation, ε, is given by;

$$\frac{D\varepsilon}{Dt} = \frac{\partial}{\partial x_k}\left[\left(\nu\delta_{kl} + c_\varepsilon\frac{k}{\varepsilon}\overline{u_k u_l}\right)\frac{\partial\varepsilon}{\partial x_j}\right] + \frac{1}{2}c_{\varepsilon 1}\frac{\varepsilon}{k}\mathcal{P}_{kk} - c_{\varepsilon 2}f_\varepsilon\tilde{\varepsilon}\frac{\varepsilon}{k} + S_\varepsilon + \mathcal{F}_\varepsilon \tag{4.3.34}$$

where $\mathcal{F}_\varepsilon$ contains contributions from body forces. The function f_ε and the additional source term S_ε are given by;

$$f_\varepsilon = 1 - \left(\frac{c_{\varepsilon 2} - 1.4}{c_{\varepsilon 2}}\right)\exp\left(\frac{Re_t}{6}\right)^2 \tag{4.3.35}$$

$$S_\varepsilon = 0.25\nu\frac{k}{\varepsilon}\overline{u_j u_k}\frac{\partial^2 U_i}{\partial x_j \partial x_l}\frac{\partial^2 U_i}{\partial x_k \partial x_l} \tag{4.3.36}$$

and;

$$\tilde{\varepsilon} = \varepsilon - 2\nu\left(\frac{\partial k^{0.5}}{\partial x_i}\right)^2 \tag{4.3.37}$$

is the so-called 'quasi-homogeneous' dissipation rate of k.

Incorporating electromagnetic effects

To account for electromagnetic effects, Kenjereš and Hanjalić (2000) and Kenjereš et al. (2004) present modifications to the above model via the inclusion of additional terms in the transport equations for $\overline{u_i u_j}$ and ε. Specifically, the incorporation of the fluctuating

Lorentz force in the derivation of the stress transport equation leads to two main sources of influence. A direct effect is seen through the presence of an additional source term, given by Equation (4.3.11), and an indirect effect is seen from the corresponding additional term in the Poisson equation for the fluctuating pressure, as seen in Equation (4.3.13).

The source term in the $\overline{u_i u_j}$ equation is comprised of two parts, $\mathcal{F}_{ij}^{L1}$ and $\mathcal{F}_{ij}^{L2}$, with only the former requiring closure. In that, the only unknown quantity is the correlation between the fluctuating electric and the fluctuating velocity field;

$$\overline{u_i \frac{\partial \phi'}{\partial x_j}} = \overline{u_i e_j} \tag{4.3.38}$$

where e_i is the fluctuating electric field. Little to no attention has been paid to this term in the literature and Kenjereš and Hanjalić (2000, 2004) propose the following relation;

$$\overline{u_i \frac{\partial \phi'}{\partial x_j}} = C_\lambda \varepsilon_{jkl} B_l \overline{u_i u_k} \tag{4.3.39}$$

where the constant $C_\lambda = 0.6$ was evaluated a priori from existing DNS data (Noguchi et al., 2004) of a channel flow exposed to a wall normal magnetic field. Unfortunately, they do not elaborate on the reasoning behind the model and instead remark that it is only a first order approximation. A possible physical explanation of the model is proposed here as follows. According to the fluctuating form of Ohm's law, $\mathbf{j} = \sigma\left(\mathbf{e} + \mathbf{u} \times \mathbf{B}\right)$, a fluctuating electric field $\mathbf{u} \times \mathbf{B}$ will be induced by the fluctuating velocity. Since from Equation (3.2.25) the divergence of the fluctuating current must be zero, an electric field $\mathbf{e}$ appears which is in resistance to the source $\mathbf{u} \times \mathbf{B}$. When the induced field and the resistant field are balanced, the charges are still, and the system reaches a steady state. Hence it can be assumed that the resistant field is proportional to the induced field, which leads to $\mathbf{e} = -C_\lambda \mathbf{u} \times \mathbf{B}$.

Substitution of Equation (4.3.39) into the first term, $\mathcal{F}_{ij}^{L1}$, results in the final form of $\mathcal{F}_{ij}^{L}$

$$\mathcal{F}_{ij}^{L} = \frac{\sigma}{\rho}\left(1 - C_\lambda\right)\left(B_i B_k \overline{u_j u_k} + B_j B_k \overline{u_i u_k} - 2B_k^2 \overline{u_i u_j}\right) \tag{4.3.40}$$

For the indirect effects, Kenjereš et al. (2004) modify the pressure strain term with an additional isotropization of production type model;

$$\Phi_{ij}^{(L)} = -c_4 \left(\mathcal{F}_{ij}^{L} - \frac{1}{3}\mathcal{F}_{kk}^{L}\delta_{ij}\right) \tag{4.3.41}$$

and a wall reflection modification in analogy with that of Gibson and Launder (1978);

$$\Phi_{ij}^{(w,L)} = c_4^w f_w \left(\Phi_{km}^{(L)} L n_k n_m \delta_{ij} - \frac{3}{2}\Phi_{ik}^{(L)} n_k n_j - \frac{3}{2}\Phi_{kj}^{(L)} n_k n_i\right) \tag{4.3.42}$$

where the function f_w is as per Equation (4.3.33). The coefficients are given by $c_4 = 0.6A^{0.5}$ and $c_4^w = 1.2$.

The electromagnetic contributions to the *exact* ε equation can be derived using the conventional approach (by taking moments of the instantaneous momentum transport equation with the instantaneous body force);

$$\mathcal{F}_\varepsilon^L = \mathcal{F}_\varepsilon^{L1} + \mathcal{F}_\varepsilon^{L2} \tag{4.3.43}$$

$$\mathcal{F}_\varepsilon^{L1} = -\frac{2\nu\sigma}{\rho}\varepsilon_{ijk}\left(\frac{\partial B_k}{\partial x_l}\overline{\frac{\partial u_i}{\partial x_l}\frac{\partial \phi}{\partial x_j}} + B_k\overline{\frac{\partial u_i}{\partial x_l}\frac{\partial^2 \phi}{\partial x_l \partial x_j}}\right)$$

$$\mathcal{F}_\varepsilon^{L2} = \frac{2\nu\sigma}{\rho}\left(B_k\frac{\partial B_i}{\partial x_l}\overline{u_k\frac{\partial u_i}{\partial x_l}} + B_i B_k\overline{\frac{\partial u_i}{\partial x_l}\frac{\partial u_k}{\partial x_l}} + B_i\frac{\partial B_k}{\partial x_l}\overline{u_k\frac{\partial u_i}{\partial x_l}}\right.$$
$$\left. - B_k^2\overline{\left(\frac{\partial u_i}{\partial x_l}\right)^2} - 2B_k\frac{\partial B_k}{\partial x_l}\overline{u_i\frac{\partial u_i}{\partial x_l}}\right) \tag{4.3.44}$$

This, evidently, is not much use. Quite apart from not containing a single closed term, the transport equation solved for ε bears little resemblance to its exact counterpart so it would be illogical to attempt to use it do derive a model here. As such, Kenjereš et al. (2004) took an approach analogous to that used in modelling ε transport in two-equation LEVM's. The dissipation rate generation is supposed to be linearly related to the source term present in the transport equation for the turbulent kinetic energy, i.e.

$$S_\varepsilon^L = c_{\varepsilon 4}\frac{1}{2}\frac{\varepsilon}{k}\mathcal{F}_{ii}^L \tag{4.3.45}$$

where the coefficient $c_{\varepsilon 4}$ is evaluated as;

$$c_{\varepsilon 4} = 6.5\min\left[A_2, 0.25\right] \tag{4.3.46}$$

In later (those in Chapter 6 and Chapter 7) calculations involving the Hanjalić and Jakirlić stress-transport model, references to an electromagnetically modified version refer to the model discussed in this section with the electromagnetic modifications by Kenjereš et al. (2004) discussed above. The unmodified version version refers to just the Hanjalić and Jakirlić low-Re stress-transport equation without these additional electromagnetic modifications.

4.3.3 Scalar transport

Whilst the previous few sections have provided a means to model the Reynolds stresses, $\overline{u_i u_j}$, the turbulent heat flux, $\overline{u_i\theta}$, still requires closure. An approach consistent with full second-moment closure would be to transport the quantity $\overline{u_i\theta}$ itself. This equation can

be obtained by multiplying the equation for the fluctuating scalar temperature θ by u_i and then adding that to the equation for u_i (3.1.5) multiplied by θ, and then averaging. The resulting equation takes the symbolic form;

$$\frac{D\overline{u_i\theta}}{Dt} = \mathcal{P}_{i\theta} + \mathcal{F}_{i\theta} + \Phi_{i\theta} - \varepsilon_{i\theta} + \mathcal{D}_{i\theta} \tag{4.3.47}$$

where the use of similar notation to that used in the equation for $\overline{u_iu_j}$, Equation (4.3.3), implies terms of similar character. The first two of these terms comprise production by mean gradients and body forces respectively;

$$\mathcal{P}_{i\theta} = -\left(\overline{u_iu_j}\frac{\partial\Theta}{\partial x_j} + \overline{u_j\theta}\frac{\partial U_i}{\partial x_j}\right) \tag{4.3.48}$$

$$\mathcal{F}_{i\theta} = \frac{1}{\rho}\sum_n \overline{\theta f_i^n} = \frac{1}{\rho}\left(\overline{f_i^b\theta} + \overline{f_i^L\theta}\right) \tag{4.3.49}$$

Thus, gradients in both mean temperature and velocity will lead to production of $\overline{u_i\theta}$, as will the fluctuating buoyant, f_i^b, and Lorentz, f_i^L, forces if present. By substituting the fluctuating buoyant force from Equation (3.1.20), the buoyant contribution to Equation (4.3.49) becomes;

$$\mathcal{F}_{i\theta}^b = -g_i\beta\overline{\theta^2} \tag{4.3.50}$$

where $\overline{\theta^2}$ is the mean-square scalar variance. This holds a similar role in characterizing a scalar field that k does for the velocity field. Insight into this can, as usual, be gleaned from the exact form of its transport equation (Hanjalic and Launder, 2011);

$$\frac{D\overline{\theta^2}}{Dt} = -2\overline{u_i\theta}\frac{\partial\Theta}{\partial x_j} - 2\alpha\overline{\frac{\partial\theta}{\partial x_j}\frac{\partial\theta}{\partial x_j}} + \frac{\partial}{\partial x_j}\left(\alpha\frac{\partial\overline{\theta^2}}{\partial x_j} - \overline{\theta^2u_j}\right) \tag{4.3.51}$$

The character of the terms is familiar. In order from left to right: production by mean scalar gradients, destruction by molecular action and diffusion. Thus generation of $\overline{\theta^2}$ is solely by mean gradients in Θ.

The contribution from the fluctuating Lorentz force to the $\overline{u_i\theta}$ equation is;

$$\mathcal{F}_{i\theta}^L = \frac{\sigma}{\rho}\left(-\varepsilon_{ijk}B_k\overline{\theta\frac{\partial\phi'}{\partial x_j}} - \overline{u_k\theta}B_iB_k - \overline{u_i\theta}B_kB_k\right) \tag{4.3.52}$$

which contains the unknown correlation between the fluctuating scalar and the fluctuating electric field.

The remaining terms in Equation (4.3.47), 'pressure scrambling' of the scalar field ($\Phi_{i\theta}$), dissipation ($\varepsilon_{i\theta}$) and diffusion ($\mathcal{D}_{i\theta}$), all require approximation.

Full second moment closure of $\overline{u_i\theta}$ thus requires, in three-dimensions, the solution of at least three additional transport equations and further treatment for the unknown terms

making the resulting model cumbersome. A simple method of obtaining a model for $\overline{u_i\theta}$, is to apply the GGDH, given by Equation (4.3.25), as was done for the triple-moments (in Equation (4.3.25)). This gives;

$$\overline{u_i\theta} = -c_\theta \frac{k}{\varepsilon} \overline{u_i u_j} \frac{\partial \Theta}{\partial x_j} \tag{4.3.53}$$

where the coefficient c_θ is taken to be 0.22. Clearly this takes similar form to the first term on the RHS in Equation (4.3.48). Since this thesis is concerned primarily with the incorporation of magnetic effects in the Reynolds stress and mean momentum fields, rather than in the thermal fields, the GGDH is a sensible first approximation for use in the flows considered in this thesis. In addition, the form for the GGDH contains the Reynolds stresses which *do* contain electromagnetic modifications and thus should provide at least some, albeit indirect, response.

4.4 Linear eddy-viscosity models

Whilst the second-moment route to closure discussed in the previous section clearly offers great capacity for modelling a diverse arrays of flows, including those subjected to complex strain fields and body forces (due, in part, to the presence of exact production and body force terms in the transport equations for the stresses themselves), such approaches do elicit greater computational expenditure when compared with one or two equation eddy-viscosity based models. Couple this with the greater understanding that is required to be in a position to properly handle and compute with such schemes, then it is perhaps not surprising that the uptake of these more advanced schemes within industry has been slow.

Two-equation eddy-viscosity models thus remain the workhorse for routine industrial computations and it is relevant to address how this class of model responds to the inclusion of the various body forces considered in this thesis.

4.4.1 Boussinesq eddy-viscosity approximation

It can be seen from Equation (3.1.11) that the Reynolds stresses, quite like the name implies, appear as an apparent stress on the mean flow field. Boussinesq (1877) supposed that the Reynolds stresses might therefore be linearly proportional to the mean strains by a turbulent, or eddy, viscosity μ_t;

$$\rho\overline{u_i u_j} = \frac{2}{3}\rho k\delta_{ij} - \mu_t\left(\frac{\partial U_i}{\partial x_j} + \frac{\partial U_j}{\partial x_i}\right) \tag{4.4.1}$$

Different classes of linear eddy viscosity model (LEVM) exist, differing mainly on the employed definition of μ_t. Since, on dimensional grounds, μ_t must have the same dimensions as μ, it can be expressed as some combination of a length scale, a time scale and density. In zero and one equation LEVM's, such as Prandtl's mixing-length model, the length scale is prescribed algebraically. This restricts the applicability of the models, since complex geometries make assigning a relationship for the lengthscale difficult. For the time scale, one equation models generally solve a transport equation for k, the turbulent kinetic energy. Then the turbulent viscosity takes the form;

$$\mu_t = \rho c_\mu k^{1/2} l_\mu \tag{4.4.2}$$

where c_μ is a constant and l_μ is the lengthscale, usually prescribed as increasing linearly with distance from a wall.

To overcome this limitation, a second variable can be solved for in order to provide a lengthscale. These two-equation models thus require no prior knowledge of the turbulent

structure and are complete in the sense that they do not require any flow-dependant specifications. The choice of variable to provide a lengthscale remains the subject of debate within the turbulence modelling community. The most common choice, and the route taken in this thesis, is to use the dissipation rate of k, ε. A suitable lengthscale is then;

$$l_\varepsilon = \frac{k^{3/2}}{\varepsilon} \tag{4.4.3}$$

4.4.2 The $k - \varepsilon$ model

Perhaps the most widely adopted of the two equation models, the $k-\varepsilon$ model solves transport equations for the turbulent kinetic energy, k, and the dissipation rate of that energy, ε. It was originally proposed by Jones and Launder (1972) with several improvements later presented by Launder and Sharma (1974) and Launder and Spalding (1974).

An exact transport equation for k, as noted briefly Section 4.3, can be conveniently formed by taking one half the trace of the transport equation for $\overline{u_i u_j}$ (4.3.3);

$$\frac{Dk}{Dt} = \underbrace{\frac{\partial}{\partial x_j}\left[\nu\frac{\partial k}{\partial x_j} - \frac{\overline{pu_j}}{\rho} - \overline{u_j\tilde{k}}\right]}_{\mathcal{D}_k} - \underbrace{\overline{u_i u_j}\frac{\partial U_i}{\partial x_j}}_{\mathcal{P}_k} - \underbrace{\nu\overline{\frac{\partial u_i}{\partial x_j}\frac{\partial u_i}{\partial x_j}}}_{\varepsilon} + \mathcal{F}_k \tag{4.4.4}$$

where $\tilde{k} = u_i u_i/2$ is the instantaneous turbulent kinetic energy. The character of the terms can readily be recognised; $\mathcal{D}_k$ represents the diffusion of k due to viscosity and turbulence (pressure-velocity and fluctuating velocity interactions), $\mathcal{P}_k$ represents the production of k due to mean strain, ε represents the dissipation of k by viscous action and $\mathcal{F}_k$ represents any contributions from fluctuating body forces.

Since ε is to be provided by its own transport equation, the only unknown in Equation (4.4.4) is part of diffusive term $\mathcal{D}_k$. The contribution to this from turbulent interactions is modelled as a gradient diffusion process, so the diffusion term becomes;

$$\mathcal{D}_k = \frac{\partial}{\partial x_j}\left[\left(\nu + \frac{\nu_t}{\sigma_k}\right)\frac{\partial k}{\partial x_j}\right] \tag{4.4.5}$$

where σ_k is referred to as the turbulent Prandtl number.

An exact transport equation for ε can also be derived, by taking suitable moments of the instantaneous Navier-Stokes equations. The result however, in not particularly enlightening and contains many unclosed terms, which require modelling. The form employed, therefore, is guided by dimensional analysis, physical intuition and DNS or experimental data.

Before the modelled transport equations are presented, however, it is worth noting that there are two forms which can be employed and the choice depends on the Reynolds

number of the flow. At high Reynolds numbers, mesh requirements in the near-wall region, where the large velocity gradients are large, can be demanding. To avoid the need to integrate the equations right up to the wall, wall-functions can be used which relate the wall shear stress to local quantities at the near wall node. These are discussed further in Section 4.5. At lower Reynolds numbers the methodology behind the wall-function approach is not valid, and modifications to the transport equations are required to allow the $k-\varepsilon$ model to be integrated right through the viscous sublayer.

The modelled transport equations for k and ε can be expressed, in both high and low Re form, as;

$$\frac{Dk}{Dt} = \frac{\partial}{\partial x_j}\left[\left(\nu + \frac{\nu_t}{\sigma_k}\right)\frac{\partial k}{\partial x_j}\right] + \mathcal{P}_k - \varepsilon + D + \mathcal{F}_k \tag{4.4.6}$$

$$\frac{D\varepsilon}{Dt} = \frac{\partial}{\partial x_j}\left[\left(\nu + \frac{\nu_t}{\sigma_\varepsilon}\right)\frac{\partial \varepsilon}{\partial x_j}\right] + c_{\varepsilon 1} f_1 \frac{\varepsilon}{k}\mathcal{P}_k - c_{\varepsilon 2} f_2 \rho \frac{\varepsilon^2}{k} + E_\varepsilon + \mathcal{F}_\varepsilon \tag{4.4.7}$$

where the terms f_1, f_2, D and E_ε represent the near-wall damping modifications required for low-Re flows. σ_k, σ_ε, $c_{\varepsilon 1}$ and $c_{\varepsilon 2}$ are model constants. The $\mathcal{F}_k$ and $\mathcal{F}_\varepsilon$ terms represent contributions from body forces. The eddy-viscosity takes the form;

$$\nu_t = c_\mu f_\mu \frac{k^2}{\varepsilon} \tag{4.4.8}$$

where c_μ is a constant and f_μ is a near-wall damping term. The production term, $\mathcal{P}_k$ is exact;

$$\mathcal{P}_k = -\overline{u_i u_j}\frac{\partial U_i}{\partial x_j} \tag{4.4.9}$$

One disadvantage to transporting ε directly is that ε itself does not vanish at the wall[1]. To overcome this, Jones and Launder (1972) used the following wall condition for ε;

$$\varepsilon_w = 2\nu\left(\frac{\partial k^{1/2}}{\partial x_2}\right)^2\Bigg|_w \tag{4.4.10}$$

where x_2 denotes the direction normal to the wall. This prompted them to introduce a new variable, the so-called 'homogeneous' dissipation rate, $\tilde{\varepsilon}$, which has already seen use in the Hanjalić and Jakirlić stress-transport variant of the ε equation (see Equation (4.3.37));

$$\tilde{\varepsilon} = \varepsilon - 2\nu\left(\frac{\partial k^{1/2}}{\partial x_2}\right)^2 \tag{4.4.11}$$

This conveniently goes to zero at the wall. Some approaches therefore transport $\tilde{\varepsilon}$ instead

[1] From its definition, $\varepsilon = 2\nu\overline{(\partial u_i/\partial x_j)^2}$. If the wall itself lies in the plane x_1, x_3 at $x_2 = 0$, then since $u_i = 0$ for all x_1, x_3 those gradients in the plane of the wall vanish. The $\partial u_2/\partial x_2$ gradient is therefore zero by continuity, leaving

$$\varepsilon = 2\nu\left[\overline{\left(\frac{\partial u_1}{\partial x_2}\right)^2} + \overline{\left(\frac{\partial u_3}{\partial x_2}\right)^2}\right]$$

of ε and set the D term in the k transport equation to account for the different near-wall variation. The low-Re Launder-Sharma model employed in this research, for example, takes $\varepsilon = \tilde{\varepsilon} + D$ with;

$$D = 2\nu \left(\frac{\partial k^{1/2}}{\partial x_2} \right)^2 \tag{4.4.12}$$

A summary of these modifications proposed in some of the literature, along with the various closure coefficients, are presented in Table 4.1.

For flows affected by buoyancy, taking one half the trace of $\mathcal{F}^b_{ij}$, Equation (4.3.9), gives the buoyant contribution to the turbulent kinetic energy;

$$\mathcal{F}^b_k = -\rho\beta g_i \overline{u_i\theta} \tag{4.4.13}$$

where $\overline{u_i\theta}$ is the turbulent heat flux, discussed further in Subsection 4.4.4.

4.4.3 Electromagnetic extensions

The exact expressions for the additional electromagnetic source terms, $\mathcal{F}^L_k$ and $\mathcal{F}^L_\varepsilon$, are obtained using the conventional approach. Taking one half the trace of Equation (4.3.11), one arrives at the source term for the k equation;

$$\mathcal{F}^L_k = \frac{\sigma}{\rho} \left(\underbrace{\varepsilon_{ijk} B_k u_i \overline{\frac{\partial \phi}{\partial x_j}}}_{\mathcal{F}^{L1}_k} + \underbrace{B_i B_k \overline{u_i u_k} - 2k B_k^2}_{\mathcal{F}^{L2}_k} \right) \tag{4.4.14}$$

As with the $\mathcal{F}^L_{ij}$ source term for the stress transport equations, the only unknown correlation is between the fluctuating velocity and the fluctuating electric field. Substitution of the model for $\overline{u_i e_j}$ proposed earlier by Kenjereš and Hanjalić (2000) in Equation (4.3.39) into Equation (4.4.14) gives;

$$\mathcal{F}^L_k = \frac{\sigma}{\rho} \left(1 - C_\lambda\right) \left(B_i B_j \overline{u_i u_j} - 2k B_k^2 \right) \tag{4.4.15}$$

This model, however, does not seem to have been adopted in the literature, presumably because it depends on an accurate representation of all individual Reynold stresses; something which turbulence models based on the linear eddy-viscosity concept are known to be lacking. This particular dependence on the individual components of the Reynolds stresses is not particularly surprising. It was seen in Subsection 4.1.2 that a major effect of an applied magnetic field was to induce anisotropy in the turbulence through preferential alignment. This, and other weaknesses of the LEVM approach, are further discussed in Subsection 4.4.5.

For $\mathcal{F}_\varepsilon$, as discussed in Subsection 4.3.2, the form of $\mathcal{F}_\varepsilon$ does not provide any real insight and is thus generally forsaken. Some models for $\mathcal{F}_k$ and $\mathcal{F}_\varepsilon$ that have been proposed in the literature are discussed in the paragraph below.

Ji and Gardner model

Ji and Gardner (1997) proposed additional terms in both the k and ε transport equations as well as an additional damping function f^L in the relationship for the eddy-viscosity. The terms were derived by considering a channel flow of conducting fluid subjected to a wall-normal magnetic field. Since in this configuration, the Lorentz force acts to damp the fluid motion, they relate the time rate of change of fluid momentum to the force imposed by the (transverse) magnetic field;

$$\rho\frac{dU_\perp}{dt} = -\sigma U_\perp B_0^2 \tag{4.4.16}$$

where the subscript $\perp$ means the velocity component perpendicular to the magnetic field. The solution to this equation is;

$$U(t) = U_0 \exp\left(-t/t_m\right) \tag{4.4.17}$$

where $t_m = \rho/\sigma B_0^2$ is the characteristic magnetic braking time. The ratio of this to the characteristic eddy turnover time, $t_\tau = k/\varepsilon$, for the largest energy containing eddies gives;

$$\frac{t_\tau}{t_m} = \frac{\sigma B_0^2}{\rho}\left(\frac{k}{\varepsilon}\right)_{\text{large}} = \frac{\sigma B_0^2}{\rho}\frac{L}{U} = N \tag{4.4.18}$$

where N is recognised as the non-dimensional interaction parameter. Hence they postulate that the average decay of turbulent kinetic energy is proportional to e^{-N}. From this, the additional source terms in the k and ε equations are proposed as;

$$\mathcal{F}_k^L = -\frac{\sigma}{\rho}B_0^2 k c_1^L \exp\left(-c_2^L N\right) \tag{4.4.19}$$

$$\mathcal{F}_\varepsilon^L = -\frac{\sigma}{\rho}B_0^2 \varepsilon c_1^L \exp\left(-c_2^L N\right) \tag{4.4.20}$$

where the model coefficients $c_1^L = 0.05$ and $c_2^L = 0.9$ are proposed. The additional damping term in the eddy-viscosity formulation was given as;

$$\nu_t = c_\mu f_\mu \frac{k^2}{\varepsilon}\exp\left(-c_2^L N\right) = c_\mu f_\mu \frac{k^2}{\varepsilon} f^L \tag{4.4.21}$$

Ji and Gardner applied the model to a turbulent pipe flow subjected to a transverse magnetic field over a range of Reynolds $(16000 \leq Re \leq 10^6)$ and Hartmann numbers $(0 \leq Ha \leq 375)$. They found the model qualitatively predicted the correct effect

(i.e. a reduction in turbulent kinetic energy as the Hartmann numbers increases) but only achieved reasonable quantitative agreement with the experiments of Gardner and Lykoudis (1971). Though this was encouraging, and certainly demonstrated potential, there are some apparent deficiencies in the model. Firstly, the use of a bulk flow parameter, N, as the basis for a damping function limits the applicability of the model to configurations in which it is possible to defined an integral value of N. This would be relatively simple in geometries such as channels or pipes subjected to homogeneous magnetic fields, but not as straightforward in more complex flows. Secondly, as pointed out by Kenjereš and Hanjalić (2000), direct damping of the eddy-viscosity through an additional function lacks physical justification, since if the source terms in the k and ε transport equations are adequately modelled the eddy-viscosity should adjust accordingly.

Kenjereš and Hanjalić model

Kenjereš and Hanjalić (2000) proposed improvements to the model by Ji and Gardner which centered on removing the use of the bulk flow interaction parameter, N, to define the magnitude of electromagnetic damping. They suggest replacing N with a local interaction parameter, defined using the usual local turbulent timescale $\tau = k/\varepsilon$ (something Ji and Gardner had already suggested). This led to the following source terms for the k and ε model equations respectively;

$$\mathcal{F}_k^L = -\frac{\sigma}{\rho} B_0^2 k \exp\left(-c_1^L \frac{\sigma}{\rho} B_0^2 \frac{k}{\varepsilon}\right) \tag{4.4.22}$$

$$\mathcal{F}_\varepsilon^L = -\frac{\sigma}{\rho} B_0^2 \varepsilon \exp\left(-c_1^L \frac{\sigma}{\rho} B_0^2 \frac{k}{\varepsilon}\right) \tag{4.4.23}$$

This reduced the number of model coefficients to one, $c_1^L = 0.025$, which was tuned using the DNS database of Noguchi et al. (2004). Kenjereš and Hanjalić (2000) tested the terms a priori against the same database. The results, presented in Figure 4.2 show the terms (denoted NEW) offer significant improvements over the model by Ji and Gardner (denoted JG), which, as it turned out, heavily underestimated the magnitude of the source terms in both the k and ε equations.

In later calculations involving the Launder-Sharma $k-\varepsilon$ model (those in Chapter 6 and Chapter 7), references to an electromagnetically modified version refer to the low-Re $k-\varepsilon$ model discussed in Subsection 4.4.2 with the addition of the two terms, Equations (4.4.22) and (4.4.23), above. The unmodified version refers to just the model as described in Subsection 4.4.2.

4.4.4 Scalar transport

In the stress transport approach, the GGDH was used to provide a model for the turbulent heat fluxes, $\overline{u_i\theta}$. Sensitizing the fluxes to the individual Reynolds stresses (as the GGDH

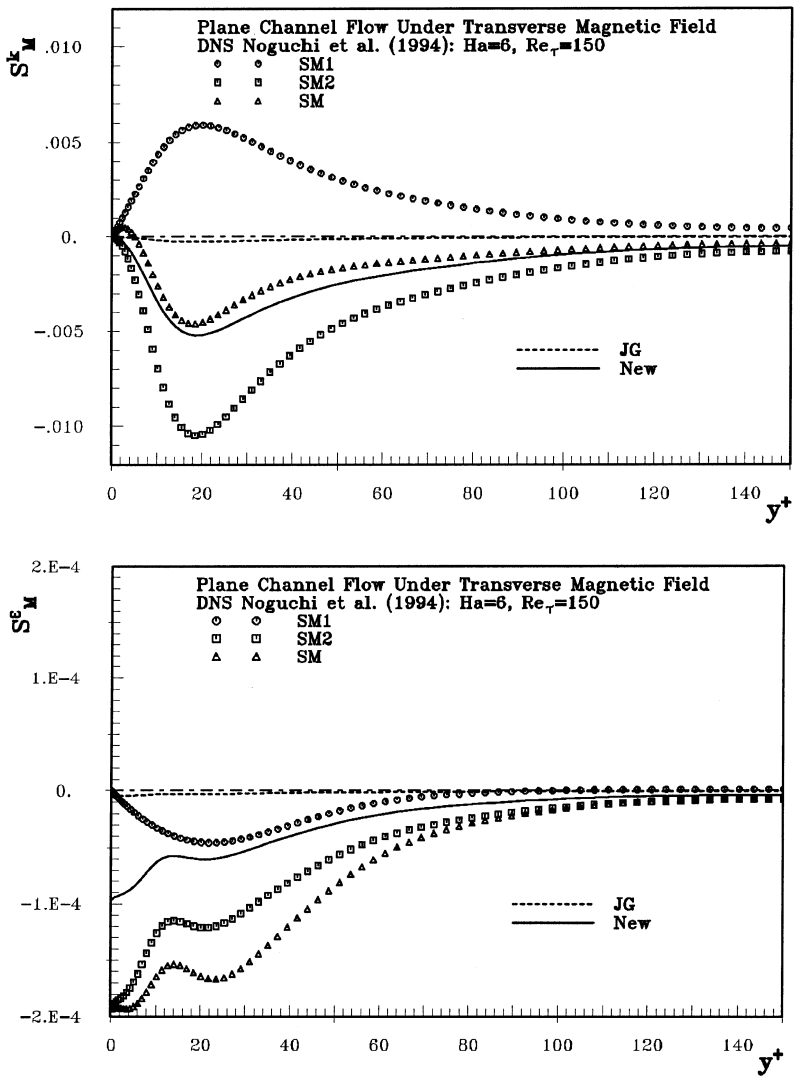

Figure 4.2: Plane channel flow subjected to a wall-normal magnetic field (Hartmann flow). Contributions $\mathcal{F}_k$ (S^k_M, top) and $\mathcal{F}_\varepsilon$ (S^ε_M, bottom) to budgets for k and ε equations respectively. Symbols are DNS data from Noguchi et al. (2004) and contain the full term SM alongside the individual contributions to constituent terms SM1 and SM2 as per the DNS results. Terms involving the fluctuating velocity electric field correlations are in SM1 with the remainder in SM2 (for ε, this split is given in Equation (4.3.43)).

does), however, requires an accurate prediction of the Reynolds stresses themselves. As further discussed in Subsection 4.4.5, the reliance of the linear eddy-viscosity approach on a linear stress-strain relationship reduces somewhat ones capability to accurately represent the Reynolds stresses in flows with prevailing anisotropy. Thus, here, an approach analogous to the linear eddy-viscosity form is taken, where the turbulent flux is supposed to be linearly related to the mean gradient. This "eddy-diffusivity" model takes the form;

$$\overline{u_i\theta} = -\frac{\nu_t}{\sigma_\alpha}\frac{\partial\Theta}{\partial x_i} \tag{4.4.24}$$

where σ_α is the turbulent Prandtl number, here taken as $\sigma_\alpha = 0.9$.

4.4.5 Weaknesses

Despite their wide adoption in industry, LEVM do have significant weaknesses when applied to specific flows. For flows in simple shear, where the only significant velocity gradient is in the wall-normal direction and the state of turbulence is said to be near local equilibrium (where $P_k \sim \varepsilon$), the $k-\varepsilon$ model has been tuned (through the c_μ coefficient) to correctly reproduce the distribution of the shear stress $\overline{uv}$. For the normal stresses however, expansion of the Boussinesq stress-strain relationship, from Equation (4.4.1), reveals it returns identical values for flows in simple shear;

$$\overline{uu} = \overline{vv} = \overline{ww} = \frac{2}{3}k \tag{4.4.25}$$

It is generally well known (see the DNS data from Kim et al. (1987), for example) that the normal stresses demonstrate anisotropy even in plane channel flows, and particularly in the near-wall region. This will pose a problem when attempting to model body forces which generally tend to promote anisotropy in the stress tensor through preferential alignment. Indeed, for the majority of flows explored in Chapter 2, this was one of the primary effects of the magnetic field. Velocity gradients parallel to the magnetic field were destroyed and this, in some cases, caused the flow to become two-dimensional in the sense that it was independent of the direction of the magnetic field. Evidently a model that, a priori, cannot accurately represent stress anisotropy might have some difficulties in reproducing flows in which magnetic effects become dominant.

That said, they can, of course, represent the general reduction in turbulent kinetic energy that the magnetic field induces. The form of the damping terms proposed by Kenjereš and Hanjalić (2000), see Equations (4.4.22) and (4.4.23), means they will always represent a sink of k and ε. This, however, does not take into account the reduction in Joule dissipation which is associated with increasing anisotropy (i.e. the flow evolves so as to minimize Joule dissipation, as per Subsection 4.1.2).

The poor performance of the LEVM approach, when it comes to correctly reproducing the normal stresses, also has consequences for the modelling of other unknown quantities that require closure within the context of a RANS approach. For example, it was seen in Subsection 4.3.3 that one of the production terms in the exact transport equation for $\overline{u_i\theta}$ contains the Reynolds stresses. Thus, without correct representation of the normal components of these, ones ability to provide accurate predictions of $\overline{u_i\theta}$ in flows with strong anisotropy also diminishes a priori. In flows which require $\overline{u_i\theta}$, such as those affected by buoyancy, this often leads to the adoption of the simple eddy-diffusivity model for $\overline{u_i\theta}$ despite it also having well known deficiencies. This, as per Equation (4.4.24), will result in a contribution to the turbulent kinetic energy equation of the form;

$$\mathcal{F}_k^b = \rho\beta g_i \frac{\nu_t}{Pr_t}\frac{\partial\Theta}{\partial x_i} \tag{4.4.26}$$

Thus, only temperature gradients which are aligned with the gravitational vector will contribute. For the systems discussed in Subsection 2.4.2, where gravity was directed vertically and the dominant temperature gradient was in either horizontal direction, the above expression for $\mathcal{F}_k^b$ would underestimate the contribution of the fluctuating buoyant force to the turbulent kinetic energy since only the weaker vertical temperature gradient would contribute. Use of the GGDH in this scenario, though at least providing some contributions from the other temperature gradients, does not guarantee improvement since it depends on an accurate representation of all the Reynolds stresses. Some modified forms of the GGDH have been seen success when used in conjunction with an LEVM, however. Ince and Launder (1989), for example, demonstrated good agreement with experiments in buoyancy driven flows within rectangular cavities by sensitizing the c_θ coefficient in the GGDH (Equation (4.3.53)) to c_μ (Equation (4.4.8)).

4.5 Wall functions

It was mentioned in Subsection 4.4.2 that wall-functions can be used to model the near-wall velocity profile when the Reynolds number is high. The presence of a wall in a particular flow, and specifically the presence of the no-slip condition on the velocity, ensures that viscous effects will always be influential in the region just adjacent to the wall, regardless of how high the Reynolds number of the bulk flow is. The shape of the velocity profile in wall-bounded flows has received significant attention in the literature, and Figure 4.3 provides typical variation throughout the various "layers".

As the Reynolds number increases, velocity gradients become steeper and the thickness of the viscous sub-layer decreases. To completely resolve this layer, using a low-Re LEVM for example, would thus requires a sufficiently high number of mesh points and this can become prohibitively expensive quite quickly. The wall-function approach aims to remove this requirement by providing a algebraic relationship between variables at the wall and variables at the first computational node adjacent to the wall.

The most well-known wall-function for the mean momentum equation is based on the *law of the wall*. If the turbulence in the vicinity of the wall is assumed to be in local equilibrium ($\mathcal{P}_k \approx \varepsilon$), and the mean velocity is a function only of the distance y from the wall, then this leads to the universal law of the wall, which supposes that the velocity profile outside of the "buffer zone" can be represented by a logarithmic distribution;

$$U^+ = \frac{1}{\kappa} \ln\left(Ey^+\right) \tag{4.5.1}$$

where $\kappa \approx 0.41$ is the von Karman constant, $E \approx 8.4$ and;

$$U^+ = \frac{U}{\sqrt{\tau_w/\rho}} \tag{4.5.2}$$

$$y^+ = \frac{y\sqrt{\tau_w/\rho}}{\nu} \tag{4.5.3}$$

In the very near-wall part of the viscous sublayer, where viscous effects are dominant and the flow laminar, the relationship between the velocity and distance from the wall is linear; $U^+ = y^+$. In practice, the relationship used depends on the location of the first computational node. Thus the velocity profile varies as;

$$U^+ = \begin{cases} \frac{1}{\kappa} \ln\left(Ey^+\right), & y^+ > y_\nu^+ \\ y^+, & y^+ < y_\nu^+ \end{cases} \tag{4.5.4}$$

where y_ν^+ represents the dimensionless thickness of the viscous sub-layer. Figure 4.3 plots Equation (4.5.4) along with DNS data for a plane channel flow. Clearly, the linear

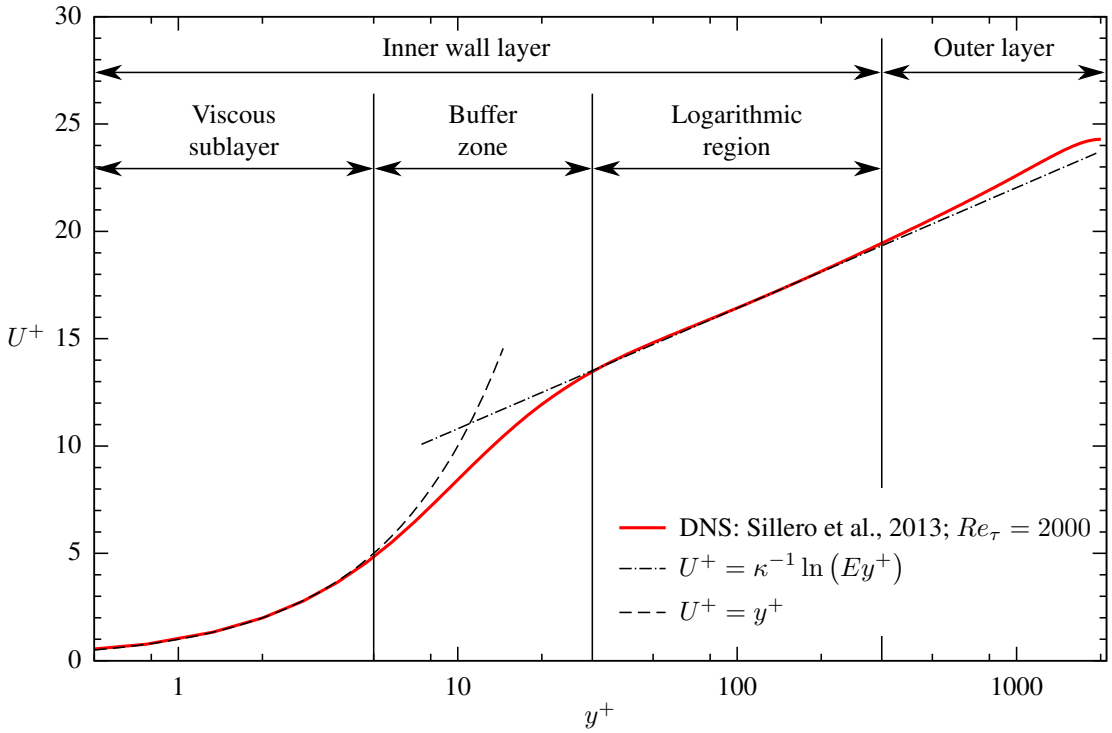

Figure 4.3: Velocity distribution and the characteristic flow regions in a constant pressure boundary layer. Red solid lines are DNS data of Sillero et al. (2013) at $Re_\tau = 2000$ with standard wall-functions shown with dashed lines.

variation is accurate up to around $y^+ \approx 5$ with the logarithmic profile being appropriate for $y^+ \gtrsim 30$.

Providing these relationships about the behaviour of the flow in the near-wall region removes the requirement to fully resolve them and thus reduces computation expenditure. Using these relationships, terms representing other quantities required to calculate the flow variables in the near-wall cell, such as the wall shear-stress and the wall-normal velocity gradient, can be formed.

The wall shear stress can be calculated from the value of U and y^+ at the near wall node by substituting Equations (4.5.2) and (4.5.3) into Equation (4.5.1). Since in the fully turbulent outer layer, molecular dissipation is negligible, the shear stress $\overline{uv}$ can be approximated as being equal to the wall shear stress. An expression for the turbulent viscosity can then be provided by;

$$\nu_t = \frac{\tau_w/\rho}{\partial U/\partial y} = \kappa y \sqrt{\tau_w/\rho} \tag{4.5.5}$$

This however returns zero when the wall shear stress becomes zero. A widely used improvement is obtained by using k_ν, the value of k at the edge of the viscous sublayer, for a velocity scale;

$$U^* = \frac{1}{\kappa^*} \ln(E^* y^*) \tag{4.5.6}$$

where;

$$U^* = \frac{U\sqrt{k_\nu}}{(\tau_w/\rho)} \tag{4.5.7}$$

$$y^* = \frac{y\sqrt{k_\nu}}{\nu} \tag{4.5.8}$$

where $\kappa^* = c_\mu^{1/4}\kappa$ and $E^* = c_\mu^{1/4}E$. In practice, k_ν is usually obtained by assuming k is constant across the fully turbulent part of the near-wall region. Then, k_P, the value of k at the near-wall node can be used. The wall shear stress becomes;

$$\frac{\tau_w}{\rho} = \frac{\kappa^* U_P k_P}{\ln\left(E^* y_P^*\right)} \tag{4.5.9}$$

The turbulent viscosity, obtained in a similar fashion to Equation (4.5.5), is given by;

$$\nu_t = \kappa^* y_P \sqrt{k_P} \tag{4.5.10}$$

The value of k_P is obtained from solution of its transport equation. Values of the $\mathcal{P}_k$ and ε terms, however, can vary quite drastically across the near-wall cell, so evaluating them at the cell-centre would lead to inaccuracies. Instead, cell-averaged values of $\mathcal{P}_k$ and ε are formed by directly integrating across the near-wall layer;

$$\overline{\mathcal{P}_k} = \frac{1}{y_n}\int_0^{y_n} \mathcal{P}_k \ \mathrm{d}y = \frac{1}{y_n}\int_0^{y_n} -\overline{uv}\frac{\partial U}{\partial y} \ \mathrm{d}y \tag{4.5.11}$$

$$\overline{\varepsilon} = \frac{1}{y_n}\int_0^{y_n} \varepsilon \ \mathrm{d}y \tag{4.5.12}$$

where y_n is the thickness of the near-wall cell. The velocity gradient can be evaluated by taking the derivative of Equation (4.5.6);

$$\frac{\partial U}{\partial y} = \frac{\tau_w}{\rho\kappa^* y\sqrt{k_P}} \tag{4.5.13}$$

To evaluate the integral in Equation (4.5.11), the assumption is made that over the fully turbulent part of the near-wall region $(y_\nu \leq y \leq y_n)$ the turbulent shear stress, $\overline{uv}$, is constant and equal to the wall shear stress, τ_w, whilst inside the viscous sublayer $(0 \leq y \leq y_\nu)$ it vanishes. Then Equation (4.5.11) becomes;

$$\overline{\mathcal{P}_k} = \frac{1}{y_n}\int_{y_\nu}^{y_n} \tau_w \frac{\tau_w}{\rho\kappa^*\sqrt{k_P}}\frac{1}{y} \ \mathrm{d}y = \frac{\tau_w^2}{\rho\kappa^* y_n\sqrt{k_P}}\ln\left(\frac{y_n}{y_\nu}\right) \tag{4.5.14}$$

The sublayer thickness, y_ν, is obtained by assuming that it extends to a fixed non-dimensional distance into the flow y_ν^*, where;

$$y_\nu^* = \frac{y_\nu\sqrt{k_\nu}}{\nu} \tag{4.5.15}$$

For the cell averaged value of ε, it is assumed that ε is constant inside the viscous sublayer

$(0 \leq y \leq y_\nu)$;

$$\varepsilon = \frac{2\nu k_P}{y_\nu^2} \tag{4.5.16}$$

and varies linearly in the fully turbulent region $(y_\nu \leq y \leq y_n)$;

$$\varepsilon = \frac{k_P^{3/2}}{c_l y} \tag{4.5.17}$$

where $c_l = \kappa^* c_\mu^{-1}$. The cell-averaged formulation, Equation (4.5.12), is then given by;

$$\begin{aligned} \overline{\varepsilon} &= \frac{1}{y_n}\left[\int_0^{y_\nu} \frac{2\nu k_P}{y_\nu^2}\ \mathrm{d}y + \int_{y_\nu}^{y_n} \frac{k_P^{3/2}}{c_l y}\, dy\right] \\ &= \frac{1}{y_n}\left[\frac{2\nu k_P}{y_\nu} + \frac{k_P^{3/2}}{c_l}\ln\left(\frac{y_n}{y_\nu}\right)\right] \end{aligned} \tag{4.5.18}$$

	c_μ	$c_{\varepsilon 1}$	$c_{\varepsilon 2}$	σ_k	σ_ε
Launder and Sharma (1974) and Launder and Spalding (1974)	0.09	1.44	1.92	1.0	1.3
Chien (1982)	0.09	1.35	1.80	1.0	1.3

(a) Coefficients for high-Re $k-\varepsilon$ models

	f_μ	D	f_1	f_2	E_ε
High-Re forms	1	0	1	1	0
Launder and Sharma (1974)	$\exp\left[\frac{-3.4}{(1+Re_t/50)^2}\right]$	$2\nu\left(\frac{\partial k^{1/2}}{\partial x_i}\right)^2$	1	$1-0.3e^{-Re_t^2}$	$2\nu\nu_t\left(\frac{\partial^2 U_i}{\partial x_j \partial x_k}\right)^2$
Chien (1982)	$1-e^{-0.0115y^+}$	$\frac{2\nu k}{y_n^2}$	1	$1-0.22e^{-(Re_t/6)^2}$	$-\frac{2\nu\varepsilon}{y_n^2}e^{-y^+/2}$

(b) Viscous damping terms for low-Re $k-\varepsilon$ models

Table 4.1: Coefficients and damping terms for selected $k-\varepsilon$ models.

CHAPTER

FIVE

NUMERICAL IMPLEMENTATION

In this chapter the numerical implementation of the governing equations used in the research is detailed. First, Section 5.1 introduces the in-house FORTRAN based numerical solver, STREAM. Then, in Section 5.2, the finite-volume method is briefly discussed, with details of the convective, diffusive and temporal discretization schemes included. The pressure-velocity linkage is then presented in Section 5.3 before the Rhie and Chow momentum interpolation method used and modified for calculating the mass flux is detailed in Section 5.4. Finally, the chapter closes in Section 5.6 with a brief description of the various boundary conditions implemented for the cases computed in this thesis.

5.1 STREAM code

The flows reported in this thesis have been computed using an extended version of the STREAM code (Lien and Leschziner, 1994a), which is a fully elliptic 3D finite volume solver capable of handling multi-block structured non-orthogonal meshes. It uses a collocated grid arrangement where all variables are stored at the cell centres and a Rhie and Chow interpolation scheme to obtain velocities at cell faces. Time dependence is handled by either a fully implicit or Crank-Nicolson scheme. The convective terms are treated with either the QUICK, UPWIND or UMIST schemes and both standard and advanced wall functions are available. A degree of parallelism is built-in using the standardized Message Passing Interface (MPI). The details of the implementation are discussed in the following sections.

5.2 Finite volume method

In the finite volume method (FVM) the solution domain is divided into a finite number of control volumes. Steady-state transport of a general variable, φ, is governed by;

$$\frac{\partial\left(\rho U_j \varphi\right)}{\partial x_j} = \frac{\partial}{\partial x_j}\left(\Gamma \frac{\partial \varphi}{\partial x_j}\right) + S_\varphi \tag{5.2.1}$$

where Γ is the diffusivity of φ and S_φ represents any sources or sinks.

Formal integration of Equation (5.2.1) is carried out over a control volume, such as that shown in Figure 5.1. To simplify the explanation of how the FVM works, the cells considered are purely rectangular, although the code employed does contain the extensions necessary for non-orthogonal meshes. Here the control volume with node P at its centre is bounded by faces to the north (n), south (s), east (e) and west (w). For a one-dimensional problem along the west-east direction, this integration leads to;

$$\int_w^e \frac{\partial\left(\rho U \varphi\right)}{\partial x}\, dx = \int_w^e \frac{\partial}{\partial x}\left(\Gamma_\varphi \frac{\partial \varphi}{\partial x}\right)\, dx + \int_V S_\varphi \, dV \tag{5.2.2}$$

which becomes;

$$\left[\rho U A\right]_e \varphi_e - \left[\rho U A\right]_w \varphi_w = \left[\Gamma A \frac{\partial \varphi}{\partial x}\right]_e - \left[\Gamma A \frac{\partial \varphi}{\partial x}\right]_w + \overline{S_\varphi}\Delta \mathrm{V} \tag{5.2.3}$$

where $[\rho U A]_e = F_e$ is the mass flux through face e and the source term integral has been approximated by taking the average value of S_φ over the control volume ΔV.

5.2.1 Diffusion terms

The diffusive fluxes are treated using the Central Differencing Scheme (CDS) which is second-order accurate. For Equation (5.2.3), this approximates the face values of the diffusion fluxes as;

$$\left[\Gamma A \frac{\partial \varphi}{\partial x}\right]_e = \Gamma_e A_e \left(\frac{\varphi_E - \varphi_P}{\Delta x_{PE}}\right) \tag{5.2.4}$$

$$\left[\Gamma A \frac{\partial \varphi}{\partial x}\right]_w = \Gamma_w A_w \left(\frac{\varphi_P - \varphi_W}{\Delta x_{WP}}\right) \tag{5.2.5}$$

where Δx_{PE}, for example, represents the distance between nodes P and E. The diffusivities are interpolated to the cell faces;

$$\Gamma_w = \left(1 - f_W\right)\Gamma_W + f_W \Gamma_P, \qquad f_W = \frac{\Delta x_{Ww}}{\Delta x_{Ww} + \Delta x_{wP}} \tag{5.2.6}$$

$$\Gamma_e = \left(1 - f_P\right)\Gamma_P + f_P \Gamma_E, \qquad f_P = \frac{\Delta x_{Pe}}{\Delta x_{Pe} + \Delta x_{eE}} \tag{5.2.7}$$

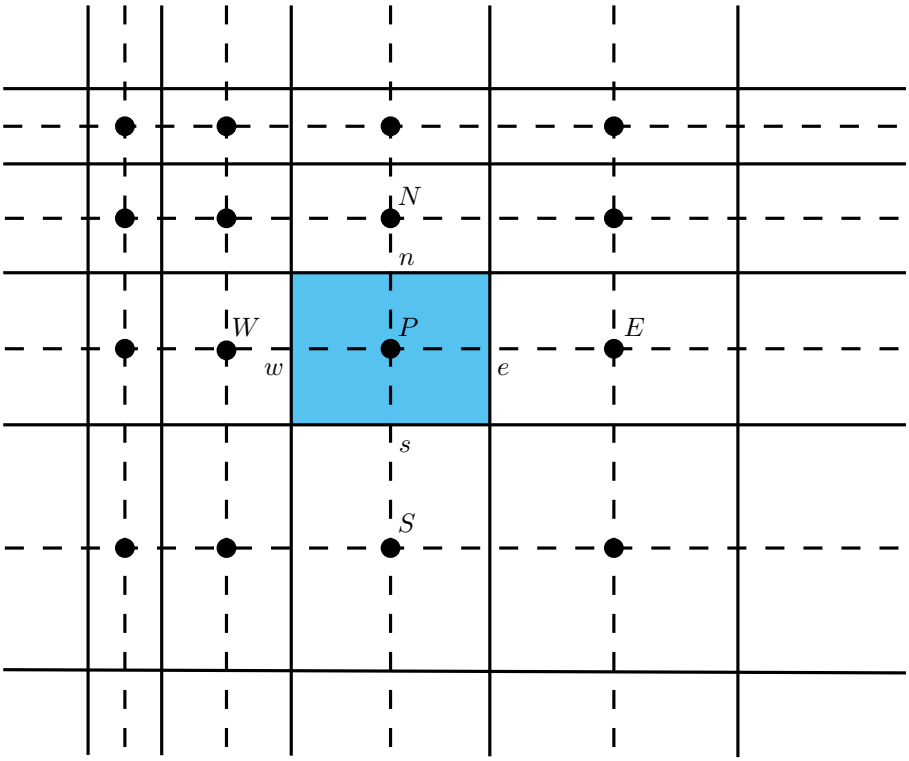

Figure 5.1: Typical finite volume cell.

where the interpolation factors f_W and f_P account for non-uniform grids. The diffusion coefficients can then be written as;

$$D_e = \frac{\Gamma_e A_e}{\Delta x_{PE}} \tag{5.2.8}$$

$$D_w = \frac{\Gamma_w A_w}{\Delta x_{WP}} \tag{5.2.9}$$

5.2.2 Convection terms

STREAM has three differencing schemes available for the convective terms. These are UPWIND, QUICK (Quadratic Upstream Interpolation for Convection Kinematics) and UMIST (Upstream Monotonic Interpolation for Scalar Transport). These schemes approximate the value of φ at the cell face. The calculation of the mass fluxes is detailed later in Section 5.4 and they are assumed as known here.

UPWIND scheme

The upwind scheme aims to take account of the prevailing flow direction when approximating the face values of φ. For example, with a given mass flux, F_e, through the face e, the velocity at the east face is given by;

$$\varphi_e = \begin{cases} \varphi_P, & F_e > 0 \\ \varphi_E, & F_e < 0 \end{cases} \tag{5.2.10}$$

The scheme is only first order accurate, but is stable and bounded. It tends to induce numerical diffusion when the flow is not aligned with the grid and with flows at a high Reynolds number, which can lead to fairly large inaccuracies, unless an extremely fine mesh is employed (Versteeg and Malalasekra, 1996).

QUICK scheme

The QUICK scheme is a third-order accurate upwind weighted scheme developed by Leonard (1979). It fits a quadratic function through two nodes upstream and one downstream of the face required. For a uniform grid, this gives;

$$\varphi_w = \begin{cases} \varphi_W + \frac{1}{2}(\varphi_P - \varphi_W) - \frac{1}{8}(\varphi_P - 2\varphi_W + \varphi_{WW}), & F_w > 0 \\ \varphi_P + \frac{1}{2}(\varphi_W - \varphi_P) - \frac{1}{8}(\varphi_W - 2\varphi_P + \varphi_E), & F_w < 0 \end{cases} \tag{5.2.11}$$

Although more accurate than the UPWIND scheme, the quadratic nature of the interpolation can produce unbounded values. This can lead to local oscillations and unphysical solutions, especially where there are sharp changes in the value of the variable.

UMIST

The UMIST scheme was proposed by Lien and Leschziner (1994b) and is designed to eliminate the oscillations caused by the QUICK scheme by forcing the quadratic function to give bounded values. For $F_e > 0$ it is of the form;

$$\varphi_e = \varphi_P + \frac{1}{2}\psi(r)(\varphi_E - \varphi_p) \tag{5.2.12}$$

where ψ is a function of $r = (\varphi_P - \varphi_W) / (\varphi_E - \varphi_P)$. Specifically;

$$\psi(r) = \max\left[0,\ \min\left(2r, \frac{1+3r}{4}, \frac{3+r}{4}, 2\right)\right] \tag{5.2.13}$$

The UMIST scheme is second-order accurate and more numerically stable when compared with the QUICK scheme, although the calculation of the function ψ can increase computation time. It does not produce oscillations and shows far less numerical diffusion when compared to the UPWIND scheme (Versteeg and Malalasekra, 1996).

5.2.3 Discretized equation

Using the UPWIND scheme for the convective terms and the CDS scheme for diffusive terms, the discretization of the Equation (5.2.3) results in the linear equation;

$$a_P\varphi_P = a_E\varphi_E + a_E\varphi_W + \overline{S}_\varphi \Delta \mathrm{V} \tag{5.2.14}$$

The source term is usually linearized for stability;

$$\overline{S}_{\varphi}\Delta \mathrm{V} = S_U + S_P\varphi_P \tag{5.2.15}$$

and S_P absorbed into the coefficient a_P, so that Equation (5.2.14) becomes;

$$a_P\varphi_P = a_E\varphi_E + a_E\varphi_W + S_U \tag{5.2.16}$$

where the coefficients are defined as;

$$a_W = D_w + \max(F_w, 0) \tag{5.2.17}$$

$$a_E = D_e + \max(0, -F_e) \tag{5.2.18}$$

$$a_P = a_E + a_W - S_P + (F_e - F_w) \tag{5.2.19}$$

The last term on the RHS of Equation (5.2.19) is the mass imbalance in the control volume. When continuity is satisfied this will vanish, and hence the term is not included in the final discretized equation. Equation (5.2.16) can be generalized to;

$$a_P\varphi_P = \sum_{nb} a_{nb}\varphi_{nb} + S_U \tag{5.2.20}$$

where nb represents the neighbouring nodes involved in the discretization and a_P is defined as;

$$a_P = \sum_{nb} a_{nb} - S_p \tag{5.2.21}$$

5.2.4 Temporal discretization

For unsteady flows, the time dependant term $\partial\varphi/\partial t$ is not omitted from Equation (5.2.1) and integration is additionally performed over a finite time step Δt. By assuming that the value of φ at the node provides an adequate approximation for the whole control volume, the time derivative integrates as;

$$\int_{CV}\left[\int_t^{t+\Delta t}\frac{\partial\left(\rho\varphi\right)}{\partial t}\right]\,\mathrm{dV} = \rho\left(\varphi - \varphi^0\right)\Delta \mathrm{V} \tag{5.2.22}$$

where the superscript 0 represents the value of φ at the previous time step. For a one-dimensional diffusion problem, where the CDS is used to approximate the fluxes, the integrated transport equation becomes;

$$\rho\left(\varphi_P - \varphi_P^0\right)\Delta \mathrm{V} = \int_t^{t+\Delta t}\left[\left(\Gamma_e A_e\frac{\varphi_E - \varphi_P}{\Delta x_{PE}}\right) - \left(\Gamma_w A_w\frac{\varphi_P - \varphi_W}{\Delta x_{WP}}\right)\right]\,\mathrm{d}t \tag{5.2.23}$$

To carry out the time integration on the right hand side of this equation, a decision needs to be made regarding the variation of φ with time. Either the values of φ at time t, at time

$t + \Delta t$, or some percentage inbetween can be used for the current time step. Introducing a weighting parameter χ, this can be conveniently expressed as;

$$\int_t^{t+\Delta t} \varphi_N \ \mathrm{d}t = \left[\chi\varphi_N + (1-\chi)\,\varphi_N^0\right]\Delta t \tag{5.2.24}$$

where N represents a particular node. By substituting this expression for φ_P, φ_W and φ_E in Equation (5.2.23) the integration can be carried out. For $\chi = 1$, the value of φ at the next time step is dependent on the values of its neighbouring nodes at the new time step. This is, therefore, a fully implicit scheme which is unconditionally stable for any size of time step but is only first order accurate. To ensure accuracy, small time steps are needed. Setting $\chi = 0.5$ gives the Crank-Nicolson scheme. This includes contributions from both time steps when solving the system of equations and thus is also implicit, but is second order accurate. The Crank-Nicolson scheme has been adopted in this thesis for the cases that are time-dependent.

5.3 Pressure-velocity coupling

In the discretized momentum equations, the pressure appears as a source term. Solution of this system of equations for the velocities U, V and W is thus possible provided that the pressure field is known. This is seldom the case and the pressure does not appear explicitly in the only other hydrodynamic equation available, continuity. To provide a means to solve for both the velocity and pressure fields an iterative scheme is used which adjusts the pressure field until the corresponding velocity field satisfies continuity. The particular scheme employed in STREAM is called SIMPLE ("Semi-Implicit Method for Pressure-Linkage Equations") and a summary of the algorithm follows (Patankar, 1980).

Consider a two-dimensional flow. Excluding other sources, the discretized momentum equation for U_P can be written as;

$$a_P U_P = \sum_{nb} a_{nb} U_{nb} + (P_w - P_e)\,\Delta y \tag{5.3.1}$$

where, as before, the lower case subscripts w and e represent face values. The equation is first solved by using a guessed pressure field, P^*. The velocity field resulting from the guessed pressure field is denoted by U^*, and obtained from the discretized equation as;

$$a_P U_P^* = \sum_{nb} a_{nb} U_{nb}^* + (P_w^* - P_e^*)\,\Delta y \tag{5.3.2}$$

It is unlikely that this velocity field will satisfy continuity. To obtain values which do, corrections are added to the velocity and pressures fields such that;

$$U = U^* + U^{'} \tag{5.3.3}$$

$$P = P^* + P^{'} \tag{5.3.4}$$

where $U^{'}$ and $P^{'}$ are the necessary corrections. The equation linking the velocity and pressure corrections is obtained by subtracting Equation (5.3.2) from Equation (5.3.1);

$$U_P^{'} = \frac{1}{a_P} \sum_{nb} a_{nb} U_{nb}^{'} + \frac{\Delta y}{a_P} \left(P_w^{'} - P_e^{'} \right) \tag{5.3.5}$$

As a first approximation, the SIMPLE scheme neglects the first term on the RHS, involving the velocity corrections from neighboring nodes. The corrected velocity field U is then linked to the pressure corrections by;

$$U_P = U_P^* + \frac{\Delta y}{a_P} \left(P_w^{'} - P_e^{'} \right) \tag{5.3.6}$$

The discretized continuity equation can be written as;

$$(\rho U A)_e - (\rho U A)_w + (\rho V A)_n - (\rho V A)_s = 0 \tag{5.3.7}$$

Expressions for the corrected velocities through the cell faces can be obtained in a similar fashion to that for U_P. By substituting these into Equation (5.3.7) and rearranging, an expression for the pressure corrections is given as;

$$a_P P_P^{'} = \sum_{nb} a_{nb} P_{nb}^{'} + S_m \tag{5.3.8}$$

where $S_m = (\rho U^* A)_e - (\rho U^* A)_w + (\rho V^* A)_n - (\rho V^* A)_s$ represents the mass imbalance in the cell. The mass fluxes at the cell faces are found using Rhie and Chow interpolation, which is discussed in Section 5.4. Equation (5.3.8) is solved over the flow domain, and the resulting pressure corrections $P^{'}$ are added to the guessed pressure P^* to obtain the corrected nodal pressure P. The corrected velocity values are obtained from Equation (5.3.6), where linear interpolation is used to obtain the face values of the pressure correction. That is;

$$P_w^{'} = (1 - f_W)\, P_W{}' + f_W P_P^{'} \tag{5.3.9}$$

where f_W is an interpolation factor, as previously defined in Equation (5.2.7).

The sequence of operations for a CFD solver employing the SIMPLE algorithm can be summarised as;

1. Guess the pressure P^* and velocity fields U_i^*.
2. Solve the discretized momentum equations (5.3.2).
3. Solve the pressure correction equation (5.3.8).
4. Correct the pressure and velocity fields using equations (5.3.4) and (5.3.6) respectively.
5. Solve any other discretized transport equations and repeat the procedure until the solution has converged.

5.4 Calculation of mass flux

The solution procedures outlined in the previous sections require values of the mass flux, $F = (\rho U A)$, at the cell faces. With a collocated grid arrangement, the discretization of the pressure gradient source term results in an expression involving the face values of pressure;

$$\int_{CV} -\frac{\partial P}{\partial x}\, \mathrm{d}x\, \mathrm{d}y\, \mathrm{d}z = -\left(P_e - P_w\right) A_P \tag{5.4.1}$$

where A_P is the area at node P whose normal is in the x direction. With a uniform grid, using linear interpolation to obtain the face values of pressure results in the elimination of the pressure at node P. For example;

$$(P_w - P_e) = \frac{P_W + P_P}{2} - \frac{P_P + P_E}{2} = \frac{P_W - P_E}{2} \tag{5.4.2}$$

The absence of the nodal value at P reduces the strength of the coupling between nodal values of velocity and pressure. This can lead to 'checkerboard' oscillations, where alternating values of nodal pressure interpolate to uniform values at the cell faces. This can be corrected by using a staggered grid arrangement, whereby scalar variables, such as pressure, temperature etc., are stored at the usual nodal values, but the velocities are calculated on a control volume centered around the cell vertices. The downside to this approach is that it becomes difficult to implement, since two sets of control volumes need to be defined and linked. For curvilinear or unstructured grids, this becomes very cumbersome.

To solve this issue, Rhie and Chow (1983) proposed a momentum interpolation method for collocated grids which eliminated the checkerboard problem. The method is detailed here with an additional modification, introduced as part of the present work, to explicitly take account for flows subject to buoyancy.

Consider the U momentum equation which has been discretized over the control volume centered around node P in Figure 5.2 and where the pressure source term has been ex-

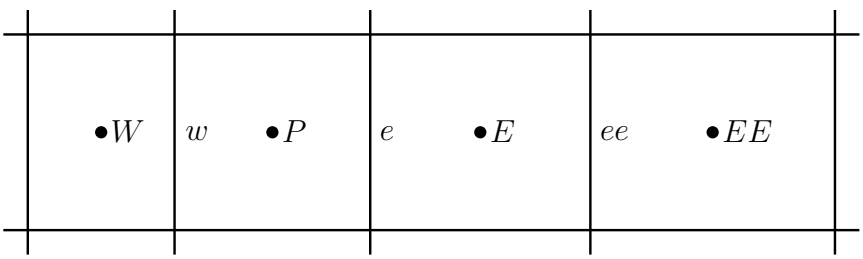

Figure 5.2: One-dimensional control volume arrangement.

cluded from the general source term S_U;

$$a_P U_P = \sum_{nb} a_{nb} U_{nb} \Bigg|_P - A_P \left(P_e - P_w\right) + S_U|_P \tag{5.4.3}$$

The terms on the RHS are evaluated such that node P is the central node, i.e. in the summation nb represents the neighbouring nodes for node P. The area A_P is the cross-sectional area at P whose normal is in the x direction. For buoyancy affected flows, the buoyant contribution to the source term S_U at node P is[1];

$$S_U|_P = \left[\,\overline{S_U}\,\right]_P \Delta \mathrm{V}_P = -\left[\rho g_x \beta \left(\Theta - \Theta_0\right)\right]_P \Delta \mathrm{V}_P = -\rho g_x \beta_P \left(\Theta_P - \Theta_0\right) \Delta \mathrm{V}_P \tag{5.4.4}$$

Then, substituting Equation (5.4.4) into Equation (5.4.3) and dividing by a_P;

$$U_P = \frac{1}{a_P} \sum_{nb} a_{nb} U_{nb} \Bigg|_P - \frac{A_P}{a_P} \left(P_e - P_w\right) + \frac{\rho g_x \beta_P}{a_P} \left(\Theta_0 - \Theta_P\right) \Delta \mathrm{V}_P \tag{5.4.5}$$

A similar expression can be formed by taking node E to be the central node;

$$U_E = \frac{1}{a_E} \sum_{nb} a_{nb} U_{nb} \Bigg|_E - \frac{A_E}{a_E} \left(P_{ee} - P_e\right) + \frac{\rho g_x \beta_E}{a_E} \left(\Theta_0 - \Theta_E\right) \Delta \mathrm{V}_E \tag{5.4.6}$$

Since the finite volume method ensures global conservation, a similar expression must also hold for the velocity at face e;

$$U_e = \frac{1}{a_e} \sum_{nb} a_{nb} U_{nb} \Bigg|_e - \frac{A_e}{a_e} \left(P_E - P_P\right) + \frac{\rho g_x \beta_e}{a_e} \left(\Theta_0 - \Theta_e\right) \Delta \mathrm{V}_e \tag{5.4.7}$$

where, conveniently, the pressures in the source term are now nodal values. The Rhie and Chow interpolation method uses Equations (5.4.5) and (5.4.6) to approximate a solution for Equation (5.4.7), and hence obtain the value for U_e. Using linear interpolation, the first term on the RHS of Equation (5.4.7) can be expressed as;

$$\frac{1}{a_e} \sum_{nb} a_{nb} U_{nb} \Bigg|_e = \left(1 - f_P\right) \frac{1}{a_P} \sum_{nb} a_{nb} U_{nb} \Bigg|_P + f_P \frac{1}{a_E} \sum_{nb} a_{nb} U_{nb} \Bigg|_E \tag{5.4.8}$$

where f_P is an interpolation factor, defined earlier in Equation (5.2.7) to account for non-uniform grids. The terms on the RHS can be obtained by rearranging Equations (5.4.5)

[1] see Subsection 3.1.3

and (5.4.6) respectively. Equation (5.4.8) then becomes;

$$\frac{1}{a_e}\sum_{nb} a_{nb}U_{nb}\bigg|_e = (1-f_P)\left[U_P + \frac{A_P}{a_P}(P_e - P_w) - \frac{\rho g_x \beta_P}{a_P}(\Theta_0 - \Theta_P)\,\Delta \mathrm{V}_P\right] + f_P\left[U_E + \frac{A_E}{a_E}(P_{ee} + P_e) - \frac{\rho g_x \beta_E}{a_E}(\Theta_0 - \Theta_E)\,\Delta \mathrm{V}_E\right] \tag{5.4.9}$$

The values of pressure at the faces are interpolated from neighbouring nodes as;

$$P_{ee} = (1-f_E)\,P_E + f_E P_{EE} \tag{5.4.10}$$

$$P_e = (1-f_P)\,P_P + f_P P_E \tag{5.4.11}$$

$$P_w = (1-f_W)\,P_W + f_W P_P \tag{5.4.12}$$

The remaining two terms in Equation (5.4.7) can be expressed in a similar fashion by interpolating the individual quantities involved. Areas and volumes are handled by taking an average. Thus with;

$$\frac{1}{a_e} = (1-f_P)\frac{1}{a_P} + f_P\frac{1}{a_E} \tag{5.4.13}$$

$$\Theta_e = (1-f_P)\,\Theta_P + f_P\Theta_E \tag{5.4.14}$$

$$\beta_e = (1-f_P)\,\beta_P + f_P\beta_E \tag{5.4.15}$$

$$\mathrm{V}_e = \frac{\mathrm{V}_P + \mathrm{V}_E}{2} \tag{5.4.16}$$

the second term on the RHS of Equation (5.4.7) becomes;

$$-\frac{A_e}{a_e}(P_E - P_P) = -\left[\frac{1-f_P}{a_P} + \frac{f_P}{a_E}\right] A_e\,(P_E - P_P) \tag{5.4.17}$$

and the third term becomes;

$$\frac{\rho g_x \beta_e}{a_e}(\Theta_0 - \Theta_e)\,\Delta \mathrm{V}_e = \rho g_x\left[\frac{1-f_P}{a_P} + \frac{f_P}{a_E}\right]\left[(1-f_P)\,\beta_P + f_P\beta_E\right] \times \left[\Theta_0 - (1-f_P)\,\Theta_P - f_P\Theta_E\right]\frac{\mathrm{V}_P + \mathrm{V}_E}{2} \tag{5.4.18}$$

Finally, substituting Equations (5.4.18), (5.4.17) and (5.4.9) into Equation (5.4.7) results in an expression for U_e. For a uniform grid, the interpolation factors $f_P = f_W = f_E = 0.5$

and the expression simplifies to;

$$
\begin{aligned}
U_e = & \underbrace{\frac{1}{2}\left(U_P + U_E\right)}_{\text{linear interpolation}} \\
& + \underbrace{\frac{1}{4}\Big[D_P A_P \left(P_E - P_W\right) - 2D_e A_e \left(P_E - P_P\right) + D_E A_E \left(P_{EE} - P_P\right)\Big]}_{\text{pressure smoothing}} \\
& - \underbrace{\frac{\rho g_x}{2}\Bigg[D_P \beta_P \mathrm{V}_P \left(\Theta_0 - \Theta_P\right) + D_E \beta_E \mathrm{V}_E \left(\Theta_0 - \Theta_E\right) \\
& \qquad\qquad -2D_e \beta_e \mathrm{V}_e \left(\Theta_0 - 0.5\left(\Theta_P + \Theta_E\right)\right)\Bigg]}_{\text{buoyant correction}}
\end{aligned}
\tag{5.4.19}
$$

where;

$$
\begin{aligned}
D_P = \frac{1}{a_P}, \qquad D_E = \frac{1}{a_E}, \qquad D_e = \frac{1}{2}\left[\frac{1}{a_P} + \frac{1}{a_E}\right], \\
A_P = \frac{A_w + A_e}{2}, \qquad A_E = \frac{A_e + A_{ee}}{2}
\end{aligned}
\tag{5.4.20}
$$

The final expression for the face velocity U_e, in Equation (5.4.19), can be seen to consist of three parts; a linear interpolation part, a pressure smoothing part and a correction due to the presence of the buoyant force. Crucially, the pressure smoothing term includes a contribution from the pressure at node P, which enforces strong coupling between the velocity and pressure. The buoyancy correction ensures that any contribution to the mass flux from gravitational interactions is included in the interpolation. All other face velocities are calculated in a similar fashion.

5.5 Poisson equation for electric potential

As discussed earlier in Subsection 3.3.2, the validity of the low Re_m approximation means that Maxwell's equations reduce to a single extra Poisson equation for the electric potential, ϕ. To detail its implementation into STREAM, the equation itself, Equation (3.3.17), is first recalled;

$$\frac{\partial^2 \phi}{\partial x_i^2} = \frac{\partial}{\partial x_i} \left(\varepsilon_{ijk} U_j B_k \right) \tag{5.5.1}$$

One way to implement this equation within the context of a finite volume solver, is to recognise that it holds similar form to a generic scalar transport equation with zero convective flux and one source term. For example, recalling the generic scalar transport equation from Equation (5.2.1);

$$\frac{\partial \left(\rho U_j \phi \right)}{\partial x_j} = \frac{\partial}{\partial x_j} \left(\Gamma \frac{\partial \phi}{\partial x_j} \right) + S_\phi \tag{5.5.2}$$

By setting the diffusivity to unity, specifying zero mass flux (to remove the convective part) and setting the source term, S_ϕ, such that;

$$S_\phi = -\frac{\partial}{\partial x_i} \left(\varepsilon_{ijk} U_j B_k \right) \tag{5.5.3}$$

one arrives back at Equation (5.5.1). As velocity values are updated by the solver, values of ϕ are calculated by solution of this equation. Gradients of ϕ, which enter into the Lorentz force term (as per Equation (3.3.11)), can be calculated in the same manner as those for other variables.

5.6 Boundary conditions

As summarised in Section 1.3, there are two main classes of flows investigated as part of this thesis and each will require different types of boundary conditions. This section primarily discusses how the types of boundary conditions are implemented in STREAM, and specific conditions for each case will be stated and discussed in their respective results chapter.

5.6.1 Wall

All of the cases considered involve walls in some capacity. As explained in Section 4.5, the approach to implementing boundary conditions at the wall depends on the mesh employed and whether the flow is laminar or turbulent. If the flow is fully laminar or the near-wall node is placed such that it lies within the viscous sub-layer (typically requiring $y^+ \leq 5$), then the near-wall flow itself will be laminar. If the flow is fully turbulent and the near-wall node lies outside of the viscous sublayer, but within the logarithmic region, wall-functions can be employed.

Velocity field

The no-slip condition ($U_i = 0$) is applied to nodes lying on the wall. For the near-wall node, the coefficient linking that node to the wall node is set to zero and the wall-shear stress, τ_w, is computed and enters the discretized momentum equation as a source term;

$$(S_U)_P = F_\tau \tag{5.6.1}$$

where F_τ is the shear force acting on the near-wall cell P.

$$F_\tau = -\tau_w A_w \tag{5.6.2}$$

where A_w is the area of the wall in the near-wall cell. If the flow at the near-wall node is laminar (and the wall itself is stationary), then the wall shear stress is obtained from;

$$\tau_w = \mu \left.\frac{\partial U}{\partial y}\right|_w = \mu_P \frac{U_P}{y_P} \tag{5.6.3}$$

where U_P is the velocity at the near-wall node and y_P is the distance from the near-wall node to the wall. If the flow at the near-wall node is turbulent, then the wall-shear stress is obtained with a wall-function;

$$\tau_w = \frac{\rho \kappa^* U_P k_P}{\ln\left(E^* y_P^*\right)} \tag{5.6.4}$$

which is as per Equation (4.5.9) and the meaning of the individual quantities are as described in Section 4.5.

Turbulence

Since the no-slip condition must hold for all the velocities, fluctuating components included, all Reynolds stresses are zero on the wall. Thus, the turbulent kinetic energy, k, is set to zero on the wall. At the near-wall node, cell-averaged values of dissipation, $\overline{\varepsilon}$, and production, $\overline{\mathcal{P}_k}$, are used in the transport equation for k as per Equations (4.5.18) and (4.5.14) respectively.

For the ε equation, the condition at the wall depends on the approach used. For approaches which solve an equation for the homogeneous part of the dissipation rate, $\tilde{\varepsilon}$, such as the low-Re Launder-Sharma $k-\varepsilon$ model used in this research, the value of $\tilde{\varepsilon}$ is zero on the wall. The coefficient linking the wall node to the near-wall fluid node is set to zero and the equivalent flux enters the discretized equation as a source term.

For approaches which solve for ε directly, such as the low-Re Hanjalić and Jakirlić model used in this research, the value at the near-wall node is set as per Equation (4.5.17);

$$\varepsilon = \frac{2\nu k_P}{y_P^2} \tag{5.6.5}$$

For stress-transport approaches that are used with wall functions, the values of the Reynolds stresses at the near-wall node are related to k by fixed ratios. In co-ordinates aligned with the wall these are;

$$\frac{\overline{u_1^2}}{k} = 1.098, \quad \frac{\overline{u_2^2}}{k} = 0.248, \quad \frac{\overline{u_3^2}}{k} = 0.654, \quad \frac{\overline{u_1 u_2}}{k} = -0.255 \tag{5.6.6}$$

where u_2 is directed normal to the wall and the value of k at the near-wall node is obtained through solution of its transport equation (4.4.6). For computational convenience the equation is solved globally, even though values of k are only required at the near-wall node. Away from the wall, k is obtained directly from the Reynolds stresses as $k = 0.5\overline{u_i u_i}$.

Thermal field

For the thermal field, either the temperature, Θ, or the heat flux, q, can be prescribed at the wall. In similar fashion to the velocity field, the approach used depends on the state of the fluid at the near-wall node. For the cases computed in this thesis, however, the

thermal field is only solved in cases where a fixed temperature is specified and where the near-wall region can be regarded as laminar (i.e. a low-Re approach).

For a prescribed temperature, the wall node is set to the wall temperature, Θ_w, and the required heat flux into the domain is computed as;

$$q_w = -k_\alpha \left.\frac{\partial \Theta}{\partial y}\right|_w = -k_\alpha \frac{\Theta_P - \Theta_w}{y_P} \tag{5.6.7}$$

where $k_\alpha = \alpha \rho c_p$ is the thermal conductivity. As before, the coefficient linking node P with the wall node is set to zero and the corresponding heat flux is added to the discretized equation for Θ as a source term;

$$(S_U)_P = q_w A_w \tag{5.6.8}$$

Pressure

Since STREAM uses a collocated grid, a boundary condition for the pressure needs to be specified. Typically this is of the form;

$$\frac{\partial P}{\partial y} = 0 \tag{5.6.9}$$

where y represents the direction normal to the wall. As seen in Subsection 3.1.3, the addition of the buoyancy force into the momentum equation resulted in a redefinition of the pressure, where the gravitational potential was included in the modified pressure, P^*, which is what is stored in the "pressure" variable in the solver. To ensure a consistent approach, the correct boundary condition for the pressure is then;

$$\frac{\partial P^*}{\partial y} = \frac{\partial}{\partial y}\left(P + \rho\overline{u_n^2} - \rho g_n \beta_P \left(\Theta_0 - \Theta_P\right) y_P\right) = 0 \tag{5.6.10}$$

where the subscript n indicates resolution of the quantity into its wall normal value, and y_P is the distance from the near-wall node to the wall. The addition of the buoyant contribution to Equation (5.6.10) has been made as part of the present work.

Electric potential

The condition for the electric potential, ϕ, depends upon the electrical properties of the wall. For perfectly electrically insulated walls, the electric current normal to the wall, J_n, is zero. The equivalent condition for the electric potential can be obtained by taking the dot product of Ohm's law, Equation (3.3.7), with $\mathbf{n}$, an inward unit vector normal to the boundary;

$$\mathbf{J} \cdot \mathbf{n} = J_n = \sigma \frac{\partial \phi}{\partial n} + \sigma \mathbf{n} \cdot (\mathbf{U} \times \mathbf{B}) \tag{5.6.11}$$

At the wall $\mathbf{U} = 0$, so specifying $J_n = 0$ leads to a Neumann condition on the electric potential;

$$\frac{\partial \phi}{\partial n} = 0 \tag{5.6.12}$$

For a perfectly conducting wall, the electric potential at the wall is uniform since differences in potential cannot exist. The value of ϕ can then be set to zero without loss of generality.

5.6.2 Periodicity

If the flow is periodic then the flow exiting the domain is mapped to the flow entering the domain. For the periodic fully developed channel flows considered in this thesis all variables except pressure are periodic in the streamwise direction. It is the pressure gradient which is periodic and this is fixed in order to drive the flow.

5.6.3 Symmetry

The conditions at a symmetry boundary require zero flow across the boundary and zero scalar flux across the boundary. Thus the velocity normal to the boundary is set to zero and a Neumann condition is applied to all other variables;

$$\frac{\partial \varphi}{\partial n} = 0 \tag{5.6.13}$$

CHAPTER

SIX

FULLY DEVELOPED CHANNEL FLOWS

In this chapter, numerical results from a series of fully developed channel and duct flows are presented. The objective is to provide, for some flows with only simple shear, a detailed assessment of how the electromagnetically extended turbulence models discussed in Chapter 4 respond to the application of a magnetic field of varying direction and intensity. Two main types of flow are considered. The first is a one-dimensional fully developed channel flow where a magnetic field is applied in either the wall-normal or streamwise direction. The second is fully developed two-dimensional duct flow where the effect of varying the electrical properties of the four walls is investigated.

A description of the considered cases, with details on the mesh and boundary conditions, is provided in Section 6.1 and Section 6.2 details the specific numerical formulation employed. Then, Section 6.3 and Section 6.4 present the main results sections of the chapter and consider laminar and turbulent flows respectively. For the former, a wall-normal magnetic field is first applied to one-dimensional, fully-developed, channel flow and a solution is obtained analytically. As a validation exercise, the analytical solutions are compared with numerical results computed with STREAM. Then, a wall-normal magnetic field is applied to the two-dimensional duct flows and results are computed for walls of differing electrical conductivity. For the latter, non-magnetic flows are first computed in the one-dimensional, fully-developed channel flow and compared against DNS data in order to both validate the numerical solver, and provide a benchmark against which to compare the magnetic cases. Then, a magnetic field is applied in the wall-normal and streamwise directions. Results are computed for a series of Reynolds and Hartmann numbers, and are compared with existing DNS datasets. Finally, Section 6.5 concludes the chapter by summarising the key findings. A selection of results from this chapter have been published in Wilson et al. (2014, 2015).

6.1 Case description

The case considered is that of a fully-developed channel flow of incompressible, electrically conducting fluid subjected to a magnetic field of varying direction and intensity. Two geometric configurations are considered.

For the first, the channel is assumed to be infinitely long in the streamwise and spanwise directions. This reduces to a one-dimensional problem, where the only variation in the flow is in the wall normal direction. Both a wall-normal (i.e. Hartmann flow) and a streamwise magnetic field of varying intensity are applied and flows in the laminar and turbulent regime are considered. Laminar flows with a wall-normal magnetic field are compared against the analytical solution, a development of which is provided. These primarily serve to validate the implementation of the electromagnetic effects in STREAM. Following this, turbulent flows, for both orientations of magnetic field, are compared against available DNS data. The Launder Sharma low-Re eddy-viscosity and the Hanjalić and Jakirlić low-Re stress transport models, as described in Chapter 4, are tested both with and without electromagnetic modifications. A summary of the parameter ranges considered is provided in the relevant results section.

For the second configuration, the channel remains infinitely long but is now bounded by additional walls normal to the spanwise direction. The aspect ratio of the duct is unity and the conductivity of the walls is varied systematically. The effect of wall-conductivity was explored briefly in Subsection 2.2.1 and the primary objective here is to confirm that some of the phenomena discussed there can be correctly reproduced by STREAM. As such, only laminar flows are considered.

With fully developed channel flows, there are two ways in which one can drive the flow. The first is by directly fixing the streamwise pressure gradient (either by setting it as a source term in the momentum equation or by setting the pressure at the two periodic faces accordingly). Once a fully developed solution has been obtained, the streamwise pressure gradient will balance the cross-stream shear-stress gradient and the Lorentz force (if it exists). Flows specified in this manner are most conveniently quantified using a Reynolds number based on the friction velocity $U_\tau = \sqrt{\tau_w/\rho}$, where τ_w is the wall-shear stress, and the channel half-width δ;

$$Re_\tau = \frac{U_\tau \delta}{\nu} \tag{6.1.1}$$

The second way is to actively modify the streamwise pressure gradient such that the mass flow rate through the channel remains constant. The streamwise pressure gradient (and thus the wall-shear stress) then forms part of the solution. Flows specified in this manner are most conveniently quantified using a Reynolds number based on the bulk velocity U_b;

$$Re = \frac{U_b \delta}{\nu} \tag{6.1.2}$$

Both methods are employed here, the most appropriate one being guided by the method used to solve the DNS used for comparisons. The magnetic field strength is quantified using the Hartmann number;

$$Ha = B_0 \delta \sqrt{\frac{\sigma}{\nu}} \tag{6.1.3}$$

where B_0 is the characteristic magnetic field strength.

The governing equations to be solved consist of continuity, Equation (3.3.14), momentum with the Lorentz force term, Equation (3.3.15), and the Poisson equation for the electric potential, Equation (3.3.17). Buoyancy is not considered here, although the effect of a magnetic field on the passive transport of a scalar (temperature) is considered in Subsection 6.4.2. As interest only lies with the fully-developed state, a small slice of the channel is computed with periodic boundary conditions employed in the streamwise direction. The geometries and typical meshes for both sub-cases are presented in the following two sections.

6.1.1 One-dimensional fully developed channel flow

Figure 6.1 provides a schematic of the channel which illustrates the orientation of the axis, the direction of the magnetic field and the channel height. The flow is in the positive x direction and the magnetic field applied in either the positive y or positive x direction. The top and bottom boundaries are specified as electrically insulating walls where, in addition to the no-slip condition on the velocity, the electric current normal to the wall, J_n, is zero.

For the computational mesh, the streamwise periodicity of the flow allows a relatively small number of control volumes (~ 10) to be used in that direction. Since low-Re models are employed, a high number of nodes was employed in the wall normal direction. A mesh was generated for each Re_τ considered to ensure that the position of the first node satisfies $y^+ \leq 1$. This ensures the validity of the low-Re approach and that the equations are solved right into the near-wall viscous sublayer. The cell spacing in this direction was computed using a geometric series expansion to cluster the nodes towards the walls. A typical mesh is superimposed over the schematic in Figure 6.1.

6.1.2 Two-dimensional fully developed duct flow

For the two-dimensional fully developed duct flows, a small slice of an infinitely long square duct is modelled as illustrated in Figure 6.2. Periodicity is employed in the streamwise direction and, since walls of differing electrical conductivity are investigated, the walls have been labelled as “Side walls” (for those parallel to the magnetic field) and “Hartmann walls” (for those normal to the magnetic field) for ease of reference. The

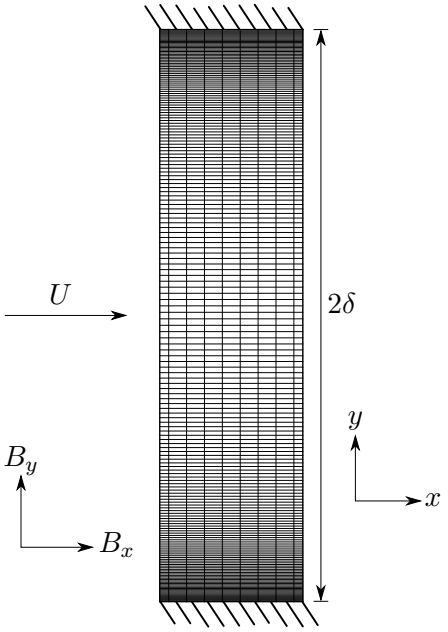

Figure 6.1: Geometry and typical low-Re mesh for one-dimensional fully developed channel flow cases.

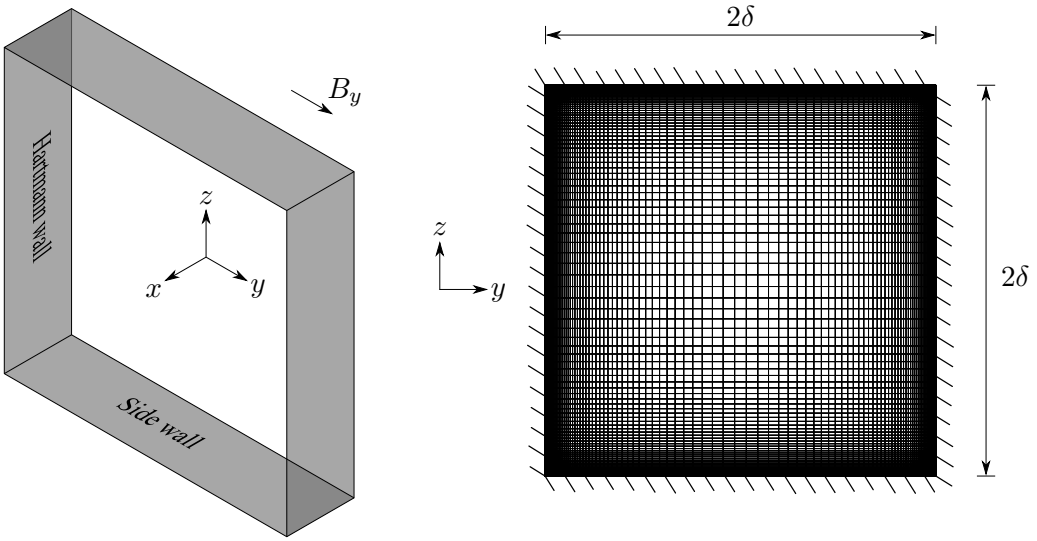

Figure 6.2: Geometry and typical mesh for two-dimensional fully developed duct flow cases.

applied streamwise pressure gradient is such that the flow is in the positive x direction and a magnetic field is applied in the positive y direction. Although the flow is laminar, the types of phenomena expected to arise (wall jets, for example, as described in Subsection 2.2.1) mean that nodes have been clustered towards to the walls to aid resolution of steep velocity gradients.

6.2 Numerical formulation

All computations have been carried out using a version of the in-house 2D/3D finite-volume flow solver STREAM which has been extended to include the electromagnetic modifications discussed in Chapters 3 and 4. Convective terms in the momentum equations are treated with the bounded high-order UMIST scheme of Lien and Leschziner (1994b) whilst those in the turbulence equations use the first order UPWIND scheme. The steady state computations ran until the solution residuals were at least $\mathcal{O}(10^{-6})$ and any variation in the streamwise direction eliminated.

6.3 Laminar flows

The solution of some relatively simple laminar flows provides an ideal means to both validate the implementation of the additional, mean, electromagnetic effects in the solver and demonstrate that the code is capable of reproducing some of the phenomena explored as part of Section 2.2. First, one-dimensional fully developed Hartmann flow is solved analytically and the results are compared with laminar numerical calculations obtained with the solver STREAM over a range of magnetic field strengths. Then, the solver is used to compute some flows through the two-dimensional duct described in Subsection 6.1.2. Results are compared with those described earlier in Section 2.2.

6.3.1 Analytical Hartmann flow

Hartmann flow describes a fully developed channel flow of an electrically conducting fluid which is subjected to a uniform wall-normal magnetic field. It was explored in detail as part of Section 2.2. Here, if attention is restricted to one-dimensional laminar flow, an analytical solution of the governing equations may be found. The momentum equation (3.3.15), rewritten here in vector notation, reduces to;

$$0 = -\nabla P + \mu \nabla^2 \mathbf{U} + \mathbf{J} \times \mathbf{B} \tag{6.3.1}$$

where the Lorentz force, the final term on the RHS, is as per Equation (3.2.28). The Lorentz force, with the help of Ohm's law, Equation (3.2.12), becomes;

$$\mathbf{J} \times \mathbf{B} = \sigma \left(\mathbf{E} + \mathbf{U} \times \mathbf{B} \right) \times \mathbf{B} \tag{6.3.2}$$

The x-component of Equation (6.3.1), given that given that $\mathbf{U} = (U, 0, 0)$ and $\mathbf{B} = (0, B_0, 0)$, reduces to;

$$0 = -\frac{\partial P}{\partial x} + \mu \frac{\partial^2 U}{\partial y^2} - \frac{\sigma}{\rho} B_0 \left(E_z + U B_0 \right) \tag{6.3.3}$$

Equation (6.3.3) can be non-dimensionalized through a choice of suitable scales. The channel half-width, δ, is chosen as a length scale and B_0 is chosen as the magnetic field scale. For the velocity scale, one can use either the bulk velocity, U_b, or the friction velocity $U_\tau = \sqrt{\tau_w / \rho}$. Choosing the bulk velocity, the variables in Equation (6.3.3) can be non-dimensionalized as;

$$x^* = \frac{x}{\delta}, \quad y^* = \frac{y}{\delta}, \quad U^* = \frac{U}{U_b}, \quad B^* = \frac{B_0}{B_0} = 1, \quad E^* = \frac{E_z}{U_b B_0}, \quad P^* = \frac{P}{\rho U_b^2} \tag{6.3.4}$$

and the resulting non-dimensional equation of motion is given by;

$$\frac{\partial P^*}{\partial x^*} = \frac{1}{Re}\frac{\partial^2 U^*}{\partial y^{*2}} - \frac{Ha^2}{Re}\left(E_z^* + U^*\right) \tag{6.3.5}$$

Since the magnetic field, $\mathbf{B}$, is constant, the electric field must be curl free (as per Equation (3.3.5a)) and can thus be represented by the gradient of the non-dimensional electrostatic potential, $\nabla\phi^*$. The Poisson equation for the electrostatic potential, Equation (3.3.17), then reduces to;

$$\nabla^2\phi^* = 0 \tag{6.3.6}$$

which implies that;

$$\nabla\phi^* = const. = -E_z^* \tag{6.3.7}$$

and thus the electric field component, E_z^*, is constant across the channel. Equation (6.3.5) is then a 2nd-order linear differential equation of the form;

$$\frac{\partial^2 U^*}{\partial y^{*2}} - C^2 U^* = D \tag{6.3.8}$$

where C and D are the constants;

$$C = Ha, \quad D = Re\frac{\partial P^*}{\partial x^*} + Ha^2 E_z^* \tag{6.3.9}$$

This can be solved to give the non-dimensional velocity profile;

$$U^*(y^*) = \left(-\frac{Re}{Ha^2}\frac{\partial P^*}{\partial x^*} - E_z^*\right)\left[1 - \frac{\cosh\left(Ha \cdot y^*\right)}{\cosh\left(Ha\right)}\right] \tag{6.3.10}$$

The role of the electric field, E_z^*, now becomes more apparent. Since it does not vary with position, it plays a similar role to the pressure gradient in that it forms part of the "driving force" which balances the wall shear stress. Neither the pressure gradient nor the electric field can modify the *shape* of the velocity profile but if, say, the flow is driven by a fixed pressure gradient, then the resulting mass flow rate will depend upon both the value of the pressure gradient *and* the electric field which exists. Whether or not an electric field exists will depend on the electrical properties of the walls normal to the z direction (*not* the walls normal to the y direction) and whether or not these walls are connected with any electrical device. This was explored in Subsection 2.2.1 and Equation (6.3.10) provides some mathematical justification to that discussion.

The "driving force" in the channel, can be related to the bulk velocity through;

$$U_b = \frac{1}{2\delta}\int_{-\delta}^{\delta} U(y)\,\mathrm{d}y \tag{6.3.11}$$

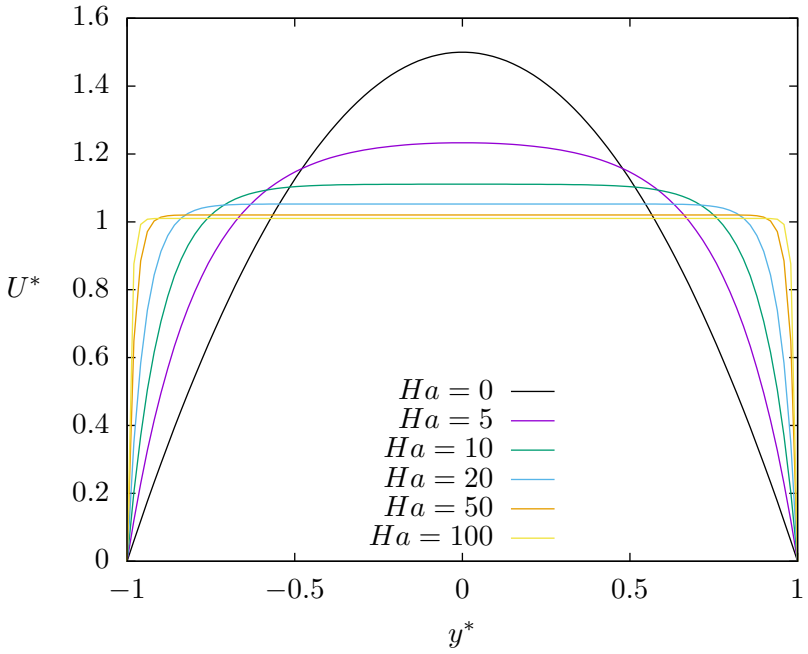

Figure 6.3: Fully developed channel flow under a wall-normal magnetic field. Analytic velocity profiles for varying Ha with a fixed mass flow rate, as given by Equation (6.3.14) for $Ha > 0$ and Equation (6.3.15) for $Ha = 0$.

which, non-dimensionalized, becomes;

$$1 = \frac{1}{2}\int_{-1}^{1} U^*(y)\,\mathrm{d}y^* \tag{6.3.12}$$

By integrating Equation (6.3.10) across the channel, Equation (6.3.12) becomes;

$$-\left(\frac{Re}{Ha^2}\frac{\partial P^*}{\partial x^*} + E_z^*\right) = \left[1 - \frac{\sinh(Ha)}{Ha\cosh(Ha)}\right]^{-1} \tag{6.3.13}$$

Substitution of this into Equation (6.3.10) and dividing by the bulk velocity gives the non-dimensional velocity profile for Hartmann flow with varying Ha;

$$U^*(y^*) = \frac{Ha\cosh(Ha) - Ha\cosh(Ha\cdot y^*)}{Ha\cosh(Ha) - \sinh(Ha)} \tag{6.3.14}$$

This is plotted for a selection of $Ha > 0$ in Figure 6.3 along with the analytical profile for non-magnetic channel flow $(Ha = 0)$, given by;

$$U^*(y^*) = \frac{3}{2}\left(1 - y^{*2}\right) \tag{6.3.15}$$

For a fixed mass flow rate the primary effect of the wall normal magnetic field is to eliminate the velocity gradients in the centre of the channel. This reduces both the centerline velocity and boundary layer thickness.

To verify the implementation of the mean magnetic forcing in the STREAM code, laminar

simulations for $Re_\tau = 150$ and a selection of Ha were obtained. To compare these with the analytical solutions, it is convenient to first rescale the equation of motion using the friction velocity, U_τ;

$$U^+(y^*) = \left(-\frac{Re_\tau}{Ha^2}\frac{\partial P^+}{\partial x^*} - E_z^+\right)\left[1 - \frac{\cosh\left(Ha \cdot y^*\right)}{\cosh\left(Ha\right)}\right] \tag{6.3.16}$$

where the affected variables in Equation (6.3.4) are redefined as;

$$U^+ = \frac{U}{U_\tau}, \quad E_z^+ = \frac{E_z}{U_\tau B_0}, \quad P^+ = \frac{P}{\rho U_\tau^2} \tag{6.3.17}$$

The pressure gradient and electric field can be related to the wall shear stress by first taking the derivative of Equation (6.3.16) to give an equation for the non-dimensional viscous shear stress;

$$\tau^+(y^*) = \frac{1}{Re_\tau}\frac{\partial U^+}{\partial y^*} = \frac{Ha}{Re_\tau}\left(-\frac{Re_\tau}{Ha^2}\frac{\partial P^+}{\partial x^*} - E_z^+\right)\left[\frac{-\sinh(Ha \cdot y^*)}{\cosh(Ha)}\right] \tag{6.3.18}$$

The wall shear stress is then given by;

$$\tau^+(1) = \tau_w^+ = \frac{Ha}{Re_\tau}\left(-\frac{Re_\tau}{Ha^2}\frac{\partial P^*}{\partial x^*} - E_z^+\right)\left[-\tanh\left(Ha\right)\right] \tag{6.3.19}$$

Since the shear stress is non-dimensionalized using the friction velocity, the non-dimensional wall shear stress is unity and the non-dimensional "driving force" can be expressed as;

$$\left(-\frac{Re_\tau}{Ha^2}\frac{\partial P^*}{\partial x^*} - E_z^+\right) = -\frac{Re_\tau}{Ha\tanh\left(Ha\right)} \tag{6.3.20}$$

Substitution of Equation (6.3.20) into Equation (6.3.16) results in an expression describing the velocity profile for a given Re_τ and Ha;

$$U^+(y^*) = \frac{Re_\tau}{Ha\tanh(Ha)}\left[1 - \frac{\cosh\left(Ha \cdot y^*\right)}{\cosh\left(Ha\right)}\right] \tag{6.3.21}$$

Figure 6.4 compares profiles obtained with Equation (6.3.21) to the solutions given by STREAM for $Re_\tau = 150$ and a range of Ha. As can be seen, the numerical results are essentially identical to the exact solution as would be expected.

6.3.2 Two-dimensional fully developed square duct flow

Unlike the one-dimensional fully developed flows discussed in the previous section, the two-dimensional duct flows considered here allow the effects of the bounding side walls to be investigated. As was previously discussed in Subsection 2.2.1 the electrical properties of these, and the Hartmann walls, has a direct effect on the distribution of electrical

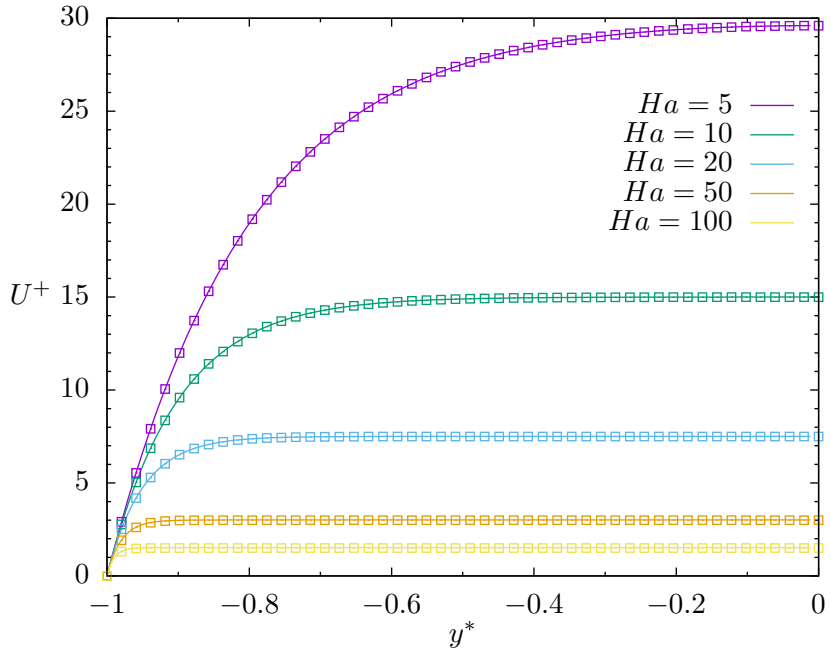

Figure 6.4: Non-dimensional velocity profiles for Hartmann flow at $Re_\tau = 150$ for various Ha. Analytic solutions (symbols) are given by Equation (6.3.21) and laminar computations represented by the solid lines.

current within the domain and this will modify the velocity profile through changes to the distribution of the Lorentz force. These effects are investigated systematically, by examining three different combinations of wall conductivity for the bounding walls. First, a fully insulated duct is considered, followed by a fully conducting duct, and then, with reference to Figure 6.2, a duct with insulating side walls and conducting Hartmann walls is investigated. In all cases, the flow is driven by a fixed streamwise pressure gradient such that $Re_\tau = 150$ and a magnetic field is applied in the positive y direction.

Fully insulating walls

In a fully insulated duct, it was observed in Subsection 2.2.1 that since the electric current must form closed loops, it has to turn along the side walls and travel back across the duct within the Hartmann layers. This causes a Lorentz force which opposes the flow in the core of the channel, flattening the velocity profile, and accelerates the flow next to the Hartmann walls, decreasing the boundary layer thickness. This is clearly shown in Figure 6.5, where the resulting velocity profile is presented alongside the current paths within the duct for a strong magnetic field ($Ha = 100$). Along the side walls ($z^* \pm 1$), the current travels in the same direction as the magnetic field and, without an accelerating Lorentz force, results in a boundary layer thicker than that seen along the Hartmann walls. These results demonstrate good agreement with numerical computations by Sterl (1990) presented in Figure 6.6.

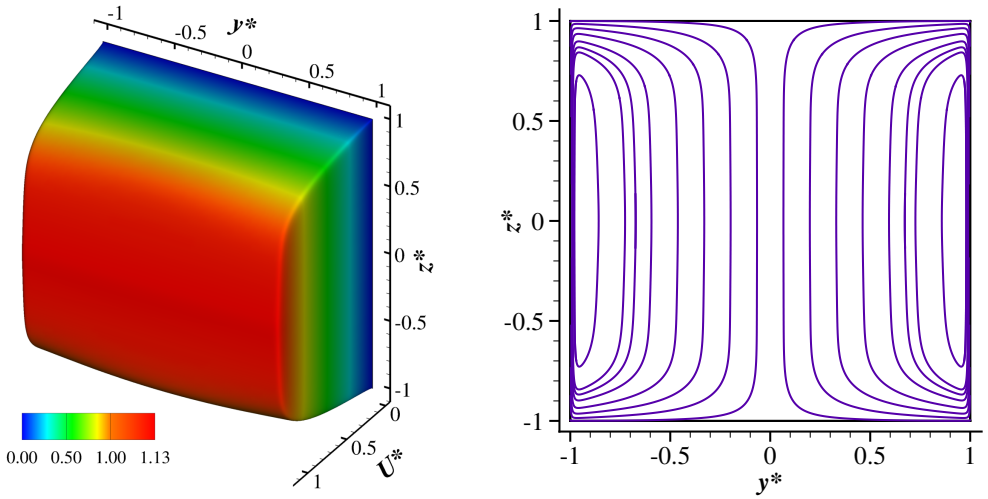

(a) (b)

Figure 6.5: Fully developed laminar flow of conducting fluid through a square duct with all walls perfectly insulating and a magnetic field applied in the y direction. (a) Non-dimensional velocity (U^*) distribution and (b) electric current paths for $Ha = 100$; $Re_\tau = 150$.

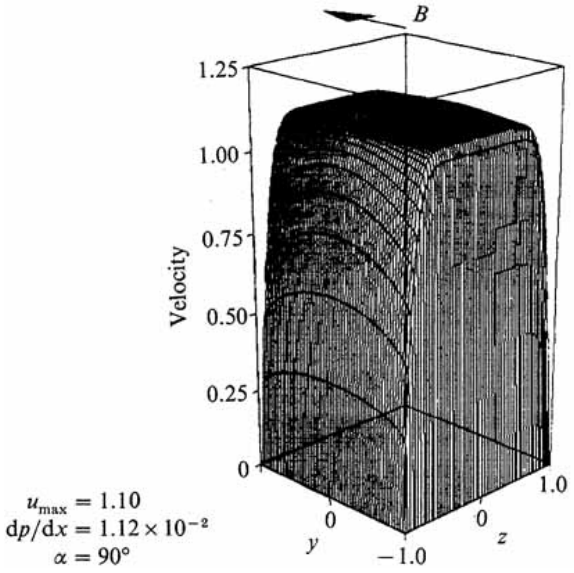

Figure 6.6: Velocity profiles obtained by Sterl (1990) for the fully-developed two-dimensional flow of conducting fluid down a duct of square cross-section with all walls insulating. Repeated from Figure 2.3(a).

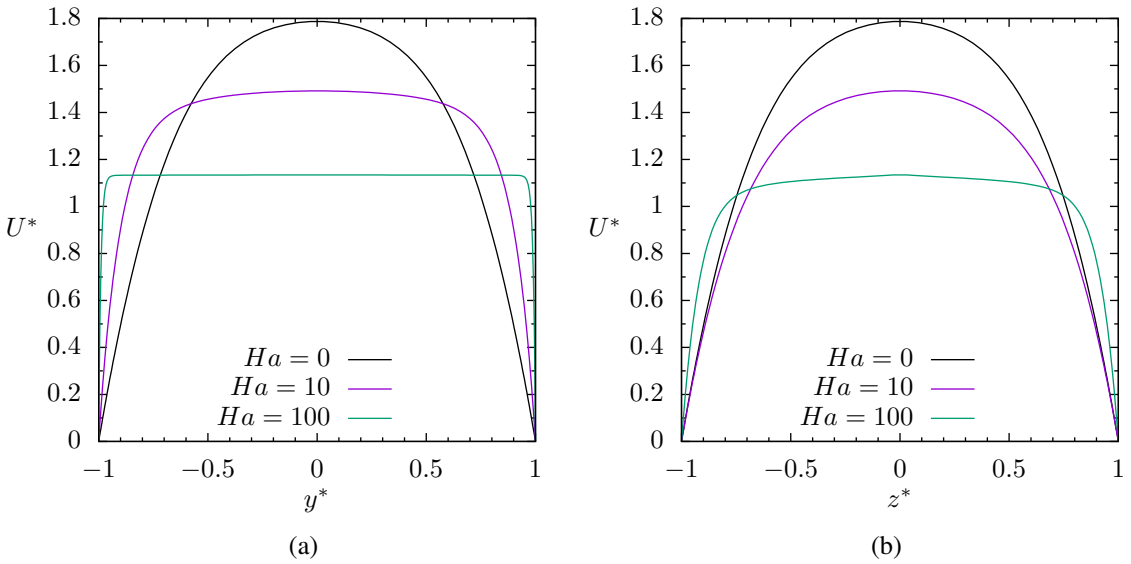

(a) (b)

Figure 6.7: Fully developed laminar flow of conducting fluid through a square duct with all walls perfectly insulating and a magnetic field applied in the y direction. Non-dimensional velocity profiles (U^*) along the two centrelines, (a) $z^* = 0$ and (b) $y^* = 0$, for varying Ha; $Re_\tau = 150$.

The above flow picture is confirmed by Figure 6.7 where velocity profiles along both centrelines are presented for $Ha = 0, 10, 100$. Along the y direction, the profiles exhibit similar behaviour as that seen for Hartmann flow, shown previously in Figure 6.3 (since without the sidewalls the flow is identical to Hartmann flow). Along the z direction the thicker boundary layers are evident. An analytical solution by Shercliff (1953) shows that the thickness of these side layers is $\mathcal{O}(Ha^{1/2})$ compared with $\mathcal{O}(Ha^{-1})$ for the Hartmann layers.

Fully conducting walls

If all the walls are perfectly conducting, then the current does not need to return across the duct through the Hartmann layers. Rather, it can return through the walls where it encounters zero resistance. Figure 6.8 shows the resulting velocity profile and electric current paths for $Ha = 100$. The current travels almost purely in the z direction, parallel to the Hartmann walls. Note, however, that as the current reaches the side walls, it turns slightly towards the Hartmann walls. This change of direction reduces slightly the component of current perpendicular to the magnetic field, leading to a reduction in the strength of the Lorentz force. This results in a local velocity maximum, which can be clearly seen in Figure 6.8(a).

Velocity profiles, shown in Figure 6.9, indicate that this maximum only becomes significant for at least $Ha > 10$ and grows as the Hartmann number increases. The velocity distribution in the y direction appears relatively unaffected. This is consistent with the

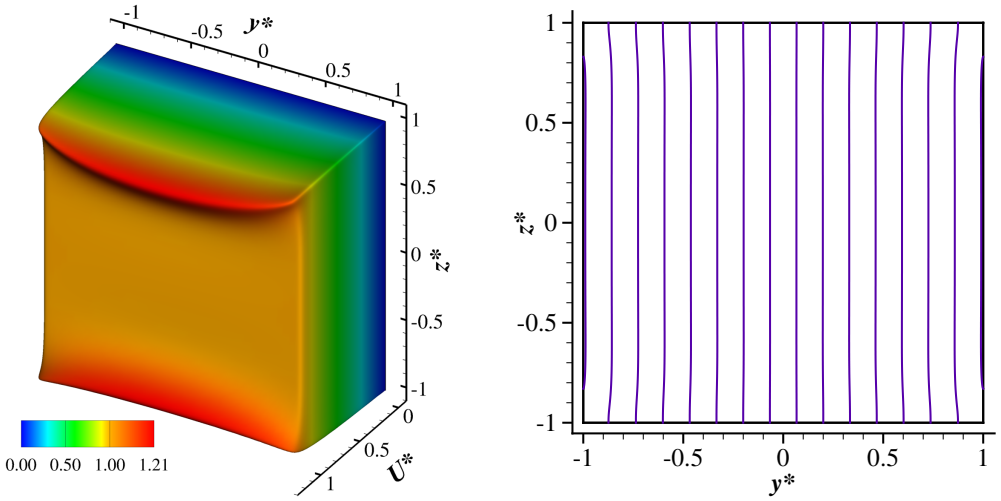

(a) (b)

Figure 6.8: Fully developed laminar flow of conducting fluid through a square duct with all walls perfectly conducting and a magnetic field applied in the y direction. (a) Non-dimensional velocity (U^*) distribution and (b) electric current paths for $Ha = 100$; $Re_\tau = 150$.

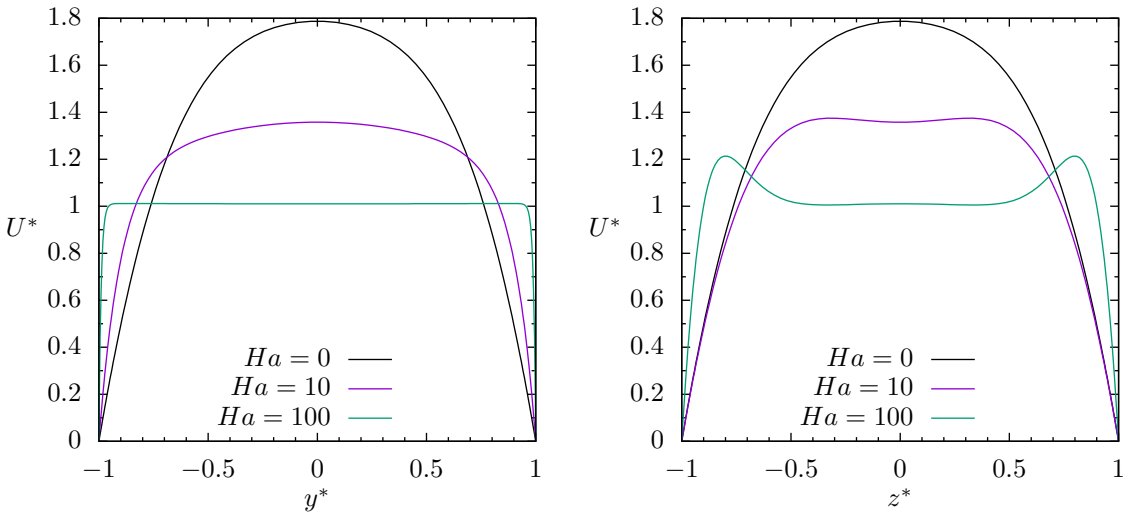

(a) (b)

Figure 6.9: Fully developed laminar flow of conducting fluid through a square duct with all walls perfectly conducting and a magnetic field applied in the y direction. Non-dimensional velocity profiles (U^*) along the two centrelines, (a) $z = 0$ and (b) $y = 0$, for varying Ha; $Re_\tau = 150$.

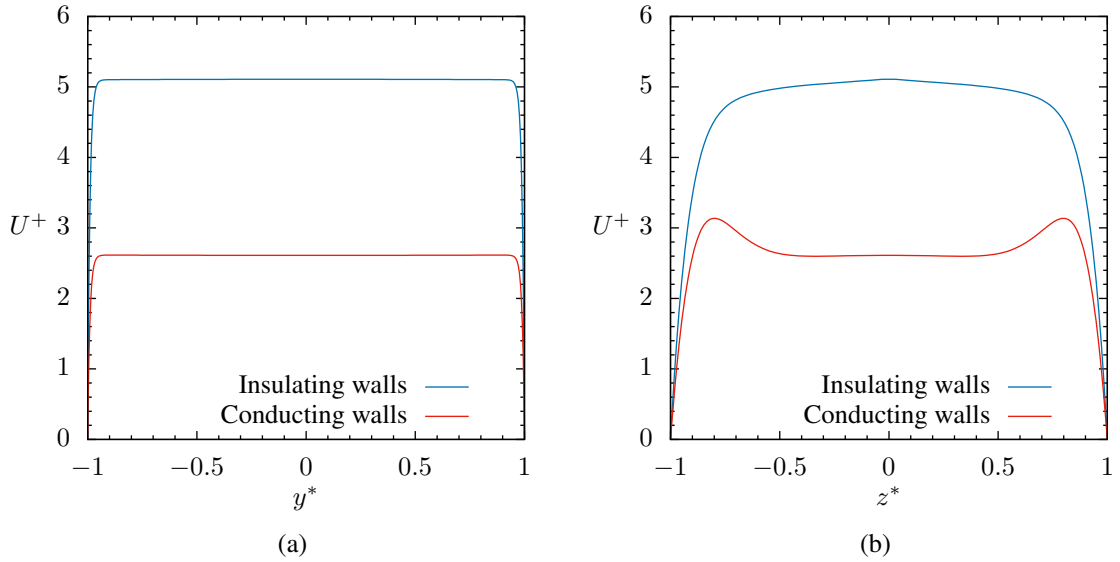

Figure 6.10: Fully developed laminar flow of conducting fluid through a square duct with a magnetic field applied in the y direction. Comparison of non-dimensional velocity profiles (U^*) along the two centrelines, (a) $z = 0$ and (b) $y = 0$, for a duct with all insulating or all conducting walls; $Ha = 100$, $Re_\tau = 150$.

conclusions drawn from the analytical exploration in Subsection 6.3.1, which noted that the presence of an electric field in the z direction could only modify the mass flow rate (or streamwise pressure gradient) through the duct and not the shape of the velocity profile (here, unlike the case with fully insulating walls, there is no electric field in the z direction since the current does not need to return across the duct). To emphasise this point, Figure 6.10 compares velocity profiles along both centre lines for conducting and insulating walls with $Ha = 100$. The profiles have been normalized with the friction velocity to highlight the differences in mass flow rate the presence of an electric field can bring. In this case, with fully conducting walls, the resulting Lorentz force is much stronger and this results in a smaller mass flow rate for a given streamwise pressure gradient.

Fully conducting Hartmann walls, insulating side walls

The final configuration of wall conductivities considered is that where the Hartmann walls are perfectly conducting and the side walls perfectly insulating. Here, the currents generated in the core cannot travel inside the side walls and, like in the fully insulating case, turn towards the Hartmann walls. Unlike in the fully insulating case, however, the currents here travel within the Hartmann walls themselves. This has quite a dramatic effect on the velocity distribution in the duct as Figure 6.11 shows.

With fully conducting walls, a slight reduction in the component of current perpendicular to the magnetic field was seen to lead to a local velocity maximum. Here, the insulating side walls force the current to turn and thus the component perpendicular to the magnetic

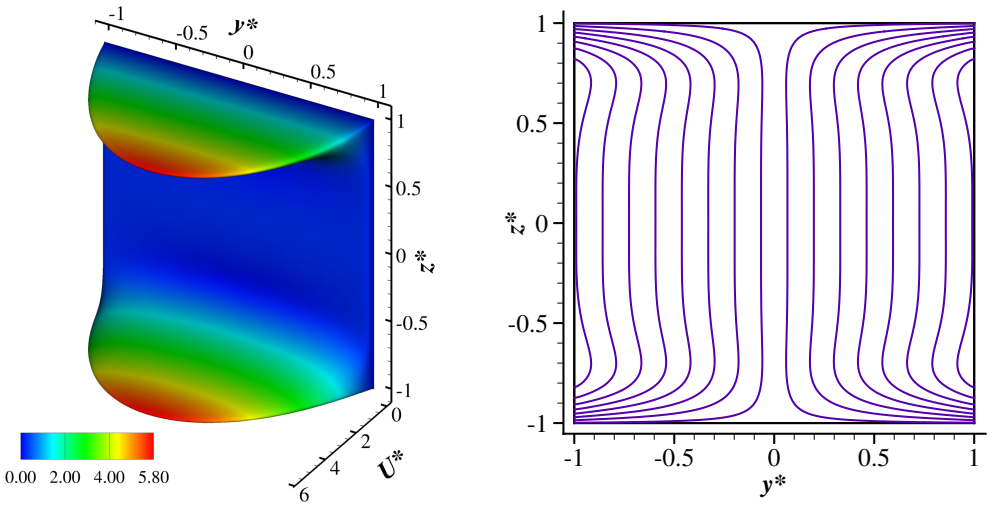

(a) Contours of U (b) Current paths

Figure 6.11: Fully developed laminar flow of conducting fluid through a square duct with perfectly conducting Hartmann walls ($z^* = \pm 1$), perfectly insulating side walls ($y^* = \pm 1$) and a magnetic field applied in the y direction. (a) Non-dimensional velocity (U^*) distribution and (b) electric current paths for $Ha = 100$; $Re_\tau = 150$.

field is substantially reduced. This leads to the formation of two opposing near-wall jets with a corresponding decrease in velocity in the core. Velocity profiles for increasing Ha are plotting along both duct centrelines in Figure 6.12. Along the z direction, the velocity distribution is frequently termed *M-shaped* and for sufficiently strong magnetic fields (here, additional simulations at $Ha = 200$ were performed to investigate this), the velocity in the core can actually reverse. These results are in good agreement with numerical predictions by Sterl (1990), presented in Figure 6.13.

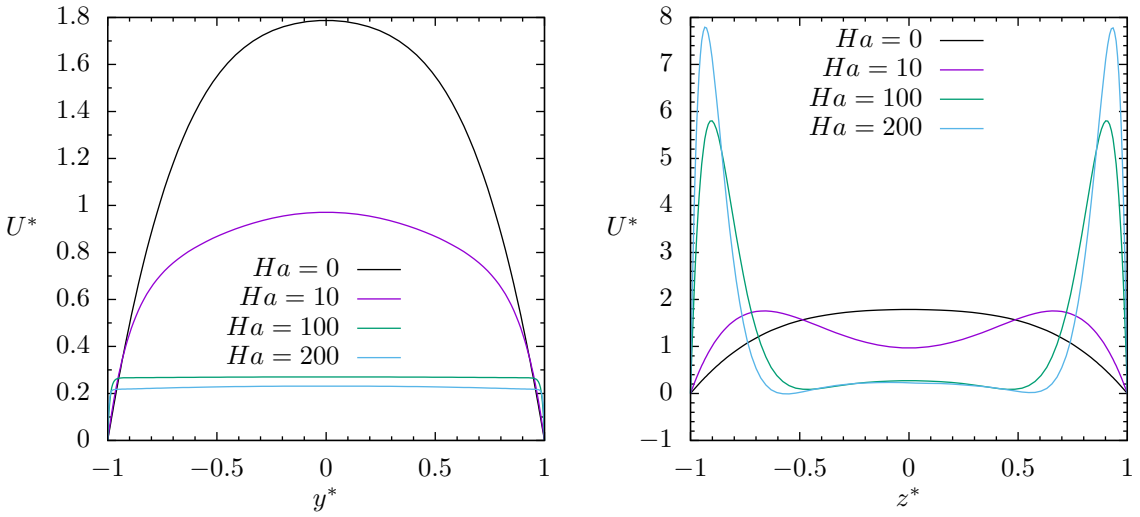

(a) (b)

Figure 6.12: Fully developed laminar flow of conducting fluid through a square duct with with perfectly conducting Hartmann walls ($z^* = \pm 1$), perfectly insulating side walls ($y^* = \pm 1$) and a magnetic field applied in the y direction. Non-dimensional velocity profiles (U^*) along the two centrelines, (a) $z = 0$ and (b) $y = 0$, for varying Ha; $Re_\tau = 150$.

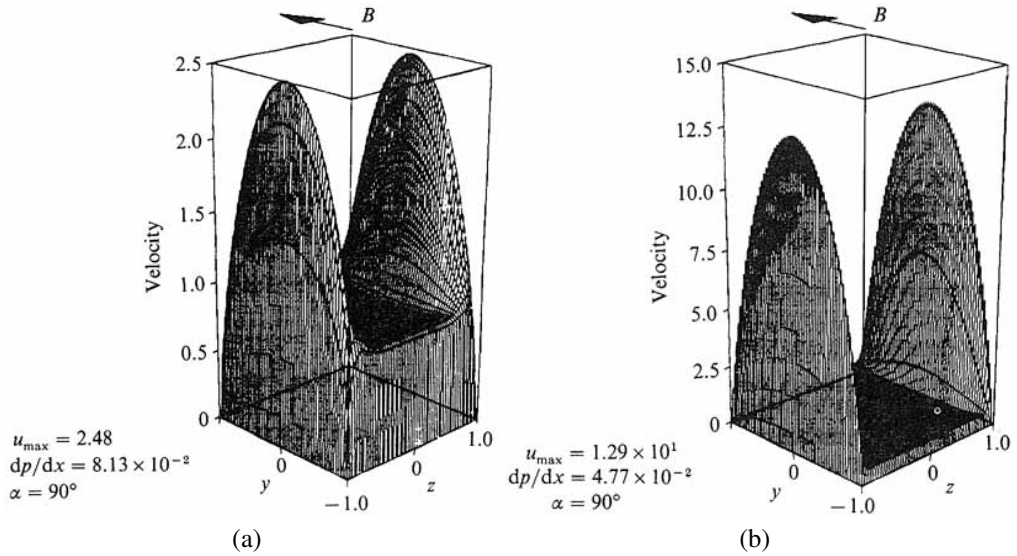

(a) (b)

Figure 6.13: Velocity profiles obtained by Sterl (1990) for the fully-developed two-dimensional flow of conducting fluid down a duct of square cross-section with conducting Hartmann walls and insulating side walls for (a) $Ha = 100$ and (b) $Ha = 1000$. Repeated from Figure 2.3 for convenience.

6.4 Turbulent flows

This section presents the results of a series of one-dimensional turbulent fully-developed channel flows. Initially, only flows in the absence of a magnetic field are considered, since this provides a means to validate the turbulence models within the numerical solver STREAM. Then the magnetic field is activated and considered for two different orientations (wall-normal and streamwise) and over a range of field strengths. Finally, the addition of a passive scalar (here, the temperature) is considered only for a wall-normal magnetic field. The geometry considered is as per Figure 6.1 and all results are compared against DNS data from a selection of sources.

6.4.1 Non-magnetic fully developed one-dimensional channel flow

The range of Re_τ considered, the mesh resolution and the source for the DNS data used are provided in Table 6.1. In what follows the unmodified Launder and Sharma (1974) model is referred to by the abbreviation LS and the unmodified Hanjalić and Jakirlić model is referred to by the abbreviation HJ.

Mean velocity profiles normalized by the friction velocity are shown in Figure 6.14. In general the results obtained with the LS model are in good agreement with the DNS data across the range of Re_τ. At the lowest Re_τ it slightly under predicts turbulence levels within the log-law region but this improves at higher Re_τ. Excellent agreement is achieved by all models in the viscous sublayer $(y^+ < 5)$ when compared with the DNS. This is not particularly surprising however, since the streamwise pressure gradient (which is fixed) is directly related to wall shear stress and, as such, fixes the velocity gradient at the wall. Outside of the near-wall region ($y^+ \geq 5$), the RSM model departs from the DNS data and shows a significant under prediction in the mass flow rate through the channel. This equates to the HJ model over predicting the level of turbulence throughout the channel (since this opposes the streamwise pressure gradient, reducing the mass flow rate achievable) and this suggests an insufficient amount of near-wall damping.

Curiously, results for a wide range of flow configurations (including channel flows), presented in Hanjalić et al. (1997), using the model did not show the discrepancy noted above.

Re_τ	$N_x \times N_y$	DNS data ref.
150	10×200	Noguchi et al. (2004)
590	10×250	Moser et al. (1999)
950	10×250	Álamo et al. (2004)
2000	10×260	

Table 6.1: Summary of RANS simulations performed for non-magnetic one-dimensional fully developed channel flow.

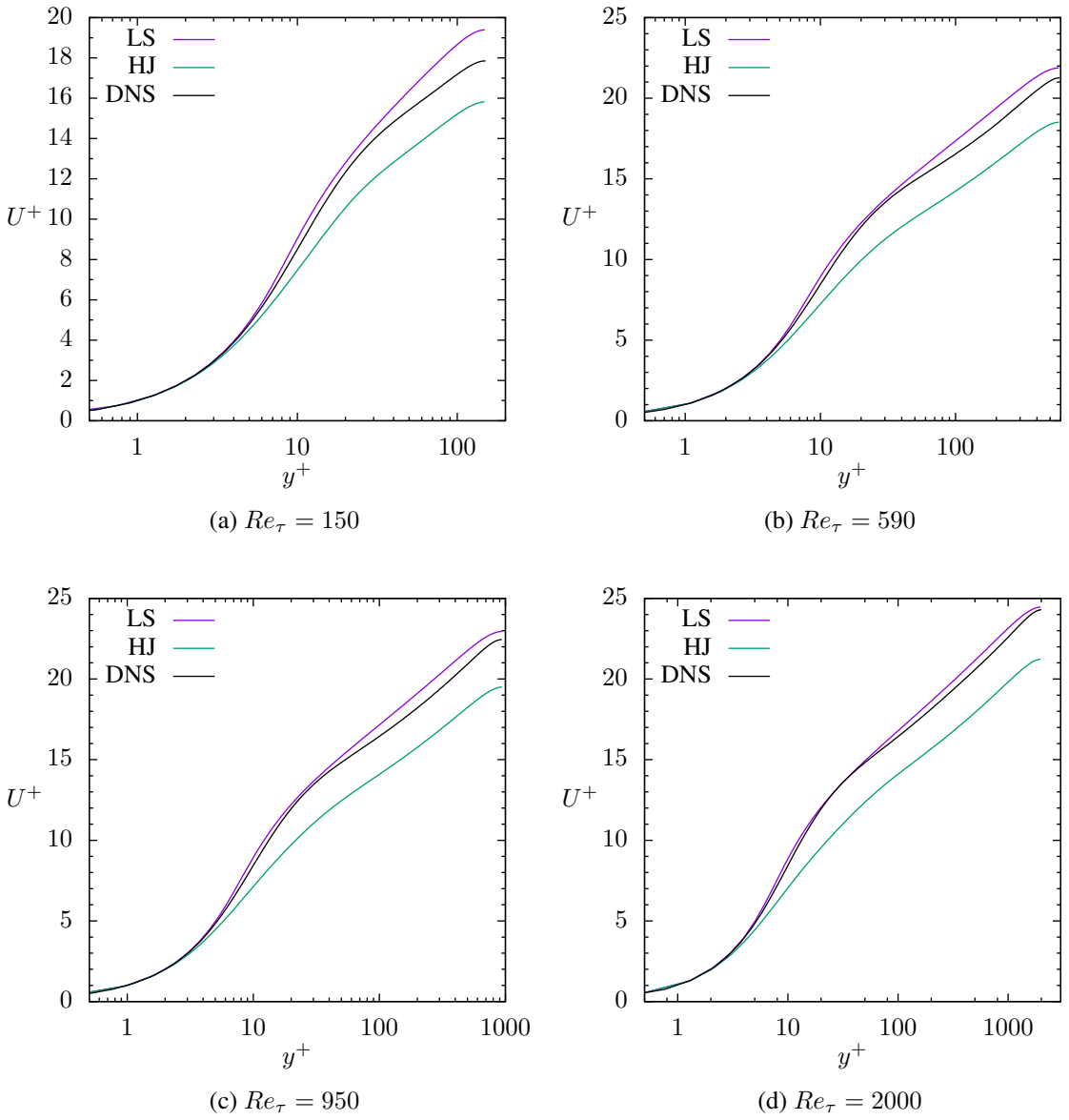

(a) $Re_\tau = 150$ (b) $Re_\tau = 590$

(c) $Re_\tau = 950$ (d) $Re_\tau = 2000$

Figure 6.14: Non-dimensional velocity profiles for fully developed non-magnetic channel flow with increasing Re_τ. Comparisons between Launder and Sharma (1974) low-Re $k-\varepsilon$ EVM (LS), Hanjalić and Jakirlić low-Re RSM (HJ) and DNS data (see Table 6.1).

Despite careful and extensive checks for errors with the implementation of the model in STREAM, no errors were found and the form of the model implemented matches that presented in Kenjereš et al. (2004). Qualitatively, all velocity profiles clearly show features typically expected from a channel flow. The linear near-wall sublayer and low-law region are clearly reproduced by all models with size of the log-law region increasing with Re_τ.

Figure 6.15 shows profiles of the non-dimensional turbulent shear stress $\overline{uv}^+$. Agreement with the DNS is good for both the models over all Re_τ considered. There are some noticeable differences in the near-wall region ($y^+ < 30$) for $Re_\tau = 150$, where the overall contribution of the turbulent shear stress to the total shear stress is under predicted by the LS model and over predicted by the HJ model. This agrees with the earlier observations drawn from the velocity profiles in Figure 6.14. As the Reynolds number is increased the

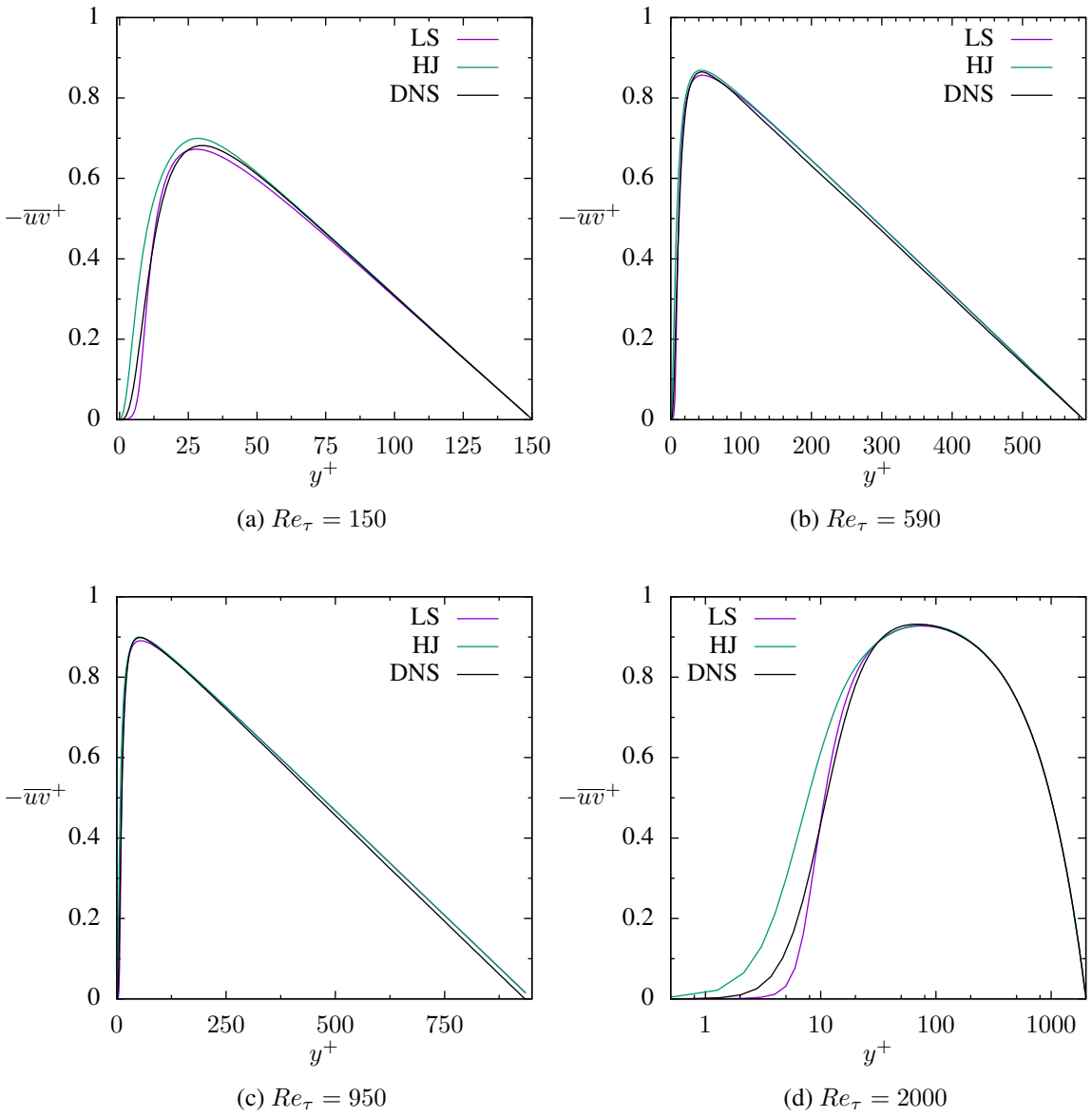

(a) $Re_\tau = 150$ (b) $Re_\tau = 590$

(c) $Re_\tau = 950$ (d) $Re_\tau = 2000$

Figure 6.15: Fully developed non-magnetic channel flow: non-dimensional shear-stress $(\overline{uv}^+)$ profiles for increasing Re_τ. Comparisons between Launder and Sharma (1974) low-Re $k-\varepsilon$ EVM (LS), Hanjalić and Jakirlić low-Re RSM (HJ) and DNS data (see Table 6.1).

contribution from the viscous stresses decreases, as one would expect, and the turbulent shear stress dominates. The $\overline{uv}^+$ profile at $Re_\tau = 2000$, shown in Figure 6.15(d) has been plotted against a logarithmic scale to highlight the subtle differences in $\overline{uv}^+$ reported by the models. These correlate with the differences in mass flow seen in the velocity profiles.

Comparisons of the turbulent kinetic energy (k^+) profiles across the channel are provided in Figure 6.16. The inability of the LS model to reproduce the near-wall peak values is well known, with the HJ model offering much improved predictions (due, in part, to better representation the normal stresses which comprise k). Figure 6.17 shows the distribution of the normal stresses across the channel for the HJ model. The LS model is not shown since, for the simple shear flow considered here, the stress-strain relationship will always

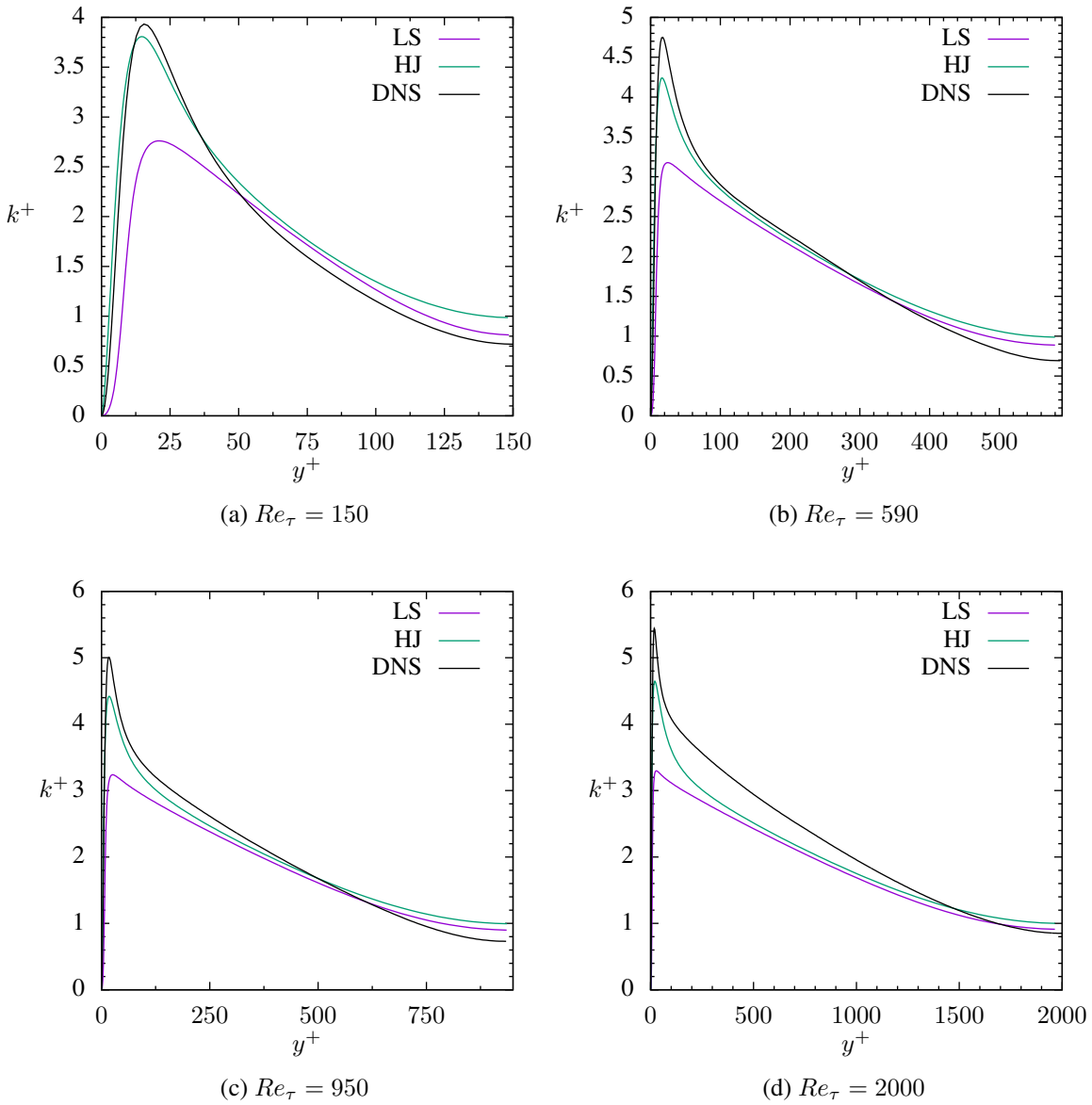

(a) $Re_\tau = 150$ (b) $Re_\tau = 590$

(c) $Re_\tau = 950$ (d) $Re_\tau = 2000$

Figure 6.16: Fully developed non-magnetic channel flow: non-dimensional turbulent kinetic energy (k^+) profiles for increasing Re_τ. Comparisons between Launder and Sharma (1974) low-Re $k-\varepsilon$ EVM (LS), Hanjalić and Jakirlić low-Re RSM (HJ) and DNS data (see Table 6.1).

return isotropic normal stresses (equal to $2/3k$). The agreement is generally good and the HJ model predicts the correct distribution of anisotropy across the channel.

Despite the discrepancies seen in the mass flow reported by the two turbulence models, the results are in agreement with physical intuition and show good qualitative (and in most cases quantitative) agreement with the DNS data. As such, the implementation of the models in the solver is believed to be correct.

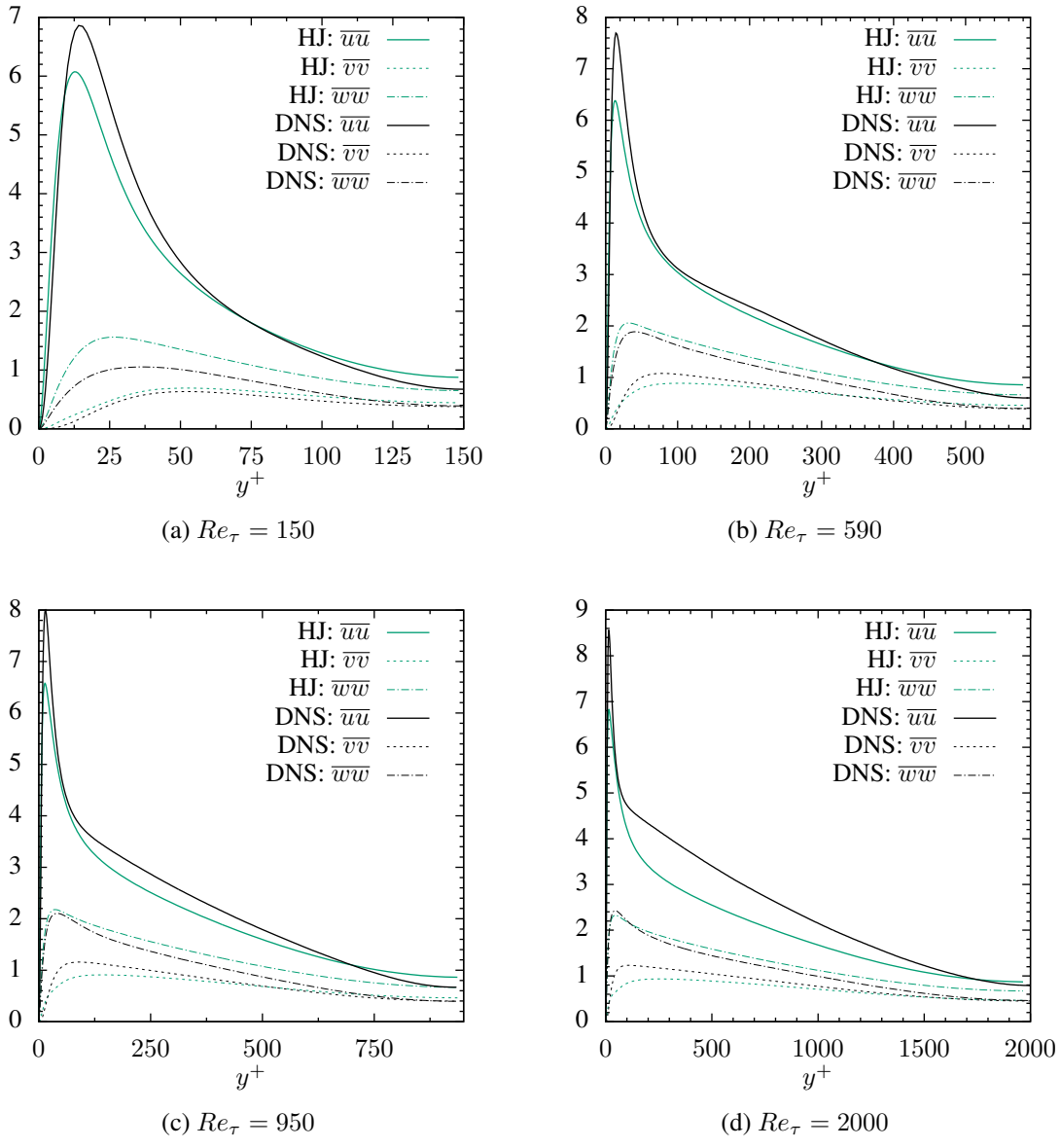

(a) $Re_\tau = 150$

(b) $Re_\tau = 590$

(c) $Re_\tau = 950$

(d) $Re_\tau = 2000$

Figure 6.17: Fully developed non-magnetic channel flow: non-dimensional normal stress profiles for increasing Re_τ. Comparisons between Hanjalić and Jakirlić low-Re RSM (HJ) and DNS data (see Table 6.1).

6.4.2 Hartmann flow

Solutions for turbulent Hartmann flow at a range of Re_τ and Ha are presented here with the aim of comparing the performance of the Launder and Sharma (1974) low-Re $k-\varepsilon$ and the low-Re Hanjalić and Jakirlić RSM against DNS data. Both the electromagnetically modified and the unmodified versions of the turbulence models are compared; in the case of the latter, the magnetic field can only affect the turbulence through deforming the mean rate of strain. In what follows the standard and electromagnetically modified Launder and Sharma (1974) models are referred to as the LS and LSM model respectively. Similarly, the standard and electromagnetically modified Hanjalić and Jakirlić models are referred to as the HJ and HJM model respectively.

The geometry considered is as per Figure 6.1 where only a wall-normal magnetic field (Hartmann flow) is examined. The parameter ranges considered are $Ha = 0, 4, 6, 8$ at a relatively low Reynolds number of $Re_\tau = 150$, for which comparisons are made against DNS data from Noguchi et al. (2004) and Yamamoto et al. (2008), $Ha = 0, 5, 10, 13.3$ at the moderate bulk Reynolds number of $Re = 6000$ ($Re_\tau \approx 325$), for which comparisons are made against DNS data by Dey and Zikanov (2012), and $Ha = 0, 16.25, 32.5$ at the higher Reynolds numbers of $Re_\tau = 1120, 1150, 1194$ respectively, for which comparisons are made against Satake et al. (2008). Table 6.2 provides a summary of this along with details on the mesh resolution employed. Within the table, the interaction parameter, $N = Ha^2/Re_\tau$ which is the ratio of the Lorentz forces to the inertial forces, is also listed since it provides a means to compare magnetic field strengths across Reynolds numbers.

Performance of the eddy-viscosity approach

At low Re_τ, profiles of Reynolds shear stress ($\overline{uv}^+$) in Figure 6.18 demonstrate that both forms of the model respond qualitatively well to the increase in magnetic field strength. The reduction in shear stress is slightly over-predicted by both at low Ha, with the damping type terms in the LSM model providing a small further reduction. At $Ha = 6$ however, the LSM modification predicts an excessive reduction, with a much lower peak value and a laminar core region. At $Ha = 8$, both models correctly predict relaminarization of the flow in line with the DNS data.

The above behaviour is confirmed from inspection of the corresponding velocity profiles, presented in Figure 6.19. For $Ha = 0$, Figure 6.19 shows that the LS model overpredicts the mass flow rate through the channel, making quantitative agreement with the DNS relatively poor. This is a direct result of an under prediction of the near-wall turbulent shear stress (as can be seen here for $Ha = 0$ in Figure 6.19 and as highlighted earlier in Subsection 6.4.1) since, for a fixed streamwise pressure gradient, this will increase the amount of mass predicted to flow through the channel. As the magnetic field strength

Re_τ	Re	Ha	N_τ	$N_x \times N_y$	DNS data
150	2.3×10^3 (c)	0	0	10×200	Noguchi et al. (2004)
150	2.460×10^3 (c)	4	0.1	10×200	Noguchi et al. (2004)
150	2.460×10^3 (c)	6	0.24	10×200	Noguchi et al. (2004)
150	2.479×10^3 (c)	8	0.42	10×200	Yamamoto et al. (2008)
328.5 (c)	6000	0	0	10×240	Dey and Zikanov (2012)
327.7 (c)	6000	5	0.07	10×240	
326.0 (c)	6000	10	0.3	10×240	
324.8 (c)	6000	13.3	0.5	10×240	
1120	2.3×10^4 (c)	0	0	10×250	Satake et al. (2008)
1150	2.418×10^4 (c)	16.25	0.23	10×260	
1194	2.461×10^4 (c)	32.5	0.88	10×260	

Table 6.2: Summary of RANS simulations performed for turbulent Hartmann flow, where $N_\tau = Ha^2/Re_\tau$. Values with a "(c)" are quantities computed as part of the simulation and, since the computed value is model dependent, are only indicative here.

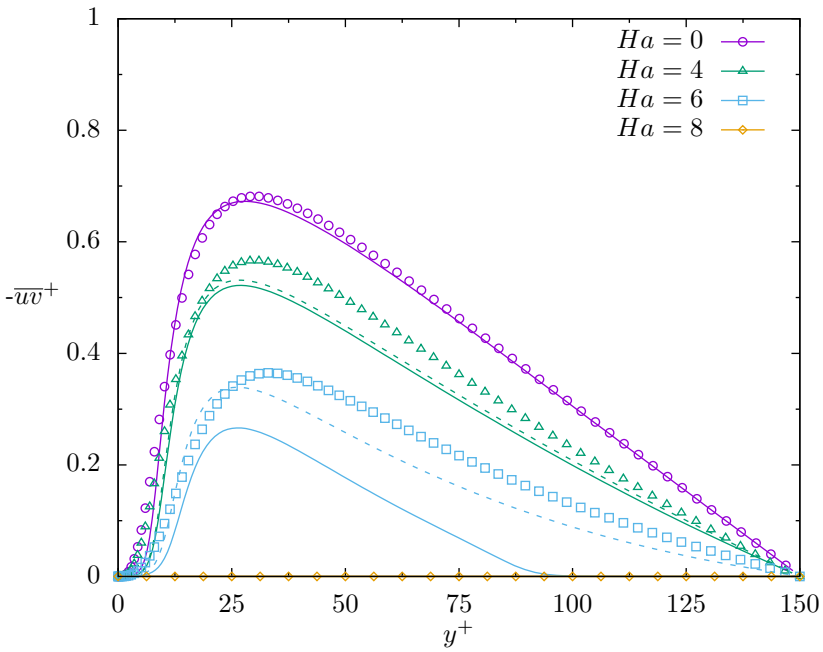

Figure 6.18: Non-dimensional Reynolds shear stress profiles for fully developed channel flow subjected to a wall-normal magnetic field at different Ha. Comparison between LSM model (solid lines), LS model (dashed lines) and DNS (symbols) of Noguchi et al. (2004) for $Ha = 0, 4, 6$ and Yamamoto et al. (2008) for $Ha = 8$; $Re_\tau = 150$.

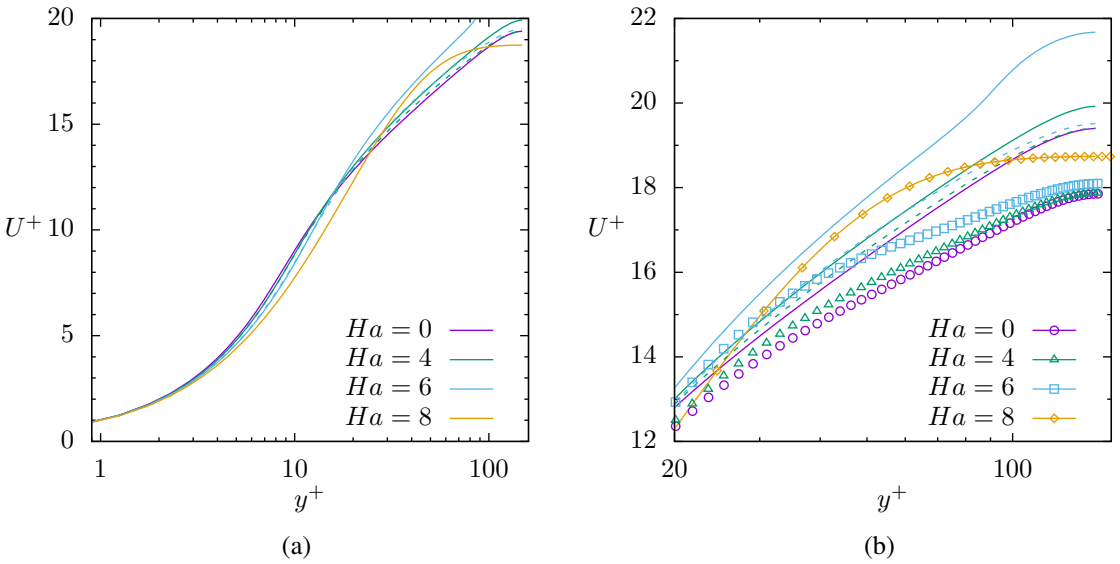

Figure 6.19: Non-dimensional mean velocity profiles for fully developed channel flow subjected to a wall-normal magnetic field at different Ha. (a) Comparison between LSM (solid lines) and LS (dashed lines) models across the full channel, and (b) comparison within the log-law region between LSM (solid lines), LS (dashed lines) and DNS (symbols) of Noguchi et al. (2004) for $Ha = 0, 4, 6$ and Yamamoto et al. (2008) for $Ha = 8$; $Re_\tau = 150$.

increases however, the profiles do show the correct qualitative response. At the start of the logarithmic region (between around $y^+ = 20$ and $y^+ = 30$) a correct mass flow rate would result in better quantitative agreement. The laminar core predicted by the LSM model at $Ha = 6$ is shown by the departure of the profile from typical log-law behaviour and this is clearly not supported by the DNS data. The completely laminar flow predicted at $Ha = 8$, which corresponds to Hartmann's analytical solution presented earlier in Subsection 6.3.1, gives excellent agreement as expected.

The reduction in turbulence levels as the magnetic field strength increases (as implied by both the velocity profiles and turbulent shear stress profiles) is confirmed through examination of the turbulent kinetic energy k^+ and its dissipation rate ε^+, shown in Figure 6.20. The inability of the LS model to reproduce the near-wall peak values in conventional channel flow is well known but quantitative agreement in the core region of the channel is better for $Ha \leq 6$. Against the DNS data, it becomes clear that the LS model already slightly overpredicts the reduction in turbulent kinetic energy afforded by the magnetic field, with the LSM terms providing a substantial further reduction which increases with Ha. The prediction of a laminar core at $Ha = 6$ with the LSM model is clearly shown. For the LS model, the only mechanism which would reduce turbulence levels would be a reduction in the mean wall-normal velocity gradient, which would lead to a reduction in the production term in the k equation. As demonstrated with the laminar flows in Section 6.3, the mean Lorentz force tends to reduce velocity gradients in the centre of the channel and hence this is something that would be expected to be well represented by

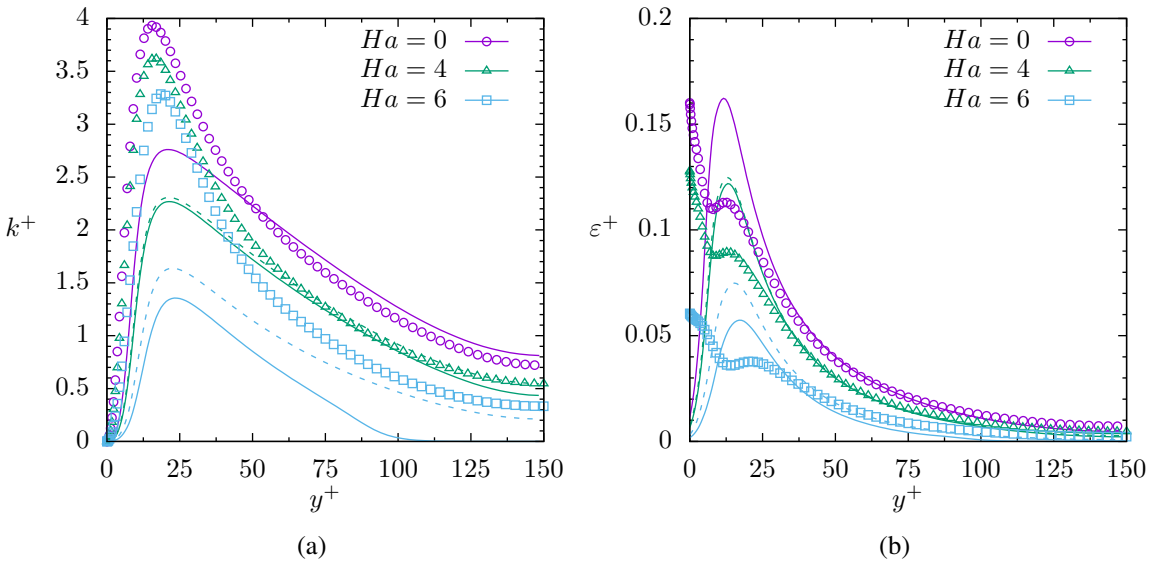

Figure 6.20: Profiles of non-dimensional (a) turbulent kinetic energy and (b) dissipation of turbulent kinetic energy for fully developed channel flow subjected to a wall-normal magnetic field at different Ha. Comparison between LSM (solid lines), LS (dashed lines) and DNS (symbols) of Noguchi et al. (2004); $Re_\tau = 150$.

the unmodified turbulence models. Apart from the laminar predictions for $Ha = 6$ after $y^+ = 100$, agreement for ε^+ is generally good from $y^+ > 50$. Within the near-wall region agreement is worse, but the inability of the LS model in accurately predicting ε here in non-magnetic channel flow is also well documented (see, for example, Craft et al. (2010)). Despite this known deficiency in the LS model, the accuracy and resolution of the DNS data provided by Noguchi et al. (2004) (with which comparisons are made) is not, of course, above scrutiny. This is especially important in comparisons of ε since it comprises the smallest, and therefore most difficult to resolve, scales of motion. However, their solution was achieved using a commonly used high-order spectral method (Chebyshev-tau) and an assessment of the statistics provided in the dataset (including those not presented here) did not arouse any suspicion regarding the accuracy and suitability of the data.

The DNS results at $Re = 6000$, presented by Dey and Zikanov (2012), were computed by fixing the mass flow rate through the channel, rather than the streamwise pressure gradient as was the case with the previous set of DNS data (at $Re_\tau = 150$). To enable easier comparison, the numerical computations were also performed by fixing the mass flow rate. The streamwise pressure gradient now comes out as part of the solution and, since it balances the wall stress, will appear here as quantitative differences in the magnitude of the contribution of the turbulent shear stress across the channel. It is known from the earlier analytical explorations (in Subsection 6.3.1) that the mean Lorentz force acts directly to reduce the centreline velocity, and this reduction increases with Ha. This is accompanied by a corresponding velocity increase in the region adjacent to the boundary layer. As the magnetic field strength increases, Figure 6.21 demonstrates this general effect and shows the LS model predicts a more gradual shift away from the neutral state, towards the

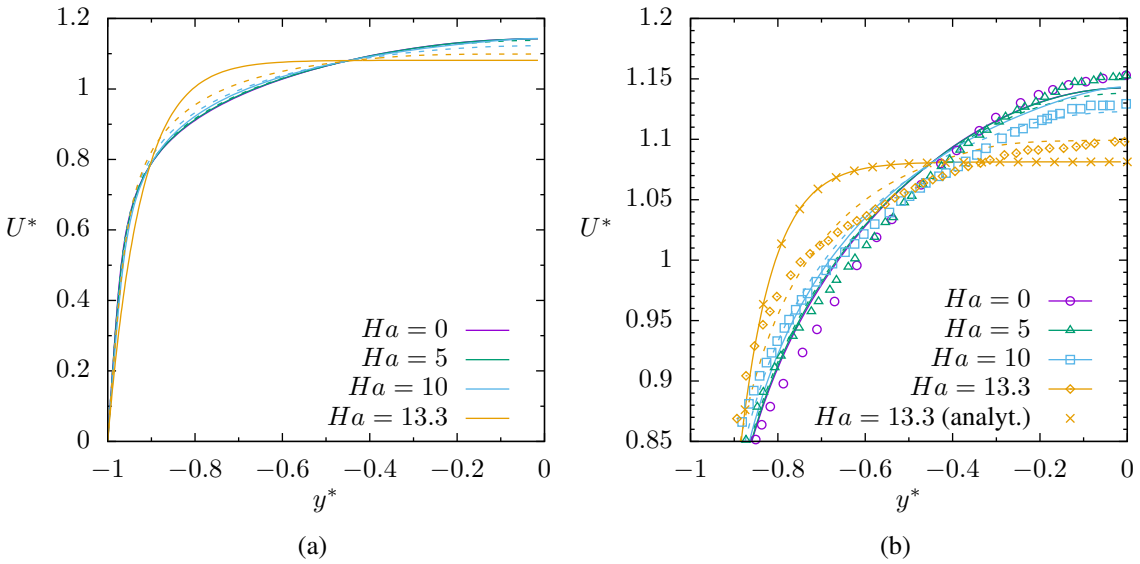

Figure 6.21: Non-dimensional mean velocity profiles for fully developed channel flow subjected to a wall-normal magnetic field at different Ha. (a) Comparison between LSM (solid lines) and LS (dashed lines) models across the full channel, and (b) a blow up of (a) with comparisons between LSM (solid lines), LS (dashed lines) and DNS (symbols) of Dey and Zikanov (2012). The crosses are the analytical solution of Equation (6.3.14) for $Ha = 13.3$; $Re = 6000$ $(Re_\tau \approx 325)$.

(laminar) Hartmann solution, than the LSM model. The latter model does show the same qualitative trend, but the change is much smaller across $0 < Ha < 10$ before jumping, at $Ha = 13.3$, to an entirely laminar solution, as evidenced by the excellent agreement with the analytical solution of Equation (6.3.14) (added to Figure 6.21(b)). This, however, contradicts the DNS results which indicate the flow remains turbulent.

The above observations are supported by Figure 6.22 which presents profiles of $\overline{uv}^*$ and k^*. The DNS data shows that an increase in Ha causes an overall reduction in both of these quantities across the channel, and the response of both the LS and LSM models can be seen to be qualitatively correct. As was seen earlier at the lower $Re_\tau = 150$ (Figures 6.18 and 6.20(a)), the modifications to the k and ε equations as part of the LSM model again provide a further, unnecessary, reduction which reduces quantitative agreement. At the strongest magnetic field considered $(Ha = 13.3)$, both k^* and $\overline{uv}^*$ profiles indicate the LS model predicts a laminar core region which contradicts the DNS data. From the results at $Ha = 0$, it is clear that the LS model under-predicts the contribution of the turbulent shear stress to the total shear stress across the channel. This is consistent with earlier observations for both ordinary channel flow, in Subsection 6.4.1, and for the magnetic results obtained at the lower $Re_\tau = 150$. Given the quantitative differences shown between the profiles in Figure 6.22(a) it appears as though, even if this deficiency in the LS model was corrected, the electromagnetic contributions would still provide an incorrect reduction which may worsen quantitative agreement. The results obtained at the lower $Re_\tau = 150$, where the wall shear stress has been matched, are consistent with this

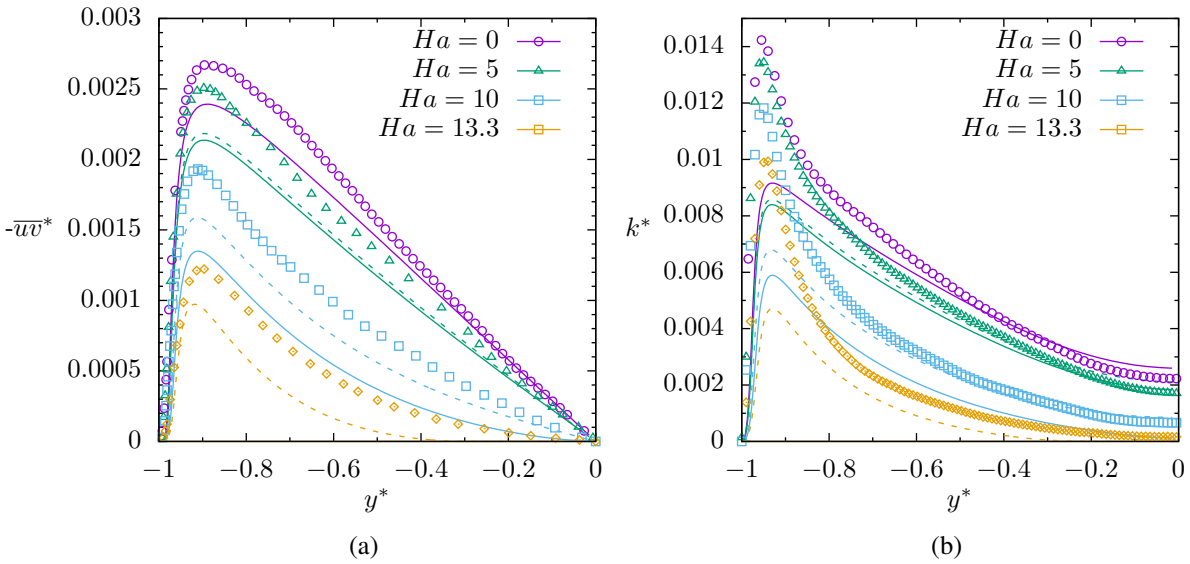

Figure 6.22: Profiles of non-dimensional (a) Reynolds shear stress and (b) turbulent kinetic energy for fully developed channel flow subjected to a wall-normal magnetic field at different Ha. Comparison between LSM (solid lines), LS (dashed lines) and DNS (symbols) of Dey and Zikanov (2012); $Re = 6000$ $(Re_\tau \approx 325)$.

observation.

For the higher Re_τ cases, where the flow is solved by fixing the streamwise pressure gradient, velocity profiles presented in Figure 6.23 again show some differences between the RANS and the DNS in terms of mass flow rate, but do show that the LSM model broadly reproduces the correct qualitative effect. The DNS reports a smaller logarithmic region for the strongest magnetic field $(Ha = 32.5)$, and this is shown to some degree by both the models. At this field strength, the LSM model, however, produces a velocity profile which becomes abruptly flatter in the centre of the channel. Profiles of $\overline{uv}^+$ and k^+, shown in Figure 6.24, demonstrate that this is due to the premature laminarization of the channel core by the additional electromagnetic damping terms in the k and ε equations.

Figure 6.24(a) shows that for $Ha = 32.5$, the LS model actually provides superior predictions of $\overline{uv}$, with the flow remaining turbulent in line with the DNS data. Compared with the lower Reynolds number cases (primarily $Re_\tau = 150$) the magnetic field can be seen to not only cause an overall reduction in the turbulent shear stress across the channel, but to increasingly deform the gradient of it as well. This effect is correctly picked up by the LS model which implies it is almost entirely due to the change in mean strain, rather than the direct damping of the turbulent kinetic energy which the LSM model attempts to incorporate. Predictions of k for this magnetic field strength, shown in Figure 6.24(b), demonstrate that these additional terms do indeed reduce quantitative agreement.

In addition to the effect of the magnetic field on the primary flow variables, Satake et al. (2008) provided profiles of the non-dimensional temperature across the channel for

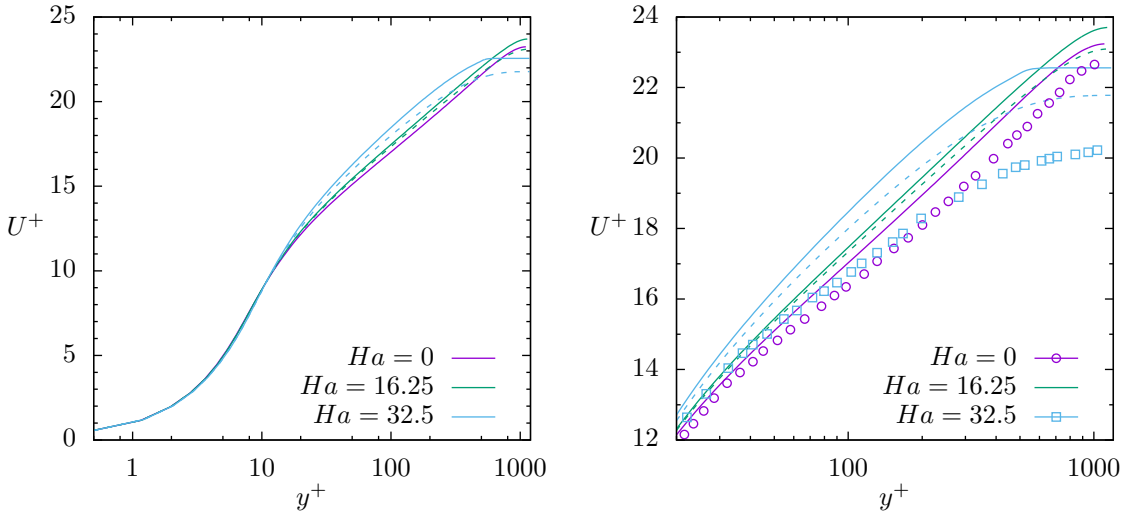

Figure 6.23: Non-dimensional mean velocity profiles for fully developed channel flow subjected to a wall-normal magnetic field at different Ha. (a) comparison between LSM (solid lines) and LS (dashed lines) models across the full channel, and (b) comparison between LSM (solid lines), LS (dashed lines) and DNS (symbols) of Satake et al. (2008) within the log-law region; $Re_\tau \approx 1150$.

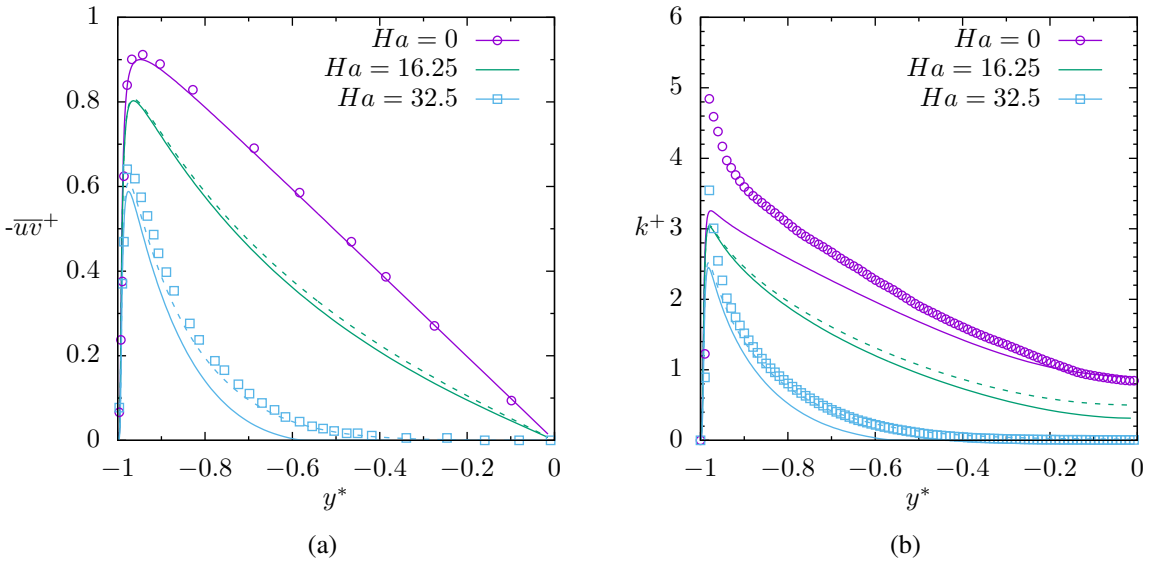

Figure 6.24: Profiles of non-dimensional (a) Reynolds shear stress and (b) turbulent kinetic energy for fully developed channel flow subjected to a wall-normal magnetic field at different Ha. Comparison between LSM (solid lines), LS (dashed lines) and DNS (symbols) of Satake et al. (2008); $Re_\tau \approx 1150$.

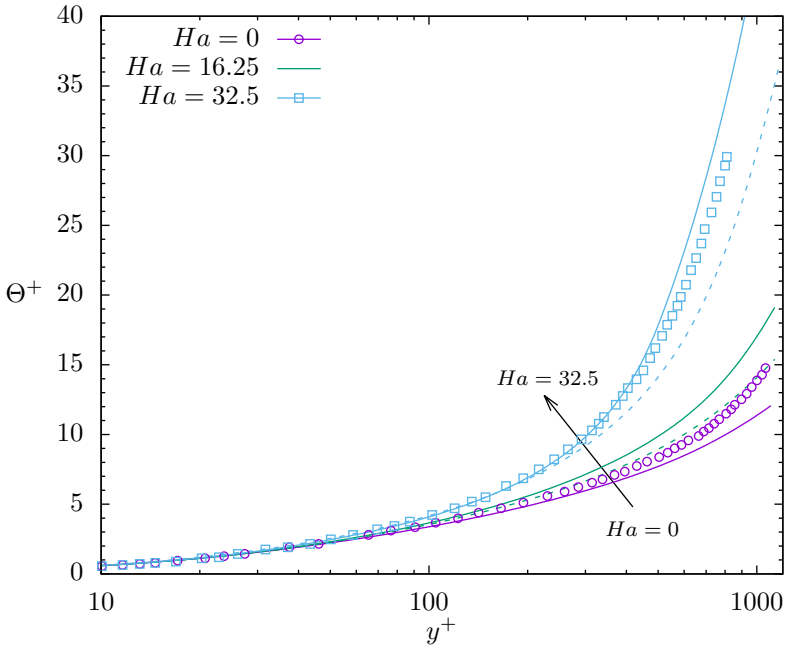

Figure 6.25: Non-dimensional mean temperature profiles for fully developed channel flow subjected to a wall-normal magnetic field at different Ha. Comparison between LSM model (solid lines), LS model (dashed lines) and DNS (symbols) of Satake et al. (2008); $Re_\tau \approx 1150$, $Pr = 0.06$.

$Pr = 0.06$. It was treated as a passive scalar, and thus has no influence on the dynamic fields. Figure 6.25 provides comparisons between their DNS data and predictions by the LS and LSM models, where both provide the correct qualitative response. At $Ha = 32.5$, and contrary to the general picture painted above, the LSM model actually provides better agreement against the DNS.

In the case described above, both the wall and reference temperature are fixed. Thus the higher Θ^+, shown in Figure 6.25, indicates that the magnetic field increases the wall heat flux. Whilst the magnetic field might actually be expected to reduce heat transfer, since the reduction in turbulence that it clearly causes in this case will suppress turbulent mixing (i.e. reduce $\overline{u_i\theta}$), the low Prandtl number used here means that changes to the near-wall mean velocity profile might be expected to be more influential (since the molecular affected thermal layer is much larger than its viscous counterpart). From the velocity profiles in Figure 6.23, it is clear that near-wall velocities do increase as the magnetic field strength increases and this would lead to higher convective heat transfer, and higher values of Θ^+.

Performance of the stress-transport approach

The results from the previous section, which investigated the performance of an electromagnetically extended eddy-viscosity model, showed that for a simple channel flow subjected to a wall normal magnetic field, where the primary effect of the mean Lorentz

force is to destroy the wall normal velocity gradient, the additional source terms in the k and ε equations provided generally unnecessary reductions to the turbulence levels within the channel. There are two main reasons for this. The first is that changes to the wall-normal velocity gradient are readily captured by the production term in the k equation (which is exact) and thus the LS model, without any modification, is able to capture the correct effect, often with surprisingly good quantitative agreement. Second, the form of the additional source terms, as exponential damping functions tied to the local turbulent time-scale, means they can only indirectly take account of the directionality associated with the magnetic field.

With the stress-transport approach, it was seen in Subsection 4.3.2 that inclusion of the fluctuating Lorentz force in the derivation of the $\overline{u_i u_j}$ transport equation produced a source term which comprised two main parts. Only one of these required modelling, and the model used here retains only that exact part, multiplied by a constant. The form of the term, given in Equation (4.3.40), contains contributions from the Reynolds stresses and thus, at least in principle, should be able to take some account of the current state of the stress field.

Figure 6.26 presents profiles of the Reynolds stresses ($\overline{uv}^+$ and the three normal stresses) at the lower $Re_\tau = 150$. As before, the DNS results show that the primary effect of the magnetic field is to reduce the magnitude of all the stress components (though not by equal amounts) and both forms of the RSM can be seen to give good qualitative agreement. For the shear stress $\overline{uv}^+$, quantitative agreement is good for $Ha = 0$, with a slight overprediction below $y^+ \approx 20$ at $Ha = 4$ and more significant overprediction at $Ha = 6$ with a noticeable misplaced peak. Similar misplaced peaks are also seen at this Hartmann number in the profiles of the wall-normal ($\overline{vv}^+$) and spanwise ($\overline{ww}^+$) normal stresses, where the DNS indicates the peaks shift slightly towards the centre of the channel; something which, in the case of $\overline{ww}^+$, the model does not reproduce, and predicts the reverse for in the case of $\overline{vv}^+$. For $\overline{ww}^+$, whilst quantitative agreement with the DNS is poor, this can be seen to be predominantly due to an overprediction in the neutral state as the predicted change in behaviour with increasing Ha is qualitatively correct.

In the near-wall region there are some notable differences in the behaviour of the normal stresses. The streamwise component $\overline{uu}^+$ appears much less affected by the magnetic field than the other two components, which see significant changes. In general, the additional electromagnetic terms provided by the HJM model appear to have an insignificant effect at lower Ha for both $\overline{uv}^+$ and $\overline{uu}^+$ but do result in some, qualitatively correct, differences in $\overline{vv}^+$ and $\overline{ww}^+$ at the higher Ha. Both forms of the model correctly predict laminar flow at $Ha = 8$ (not shown).

The mechanism by which these stress components are reduced can be deduced from the considering the various terms in the $\overline{u_i u_j}$ transport equations. In a simple shear flow

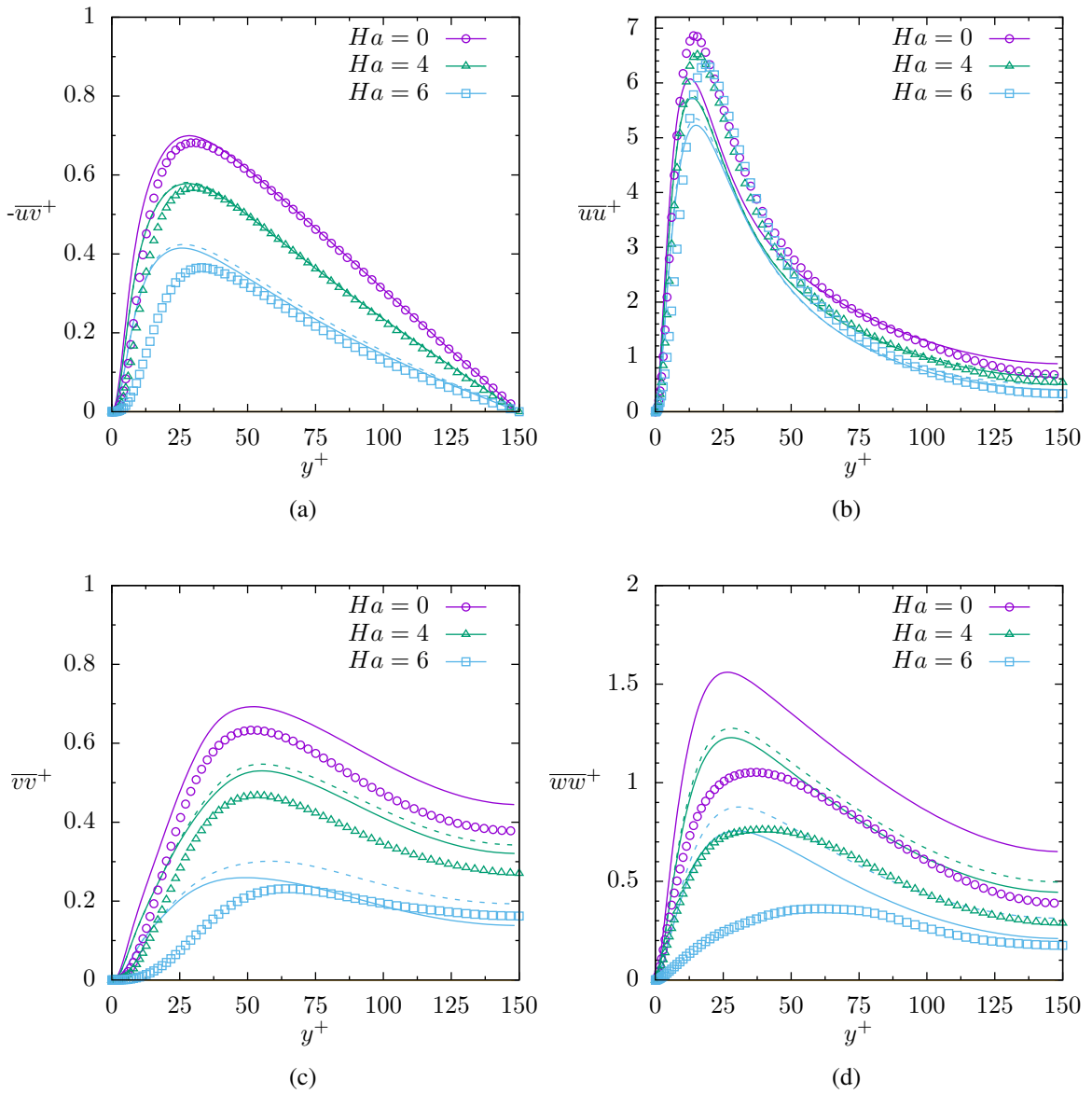

Figure 6.26: Non-dimensional Reynolds stress profiles for fully developed channel flow subjected to wall-normal magnetic field at different Ha. Comparison between HJM model (solid lines), HJ model (dashed lines) and DNS (symbols) of Noguchi et al. (2004); $Re_\tau = 150$.

such as this the only non-zero production terms in the $\overline{u_i u_j}$ equation are those containing the mean wall-normal velocity gradient $\partial U/\partial y$. Thus, the production terms for both the $\overline{vv}$ and $\overline{ww}$ equations will vanish and the primary contribution to the budgets for these components is the pressure strain effect. This pulls turbulent energy from the dominant $\overline{uu}$ component and redistributes it into the smaller $\overline{vv}$ and $\overline{ww}$ components in an attempt to return the stress field to isotropy. In the RSM considered here, this is modelled through the rapid part of the pressure-strain term (through the isotropization of production model used for $\Phi_{ij}^{(2)}$, see Equation (4.3.41)). Thus, since the magnetic field causes a reduction in $\overline{uu}$ through directly reducing the level of its production, this will result in less $\overline{uu}$ available for redistribution and subsequently cause a reduction in levels of $\overline{vv}$ and $\overline{ww}$. In

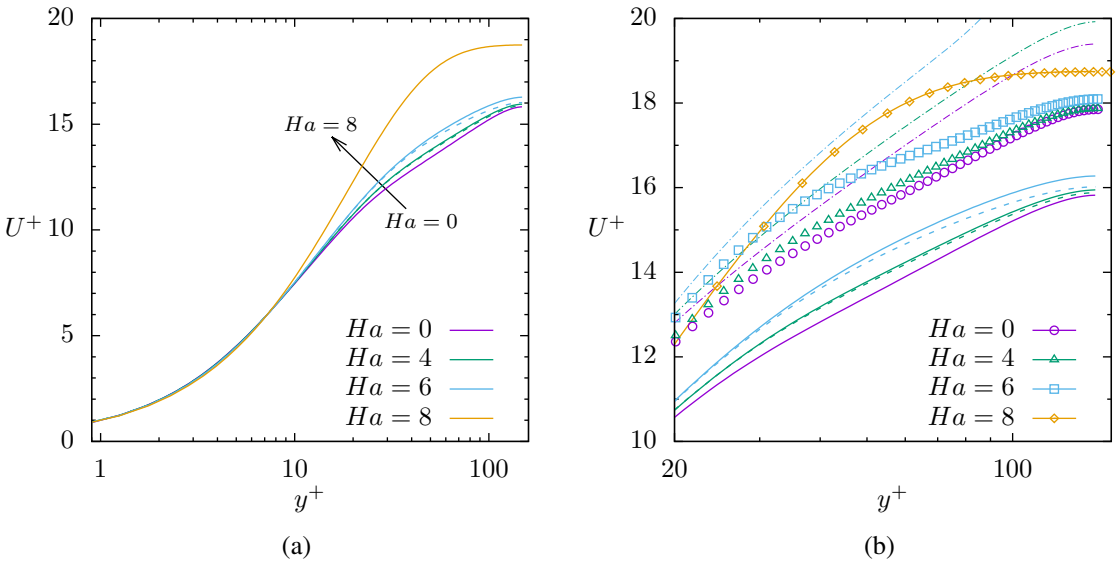

Figure 6.27: Non-dimensional mean velocity profiles for fully developed channel flow subjected to a wall-normal magnetic field at different Ha. (a) Comparison between HJM (solid lines) and HJ (dashed lines) models across the full channel, and (b) comparison within the log-law region between HJM (solid lines), HJ (dashed lines), LSM (dot dashed lines) and DNS (symbols) of Noguchi et al. (2004) for $Ha = 0, 4, 6$ and Yamamoto et al. (2008) for $Ha = 8$; $Re_\tau = 150$.

addition, a reduction in mean shear will also directly reduce the production term in the $\overline{uv}$ equation (since it also contains $\partial U/\partial y$). This, by reducing the magnitude of $\overline{uv}$, will also contribute directly to the reduction of the production term in $\overline{uu}$ (since it multiplies the mean velocity gradient) and indirectly to the reduction of $\overline{vv}$ and $\overline{ww}$ (through a reduction of the pressure-strain term).

The contributions from the additional electromagnetic terms, as far as the HJM model goes, are relatively modest. That said, the modelled contributions to $\mathcal{F}^L_{ij}$ can be readily obtained via Equation (4.3.40) and for a wall-normal magnetic field are given in non-dimensional form as;

$$\mathcal{F}^L_{uu} = -2N\,(1 - C_\lambda)\,\overline{uu}^+ \tag{6.4.1a}$$

$$\mathcal{F}^L_{vv} = 0 \tag{6.4.1b}$$

$$\mathcal{F}^L_{ww} = -2N\,(1 - C_\lambda)\,\overline{ww}^+ \tag{6.4.1c}$$

$$\mathcal{F}^L_{uv} = -N\,(1 - C_\lambda)\,\overline{uv}^+ \tag{6.4.1d}$$

It can be seen that the contribution in the direction of the magnetic field, $\mathcal{F}^L_{vv}$, is zero and this is regardless of the strain field which exists. The other components are attenuated in proportion to themselves. Hence, it can be seen that the magnetic field acts on the Reynolds stresses in a highly anisotropic fashion.

Figure 6.27 shows the corresponding velocity profiles along with a blow-up of the log-law region. As the magnetic field strength is increased, the departure of the velocity profile

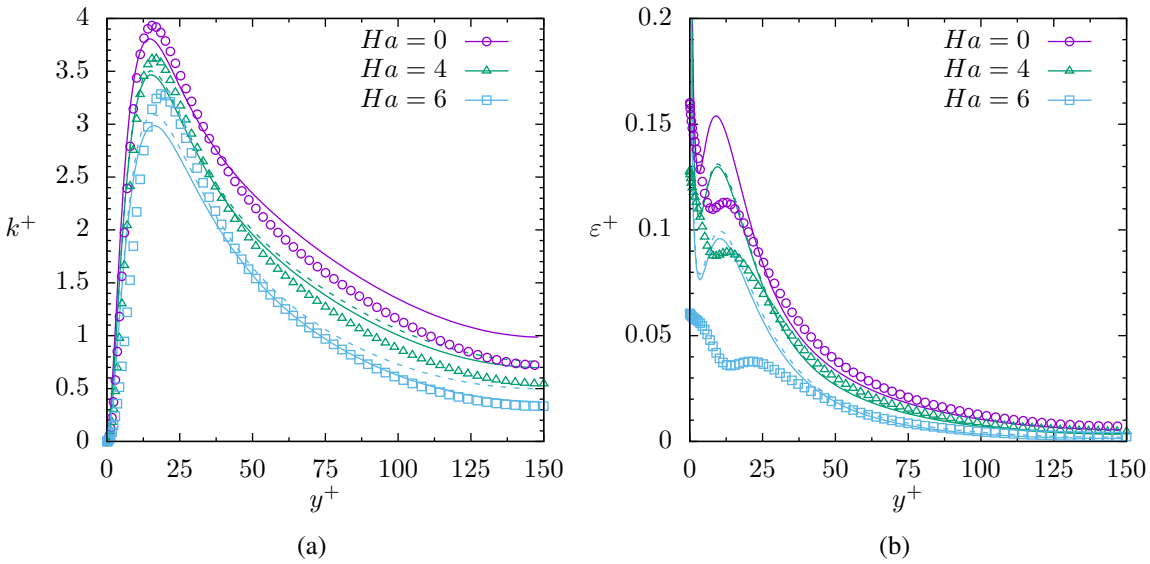

Figure 6.28: Profiles of non-dimensional (a) turbulent kinetic energy and (b) dissipation of turbulent kinetic energy for fully developed channel flow subjected to a wall-normal magnetic field at different Ha. Comparison between HJM (solid lines), HJ (dashed lines) and DNS (symbols) of Noguchi et al. (2004); $Re_\tau = 150$.

from typical log-law shape is qualitatively picked up by the HJM model and, taking into account the under prediction in mass flow rate seen by the base HJ model at $Ha = 0$ (which was also noted in Subsection 6.4.1), the correct quantitative changes in the velocity profile behaviour are predicted. Comparisons with the LSM model (dot dashed lines in Figure 6.27(b)), show that the performance of the RSM is, taking into account the differences in mass flow rate, significantly better and provides a much more accurate representation of the deformation in the velocity profile that the Lorentz force creates.

Profiles of k^+ and ε^+ are provided in Figure 6.28. The electromagnetic modifications in the HJM model have very little influence on the distribution of ε^+, only providing a very minor, albeit correct, reduction to the near-wall peak at $Ha = 6$. Beyond $y^+ = 50$, both forms of the RSM provide good agreement with the DNS data for $Ha = 0, 4$, though this does not offer any substantial improvement over the EVM. Where the RSM does provide improvement, is in the prediction of turbulent flow throughout the domain for $Ha = 6$ (which is correct, as indicated by the DNS). This is something that was not achieved with the LSM model (see Figure 6.20(a), for example).

Further comparisons of model performance are provided in Figure 6.29 for the $Ha = 6$ case. The significant improvement afforded by the base RSM, in regards to k^+ in particular, is not entirely surprising; a stress-transport type model should in many cases be expected to provide better predictions of the stresses (and hence k) than an EVM, because of the correct representation of generation and other processes. The additional electromagnetic terms in the LSM model, which provide a more ad-hoc form of damping than

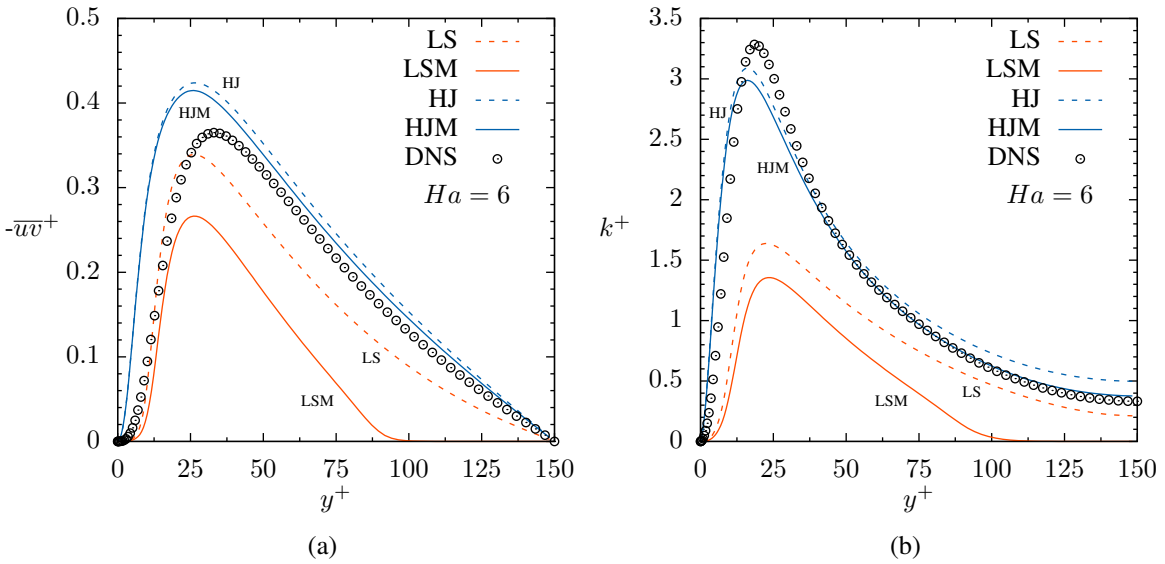

Figure 6.29: Performance of stress-transport and eddy-viscosity type models both with (solid lines) and without (dashed lines) electromagnetic modifications for fully developed channel flow subjected to a wall-normal magnetic field at $Ha = 6$. (a) profiles of non-dimensional turbulent shear stress $(\overline{uv}^+)$ and (b) profiles of non-dimensional turbulent kinetic energy (k^+). DNS data of Noguchi et al. (2004); $Re_\tau = 150$

those employed in the HJM model, significantly over predict the reduction in turbulence levels and lead to premature relaminarization in the centre of the channel.

In the near-wall region, however, it can be seen that the eddy-viscosity based models offer much better predictions of $\overline{uv}^+$ than the stress-transport models. This does not extend to k^+ and, as will be seen later, is only apparent in the very low Reynolds number case considered here $(Re_\tau = 150)$. Particularly good quantitative agreement is provided for k^+ by the HJM model outside the near-wall region, where the additional terms bring centreline values of k^+ down in line with the DNS data (although the near-wall peak values are slightly under-estimated). Again, the small difference that the HJM model provides over the HJ model suggests that the reduction in $\overline{uv}^+$ and k^+ from the presence of the magnetic field originates mainly from the deformed mean rate of strain, caused by the Lorentz force term in the streamwise mean momentum equation, rather than any substantial direct electromagnetic sink term in the transport equations for $\overline{u_i u_j}$ or ε.

To investigate this further, Figure 6.30 presents budgets of the k, $\overline{uv}$ and $\overline{uu}$ equations and Figure 6.31 presents budgets of the $\overline{vv}$ and $\overline{ww}$ equations[1], as obtained from the DNS database of Noguchi et al. (2004), for $Ha = 0$ and $Ha = 6$. For the magnetic cases, the total magnetic source term 'mhdtot' and the two contributions towards it, 'mhd1' and 'mhddiss', have also been plotted for each equation. With the k equation, 'mhd1' corresponds to $\mathcal{F}_k^{L1}$ and 'mhddiss' corresponds to $\mathcal{F}_k^{L2}$ as defined in Equation (4.4.14).

[1]The rationale behind plotting k, $\overline{uv}$ and $\overline{uu}$ in the figure (as opposed to $\overline{uu}$, $\overline{vv}$, $\overline{ww}$ in one figure, as may seem more conventional) is that the former all have non-zero production, and it is this which is the subject of discussion.

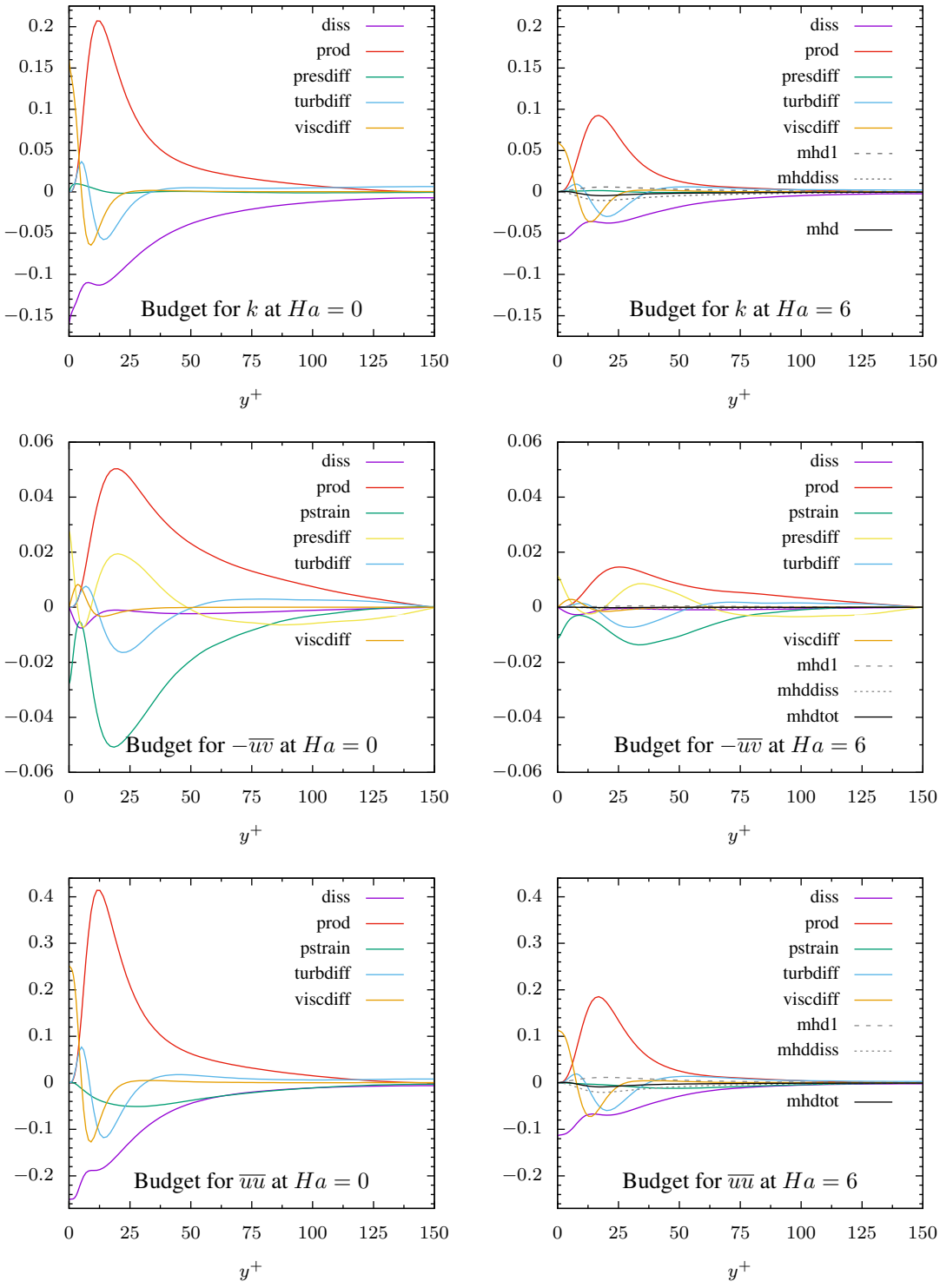

Figure 6.30: Budgets of terms in the k, $\overline{uv}$ and $\overline{uu}$ equations for (left) $Ha = 0$ and (right) $Ha = 6$ as provided in the DNS database of Noguchi et al. (2004) for fully developed channel flow at $Re_\tau = 150$ subjected to a wall-normal magnetic field.

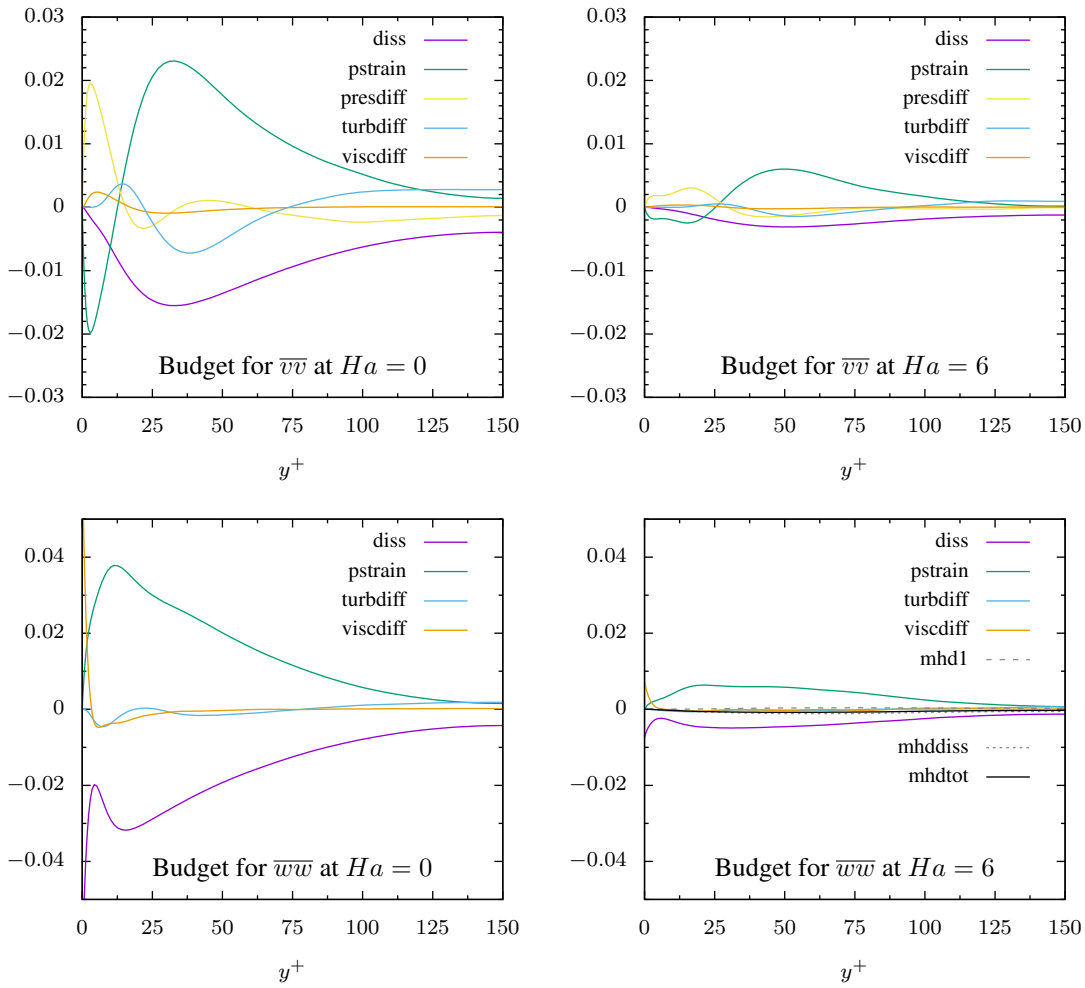

Figure 6.31: Budgets of terms in the $\overline{vv}$ and $\overline{ww}$ equations for (left) $Ha = 0$ and (right) $Ha = 6$ as provided in the DNS database of Noguchi et al. (2004) for fully developed channel flow at $Re_\tau = 150$ subjected to a wall-normal magnetic field.

For the terms in the Reynolds stress budgets, 'mhd1' corresponds to $\mathcal{F}_{ij}^{L1}$ and 'mhddiss' corresponds to $\mathcal{F}_{ij}^{L2}$ as defined in Equation (4.3.11).

In a simple shear flow such as this, where the only non-zero mean velocity gradient is in the wall-normal direction, the production term (see equation 4.3.4) in the $\overline{u_i u_j}$ transport equation will only be non-zero for the $\overline{uu}$ and $\overline{uv}$ components (and, by extension, for the k equation). For the k, $\overline{uu}$ and $\overline{uv}$ equations then, the effect of the magnetic field on the production term is clear. It primarily acts to reduce the production term (via a reduction in mean velocity gradient) which is accompanied by a corresponding reduction in dissipation. Even with this reduction, the production and dissipation terms still dominate over the contribution from the magnetic source term. This confirms previous observations that the mechanism by which the magnetic field acts to reduce turbulence in a simple shear flow is through reduction in mean strain, rather than any substantial direct electromagnetic effect on the turbulence itself.

The budgets for $\overline{vv}$ and $\overline{ww}$ (in Figure 6.31) illustrate that, in lieu of production, turbulent energy indeed feeds into these components through the pressure-strain effect. As detailed

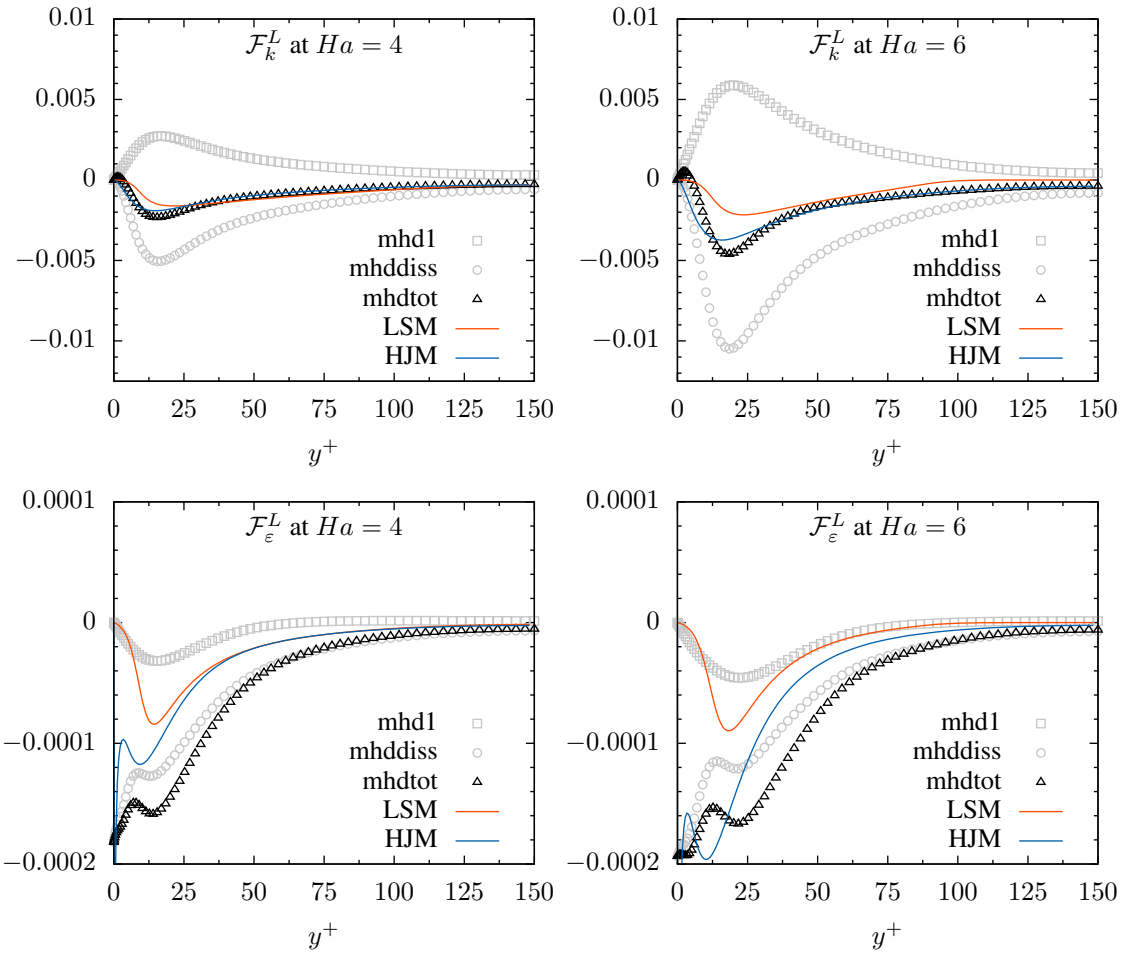

Figure 6.32: Contributions from the additional electromagnetic source terms $\mathcal{F}_k^L$ (top) and $\mathcal{F}_\varepsilon^L$ (bottom) to the budgets of k and ε respectively for turbulent Hartmann flow at (left) $Ha = 4$ and (right) $Ha = 6$. Comparisons between DNS (symbols) of Noguchi et al. (2004) and numerical simulations (solid lines). For the DNS terms, 'mhdtot' represents the total contribution to the budget with 'mhd1' representing the $L1$ contribution and 'mhddiss' representing the $L2$ contribution as per Equations (4.3.43) and (4.4.14); $Re_\tau = 150$.

in Section 4.3, the Lorentz force will influence this process since the fluctuating Lorentz force appears in the equation for the fluctuating pressure. Unfortunately, Noguchi et al. do not provide details of this contribution to the overall pressure strain effect so its influence cannot be assessed. What is apparent, is that the magnetic field significantly reduces the contribution of the pressure strain term to the overall budget and this is due to the large reduction seen in the magnitude of $\overline{uu}$ production. Note also that, as Equation (6.4.1) shows, the contribution from the direct magnetic source terms to the $\overline{vv}$ equation, is zero.

Despite not forming a significant part of the Reynolds stress budgets, the data from the DNS database provides values for the terms which the electromagnetic modifications are attempting to emulate and thus this can be used to further assess their performance. Figure 6.32 presents the contributions of $\mathcal{F}_k^L$ and $\mathcal{F}_\varepsilon^L$ to the budgets of k and ε respectively, both from the DNS data and the modelled forms from the results of the RANS simula-

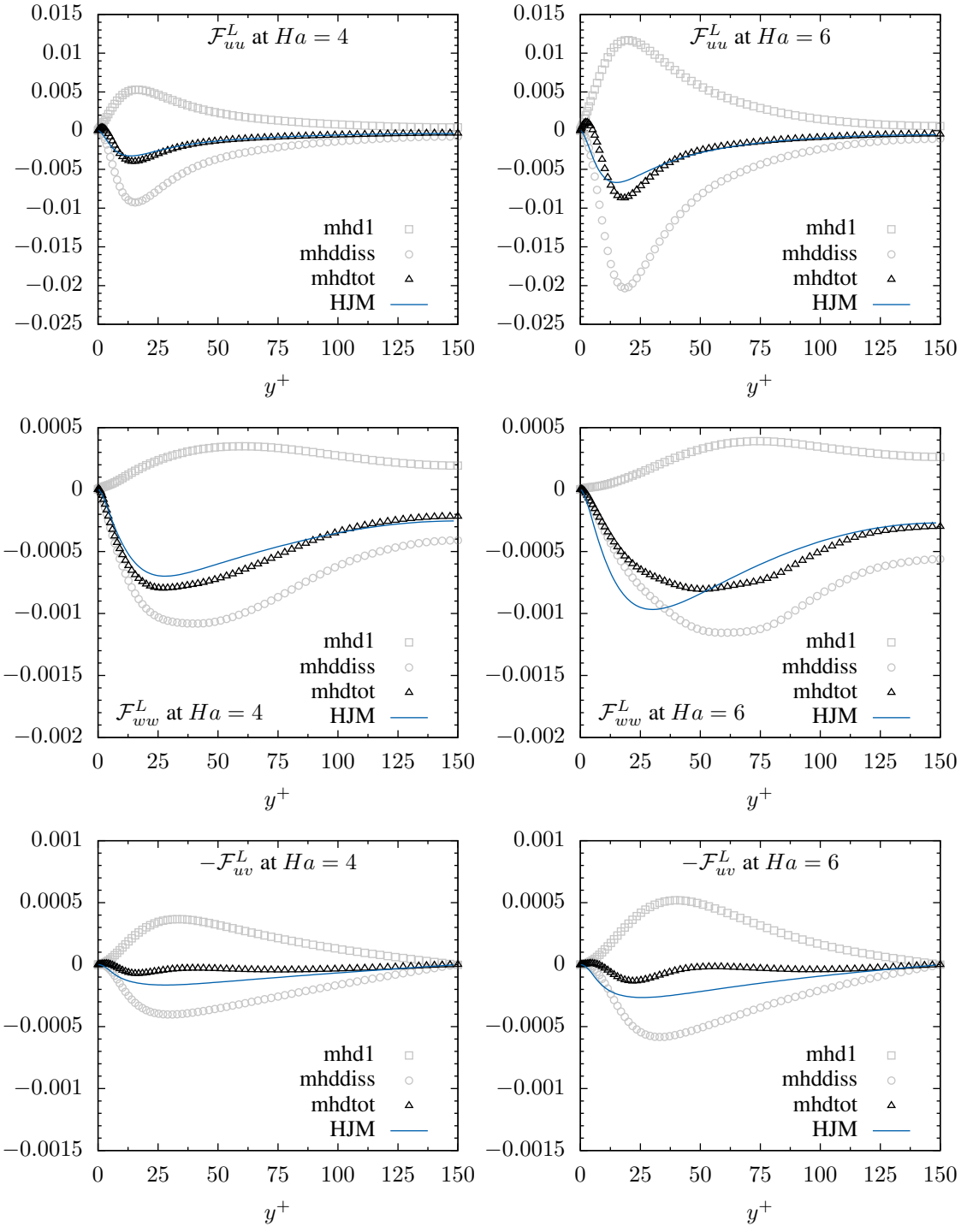

Figure 6.33: Contributions from the additional electromagnetic source terms, from top to bottom, $\mathcal{F}^L_{uu}$, $\mathcal{F}^L_{ww}$ and $\mathcal{F}^L_{uv}$ to their respective budgets for turbulent Hartmann flow at (left) $Ha = 4$ and (right) $Ha = 6$. Comparisons between DNS (symbols) of Noguchi et al. (2004) and numerical simulations (solid lines). For the DNS terms, 'mhdtot' represents the total contribution to the budget with 'mhd1' representing the $L1$ contribution and 'mhddiss' representing the $L2$ contribution as per Equation (4.3.11); $Re_\tau = 150$.

tions.

The HJM model provides superior predictions for $\mathcal{F}_k^L$ for both Ha values, though this is not particularly surprising, given that the HJM form of $\mathcal{F}_k^L$ still retains the majority of its exact counterpart. At $Ha = 6$ the peak is slightly misplaced but agreement throughout the central section of the channel is excellent. The LSM form of $\mathcal{F}_k^L$, which was based on an exponential damping term, still provides reasonable agreement at $Ha = 4$ (though it under predicts the dip at $y^+ \approx 20$) but fails to respond adequately to the increase in field strength at $Ha = 6$. Both models under predict the value of $\mathcal{F}_\varepsilon^L$ across the channel for $Ha = 4$, with the HJM model providing better quantitative agreement. With the increase in magnetic field strength, the LSM fails to respond (as it did with $\mathcal{F}_L^k$), but the HJM provides good agreement. The heavy underestimation of $\mathcal{F}_\varepsilon^L$ throughout the region $0 < y^+ < 50$ by the LSM model corresponds to the location of the near-wall peak in $\overline{uv}^+$ (see Figure 6.29) and, since in an LEVM $\overline{uv} \propto k^2/\varepsilon$, an underestimated sink term for ε would cause an over prediction of ε and hence an under prediction of $\overline{uv}$.

Similar plots of the contributions to selected components of the Reynolds stress equations have been presented in Figure 6.33. The HJM form of $\mathcal{F}_{ij}^L$ can be seen to give generally good agreement with the DNS data with the only real major discrepancy being an over-prediction of the magnitude of $\mathcal{F}_{uv}^L$ between $0 < y^+ < 100$. Notably, all the terms act as sinks across the channel, which is correctly reproduced by the HJM model.

Moving on to the moderate Reynolds number of $Re = 6000$ ($Re_\tau \approx 325$), predictions of $\overline{uv}$ and the three normal stresses are presented in Figure 6.34. Since, as described before, the mass flow rate for the flows at this Reynolds number is fixed, differences in the predicted streamwise pressure gradient required to drive the flow manifest as differences in the wall-shear stress (and hence change the magnitude of the turbulent contribution to the overall shear stress in the channel). Whilst the EVM's tended to slightly under-predict the streamwise pressure gradient, the RSM's give a significant over prediction. Taking into account this difference at $Ha = 0$, both forms of the model predict the correct qualitative effect (a reduction in all stress levels across the channel, though this is not by equal amounts). The electromagnetic modifications in the HJM model only offer modest changes which, although they increase with Ha, do not alter the shape of the profiles.

Velocity profiles for $Re = 6000$ are shown in Figure 6.35, where it can be seen that the HJM offers essentially no difference over the HJ model. Given the modest changes that the electromagnetic terms were seen to cause in the Reynolds stress profiles this is not surprising. Figure 6.35(b) shows a blow up of the velocity profiles and adds results from the LSM model (presented earlier) for comparison. The RSM does give better quantitative agreement and predicts the change in the profile, as the Hartmann number increases, to be more gradual, which is in line with the DNS data.

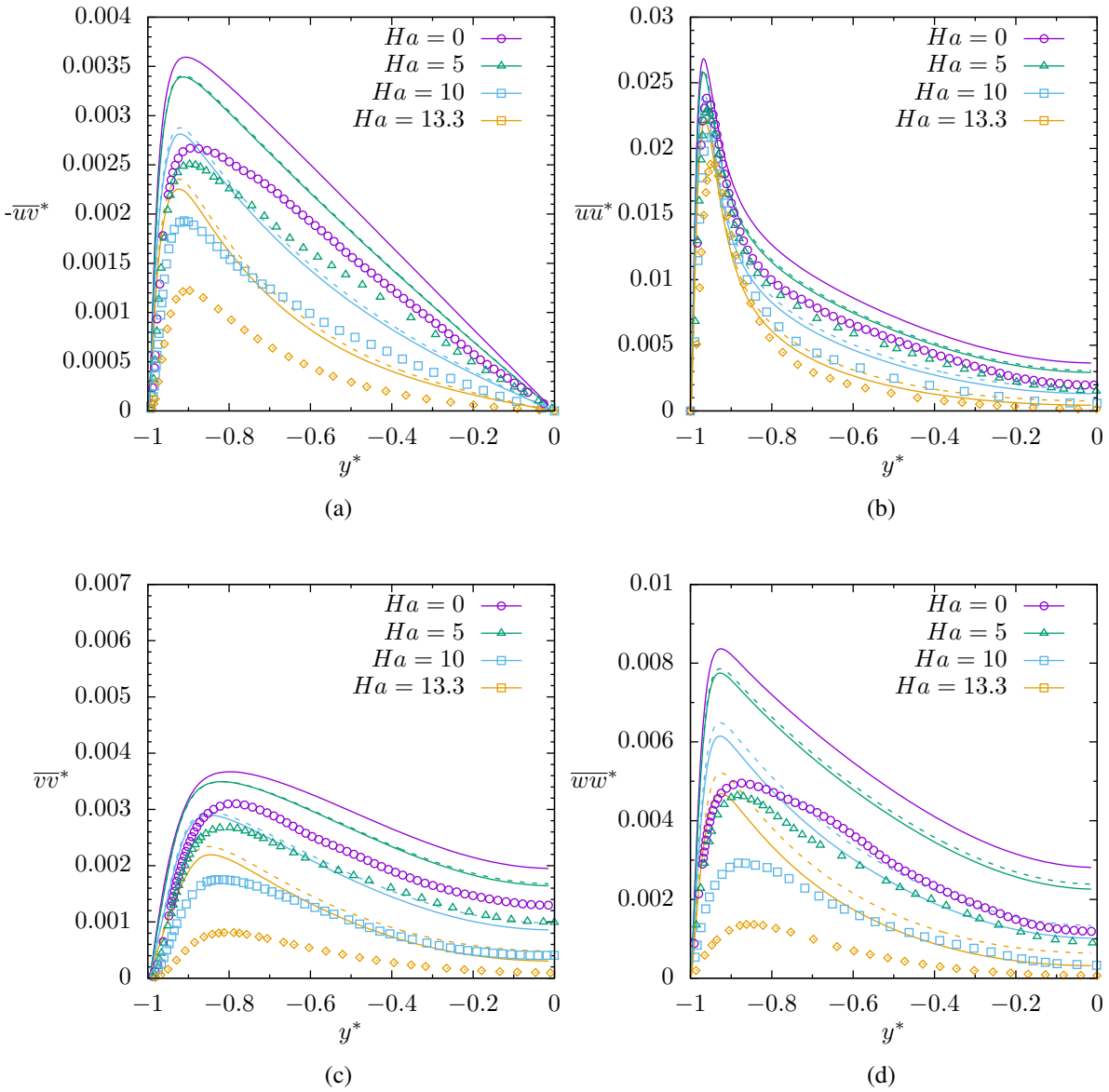

Figure 6.34: Non-dimensional Reynolds stress profiles for channel flow subjected to wall-normal magnetic field at different Ha. Comparison between HJM model (solid lines), HJ model (dashed lines) and DNS (symbols) of Dey and Zikanov (2012); $Re = 6000$ ($Re_\tau \approx 325$).

Further comparisons between the performance of the two approaches are provided in Figure 6.36 where profiles of $\overline{uv}^*$ and k^* have been plotted at $Ha = 10$ and for all models tested. As previously discussed, since the different models predict different values of wall shear stress it is difficult to provide a direct comparison of the electromagnetic contributions within the LSM and HJM models. Both modifications cause an additional reduction in $-\overline{uv}^*$, the one in the LSM model being much more significant, but since the LS model predicts a much lower value of wall shear stress this only serves to reduce quantitative agreement with the DNS further. A similar trend is apparent when considering the distribution of k^* in Figure 6.36(b). In the centre of the channel the LS model gives the best agreement with the DNS data, but fails to capture the near-wall peak. The HJ and HJM

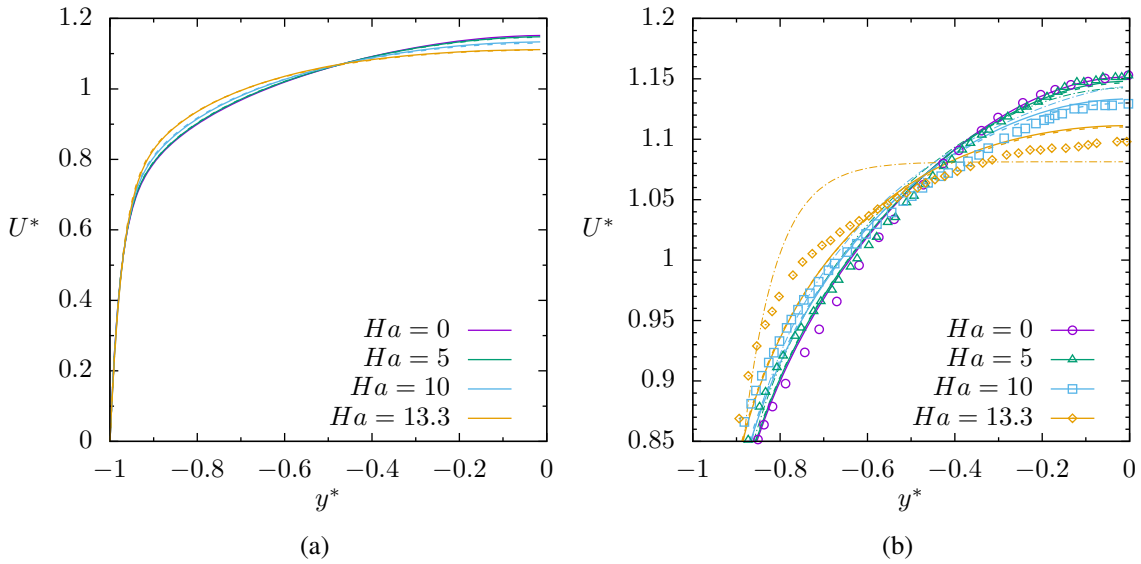

Figure 6.35: Non-dimensional mean velocity profiles for fully developed channel flow subjected to a wall-normal magnetic field at different Ha. (a) Comparison between HJM (solid lines) and HJ (dashed lines) models across the full channel, and (b) a blow up of (a) with comparisons between HJM (solid lines), HJ (dashed lines), LSM (dot-dashed lines) and DNS (symbols) of Dey and Zikanov (2012); $Re = 6000$ $(Re_\tau \approx 325)$.

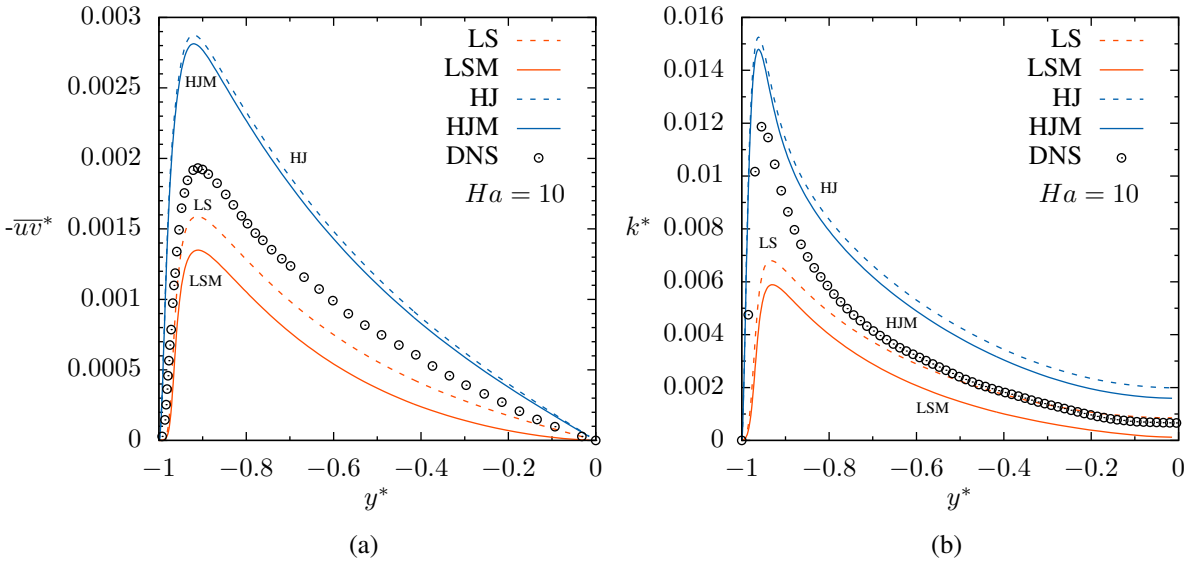

Figure 6.36: Performance of stress-transport and eddy-viscosity type models both with (solid lines) and without (dashed lines) electromagnetic modifications for fully developed channel flow subjected to a wall-normal magnetic field at $Ha = 6$. (a) profiles of non-dimensional turbulent shear stress $(\overline{uv}^+)$ and (b) profiles of non-dimensional turbulent kinetic energy (k^+). DNS data from Dey and Zikanov (2012); $Re = 6000$ $(Re_\tau \approx 325)$.

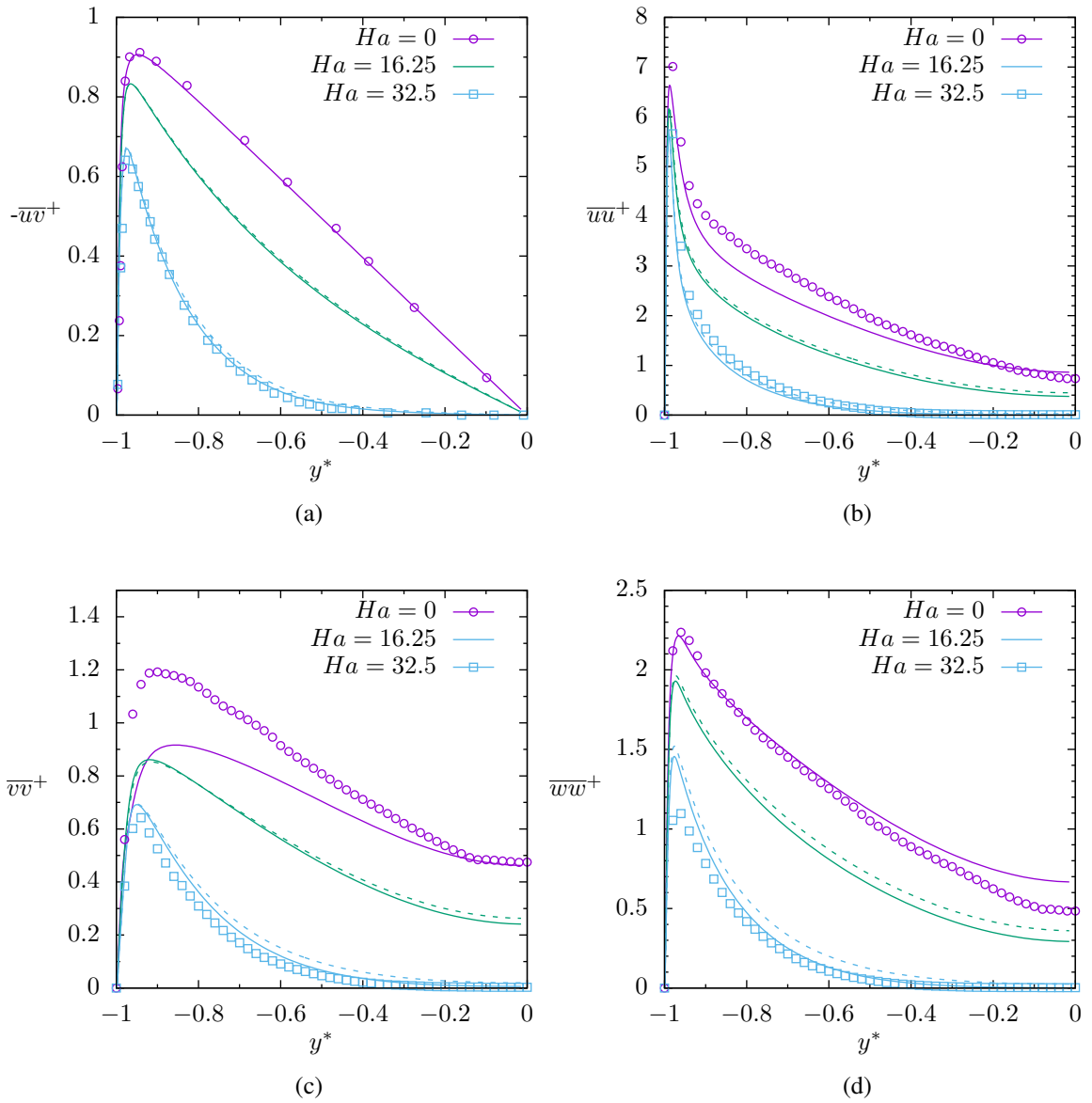

Figure 6.37: Non-dimensional Reynolds stress profiles for fully developed channel flow subjected to wall-normal magnetic field at different Ha. Comparison between HJM model (solid lines), HJ model (dashed lines) and DNS (symbols) of Satake et al. (2008); $Re_\tau \approx 1150$.

models do much better in this regard, but over predict the value of k across the channel.

For the highest Reynolds number considered ($Re_\tau \approx 1150$) Figure 6.37 presents profiles of the turbulent shear stress and three normal stresses. These again illustrate the general effect of the magnetic field is to reduce the level of turbulence but, in addition to this general reduction, the Lorentz force clearly causes significant deformation in the gradients of the stress components outside the near-wall region. This was seen before in the lower Re cases, at the higher Ha (see Figure 6.26(a) and Figure 6.34(a), for example) but is much more significant at the higher values of Re_τ and Ha considered here.

The addition of the Lorentz force to the governing equation means it now forms a significant part of the overall forcing (Lorentz force + viscous stress + turbulent shear stress)

which opposes the pressure gradient driving the flow. The strength of this "magnetic stress" can be quantified by inspection of the non-dimensional form of the equation of motion. For the case here, where no electric field exists (because the simulation is one-dimensional), the RANS equivalent of Equation (6.3.5) is given by;

$$\frac{\partial P^*}{\partial x^*} = \frac{\partial}{\partial y^*}\left(\frac{1}{Re}\frac{\partial U^+}{\partial y^*} - \overline{uv}^+\right) - \frac{Ha^2}{Re}U^+ \tag{6.4.2}$$

where the velocity has been rescaled with the friction velocity. This can be recast as;

$$\frac{\partial P^*}{\partial x^*} = \frac{\partial \tau^+}{\partial y^*} \tag{6.4.3}$$

where τ^+ is the total shear stress;

$$\tau^+ = \underbrace{\frac{1}{Re_\tau}\frac{\partial U^+}{\partial y^*}}_{\text{viscous}} - \underbrace{\overline{uv}^+}_{\text{turbulent}} \underbrace{- N_\tau \int_{-1}^{+1} U^+ \, \mathrm{d}y^*}_{\text{magnetic}} \tag{6.4.4}$$

and $N_\tau = Ha^2/Re_\tau$ is the magnetic interaction parameter. Thus, as N_τ increases, the magnetic contribution to the total shear stress increases at the expense of the turbulent contribution (since the viscous contribution is negligible outside the near-wall sublayer).

Figure 6.37 shows that this is correctly picked up by both forms of the RSM, where at $Ha = 32.5$ agreement with the DNS is excellent and the additional electromagnetic terms provide small, but useful, contributions. The small magnitude of these contributions is consistent with earlier observations that the primary influence of the magnetic field in these flows is to destroy mean velocity gradients; something which is well represented in RSM type models.

The velocity profiles presented in Figure 6.38 again show some inconsistencies between the models in terms of predicted mass flow rates, but the qualitative effects are generally well reproduced. The smaller logarithmic region predicted at the strongest magnetic field is in agreement with the DNS data. Comparisons with the LSM model, presented in Figure 6.38(b), show that the RSM approach provides better prediction of the change in the velocity profile that an increase in magnetic field strength, from $Ha = 0$ to $Ha = 32.5$, brings. For $Ha = 32.5$ this is mostly since the RSM predicts turbulent flow throughout the channel. Curiously, the profile predicted by the HJM model at the intermediate magnetic field strength, for which DNS data was not available, offers no change in centreline velocity from the non-magnetic case.

Further comparisons between all the considered models are provided in Figure 6.39, where profiles of $\overline{uv}^+$ and k^+ are presented at the highest Ha. All except the LSM model perform well, with the HJM model providing the best quantitative agreement. The performance of the LSM is particularly poor, signifying that the additional damping terms

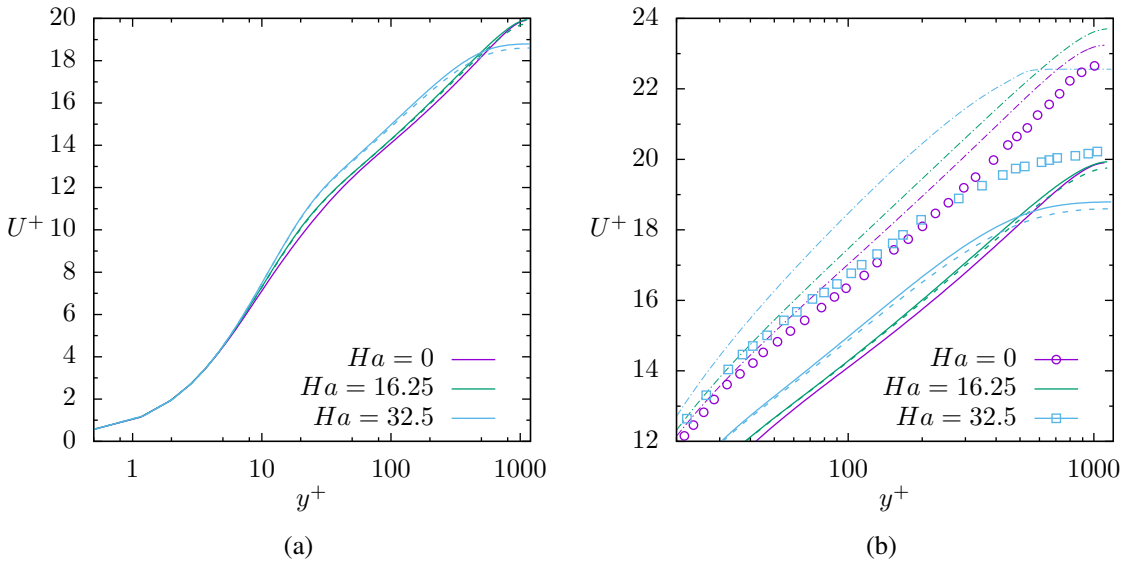

Figure 6.38: Non-dimensional mean velocity profiles for fully developed channel flow subjected to a wall-normal magnetic field at different Ha. (a) Comparison between HJM (solid lines) and HJ (dashed lines) models across the full channel, and (b) comparison within the log-law region between HJM (solid lines), HJ (dashed lines), LSM (dot dashed lines) and DNS (symbols) of Satake et al. (2008); $Re_\tau \approx 1150$.

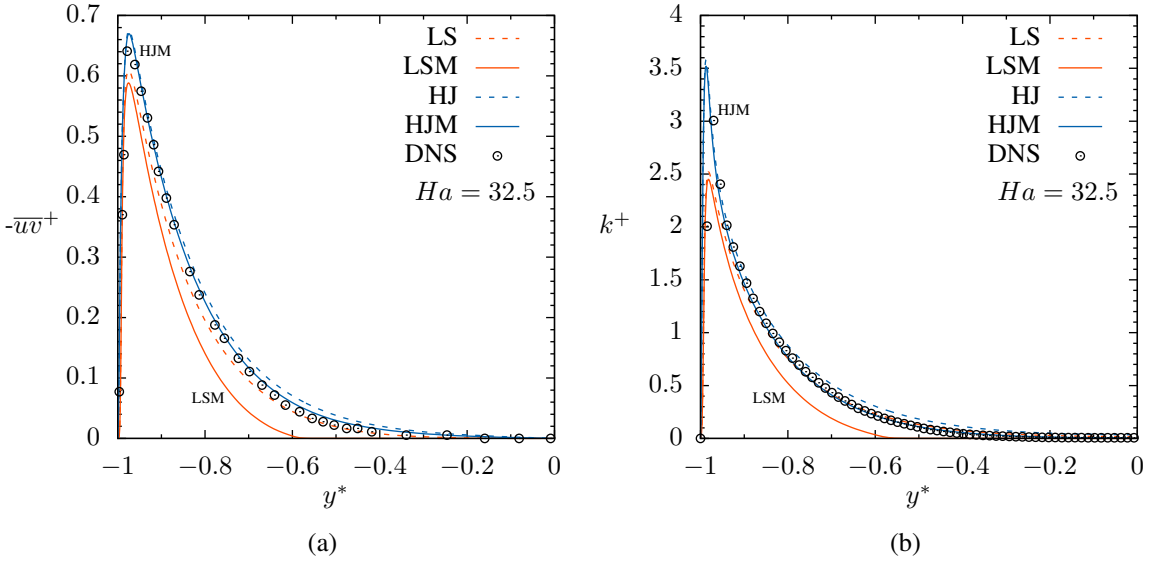

Figure 6.39: Performance of stress-transport and eddy-viscosity type models both with (solid lines) and without (dashed lines) electromagnetic modifications for fully developed channel flow subjected to a wall-normal magnetic field at $Ha = 6$. (a) profiles of non-dimensional turbulent shear stress $(\overline{uv}^+)$ and (b) profiles of non-dimensional turbulent kinetic energy (k^+); $Re_\tau \approx 1150$.

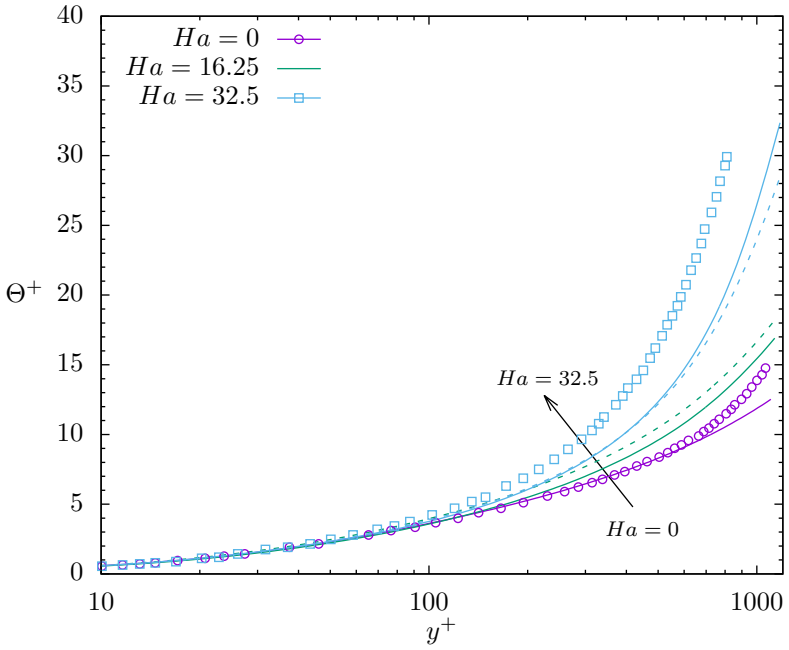

Figure 6.40: Non-dimensional mean temperature profiles for fully developed channel flow subjected to a wall-normal magnetic field at different Ha. Comparison between HJM model (solid lines), HJ model (dashed lines) and DNS (symbols) of Satake et al. (2008); $Re_\tau \approx 1150$, $Pr = 0.06$.

provide an overly excessive reduction to values of k away from areas with strong production.

Finally, Figure 6.40 shows the response of the non-dimensional temperature profiles to an increase in magnetic field strength. Both the HJ and HJM provide the correct qualitative response, but the HJ model provides better agreement at $Ha = 32.5$. Although the additional magnetic terms in the HJM model had only a relatively minor effect on the Reynolds stresses, the resultant effect of these changes on the turbulent heat fluxes (via the GGDH approximation of Equation (4.4.24)) lead to a noticeable impact on the mean temperature profile.

6.4.3 Streamwise magnetic field

The alignment of the magnetic field vector with the fluid velocity vector means that the mean streamwise Lorentz force is zero (since $\mathbf{U} \times \mathbf{B}$ must vanish). This eliminates what was established to be the primary mechanism by which the wall-normal magnetic field reduced turbulence levels in the flow (by reducing the mean wall-normal velocity gradient). Here, the streamwise magnetic field can only interact with the turbulence through the fluctuating Lorentz force. This has to be provided by the additional modelled sink terms in the turbulence equations (LSM and HJM) and the unmodified models will provide no change from the neutral state.

The geometry considered remains as per Figure 6.1. The parameter range considered is $Ha = 0, 6, 20$ at the relatively low Reynolds number of $Re_\tau = 150$ where comparisons are made against DNS data from Noguchi et al. (2004). Table 6.3 provides a summary of the cases computed.

Velocity profiles for the $Re_\tau = 150$ case are presented in Figure 6.41, where the DNS data indicates the magnetic field tends to push the profile away from the log-law. For low Ha, and differences in mass flow rate aside, this trend is captured, though quite overpredicted, by the LSM model. The response from the HJM model, from $Ha = 0$ to $Ha = 6$, is quantitatively much closer to what the DNS demonstrates. Both models, however, incorrectly return laminar flow for the highest strength magnetic field considered.

Figure 6.42 presents profiles of $\overline{uv}^+$ and the three normal stresses. Comparisons with the LSM model are only provided for the shear stress[1] $\overline{uv}^+$. The effect of the magnetic field on $\overline{uv}$, as per the DNS data, is essentially insignificant for all Ha considered. Both the LSM and HJM models give good agreement beyond $y+ = 25$, with a slight reduction in peak value predicted at $Ha = 6$ by the LSM model, but differ in the near-wall region.

For the normal stresses, whilst $\overline{ww}^+$ and $\overline{vv}^+$ are reduced, an increase in the near-wall peak of the streamwise normal stress $\overline{uu}^+$ is observed as the magnetic field strength increases. This behaviour has also been reported in other DNS studies (Lee and Choi,

Re_τ	Re	Ha	$N_x \times N_y$	DNS data
150	2.3×10^3 (c)	0	10×200	
150	2.460×10^3 (c)	6	10×200	Noguchi et al. (2004)
150	2.460×10^3 (c)	20	10×200	

Table 6.3: Summary of RANS simulations performed for turbulent fully developed channel flow subjected to a streamwise magnetic field. Values with a "(c)" are quantities computed as part of the simulation and, since the computed value is model dependent, are only indicative here.

[1] Since, as previously mentioned, the LEVM approach will always return a value of $2/3k$ for the normal stresses in simple shear flow

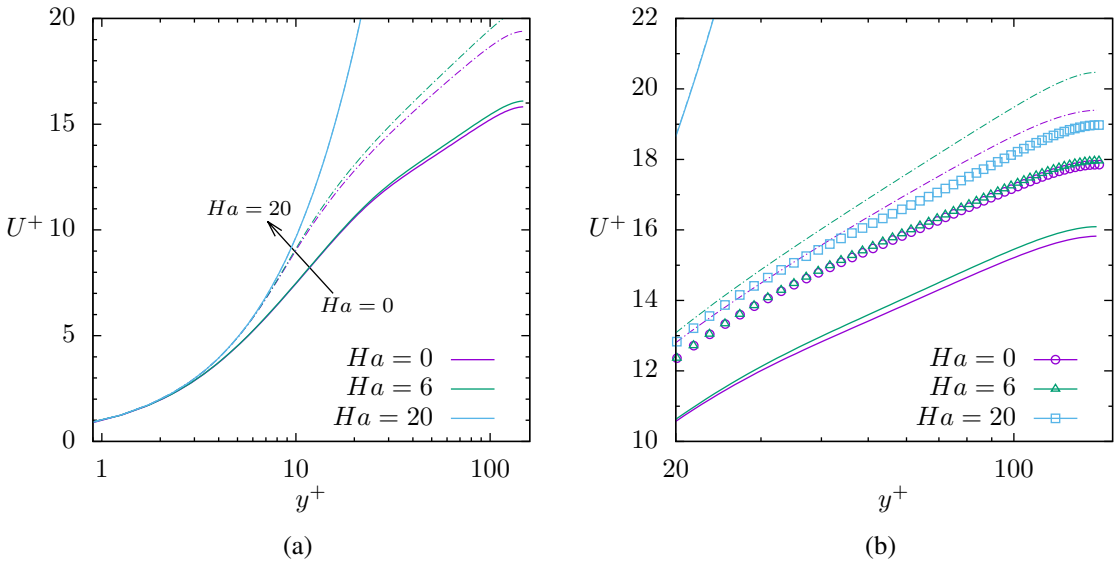

Figure 6.41: Non-dimensional mean velocity profiles for fully developed channel flow subjected to a streamwise magnetic field at different Ha. (a) Comparison between HJM (solid lines) and LSM (dot-dashed lines) models across the full channel, and (b) comparison within the log-law region of the same with DNS data (symbols) of Noguchi et al. (2004); $Re_\tau = 150$.

2001, for example) and is discussed further below. For the moderate Hartmann number $(Ha = 6)$ the HJM model correctly picks up this effect and gives generally good agreement for all the normal stress components (though values at $Ha = 0$ are under predicted). Numerical results for $Ha = 20$ are absent since, as mentioned above, both models predict entirely laminar flow contrary to the DNS data. With a strong enough streamwise magnetic field, and given the trends displayed here, the flow would be expected to eventually laminarize at some Hartmann number $(Ha > 20)$ but without further DNS data it is difficult to suggest how premature the predicted relaminarization by the models is.

The profiles of turbulent kinetic energy k^+ and its dissipation rate ε^+, which are shown in Figure 6.43, show that whilst an increase in magnetic field strength provides a modest reduction in k in the channel centre, the near wall peak shows a notable increase. Thus, the earlier decrease observed in both $\overline{vv}$ and $\overline{ww}$ (Figure 6.42) is countered, and exceeded, by the increase observed in $\overline{uu}$. Here, the LSM model gives qualitatively the wrong response, predicting a decrease in the value of k throughout the channel. Again, this is due to the form of the addition source terms in the LSM model, as they are unable to take account of any anisotropy in either the turbulent stress field or the fluctuating Lorentz force. The HJM model does correctly predict an increase, and this does serve to demonstrate the capabilities of the stress transport approach.

To investigate the increase observed in the peak values of $\overline{uu}$, and hence k, budgets of the terms within the equations for k, $\overline{uv}$ and $\overline{uu}$ are plotted in Figure 6.44 and budgets for the terms with the equations for $\overline{vv}$ and $\overline{ww}$ are plotted in Figure 6.45. As before, for the

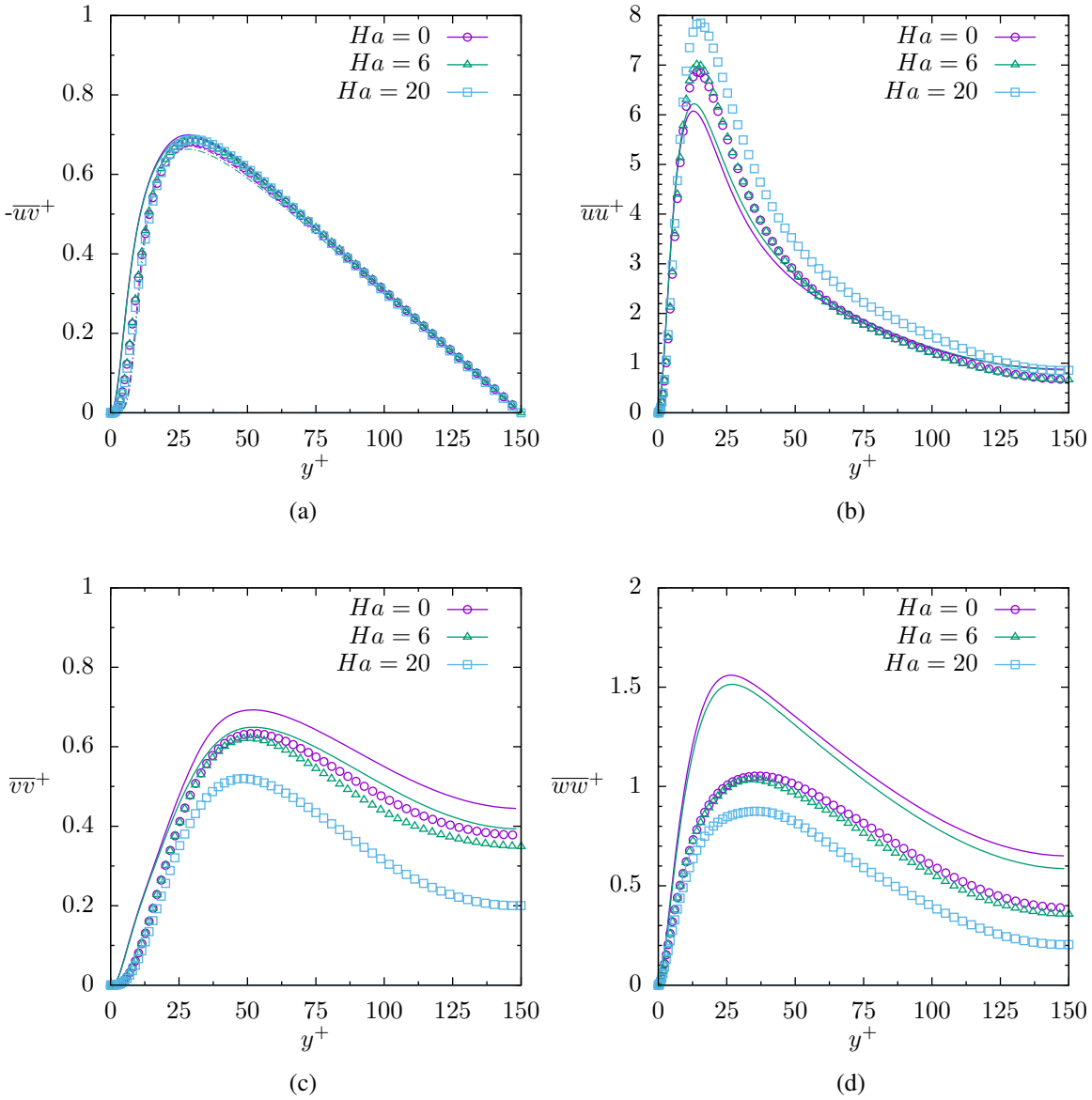

Figure 6.42: Non-dimensional Reynolds stress profiles for fully developed channel flow subjected to streamwise magnetic field at different Ha. Comparison between HJM (solid lines), LSM (dot-dashed lines) models and DNS data (symbols) of Noguchi et al. (2004). Note that only numerical predictions of $\overline{uv}$ are presented for the LSM model; $Re_\tau = 150$.

magnetic cases, the individual contributions ('mhd1' and 'mhddiss') to the total magnetic source term ('mhdtot') have been added[1].

From the budgets of k, $\overline{uv}$ and $\overline{uu}$ in Figure 6.44 the effect of the streamwise magnetic field, in direct contrast to the wall-normal magnetic field, is to actually increase the magnitude of the production term for these equations. The only non-zero contribution to these production terms will, as before, be those involving the wall-normal velocity gradient, $\partial U/\partial y$. For k, this term ($\mathcal{P}_k$ from Equation (4.4.9)) is multiplied by $\overline{uv}$ and since Fig-

[1]As a reminder, 'mhd1' corresponds to $\mathcal{F}_k^{L1}$ and 'mhddiss' corresponds to $\mathcal{F}_k^{L2}$ (as defined in Equation (4.4.14)) for terms in the k equation. For the terms in the Reynolds stress budgets, 'mhd1' corresponds to $\mathcal{F}_{ij}^{L1}$ and 'mhddiss' corresponds to $\mathcal{F}_{ij}^{L2}$ as defined in Equation (4.3.11).

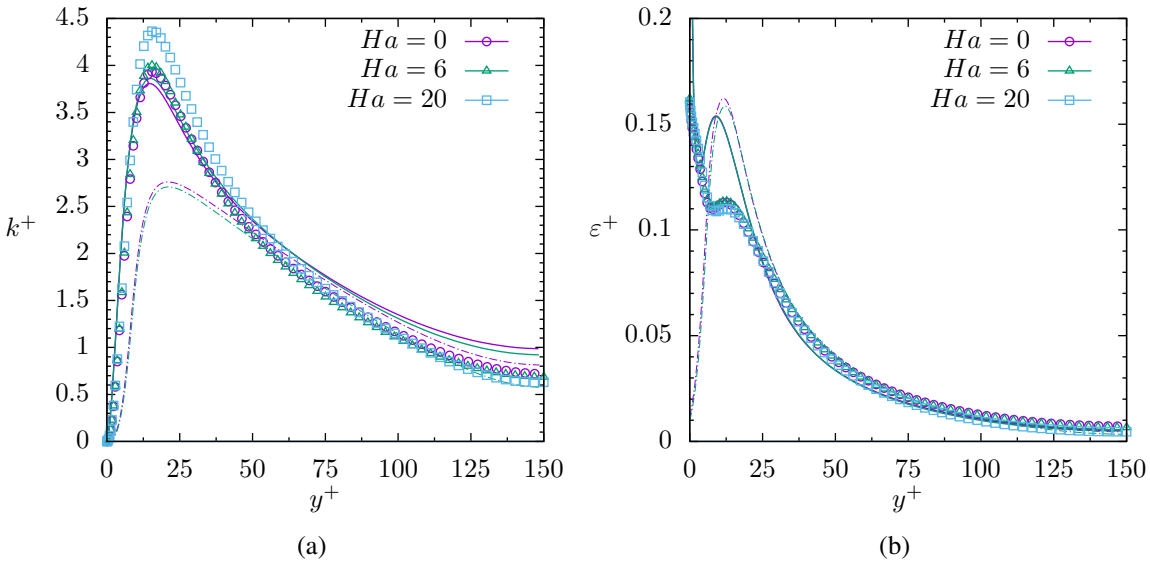

Figure 6.43: Velocity profiles at $Re_\tau = 150$ for varying Ha showing (a) the full channel half-width and (b) a blow up of the region $20 < y^+ < 150$. Solid lines are the LSM model, dashed lines are the LS model and symbols represent DNS data as per Table 6.2

ure 6.42 indicates no significant change to this, the increase in production must arise from an increase in the velocity gradient. Similar arguments can also be made for $\mathcal{P}_{12}$ (multiplied by $\overline{vv}$[1]) and $\mathcal{P}_{11}$ (multiplied again with $\overline{uv}$). The direct magnetic contributions do not appear significant in the k equation but, curiously, those in the $\overline{uv}$ equations contribute positively to the budget of $-\overline{uv}$. The dominant sink in this, the pressure strain term, also increases in line with the increase in production.

For the $\overline{vv}$ and $\overline{ww}$ equations, the magnetic field causes reductions to the contributions from the pressure strain and dissipation terms. In addition, the direct magnetic sink term, whilst negligible close to the wall, is influential past $y^+ \approx 25$. Note that, compared with the budgets for the wall-normal magnetic field (in Figure 6.30 and Figure 6.31), the constituent terms within $\mathcal{F}^L_{ij}$ are far more significant, though this is predominantly due to the difference in Hartmann number between the two magnetic field orientations.

The performance of the LSM and HJM models in reproducing the direct magnetic source term is again assessed through comparisons with the DNS budget data. Data is shown for both $Ha = 6$ and $Ha = 20$ but, unfortunately, since both models returned laminar flow at the higher field strength a direct comparison is not possible. The plots have been left to give a clearer indication (than that in Figure 6.44 and Figure 6.31) of how the terms vary with Ha. For the $\mathcal{F}^L_k$ and $\mathcal{F}^L_\varepsilon$ terms, shown in Figure 6.46, the LSM model grossly over predicts the (negative) magnitude of the term and this leads to a corresponding over prediction in the $\mathcal{F}^L_\varepsilon$ term with a significantly large negative peak. With the level of over prediction seen here at $Ha = 6$, it is easy to see why the model predicted laminar flow at

[1] Although Figure 6.42 indicates the magnetic field causes a quite significant reduction in the peak value of $\overline{vv}$, the reduction at the location of the peak in $\mathcal{P}_{12}$ (at $y^+ \approx 18$) is more modest.

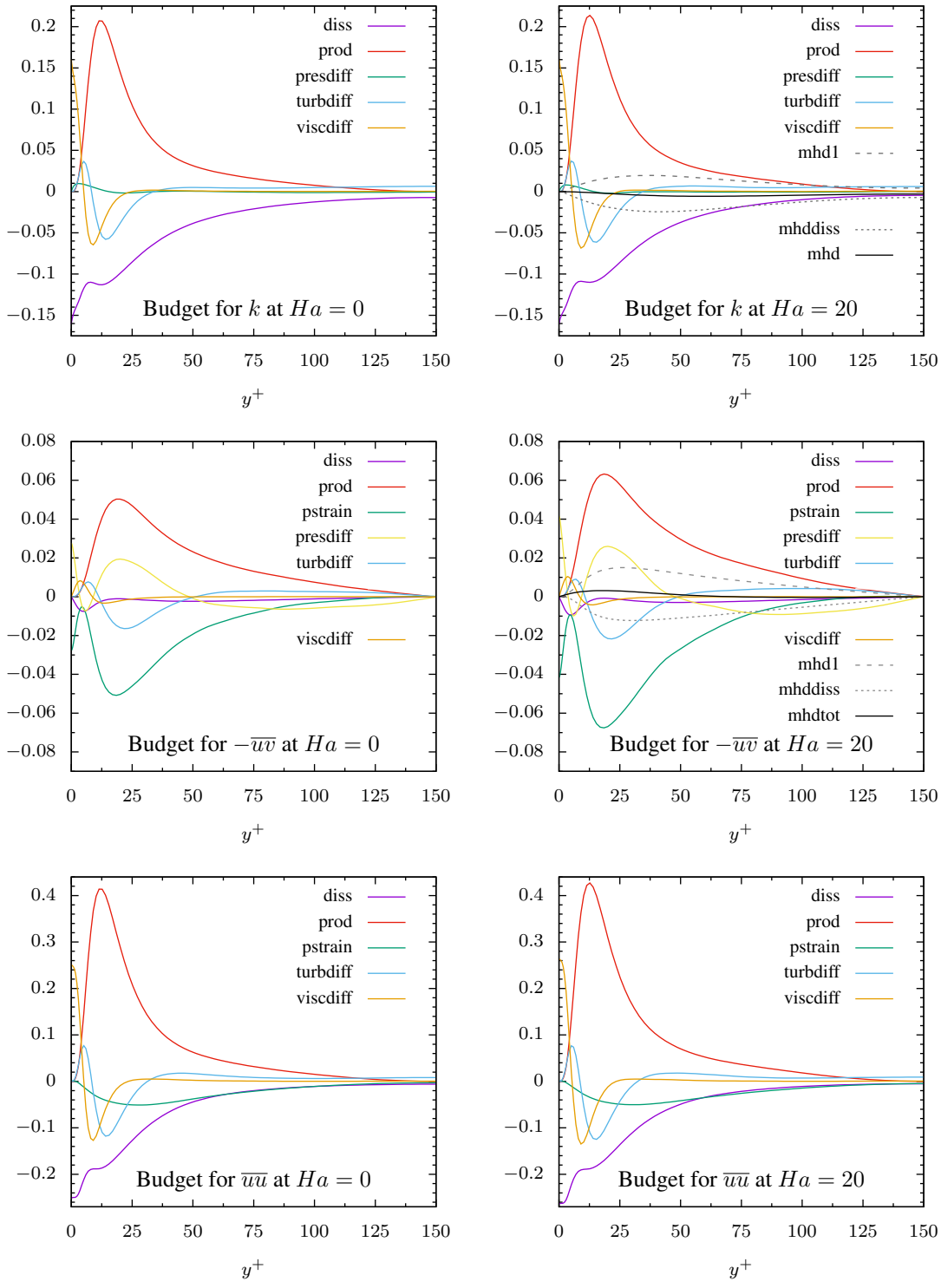

Figure 6.44: Budgets of terms in the k, $\overline{uv}$ and $\overline{uu}$ equations for (left) $Ha = 0$ and (right) $Ha = 20$ as provided in the DNS database of Noguchi et al. (2004) for fully developed channel flow at $Re_\tau = 150$ subjected to a streamwise magnetic field.

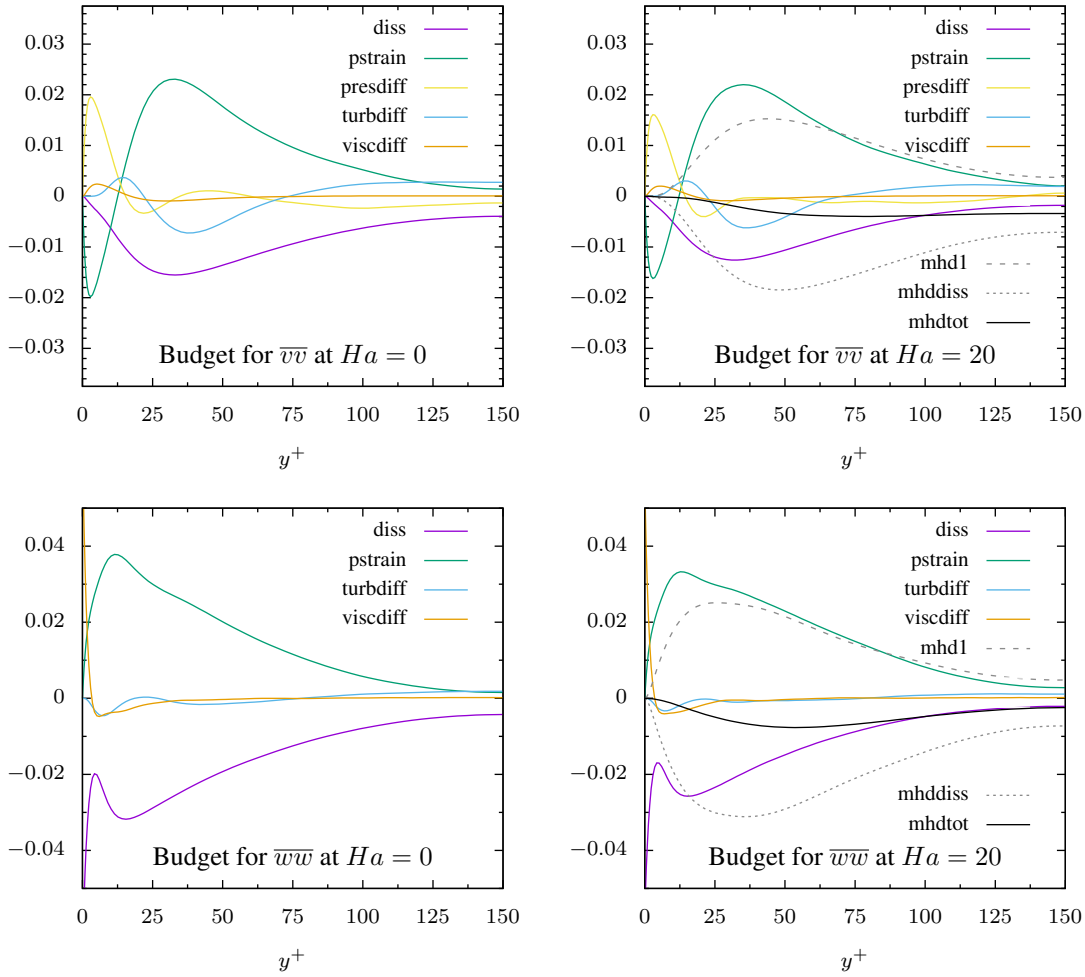

Figure 6.45: Budgets of terms in the $\overline{vv}$ and $\overline{ww}$ equations for (left) $Ha = 0$ and (right) $Ha = 20$ as provided in the DNS database of Noguchi et al. (2004) for fully developed channel flow at $Re_\tau = 150$ subjected to a streamwise magnetic field.

$Ha = 20$. The HJM model does perform better but does also over estimate the magnitude of both terms.

With the $\mathcal{F}^L_{vv}$ and $\mathcal{F}^L_{ww}$ terms[1], the HJM model provides adequate results though, as can be inferred from the $\mathcal{F}^L_k$ contribution, the magnitude of both terms is over estimated. For the $\mathcal{F}^L_{uv}$ contribution, the HJM model provides qualitatively incorrect results, as it predicts values opposite in sign to the DNS. The expression for $\mathcal{F}^L_{uv}$, given this particular magnetic field vector, can be obtained from expansion of Equation (4.3.40);

$$\mathcal{F}^L_{uv} = \frac{\sigma}{\rho}\left(1 - C_\lambda\right)\left(-2B_x^2\overline{uv}\right) \tag{6.4.5}$$

whilst, for comparison, the expression with an applied wall-normal magnetic field is given by;

$$\mathcal{F}^L_{uv} = \frac{\sigma}{\rho}\left(1 - C_\lambda\right)\left(-2B_y^2\overline{uv}\right) \tag{6.4.6}$$

[1]Note that for the streamwise magnetic field, the $\mathcal{F}^L_{uu}$ contribution will vanish, much like the $\mathcal{F}^L_{vv}$ contribution did for the wall-normal magnetic field.

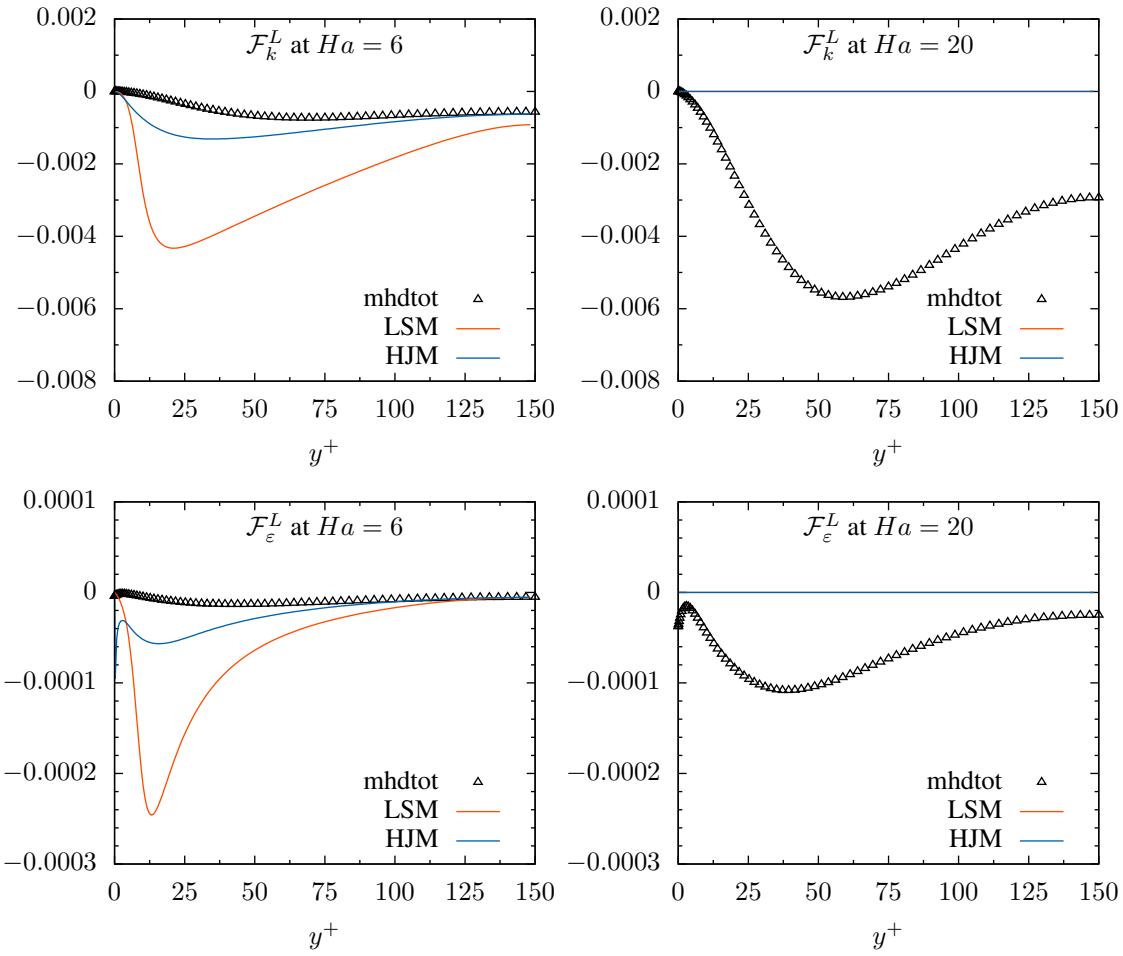

Figure 6.46: Contributions from the additional electromagnetic source terms $\mathcal{F}_k^L$ (top) and $\mathcal{F}_\varepsilon^L$ (bottom) to the budgets of k and ε respectively for turbulent Hartmann flow at (left) $Ha = 4$ and (right) $Ha = 6$. Comparisons between DNS (symbols) of Noguchi et al. (2004) and numerical simulations (solid lines). For the DNS terms, 'mhdtot' represents the total contribution to the budget with 'mhd1' representing the $L1$ contribution and 'mhddiss' representing the $L2$ contribution as per Equations (4.3.43) and (4.4.14) respectively; $Re_\tau = 150$.

that is, they are of equivalent form. Since the values of $\overline{uv}$ throughout the first half of the channel are negative, and B_i^2 must be positive, $\mathcal{F}_{uv}^L$ will always be positive (and hence $-\mathcal{F}_{uv}^L$ always negative), for $C_\lambda > 0$ (which is the case here). Since the term, as detailed earlier in Subsection 4.3.2, only uses the exact part $(\mathcal{F}_{ij}^{L2})$ of the full expression for $\mathcal{F}_{ij}^L$ (as presented in Equation (4.3.11)), this deficiency arises from an inadequate model for $\mathcal{F}_{ij}^{L1}$.

The above observations suggest that at the higher magnetic field strength $(Ha = 20)$ the incorrect sign for the source term in the $\overline{uv}$ equation could have contributed to the laminarization of the flow with the HJM model. $\overline{uv}$ itself forms part of both the production term in the $\overline{uu}$ equation and the pressure strain source terms in the $\overline{vv}$ and $\overline{ww}$ equations, and hence a significant overprediction of am (incorrect) $\overline{uv}$ sink may reduces levels such that turbulence can not longer be sustained. Despite this, quantitative predictions with the HJM model at $Ha = 6$ were satisfactory and predicted the correct qualitative behaviour.

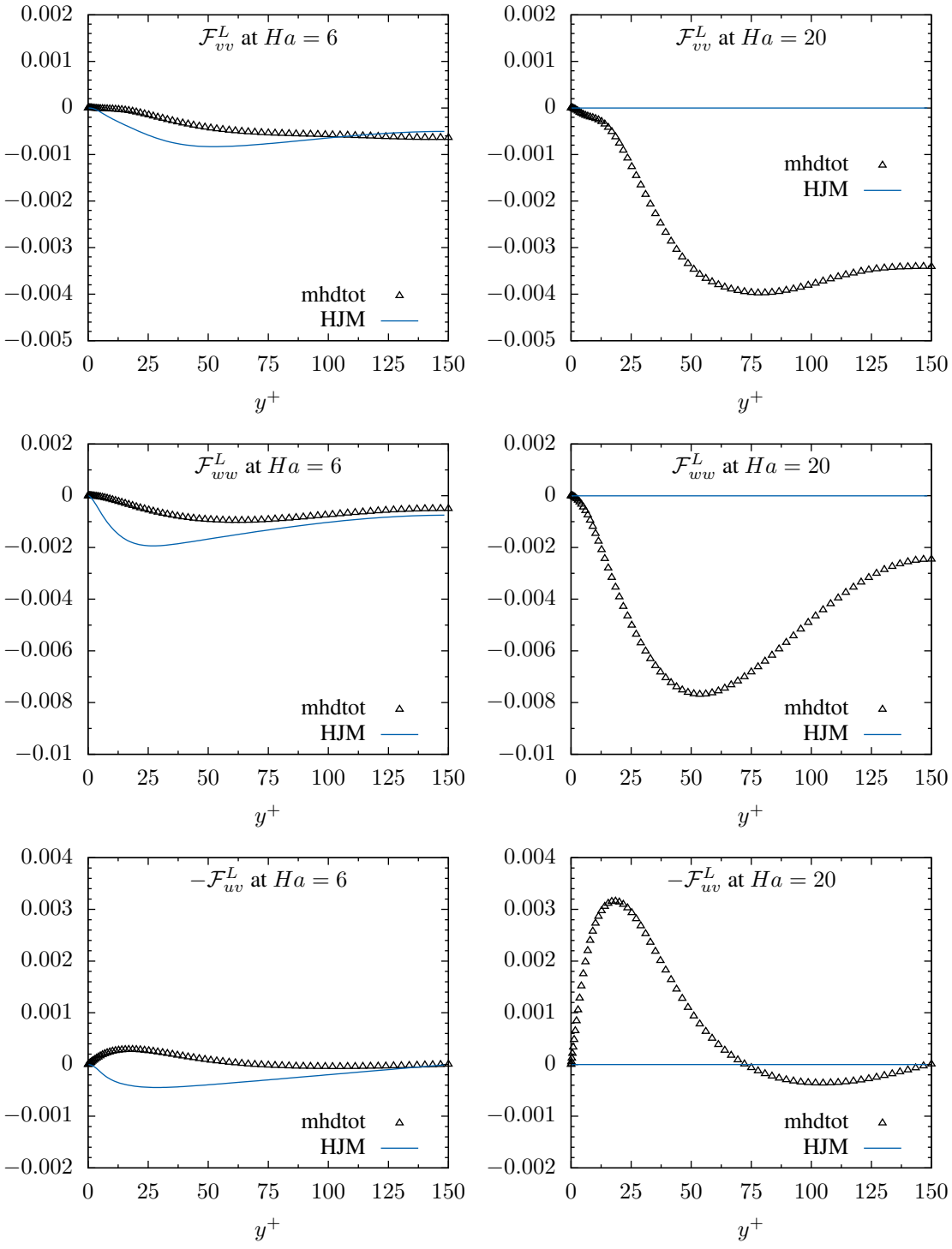

Figure 6.47: Contributions from the additional electromagnetic source terms, from top to bottom, $\mathcal{F}^L_{uu}$, $\mathcal{F}^L_{ww}$ and $\mathcal{F}^L_{uv}$ to their respective budgets for turbulent Hartmann flow at (left) $Ha = 4$ and (right) $Ha = 6$. Comparisons between DNS (symbols) of Noguchi et al. (2004) and numerical simulations (solid lines). For the DNS terms, 'mhdtot' represents the total contribution to the budget with 'mhd1' representing the $L1$ contribution and 'mhddiss' representing the $L2$ contribution as per Equation (4.3.11); $Re_\tau = 150$.

6.5 Conclusion

The objective of this chapter was to first provide confidence in the ability of the numerical solver STREAM in predicting some elementary magnetically influenced flows, and second to provide a detailed assessment of how the electromagnetically extended turbulence models, discussed in Chapter 4, respond to the application of a magnetic field in a one-dimensional fully developed turbulent channel flow.

To validate the implementation of the electromagnetic terms in STREAM a series of laminar flow calculations was presented. For fully developed one-dimensional channel flow subjected to a wall-normal magnetic field, results showed excellent agreement with the analytical solution; a development and description of which was provided. Laminar computations for flow through an infinitely long square duct verified phenomena discussed earlier in Chapter 2, which detailed how the electrical properties of the four bounding walls can have a significant effect on the distribution of velocity and electrical current across the duct. The results showed that STREAM was capable of correctly of reproducing some key features of the flows, such as the presence of wall bounded jets in a duct where the Hartmann walls are conducting and the side walls are insulating, which were consistent with physical arguments and results presented by Sterl (1990).

To provide a benchmark against which to compare the magnetic cases, one-dimensional fully developed turbulent channel flows are computed for a series of Reynolds numbers $(150 \leq Re_\tau \leq 2000)$. Whilst the Hanjalić and Jakirlić RSM was seen to over predict the level of $\overline{uv}$ in the near-wall region, in contrast to the under prediction seen by the Launder-Sharma EVM, the models correctly reproduced the well known features of channel flows and showed good quantitative agreement with the available DNS data.

A wall-normal magnetic field was then imposed, and a series of turbulent flows computed over a range of Reynolds $(150 \leq Re_\tau \leq 1194)$ and Hartmann $(0 \leq Ha \leq 32.5)$ numbers. The results showed that, with an increase in magnetic field strength, the electromagnetically modified Launder-Sharma model consistently over estimated the reduction in turbulence that the DNS results showed. This led to premature laminarization of the flow initially in the core of the channel but, for sufficiently strong magnetic fields, also across the entire channel width. In most cases, the unmodified version of the model actually provided more accurate predictions. Whilst the additional source term in the k equation gave reasonable quantitative agreement with the DNS, the sink term in the ε equation was consistently under predicted. This led to an over estimation of ε and hence an over estimation in the reduction of $\overline{uv}$.

The Hanjalić and Jakirlić RSM model consistently provided better results and kept the flow turbulent across the entire range of Ha considered. The electromagnetic modifications, however, were seen to make only modest adjustments to the primary variables

and any lack of quantitative agreement with DNS data could more easily be attributed to inaccuracies in the unmodified model i.e. deficiencies noted at $Ha = 0$. That said, numerical predictions of the additional electromagnetic source terms in the $\overline{u_i u_j}$ equations gave generally good agreement with the DNS data.

The physical mechanism behind the reduction in turbulence levels that the wall-normal magnetic field brings was explained with reference to budgets of the $\overline{u_i u_j}$ and k equations as provided by the DNS. The most significant effect was a reduction in the mean wall-normal velocity gradient brought on by the presence of a mean decelerating streamwise Lorentz force. This served to directly reduce the magnitude of the non-zero production terms in the Reynolds stress equations and hence reduce levels of all stress components ($\overline{uv}$ and $\overline{uu}$ through a direct reduction in production, and $\overline{vv}$ and $\overline{ww}$ via reduced redistribution i.e. pressure strain), and thus k, across the channel. Given this, and since the production terms in the $\overline{u_i u_j}$ and k equations are treated exactly, it is not surprising that the unmodified versions of both the RSM and EVM were able to provide qualitatively (and in some cases, quantitatively) accurate predictions of the effect of a wall-normal magnetic field on the flow.

Following the application of a wall-normal magnetic field, a streamwise magnetic field was applied and numerical simulations were performed, with both turbulence models, for $Re_\tau = 150$ and $0 \leq Ha \leq 20$. The change in magnetic field orientation resulted in a vanishing streamwise mean Lorentz force and thus the elimination of what was seen to be the primary turbulence reduction mechanism by the wall-normal magnetic field; a reduction in turbulent stress production caused by the destruction of mean wall-normal velocity gradients via the Lorentz force. Thus, the magnetic field can only affect the mean flow by augmenting the Reynolds stresses through the fluctuating part of the Lorentz force. The unmodified turbulence models were not tested since they would not predict any change from the neutral state.

The results showed that observed change in the velocity profile as the magnetic field strength was increased (from $Ha = 0$ to $Ha = 6$) was best predicted by the RSM. Both models, however, returned laminar flow at the highest Hartmann number considered, $Ha = 20$. The DNS data showed that whilst $\overline{vv}$ and $\overline{ww}$ were reduced, the values of the near-wall peak in $\overline{uu}$ and k were actually increased. This was correctly picked up by the RSM, whilst the EVM predicted a reduction (albeit slight) in k. At $Ha = 6$, comparisons between the values of the additional source terms in the k and ε equations with the DNS data showed that the EVM grossly over predicted the magnitudes of both (sink) terms, revealing the reason for the premature laminarization at $Ha = 20$. This deficiency in the EVM was attributed to the ad-hoc form of the additional source terms, which were unable to take account of the change in magnetic field direction.

A notable deficiency with the RSM was the prediction of a sink term in the budget for $-\overline{uv}$ when the DNS clearly indicated the term should have been a source. Since continued reduction, and the eventual elimination, of $\overline{uv}$ will cause the flow to laminarize, this

inaccuracy was posited to have contributed to the prediction of laminar flow at $Ha = 20$. Since the mathematical form of the term uses only the exact part of the full expression for $\mathcal{F}_{ij}^L$, this deficiency must arise from an inadequate model for the modelled part of $\mathcal{F}_{ij}^L$.

In summary, the superior performance of the RSM over the EVM in these magnetic channel flows can be attributed to both its ability to provide better representation of stress generation and other physical processes, and its ability to accommodate the electromagnetic modifications in a more natural (and exact) fashion.

CHAPTER

SEVEN

MAGNETIC RAYLEIGH-BÈNARD CONVECTION

In this chapter, numerical results from a series of three-dimensional time-dependant turbulent Rayleigh-Bènard convection flows are presented. The objective is to provide insight into how, for some more complex flows, the electromagnetically extended turbulence models discussed in Chapter 4 predict the flow to behave when a magnetic field is applied over a range of field intensities and directions.

The chapter begins in Section 7.1 with a detailed description of the case and Section 7.2 follows with information on the mesh and the boundary conditions employed. Section 7.3 provides details on identifying coherent structures in convective flows and Section 7.4 presents results for non-magnetic Rayleigh-Bènard convection, with comparisons made against existing DNS data for the purposes of code validation. Section 7.5 then looks at results obtained at the moderate Prandtl number of $Pr = 0.71$ where both a vertically and horizontally oriented magnetic field are investigated. For the vertical magnetic field, a reduction in Prandtl number is considered in Section 7.6. Finally, Section 7.7 concludes the chapter by providing a summary of the key findings.

Unfortunately no suitable DNS data exists for magnetic Rayleigh-Bènard convection (with the exception of Yanagisawa et al. (2015), which appeared just as this work was completed) but comparisons are made with a series of existing RANS results, obtained with the EVM approach, published by Hanjalić and Kenjereš (2000, 2001, 2006) and Kenjereš and Hanjalić (2004) and assessed by physical intuition. A selection of results from this Chapter have been published in Wilson et al. (2014, 2015).

7.1 Case description

As described earlier in Section 2.3, Rayleigh-Bènard convection is a type of natural convection which occurs when a horizontal layer of fluid is heated from below. Thermal expansion of the fluid adjacent to the heated surface generates an unstable density distribution which, in a gravitational field, will lead to buoyant forces. If these are sufficient to overcome the dissipative mechanisms of heat transfer (conduction) and viscosity then vertical fluid motion will result. For fluid which is bound between two horizontal solid surfaces, the impingement of fluid plumes will generate horizontal motion and a series of convective roll cells can become established. As before, the ratio of the buoyant "driving force" to the dissipation mechanisms of heat and viscosity is given by the non-dimensional Rayleigh number;

$$Ra = \frac{g\beta\Delta\Theta L_z^3}{\nu\alpha} \tag{7.1.1}$$

where L_z is the distance between the two plates. The state of the system is additionally described by the Prandtl number, which controls the relative sizes of the thermal and momentum boundary layers;

$$Pr = \frac{\nu}{\alpha} \tag{7.1.2}$$

The addition of a uniform magnetic field causes the appearance of Lorentz forces which, typically, will oppose both mean and fluctuating fluid motion. It was seen in both Section 2.3 and Subsection 4.1.2 that this can have quite an effect on the vortical flow structures which comprise Rayleigh-Bènard convection. In the direction of the magnetic field, velocity gradients were significantly reduced and this, as a result, tended to align the axes of the vortices with the magnetic field lines. The emerging flow structure will thus depend on the mutual orientation and strength of the buoyant and Lorentz forces. For the latter, this is quantified, as before, by the non-dimensional Hartmann number, $Ha = B_0 L_z \sqrt{\sigma/\mu}$.

To investigate the above effects, and the extent to which the numerical models can reproduce them, computations of Rayleigh-Bènard convection are carried out between two infinite horizontal flat plates. Since the plates are horizontally infinite, the vertical distance between them will govern the typical size of the expected flow structures (for the non-magnetic cases at least). To represent the problem numerically an 8:8:1 aspect ratio rectangular cavity is used as shown in Figure 7.1. Symmetry boundary conditions are imposed at the sides by setting the velocity normal to the boundary to zero and imposing Neumann conditions on all other variables (except pressure). Since symmetry boundaries do not allow mass to pass through them, the lateral dimensions of the domain will inevitably have some influence on the number and characteristic size of the roll cells which can develop. However, choosing a large width to depth ratio (8) should help to reduce this influence. The upper and lower surfaces are taken as electrically insulating walls and their temperatures, Θ_t and Θ_b, respectively, are constant and set such that $\Theta_b > \Theta_t$.

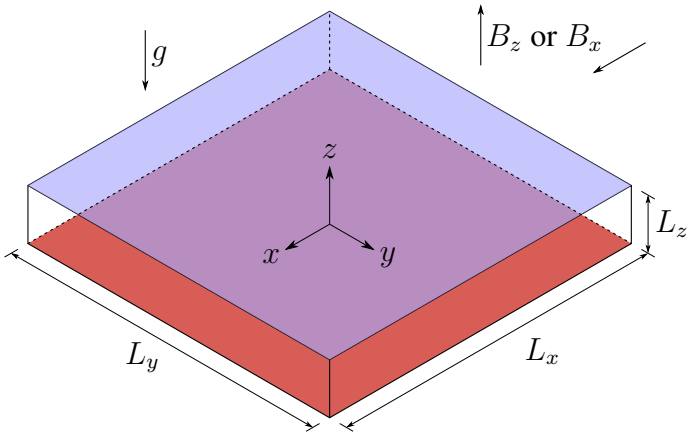

Figure 7.1: Geometry for Rayleigh-Bènard convection cases.

Since motion arising from natural convection is typically unsteady, the numerical solver STREAM is switched to time-dependant mode and the ensemble averaged form (see Subsection 3.1.2) of the governing equations are solved. The letter U (for unsteady) is typically prepended to the acronym RANS to signify this. The equation set comprises continuity, Equation (3.3.14), momentum with the Lorentz and buoyancy force terms, Equation (3.3.15), the Poisson equation for the electric potential, Equation (3.3.12), and the scalar transport equation for the mean temperature, Equation (3.1.12). For the turbulence, the investigation aims to provide some comparisons between the performance of the eddy-viscosity and stress-transport models detailed in Chapter 4 with a slight focus on the stress-transport model, since the results obtained in Chapter 6 showed it to be generally superior.

The low-Re Launder and Sharma (1974) $k-\varepsilon$ model, both with (LSM) and without (LS) the additional electromagnetic terms provided by Kenjereš and Hanjalić (2000), is tested where the eddy-diffusivity model, described in Subsection 4.4.4, provides the turbulent heat flux. With the Hanjalić and Jakirlić stress-transport model, only the electromagnetically extended version (HJM) is tested. The form of the additional modelled terms within this are based on their exact counterparts (unlike the terms proposed for the $k-\varepsilon$ model), so omission of them lacks physical justification. The GGDH model described in Subsection 4.3.3 provides the turbulent heat flux.

The Rayleigh number considered here, $Ra = 10^7$, is well within the turbulent regime for the non-magnetic case and both a wall-normal (vertical) and wall-parallel (horizontal) magnetic field are applied with field strengths considered in the range $0 < Ha < 200$. For the vertical magnetic field, two Prandtl numbers are considered. The first, $Pr = 0.71$, allows comparisons to be made with other URANS results presented by Hanjalić and Kenjereš whilst the second, $Pr = 0.01$, is, in most cases, much more physically relevant since the most common electrically conducting fluids are liquid metals. With

the horizontal magnetic field, only the more moderate Prandtl number $(Pr = 0.71)$ is considered. A summary of the cases computed is provided in Table 7.1.

As the case is time-dependant it requires the specification of initial conditions. Here, the fluid is supposed to be in an initially quiescent state $(U = 0, V = 0, W = 0)$ with the thermal conditions given by a temperature distribution decreasing linearly from $\Theta = \Theta_b$ at the bottom wall to $\Theta = \Theta_t$ at the top wall. A reference temperature of $\Theta_0 = (\Theta_t + \Theta_b)/2$ is taken and the pressure field is set to zero. In the two-equation eddy-viscosity approach, initial conditions for the k and ε equations are calculated from the relationships provided by Versteeg and Malalasekra (1996);

$$k = \frac{2}{3}(W_b I)^2 \tag{7.1.3}$$

$$\varepsilon = c_\mu^{3/4} \frac{k^{3/2}}{\ell} \tag{7.1.4}$$

$$\ell = 0.07 L_z \tag{7.1.5}$$

where the buoyant reference velocity W_b is,

$$W_b = \sqrt{g\beta\Delta\Theta L_z} \tag{7.1.6}$$

and the turbulent intensity, I is 0.2. In the stress transport approach, values of k and ε are computed as above and the normal stresses are all set equal to $2/3k$.

The temperature in the domain is non-dimensionalized using the upper and lower surface temperatures;

$$\Theta^* = \frac{\Theta - \Theta_t}{\Theta_b - \Theta_t} \tag{7.1.7}$$

so that the Θ^* takes a value of 1 on the hot surface and 0 on the cold surface.

Ra	Ha	Pr	$\mathbf{B}$	Models tested		
10^7	0	0.71		LS	HJ	
10^7	20	0.71	$\mathbf{B} \parallel z$	LS	LSM	HJM
10^7	50				LSM	HJM
10^7	100			LS	LSM	HJM
10^7	200				LSM	HJM
10^7	400					HJM
10^7	800					HJM
10^7	20	0.71	$\mathbf{B} \parallel x$			HJM
10^7	50					HJM
10^7	100					HJM
10^7	200					HJM
10^7	400					HJM
10^7	800					HJM
10^7	0	0.01			HJ	
10^7	20	0.01	$\mathbf{B} \parallel z$			HJM
10^7	50					HJM
10^7	100					HJM
10^7	200					HJM
10^7	400					HJM
10^7	800					HJM

Table 7.1: Summary of URANS simulations performed for magnetic Rayleigh-Bénard convection. For the models tested, LS represents the low-Re Launder Sharma $k-\varepsilon$ model and HJ represents the low-Re Hanjalić and Jakirlić stress transport model. An appended "M" indications the inclusion of electromagnetic modifications as detailed in Chapter 4.

7.2 Numerical method and computational mesh

The roll cell formations typical of Rayleigh-Bènard convection can be considered as a form of large-scale deterministic coherent motion which is in addition to the small-scale stochastic motions traditionally thought to comprise the turbulence. This separation of scales invites the possibility to apply the RANS approach in unsteady mode and it has been well-established that this can provide resolution of these cell structures (see Kenjereš and Hanjalić (1999b), for example). To do this, if one assumes that the scale of these large structures is distinct in spectral space to the rest of the turbulence, then it becomes permissible to decompose an instantaneous variable $\tilde{\Psi}(x_i,t)$ into a time mean $\overline{\Psi}(x_i)$, a stochastic $\psi(x_i,t)$ component, and a deterministic $\hat{\Psi}(x_i,t)$;

$$\tilde{\Psi}(x_i,t) = \overline{\Psi}(x_i) + \hat{\Psi}(x_i,t) + \psi(x_i,t) = \langle\Psi\rangle(x_i,t) + \psi(x_i,t) \tag{7.2.1}$$

where the quantity in angled brackets represents the ensemble average. The second moment of two arbitrary variables Ψ and Φ becomes;

$$\overline{\tilde{\Psi}\tilde{\Phi}} = \overline{\overline{\Psi}\,\overline{\Phi}} + \overline{\hat{\Psi}\hat{\Phi}} + \overline{\psi\phi} = \overline{\langle\Psi\rangle\langle\Phi\rangle} + \overline{\psi\phi} \tag{7.2.2}$$

where $\overline{\psi\phi}$ is the modelled contribution, $\overline{\hat{\Psi}\hat{\Phi}}$ is the deterministic or 'resolved' contribution and $\overline{\langle\Psi\rangle\langle\Phi\rangle} = \overline{\overline{\Psi}\,\overline{\Phi}} + \overline{\hat{\Psi}\hat{\Phi}} = \overline{\Psi}\,\overline{\Phi} + \overline{\hat{\Psi}\hat{\Phi}}$. Separating the contributions to the second moments as such allows one to assess the relative importance of the turbulence model in reproducing the flow patterns seen.

To solve the problem as unsteady, the time-dependent three-dimensional version of STREAM is employed. Other details are as described earlier in Section 6.2. A time scale for the convective motion, in the absence of a magnetic field, can be formed from the buoyant velocity scale W_b, defined in Equation (7.1.6), and the height of the domain L_z. In one convective rotation the fluid can be expected to traverse this length roughly twice, hence;

$$\tau_b = \frac{2L_z}{\sqrt{g\beta\Delta\Theta L_z}} \tag{7.2.3}$$

Using this time-scale, Hanjalić and Kenjereš (2000) arrived at a non-dimensional time-step of;

$$\Delta t\sqrt{g\beta\Delta\Theta/L_z} = 0.02 \tag{7.2.4}$$

which equates to resolving this typical cell motion in 100 time-steps. It can be inferred from the channel flow results presented in Chapter 6, where the application of a magnetic field was seen to generally oppose motion (mean and fluctuating) across the field lines, that a magnetic field here would generally cause the time-scale of the motion to increase. Thus, this time-step provides an upper bound and has been taken for all cases computed. For temporal discretization, the Crank-Nicolson scheme was used as detailed

in Subsection 5.2.4 and the computations were run until long-term time averaged statistics remained stationary.

Both of the turbulence models used to compute this case are low Reynolds number models and thus the near-wall node resolution must be such that the non-dimensional wall distance (z^+ here) is less than unity. The mesh employed has a resolution of $80 \times 80 \times 100$ nodes and was generated using the author's own code. The nodes are distributed uniformly in the horizontal directions and clustered towards the walls, using geometric progression, in the vertical direction. In addition, to enable the STREAM solver to be run in parallel mode, the mesh was split into 16 blocks arranged in a 4×4 fashion. The speed up gained by the ability to run the code in parallel largely offsets the increased time arising from using a low-Re approach. Figure 7.2 provides illustrations of the mesh, showing both the multiblock arrangement and the node distributions in the $x - y$ and $x - z$ planes.

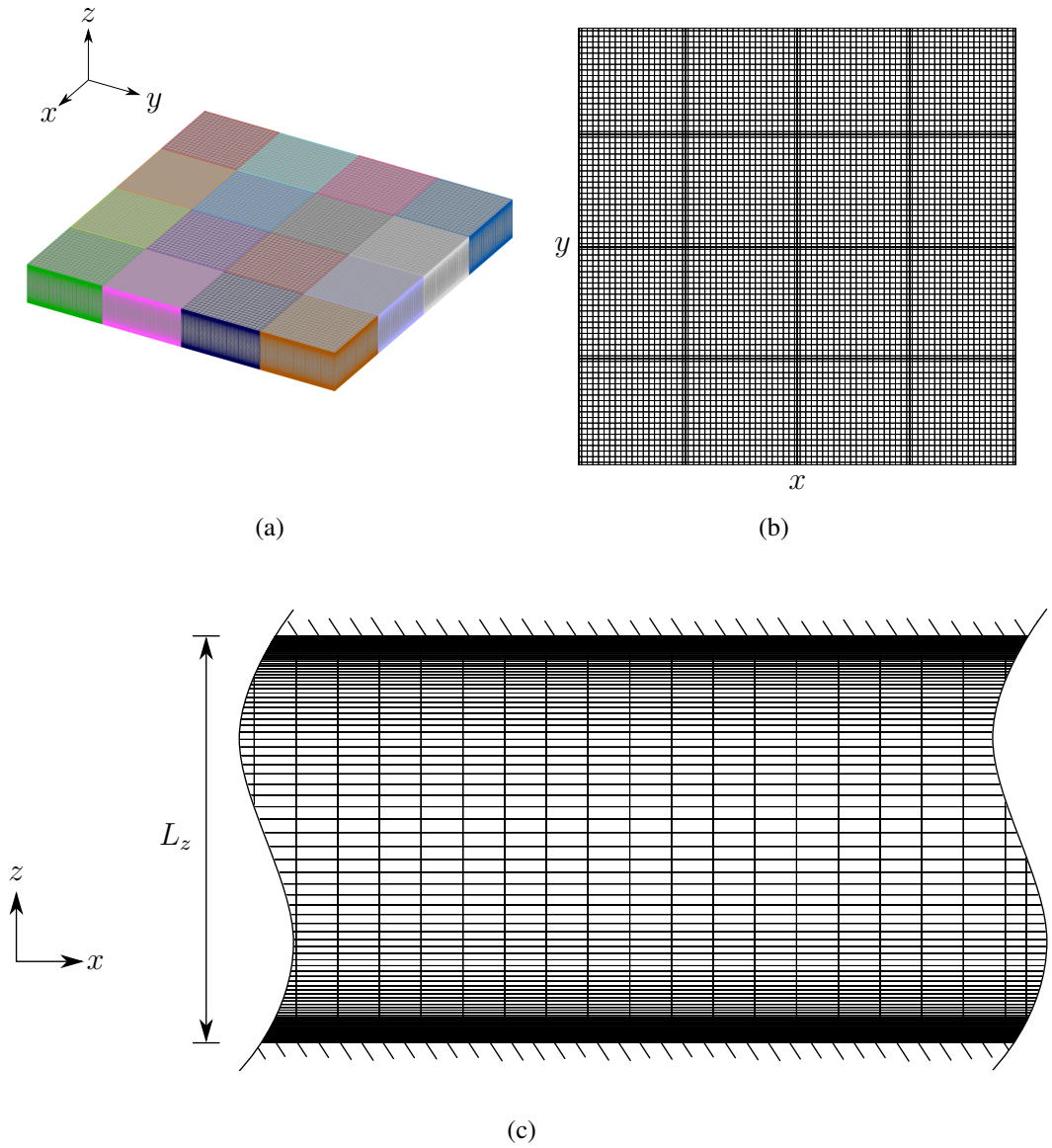

Figure 7.2: Mesh employed for computing Rayleigh-Bènard convection cases showing (a) 3D view of multi-block arrangement, (b) node resolution in the $x - y$ plane and (c) node resolution in the $x - z$ plane. The mesh has a resolution of $80 \times 80 \times 100$.

7.3 Identification of coherent structures

A distinct feature of Rayleigh-Bènard convection is the persistence of large scale coherent flow structures despite the high turbulence levels achieved at high Rayleigh numbers (Chu and Goldstein, 1973; Grötzbach, 1982; Theerthan and Arakeri, 1994). The time-dependent, three-dimensional, chaotic nature of the turbulence associated with these motions, however, makes the task of identifying and visualizing the flow structures quite challenging.

The more orthodox visualization methods involve viewing velocity streamlines, contours, vector plots, and isosurfaces of temperature in one given instantaneous realization. Whilst these clearly provide useful information in most cases, and are employed here, several authors have proposed other, more elaborate, methods by which to identify such structures. Most of these centre around associating 'coherent structures' with vortical motion and typically make use of the eigenvalues and eigenvectors of the velocity gradient tensor, A_{ij};

$$A_{ij} = \frac{\partial U_i}{\partial x_j} \tag{7.3.1}$$

The second of the three invariants of A_{ij} was used by Hunt et al. (1988) to define the so-called Q-criterion;

$$Q = \frac{1}{2}\left(\Omega_{ij}\Omega_{ij} - S_{ij}S_{ij}\right) \tag{7.3.2}$$

where S_{ij} and Ω_{ij} are the symmetric (mean rate of strain) and anti-symmetric (mean rate of rotation) parts of A_{ij} respectively;

$$S_{ij} = \frac{1}{2}\left(\frac{\partial U_i}{\partial x_j} + \frac{\partial U_j}{\partial x_i}\right), \quad \Omega_{ij} = \frac{1}{2}\left(\frac{\partial U_i}{\partial x_j} - \frac{\partial U_j}{\partial x_i}\right) \tag{7.3.3}$$

The Q criterion thus describes the balance between the moduli of the shear strain rate tensor and rate of rotation tensor. In regions where Q is negative, the strain rate presides over the rate of rotation. For regions of positive Q, rotation is the dominant form of motion and it is these areas that Hunt et al. (1988) define as areas containing a coherent vortex. The Q-criterion will thus be used in the results section of this chapter to provide visualization of the coherent structures.

Further details on methods to identify coherent structures in Rayleigh-Bènard convection can be found in Kenjereš and Hanjalić (1999a).

7.4 Non-magnetic Rayleigh-Bènard convection

As a validation exercise, computations were first performed at the lower Rayleigh number of $Ra = 6.3 \times 10^5$ to compare against the DNS results of Wörner (1994). Long-term time averaged temperature profiles in the vertical plane, presented in Figure 7.3, show excellent agreement with the DNS data.

Both turbulence models tested returned zero contribution to the modelled turbulence and hence they predict identical long-term time averaged temperature profiles. Since the DNS data indicates that the flow does demonstrate a small amount of turbulence, it is likely that the Rayleigh number of this particular flow is too low for the models to sustain what may be a rather low level of turbulence. The close agreement between the URANS simulations and the DNS supports the conclusion that the turbulence levels should be quite low, and not particularly important, in this case.

The profiles exhibit a uniform core region, which results from the mixing of the fluid by convective and turbulent motion, flanked by thermal boundary layers. The profiles are characteristic of Rayleigh-Bènard convection and this, together with the excellent agreement with the DNS data, provide confidence in the solver and case set-up.

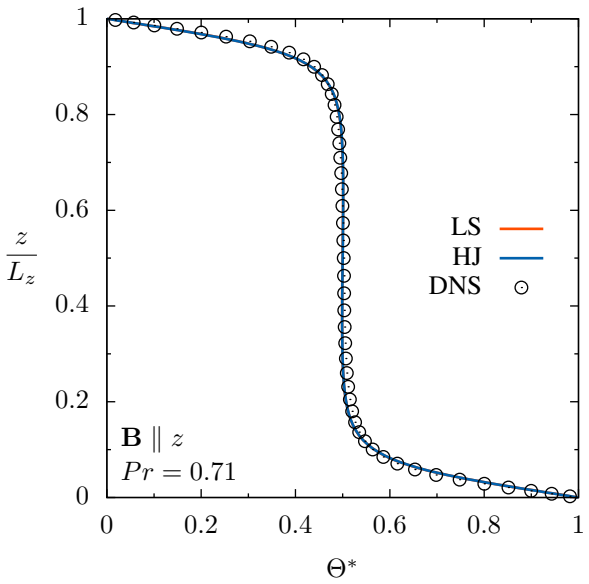

Figure 7.3: Long-term time averaged vertical non-dimensional temperature profiles in non-magnetic Rayleigh-Bènard convection at $Ra = 6.3 \times 10^5$ and $Pr = 0.71$. Comparisons of the LS and HJ models with the DNS results from Wörner (1994). Both models return identical profiles, and hence only the last plotted (the line for the HJ model) is visible.

7.5 Moderate Prandtl number: $Pr = 0.71$

Results are presented here for magnetic Rayleigh-Bènard convection at the moderate Prandtl number of $Pr = 0.71$. Both a vertical and horizontally oriented magnetic field are considered and each of these will, in a similar fashion to the effects seen in Chapter 6, influence the flow in different ways. In both cases, only motion across the magnetic field lines will generate a Lorentz force. For the vertical magnetic field, where the gravitational vector is parallel to the magnetic field lines, this will initially oppose the onset of convective motion (since roll cells cannot exist without horizontal motion) and, after convection has commenced, will tend to change the horizontal lengthscale of the rolls cells (through the action of the Lorentz force). For the horizontal magnetic field, the Lorentz force is active in the vertical and other horizontal direction. From the earlier discussion in Section 2.3 and Subsection 4.1.2, it was seen that the magnetic field tends to elongate vortices along the direction of the magnetic field lines by selectively destroying all velocity gradients in that direction. Since convection cells are simply just arrangements of vortices, it is expected that whatever cell structures exist in the plane normal to the magnetic field will elongate across the domain.

7.5.1 Influence on the mean flow

Figure 7.4 shows the effect of both a vertical and horizontal magnetic field on the long-term time averaged temperature in the wall-normal direction where, for the vertical magnetic field, comparisons are made between the HJM and LSM models. Generally, a low strength magnetic field ($Ha = 20$), has little effect when in the vertical direction and provides slight, but noticeable, deformation in the temperature profile when in the horizontal direction. As the field strength increases, the temperature profiles continue to deform and, up to around $Ha = 200$, show a continuing elongation of the uniform core region and a thinning of the thermal boundary layers. The HJM predicts this transition, for both field directions, to be more gradual than that shown by the LSM model. With the latter, very little deformation is seen at $Ha = 20$ and, after that, little difference is seen between $Ha = 50$, 100 and 200. Simulations were not performed for $Ha > 200$ with the LSM model since, as will be discussed later, by this field strength both models return zero contribution to the modelled turbulence and thus would report the same temperature profiles (as they did with the non-magnetic Rayleigh-Bènard convection in Section 7.4).

With the horizontal magnetic field, this deformation of the temperature profile is accompanied by a clear gradual thickening of the thermal boundary layers, in additional to the extension of the near-wall linear change in temperature. After $Ha = 200$ the HJM model predicts, for both magnetic field directions, a significant inversion in the temperature profile and, for the highest magnetic field strength, an increase in the size of the thermal

boundary layers beyond that seen in the neutral state. These results are qualitatively consistent with those by Hanjalić and Kenjereš (2000) and Kenjereš and Hanjalić (1999b, 2004) who used a three equation $k - \varepsilon - \theta^2$ eddy-viscosity model (with the electromagnetic extensions described in Section 4.4) though they report the deformation in the temperature profile to be more significant at lower Ha.

7.5.2 Influence on the turbulence

In non-magnetic convection an extension to the uniform core region is usually brought about by an increase in Rayleigh number, since the higher level of associated turbulence leads to increased mixing. From the earlier results presented in Chapter 6, however, it was seen that the magnetic field generally acts to reduce turbulence throughout the flow and the strength of this effect increases with Ha. Profiles of the contributions to the turbulent kinetic energy, in Figure 7.5 for a horizontal magnetic field and a selection of Ha, show that this is indeed the case here. As the Hartmann number increases, both resolved and modelled contributions fall fairly uniformly across the channel. A curious exception is the prediction of an increase in the resolved contribution[1] to the total turbulent kinetic energy at $Ha = 20$ by the LSM model. For $Ha \geq 50$, the magnetic field has reduced turbulence to the extent that both models provide no contribution and only large scale deterministic motion remains. In the neutral state, there are some clear differences between the models in terms of contributions towards the total turbulence; the LSM predicts a much greater (around twice) contribution from modelled k. Total turbulence levels predicted by the models are comparable, and thus this is mostly considered to be due to the ability of the stress transport model to provide a better representation of the normal stresses (and hence k).

For the HJM model, profiles of the long-term time averaged normal stresses are provided in Figure 7.6 for the vertical magnetic field and in Figure 7.7 for the horizontal magnetic field. In the neutral state, the modelled contribution to the normal stresses is uniform across the channel with slightly reduced values of $\overline{ww}$ compared to the two horizontal components. The distribution of the resolved contributions follows what one would expected from a flow comprising a series of transient convective roll cells between two horizontal walls; large peaks in the horizontal components towards the walls where predominantly (correlated) horizontal motion occurs (at the tops and bottoms of the roll cells) together with large values of the vertical component in the central region, where motion is predominantly vertical.

At the lowest magnetic field strength considered ($Ha = 20$), both orientations of the magnetic field can be seen to suppress all normal stress components uniformly across the

[1] Though the scale of the plot makes this difficult to see, the modelled contribution to k in the centre falls by around 9%.

flow and by $Ha = 50$, as the turbulent kinetic energy profiles showed earlier, the modelled contributions to all stresses vanish. Beyond $Ha = 50$, the different orientations have significantly different effects on the anisotropy in the flow. The vertical magnetic field appears to have only a small effect; the reduction in the vertical component appears to be more gradual compared to both horizontal components (these are equal due to homogeneity between those directions). The horizontal magnetic field, however, generates significantly increased levels of anisotropy between the horizontal components with $\overline{\hat{V}\hat{V}}$ demonstrating peak levels higher than those seen in the neutral state. This is despite an active Lorentz force in that direction. The mean Lorentz force only vanishes in the direction of the magnetic field and the component aligned with that sees a reduction consistent with that seen in $\overline{\hat{W}\hat{W}}$. Exactly why this occurs will be fully explained below, but it is a direct consequence of how the magnetic field affects the structure of the convection cells within the flow.

Long-term time averaged profiles of the vertical component of the turbulent heat flux are shown in Figure 7.8 for a selection of Ha and both magnetic fields, where again the contributions from both the resolved large-scale motion and the turbulence model have been provided. In a small selection of the plots, the orange dashed lines provide profiles of the modelled contribution as computed by the LSM. At $Ha = 0$, and for the HJM model, the modelled part forms the main contribution in the near-wall regions with a peak that has a magnitude around 50% of the total seen in the channel centre. This contrasts with the modelled contribution as predicted by the LSM which predicts significantly higher peaks which have a much wider base[1]. Both heat flux models return very small values in the central section, with the LSM actually returning negative values over a small region (not shown), and the resolved contribution dominates.

The lowest magnetic field strength considered, in both directions, provides only a modest reduction in the turbulent heat flux uniformly across the channel, but by $Ha = 50$ the vertically orientated magnetic field has completely suppressed the modelled contribution. For the same Hartmann number the horizontal magnetic field, however, only reduces $\overline{w\theta}$ levels to half those seen at $Ha = 20$. Since the temperature profiles in Figure 7.4 show no discernible difference between the magnetic field directions at $Ha = 50$, increased levels of $\overline{u_i\theta}$ must arise from increased levels of $\overline{ww}$ (since the term involving $\overline{ww}\,\partial\Theta/\partial z$ is, as discussed in the next paragraph, effectively the only contributor to the vertical heat flux in the GGDH formulation). Figure 7.7 confirms this to be the case.

Predictions of little to no $\overline{w\theta}$ in the core region is, of course, due to the form of the models employed; both the eddy-diffusivity, Equation (4.4.24), and GGDH, Equation (4.3.53) return values only in proportion to the mean temperature gradients. As Figure 7.4 shows, these initially vanish over a large section of the core of the domain and $\partial\Theta/\partial z$ actually

[1]Unfortunately, data was not collected for the resolved contribution and thus a full quantitative comparison is not possible.

exhibits a change in sign as the magnetic field strength increases and the temperature profile inverts across the core region. Whilst the GGDH would be expected, in principle, to provide better predictions (since it sensitizes $\overline{u_i\theta}$ both to the Reynolds stress components and other mean gradients) the lack of any long-term time averaged turbulent shear stress and any horizontal mean temperature gradients means the only non-zero term in the GGDH formulation is the one containing $\overline{ww}$ and $\partial\Theta/\partial z$. Other components of the heat flux containing that temperature gradient are multiplied by the turbulent shear stresses which also vanish. Thus, in practice, both the eddy-viscosity and GGDH formulations reduce to similar forms in this flow (at least in terms of time-averaged quantities).

More advanced models for the heat flux have been proposed in the literature, including an algebraic closure by Kenjereš and Hanjalić (1999b) which retains all the major production terms in the $\overline{u_i\theta}$ equation. Though, as detailed earlier in Subsection 4.3.3, this would capture some processes absent from the GGDH, results obtained here (with the GGDH) are in good agreement with those presented by Hanjalić and Kenjereš (2000) and Kenjereš and Hanjalić (1999b). In addition, the primary effect of the magnetic field is to suppress the modelled contribution and by $Ha = 50$, this is completely absent. Results presented by Hanjalić and Kenjereš (2000), who utilized a more advanced modelled form of $\overline{u_i\theta}$, showed the modelled contribution was completely suppressed by $Ha = 100$, though they do not provide results between this and $Ha = 20$. Further exploration of this, and the influence of the magnetic field on the thermal fields in general, is proposed as further work in Chapter 8.

7.5.3 Influence on the flow structure

From the preceding, more quantitative, analysis it was seen that the general effect of the magnetic field is to reduce turbulence levels across the channel and to deform or even invert the mean temperature profile. Explanations for this behaviour can be found through investigating the effect of both magnetic field directions on the coherent structures identified within the flow.

Figures 7.9, 7.10 and 7.11 reveal that, depending on its orientation, the magnetic field brings about strikingly different reorganisations of the thermal and dynamic structures in the flow. In the neutral state, instantaneous realisations of the temperature contours in the central horizontal (Figure 7.9) and vertical (Figure 7.10) planes demonstrate the existence of a small number of thermal plumes which sparsely populate the domain. At $Ha = 50$, both orientations of the magnetic field cause the plumes to break down into a larger number of thinner, more cylindrical, plumes. Two effects contribute to this. The first, in the case of the vertical magnetic field, is the direct action of the mean Lorentz force which opposes motion in both horizontal directions and thus causes the plumes to be ‘squeezed’ laterally. The second, which is applicable to both cases, is a reduction in

horizontal turbulent mixing through suppression of the turbulent kinetic energy (clearly shown in Figure 7.5).

Beyond $Ha = 50$, differences between the effects of the two magnetic field orientations become quite apparent. With the vertical magnetic field, the previously mentioned breakdown in plume structures continues and by $Ha = 800$, the strongest magnetic field strength considered, the plumes are substantially thinner that at $Ha = 0$ and are considerably more ordered. The temperature isosurfaces in Figure 7.10, which are coloured by the non-dimensional vertical velocity, show that the intensity of the vertical motion significantly reduces between $Ha = 50$ and $Ha = 800$. As discussed previously, the tendency of the Lorentz force to inhibit horizontal motion will, for sufficiently strong magnetic fields, lead to a reduction in vertical motion via continuity. With the horizontal magnetic field, the flow structures become increasingly aligned with the direction of the magnetic field vector and by $Ha = 800$, Figure 7.11 shows complete alignment with the axes of the roll cells. The contrast between the streamline plots at $Ha = 800$ for both field directions demonstrates that the mutual orientation between the buoyant and Lorentz forces is very influential in the evolution of the flow.

To illustrate the transformation of the flow structure further, Figure 7.12 and Figure 7.13 provide instantaneous isosurfaces of the Q-criterion and non-dimensional vertical velocity component W^* respectively. With the Q-criterion, a positive value has been chosen to show regions where the rotation rate exceeds the strain rate. This corresponds to the presence of a vortex. To provide a valid comparison, this value is kept constant across all the cases presented. With the isosurfaces of velocity, regions of fluid connected by a constant velocity provide some indication of coherency since there will, invariably, be paths around a particular convection cell where this is true. The flow development and structure illustrated by both figures is consistent with the trends and structural changes described above. At the highest Hartmann number, the roll cells becomes quite clearly aligned in the direction of their respective magnetic fields. This kind of alignment has been predicted by other numerical simulations, including those by Varshney and Baig (2008a) (which were discussed earlier in Section 2.4, see Figure 2.13) and more recent DNS results by Yanagisawa et al. (2015). For the horizontal magnetic field, horizontal motion of the roll cells is now primarily in the y direction with very little in the x-direction. As a result, the primary velocity component associated with the roll cells in the near-wall region will be V. Thus, the resolved $\overline{\hat{V}\hat{V}}$ normal stress component (as the one containing the $\overline{V}\,\overline{V}$ moment) might be expected to show larger values in this case than in those cases where these structures do not align with the magnetic field. This would provide some explanation for the significant increase in $\overline{\hat{V}\hat{V}}$ that was seen in Figure 7.7.

The alignment of the vortex structures (roll cells) with the magnetic field vector was something discussed extensively in Chapter 2 and Subsection 4.1.2. It arises from a requirement to conserve the component of angular momentum parallel to the magnetic field

despite a continual reduction in the kinetic energy of the fluid through Joule dissipation. As Subsection 4.1.2 demonstrated mathematically (for an inviscid fluid), the elimination of Joule dissipation will occur when the velocity vector exhibits no variation in the direction of the magnetic field (since this eliminates the generation of current). The results presented here clearly demonstrate that this alignment has taken place. With Rayleigh-Bènard convection, so long as the vertical buoyant force is sufficient to overcome viscous dissipation the fluid will continue to move. The argument concerning angular momentum is not restricted to any particular magnetic field direction and, as such, it can be applied in both cases considered here. Elongation of the plume structures in the vertical direction, in an attempt to minimize the vertical velocity gradients, is shown somewhat in Figure 7.10.

To reveal the effect of the magnetic field on the length of the plume structures in the vertical direction, Figure 7.14 provides a side view of the Q-criterion, which takes the same value as it did previously in Figure 7.12. At $Ha = 100$, both magnetic field directions can be seen to modestly elongate these plumes towards the walls. This provides an explanation as to why the magnetic field caused an extension in the uniform temperature core region shown earlier in the mean temperature profiles (Figure 7.4). With the vertical magnetic field, and to some extent with the horizontal magnetic field, the simultaneous thinning and stretching of the thermal plumes in the vertical direction creates a coherent 'channel' which facilitates better heat transfer between the walls. This is in agreement with the results presented by Hanjalić and Kenjereš (2000) and leads to the previously observed thinning of the thermal boundary layers between $20 < Ha < 200$.

Beyond $Ha = 200$, Figure 7.14 shows that the height of the plume structures begins to reduce and at $Ha = 800$ the gap between the top of the tops of the structures and the walls is notably larger than at $Ha = 0$ and $Ha = 100$.[1] The fact the plumes penetrate less into the boundary layers, combined with the observed reduction in resolved turbulent fluctuations (and hence mixing) in the near-wall regions that the earlier quantitative comparisons suggested (Figure 7.6, for example), leads one to conclude that conductive heat transfer from the walls into the fluid will increase in importance. This would explain the previously noted thickening of the thermal boundary layers observed for both magnetic field directions at $Ha = 800$.

The inversion in the temperature profiles at high Hartmann number, for the vertically oriented magnetic field at least, can thus be considered the result of a combination of a number of the above effects. First, a reduction in the resolved contribution to the turbulence within the core region will reduce the extent to which hot and cold fluid is mixed. Second, the formation of a coherent cylindrical channel enables hot fluid to reach the upper (or lower) half of the domain much more readily than it did before. Finally, since

[1] Note that the reference to a 'gap' here is purely figurative. The Q-criterion only provides a representation of those regions for which rotational strain is dominant and changing the value of the isosurface will produce different a representation. However, since the value of the isosurface here is constant across the cases, the comparison is valid.

the vertical length scale associated with the plume structures is reduced, and with it the degree to which they penetrate the boundary layers, it leads to, on average, an increase (or decrease) in temperature in the region just outside the thermal boundaries.

Finally, it is also worth noting that simulations performed without the additional electromagnetic terms in the eddy-viscosity formulation (i.e. the LS model) did not predict such a significant structural reorganisation of the flow. Qualitative comparisons, provided in Figure 7.15, clearly show the LS model predicts very little change from the neutral state, even at $Ha = 100$. Hence, whilst in the analysis of the earlier channel flow cases in Chapter 6 the additional electromagnetic terms were shown to either have little influence or over predict the damping of the turbulence, the reduction in turbulent energy they provide here is essential in order to bring about the predicted structural reorganization.

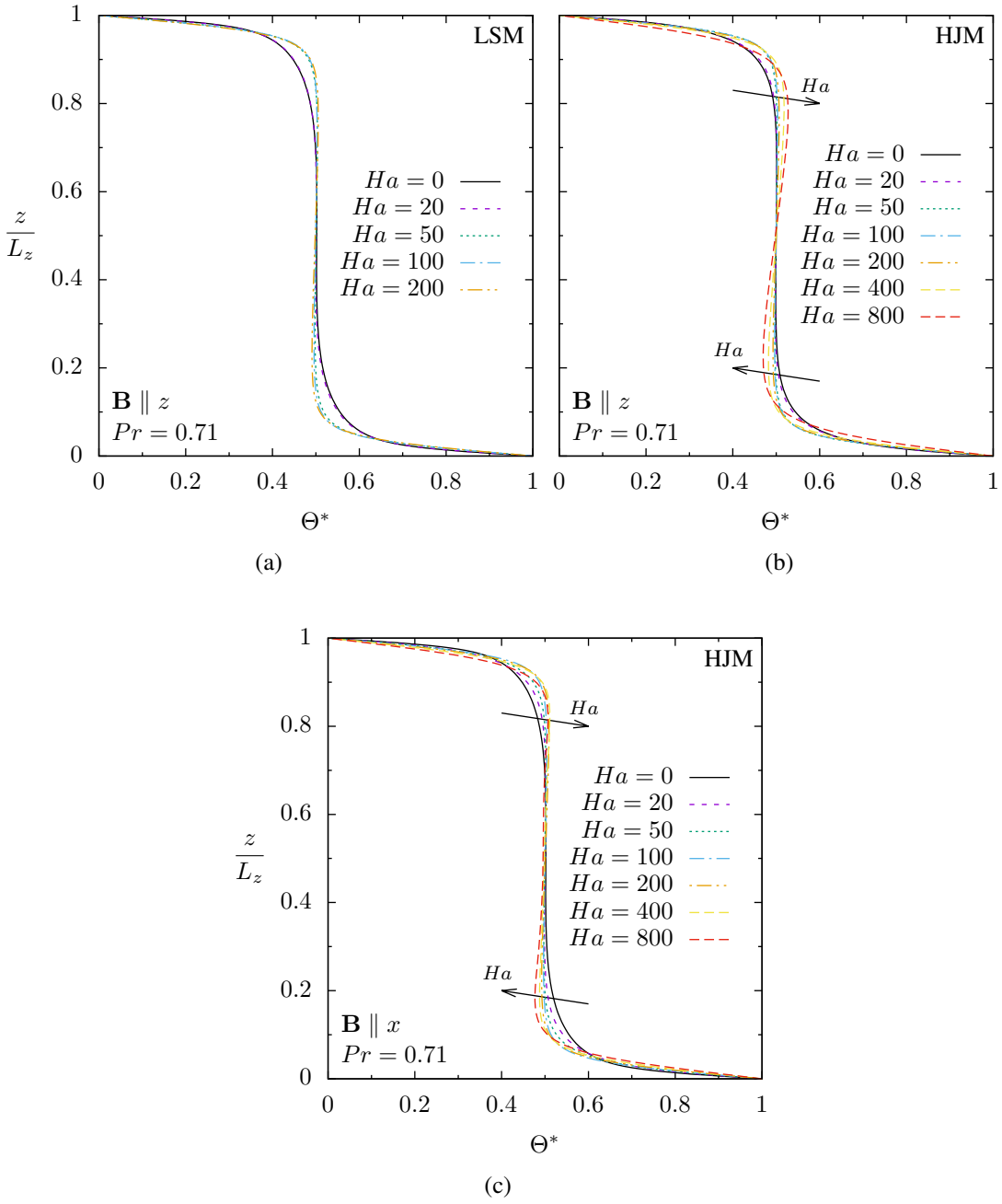

Figure 7.4: Long-term time averaged profiles of the non-dimensional temperature, Θ^*, in magnetic Rayleigh-Bènard convection. For a vertically oriented magnetic field comparisons are made between the LSM (a) and HJM (b) models. (c) provides results with the HJM model for a horizontally oriented magnetic field over a range of Hartmann numbers; $Ra = 10^7$, $Pr = 0.71$.

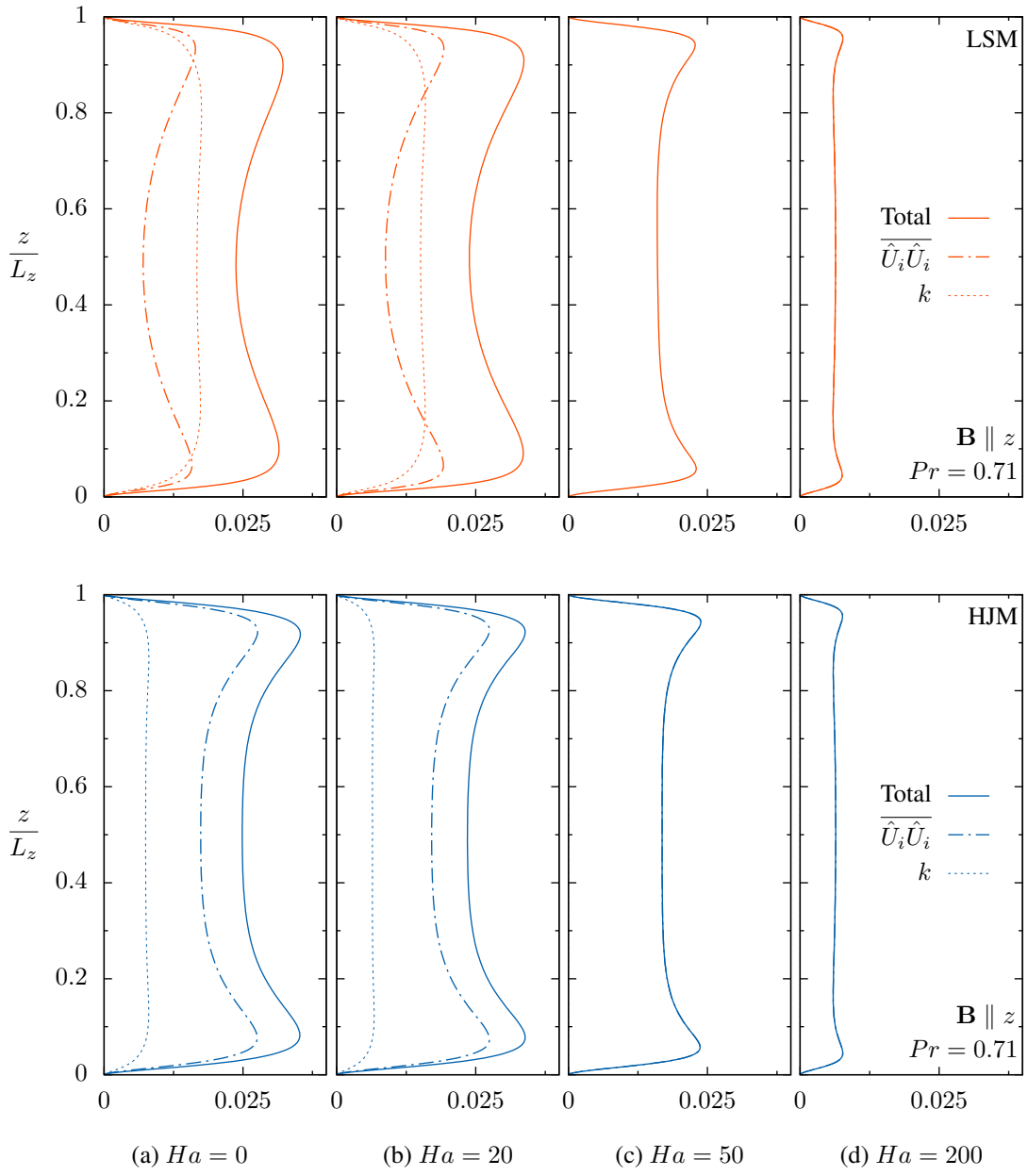

(a) $Ha = 0$ (b) $Ha = 20$ (c) $Ha = 50$ (d) $Ha = 200$

Figure 7.5: Long-term time averaged profiles of the contributions to the non-dimensional turbulent kinetic energy, k^*, in Rayleigh-Bènard convection subjected to a vertical magnetic field. Comparisons between LSM (top) and HJM (bottom) models for selected Hartmann numbers; $Ra = 10^7$, $Pr = 0.71$, $\mathbf{B} \parallel B_z$.

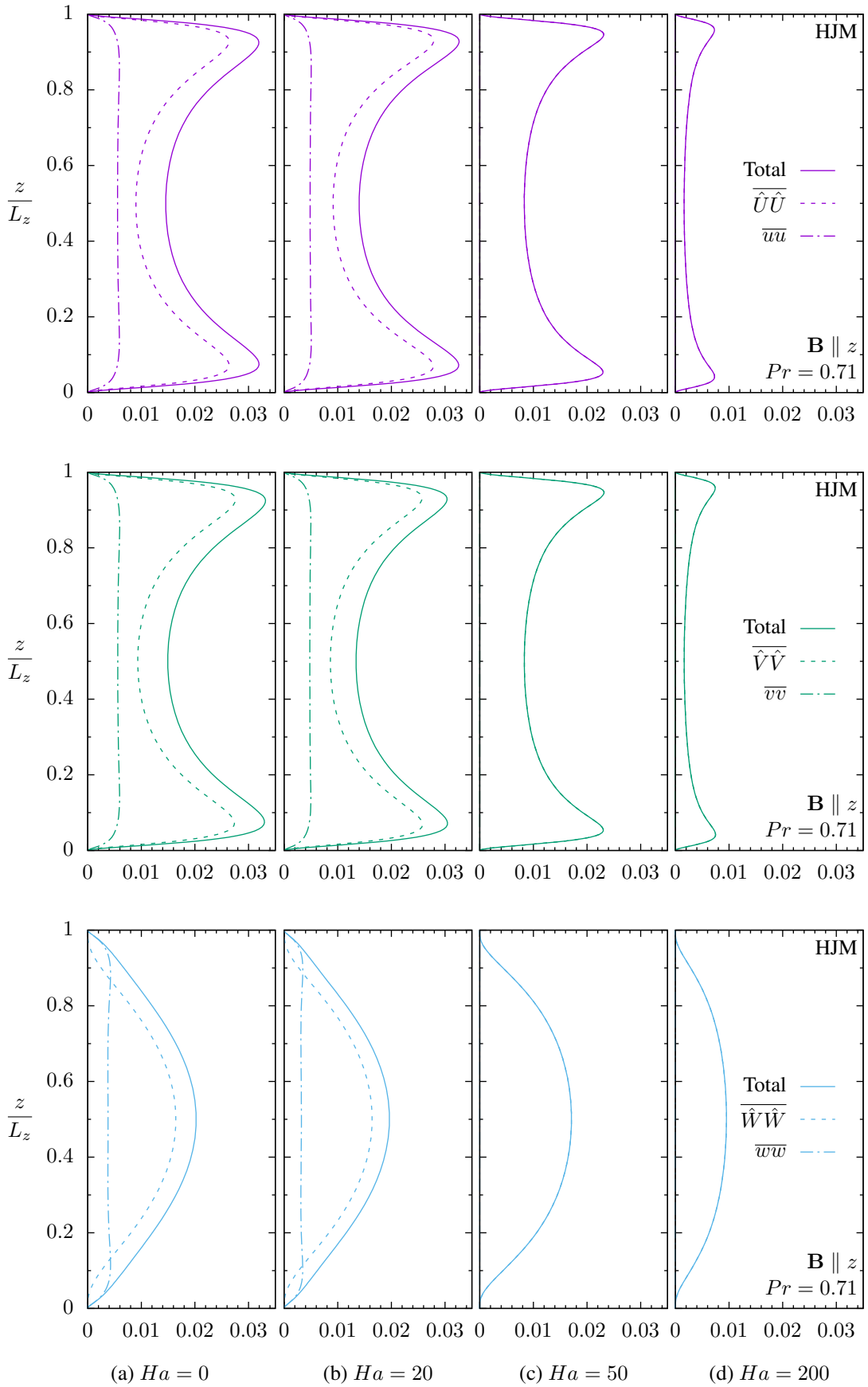

(a) $Ha = 0$ (b) $Ha = 20$ (c) $Ha = 50$ (d) $Ha = 200$

Figure 7.6: Long-term time averaged profiles of the contributions to the non-dimensional normal stresses, $\overline{uu}^*$ (top), $\overline{vv}^*$ (middle) and $\overline{ww}^*$ (bottom), in Rayleigh-Bènard convection subjected to a vertical magnetic field at selected Hartmann numbers; $Ra = 10^7$, $Pr = 0.71$, $\mathbf{B} \parallel B_z$. Homogeneity between the horizontal directions means those components are equal.

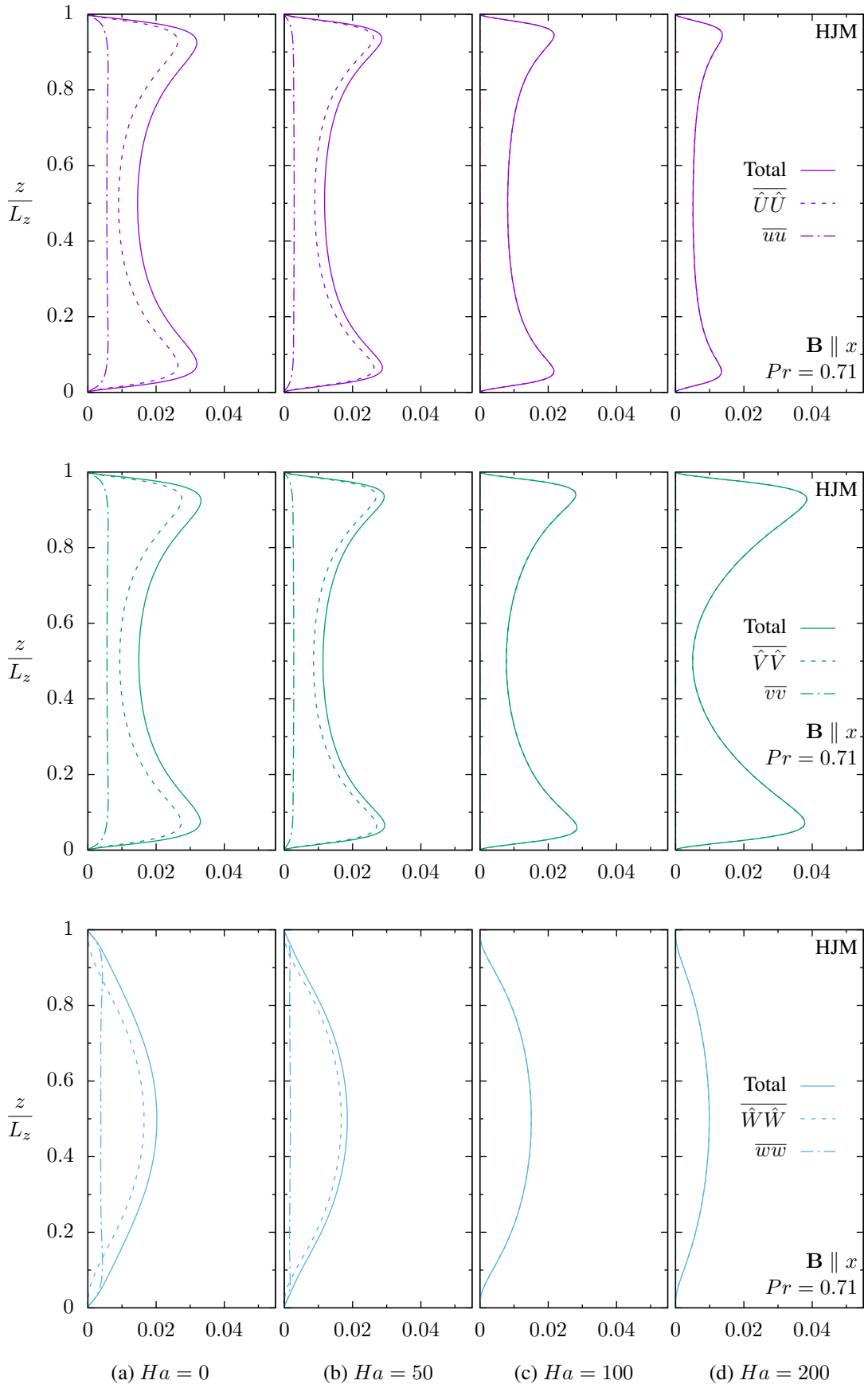

(a) $Ha = 0$ (b) $Ha = 50$ (c) $Ha = 100$ (d) $Ha = 200$

Figure 7.7: Long-term time averaged profiles of the contributions to the non-dimensional normal stresses, $\overline{uu}^*$ (top), $\overline{vv}^*$ (middle) and $\overline{ww}^*$ (bottom), in Rayleigh-Bènard convection subjected to a horizontal magnetic field at selected Hartmann numbers; $Ra = 10^7$, $Pr = 0.71$, $\mathbf{B} \parallel B_x$.

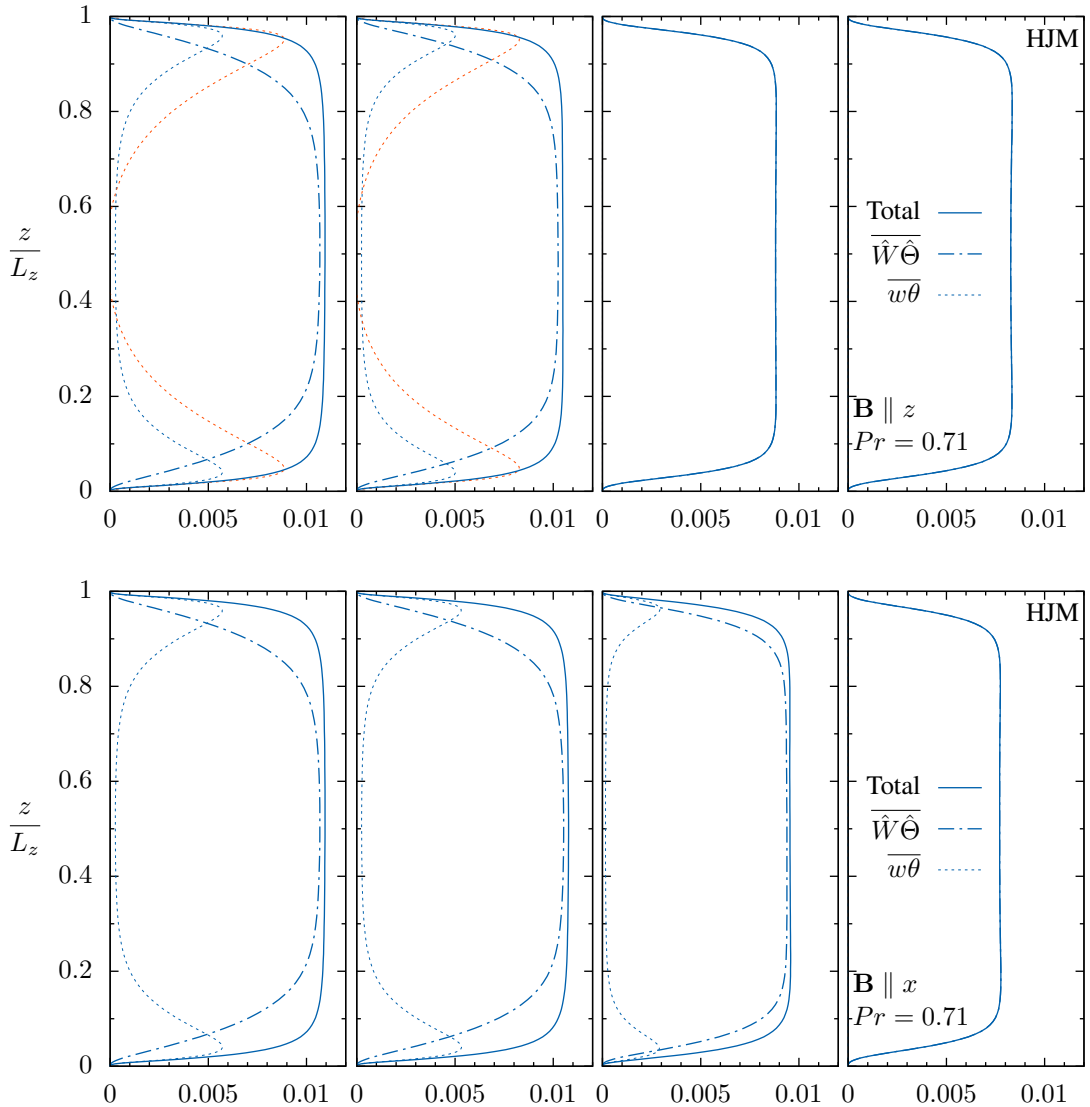

(a) $Ha = 0$ (b) $Ha = 20$ (c) $Ha = 50$ (d) $Ha = 200$

Figure 7.8: Long-term time averaged profiles of the contributions to the non-dimensional wall-normal heat flux in Rayleigh-Bènard convection subjected to a vertical (top) and horizontal (bottom) magnetic field at selected Hartmann numbers. HJM model with additional selected profiles of the modelled contribution obtained with the LSM model (orange dashed lines) at $Ha = 0, 20$ and with a vertical magnetic field. $Ra = 10^7$, $Pr = 0.71$.

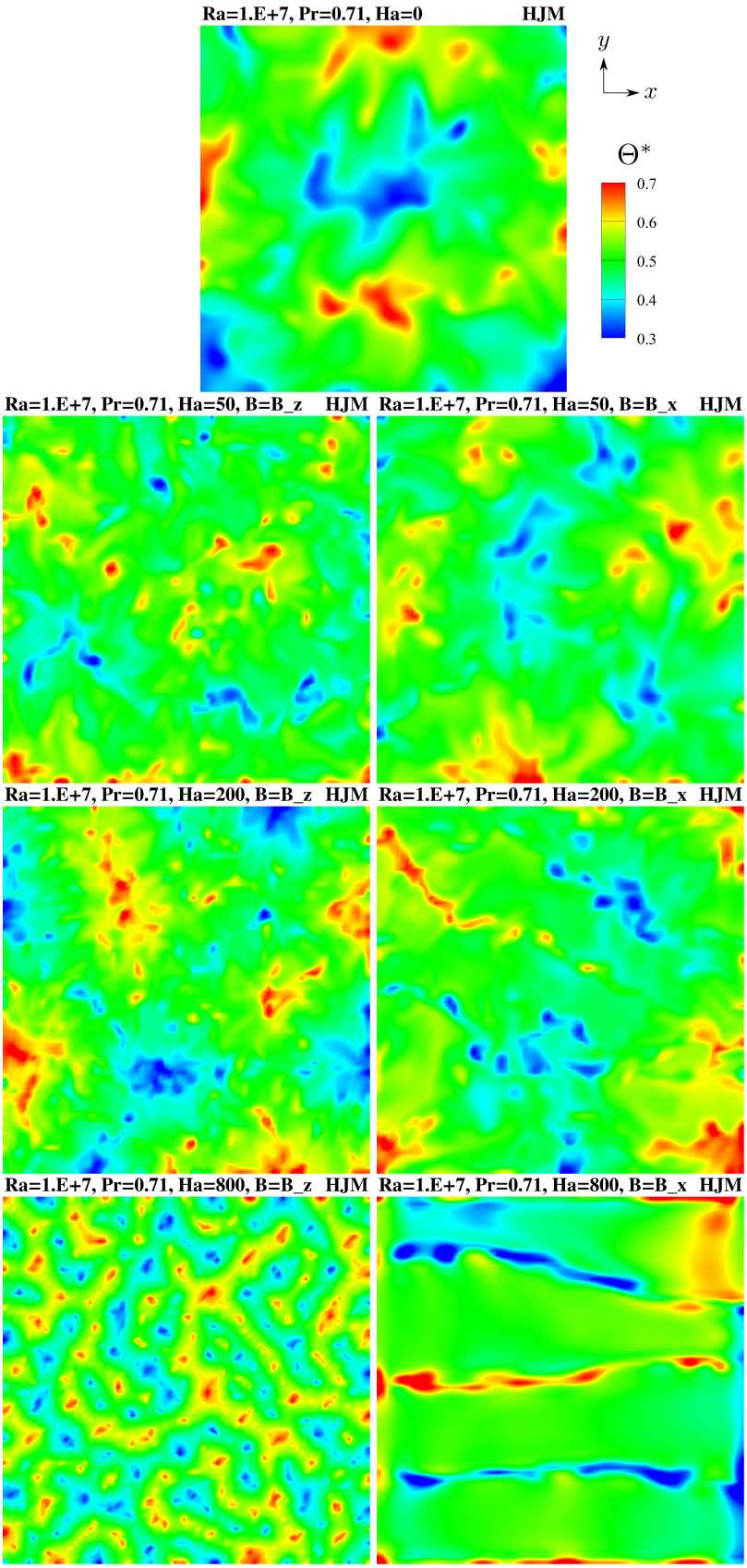

Figure 7.9: Effect of magnetic field strength and orientation on the instantaneous temperature distribution in the central $x-y$ plane $(z/L_z = 0.5)$. Comparisons between vertically (left) and horizontally (right) oriented magnetic fields for increasing Ha. HJM model; $Ra = 10^7$, $Pr = 0.71$.

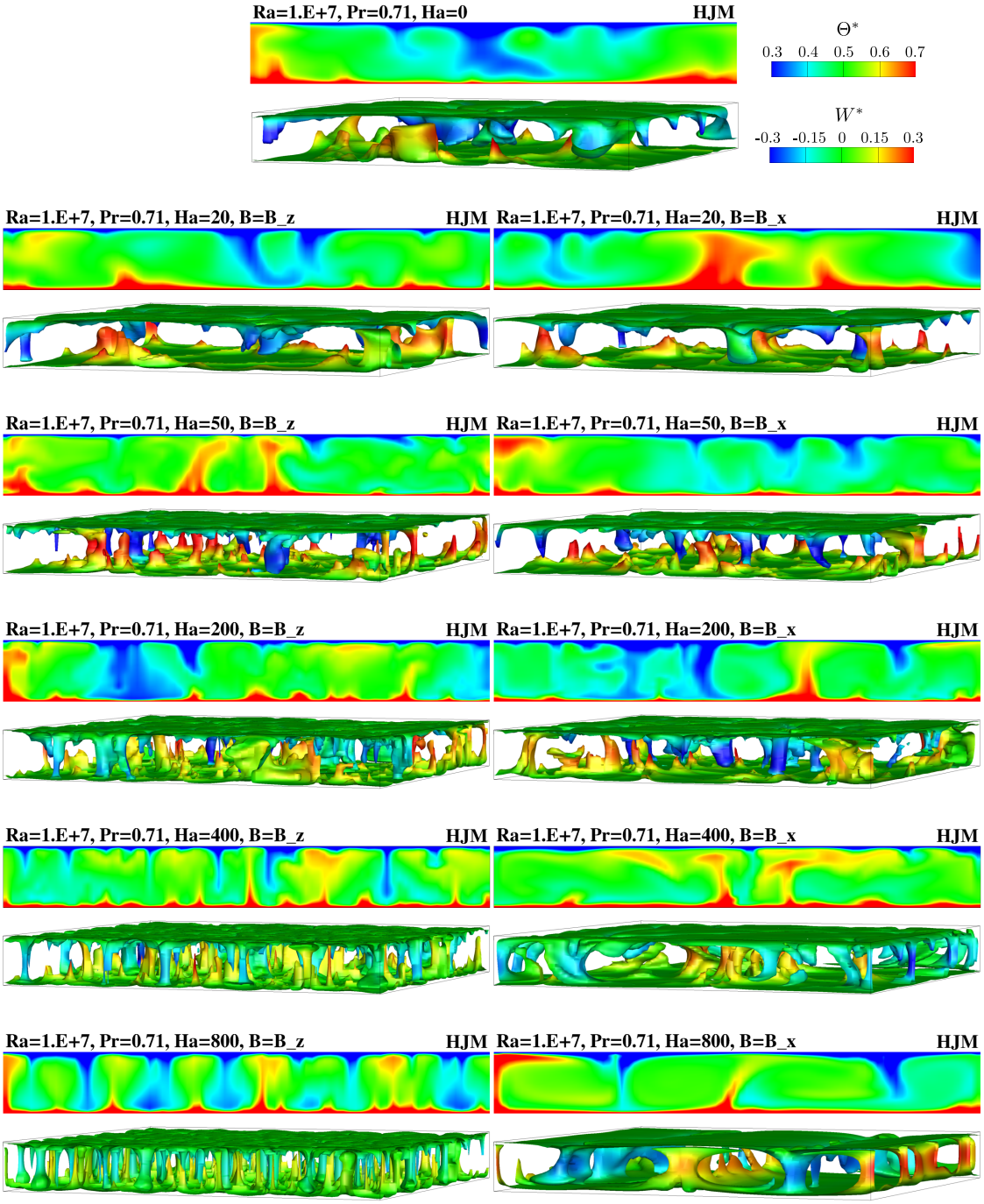

Figure 7.10: Effect of magnetic field strength and orientation on the instantaneous temperature distribution in the central $y-z$ plane $(x/L_x = 0.5)$ and isosurfaces of temperature $(\Theta^* = 0.35, 0.65)$ coloured by the non-dimensional vertical velocity $(-0.3 < W^* < 0.3)$. Comparisons between a vertically (left) and horizontally (right) oriented magnetic field for increasing Ha. HJM model; $Ra = 10^7$, $Pr = 0.71$.

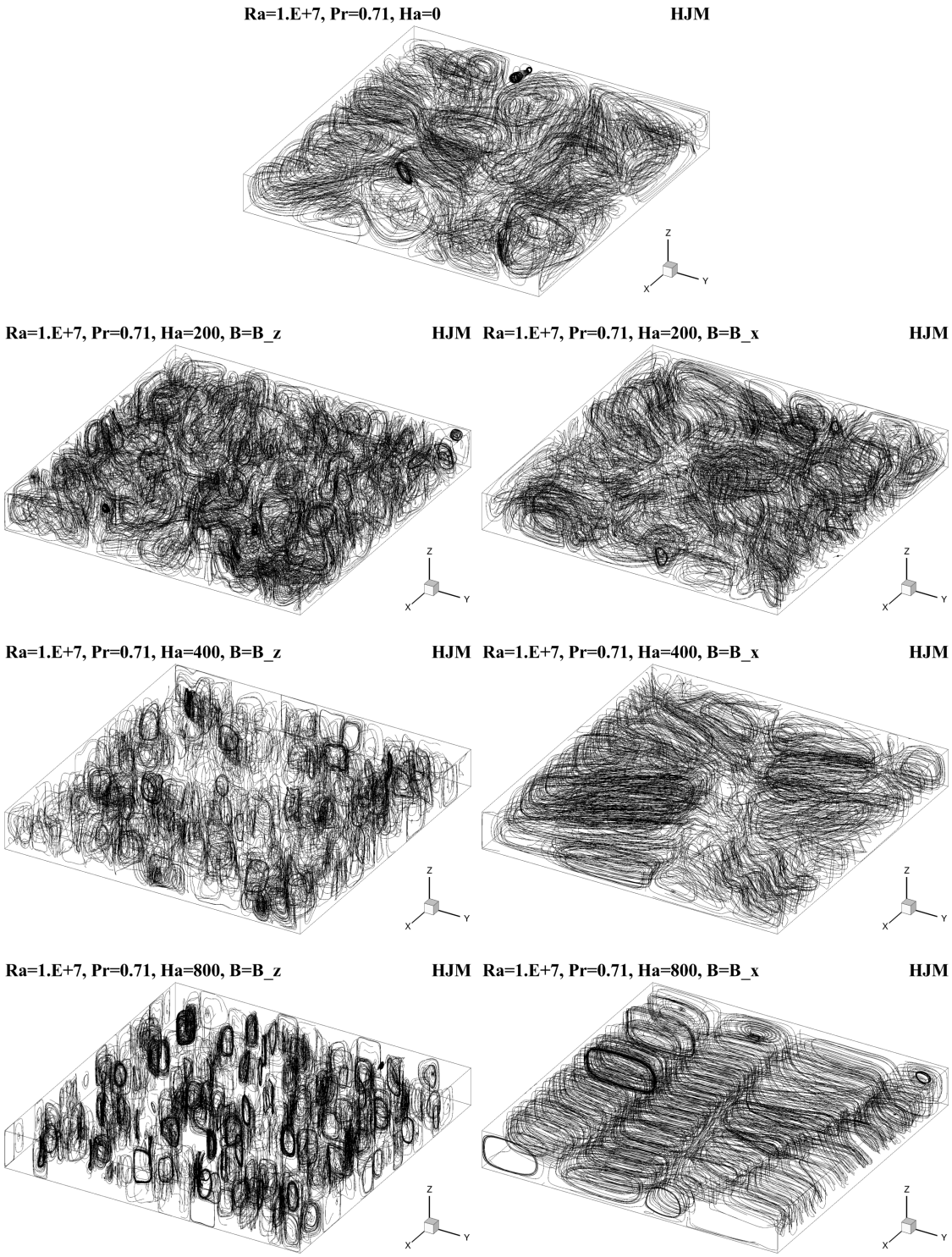

Figure 7.11: Instantaneous streamlines showing the changes in flow structure brought about by the application of a vertical (left) and horizontal (right) magnetic field to Rayleigh-Bènard convection for increasing Ha; $Ra = 10^7$, $Pr = 0.71$.

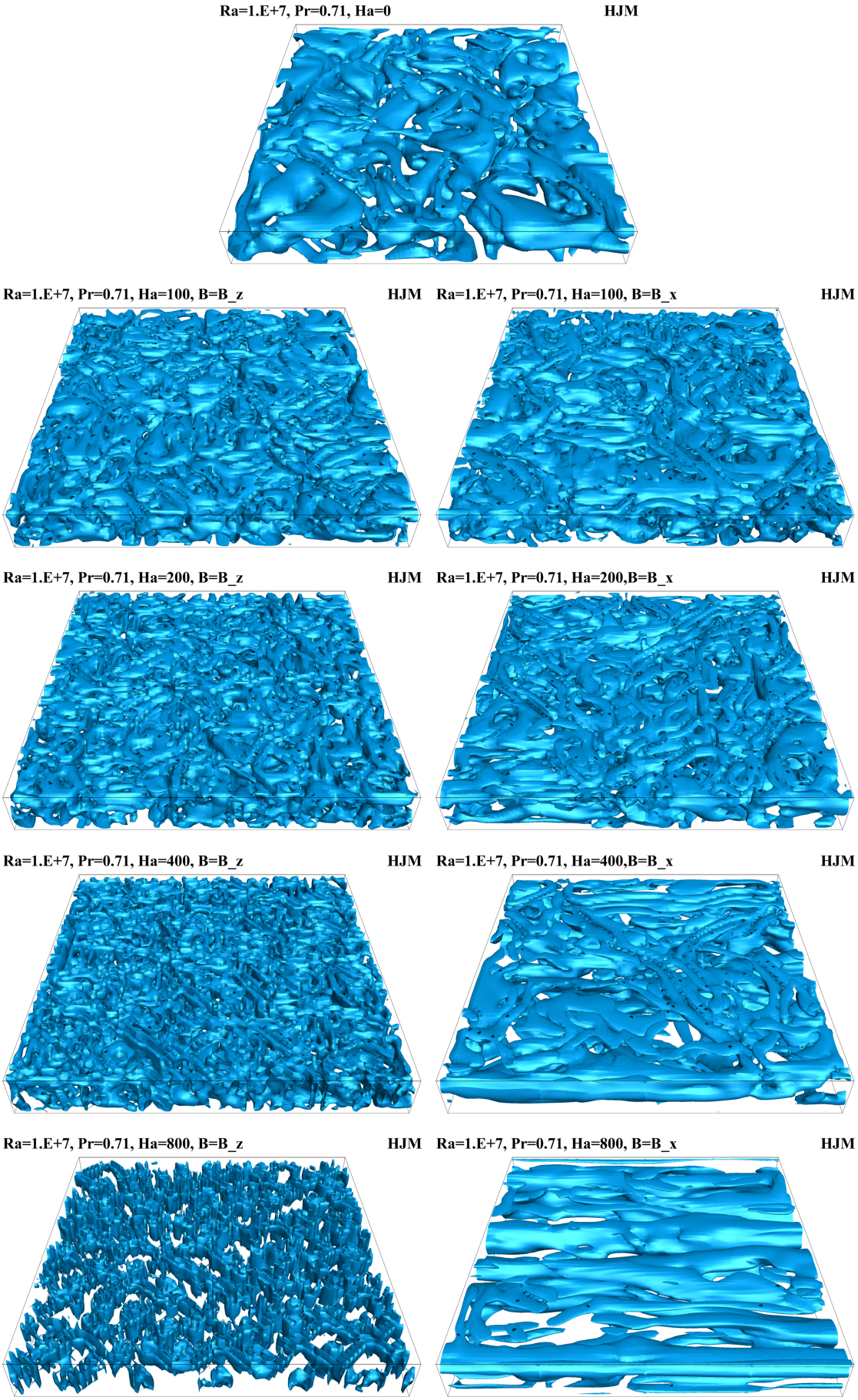

Figure 7.12: Isosurface of Q-criterion ($Q = 0.01$) showing the changes in flow structure brought about by the application of a vertical (left) and horizontal (right) magnetic field for increasing Ha. HJM model; $Ra = 10^7$, $Pr = 0.71$.

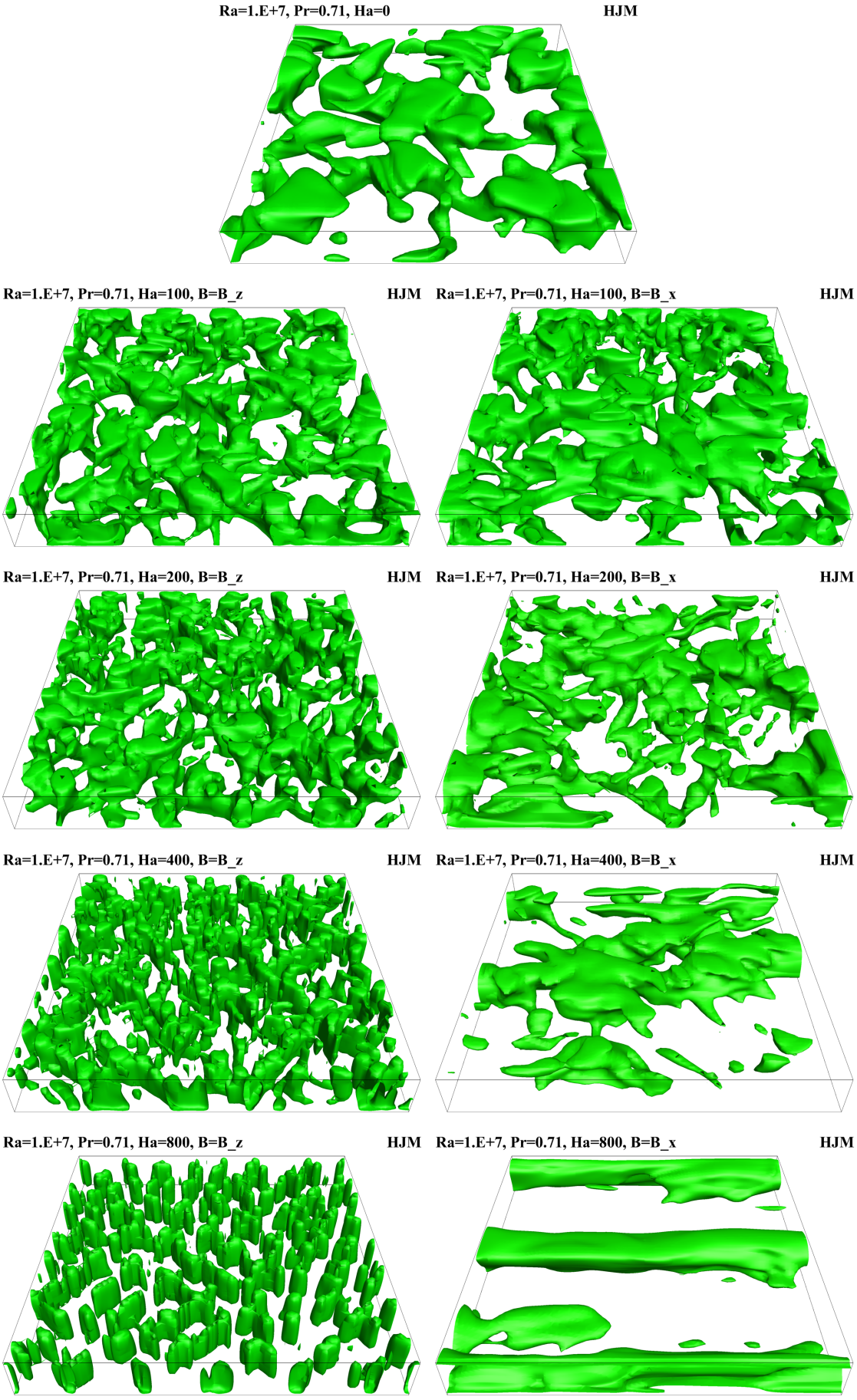

Figure 7.13: Isosurface of non-dimensional vertical velocity ($W^* = 0.025$) showing the changes in flow structure brought about by the application of a vertical (left) and horizontal (right) magnetic field for increasing Ha. HJM model; $Ra = 10^7$, $Pr = 0.71$.

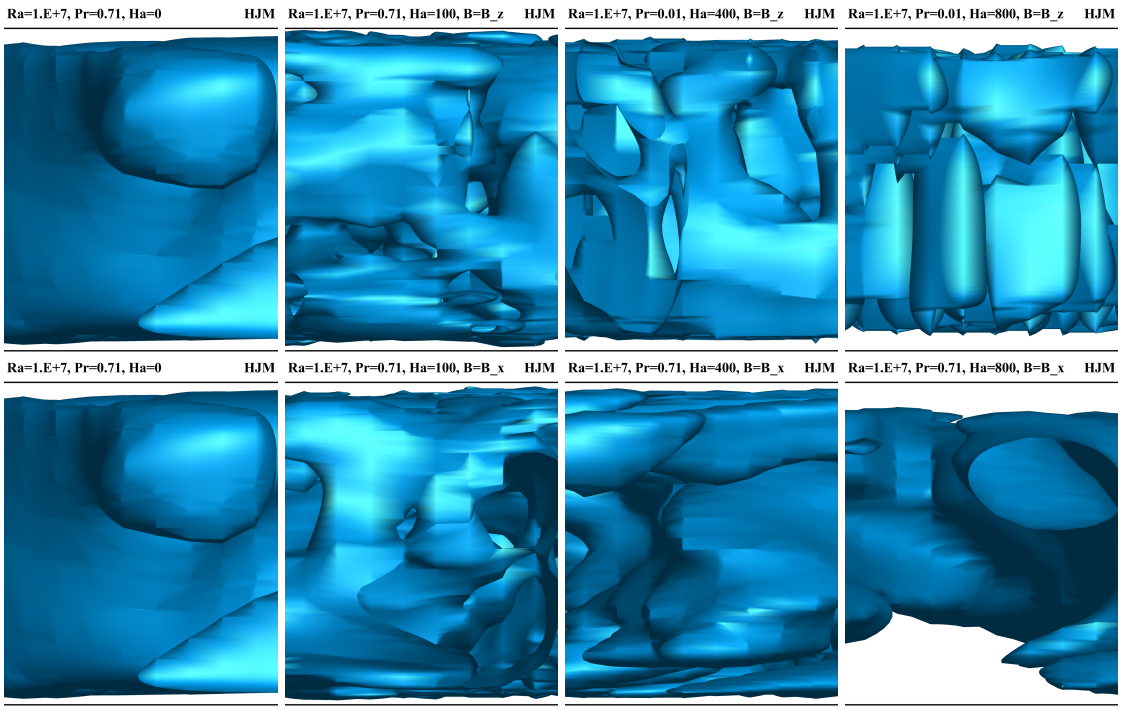

Figure 7.14: Side view, normal to the $x-z$ plane, of the isosurface of Q-criterion ($Q = 0.01$) from Figure 7.12. Looking normal to the $x-z$ plane and showing the effect of a vertical (top) and horizontal (bottom) magnetic field on the degree to which the flow structures penetrate the upper and lower boundary layers. HJM model; $Ra = 10^7$, $Pr = 0.71$.

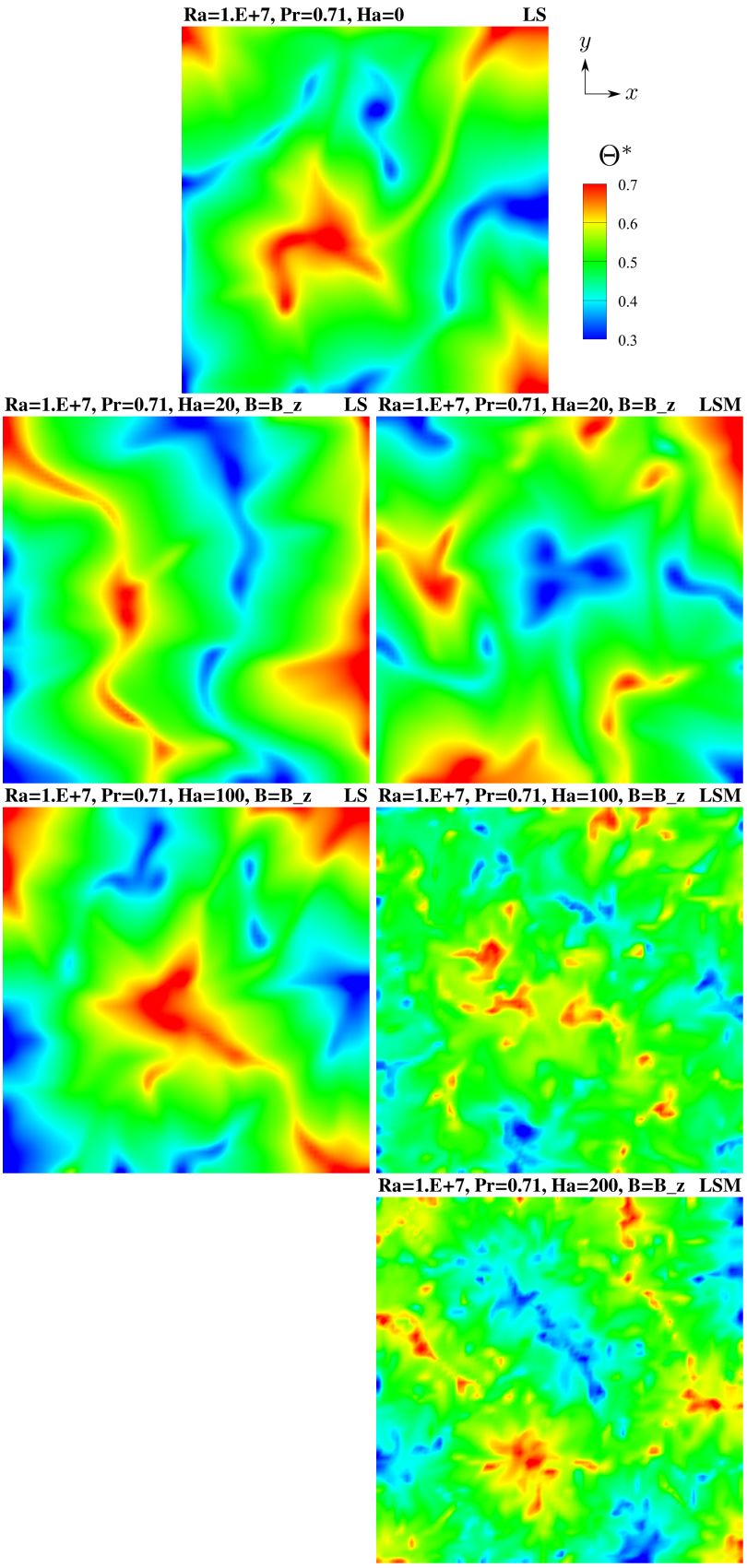

Figure 7.15: Effect of a vertically oriented magnetic field on the instantaneous temperature distribution in the central $x - y$ plane $(z/L_z = 0.5)$. Comparisons between LS (left) and LSM (right) models for increasing Ha; $Ra = 10^7$, $Pr = 0.71$.

7.6 Low Prandtl number: $Pr = 0.01$

In reality, only fluids with suitably high electrical conductivity will be affected by the imposition of a magnetic field. Typically only liquid metals or selected molten salts will fit this criteria and those types of fluids commonly have Prandtl numbers much less than 1. Physically, for a given flow, this will produce thermal boundary layers much larger than the viscous boundary layers and thus the influence of molecular thermal conduction can extend quite significantly into the fully turbulent region of the flow.

Results presented here only consider the HJM model and application of a vertically oriented magnetic field.

7.6.1 Influence on the mean flow

Figure 7.16 shows the long-term time averaged vertical temperature profiles with increasing magnetic field strength. The thicker thermal boundary layers, which are a direct consequence of the lower Prandtl number (since, for a fixed Rayleigh number, the thermal diffusivity is higher), are clearly evident when compared with the higher Prandtl number results in Figure 7.4. As the magnetic field is introduced, the lower Hartmann numbers ($Ha = 20$ and $Ha = 50$) have little influence, and the deformation in the temperature profile which was seen at the moderate Prandtl number does not occur until the higher Hartmann numbers of $Ha = 100$ and $Ha = 200$. At the latter Hartmann number, the extension to the uniform core region and reduction in the size of the thermal boundary layers is significant. Beyond this, at $Ha = 400$, a reversal of this trend is observed and the thermal boundary layers again begin to thicken, with the temperature profile moving back towards that observed in the neutral state. At $Ha = 800$, the size of the thermal boundary layers is considerably greater than those at $Ha = 0$ and the temperature profile appears to move towards a purely conductive solution (i.e. a linear temperature profile).

Compared with the results for a moderate Prandtl number (Figure 7.4) similar changes in the strength of the magnetic field here lead to quite different levels of deformation in the temperature profiles. From $Ha = 200$ to $Ha = 800$ for example, the profile in the low Prandtl number case has moved from one which exhibits the largest uniform core region to the smallest, past that seen at $Ha = 0$. In the moderate Prandtl number case a similar change in field strength only produced comparatively modest changes.

7.6.2 Influence on the turbulence

Unlike in the moderate Prandtl number cases, Figure 7.17 demonstrates that the magnetic field tends to promote more of a change in the distribution of turbulent energy between

the horizontal and vertical normal stresses. In the neutral state, the modelled contributions show some anisotropy in the core of the channel and the resolved contributions show significant anisotropy in the near-wall regions (as they did for the moderate Prandtl number). At $Ha = 100$, where significant changes were seen in the temperature profile, the modelled contributions have been reduced right across the channel, with a reduction in anisotropy in the core. The resolved contributions are also affected in an anisotropic manner, with significant reduction seen in the horizontal components and some reduction in the vertical component. By $Ha = 200$, the modelled contribution to all the normal stresses is suppressed by the magnetic field. Notably, the near-wall peaks of the resolved parts in the two horizontal components appear more pronounced and shift further towards the walls. This indicates the convective cell structures penetrate further towards the walls, something consistent with what was observed at the moderate Prandtl number (though at a different Ha).

At $Ha = 0$, profiles of the vertical component of the turbulent heat flux, presented in Figure 7.8, show peaks which extend further into the core region (again, a direct consequence of the lower Prandtl number). As the magnetic field strength is increased, these reduce fairly uniformly between $Ha = 50$ and $Ha = 100$ with complete suppression by $Ha = 200$. The profiles of the resolved contributions become flatter and more uniform with an increase in the magnetic field strength.

With an increase in magnetic field strength, both Prandtl number cases exhibit qualitatively similar behaviour (i.e. suppression of turbulence) but, for a given Hartmann number, the suppression of turbulence is much more effective at the moderate Prandtl number. This is largely due to increased levels of turbulence present in the neutral case at the lower Prandtl number. The magnitude of the turbulent heat flux contribution to the total vertical component, for example, is around five times its value seen with the moderate Prandtl number. One possible reason for this relates to the size of the thermal layers over which the buoyant force is generated. As noted in the previous subsection, the thermal boundary layers are much thicker in the lower Prandtl number case than they are in the moderate Prandtl number case. Consequently, at the lower Prandtl number, the area over which unstable motion is initiated (by the temperature gradients), thus producing turbulence, is much larger, and might require higher magnetic forces in order to achieve levels of turbulence suppression similar to that seen at the moderate Prandtl number.

7.6.3 Influence on the flow structure

Changes to the structural patterns, presented through several instantaneous realizations in Figure 7.19 and Figure 7.20, show that the magnetic field brings about a similar reorganization to that seen in the higher Prandtl number case with the vertical magnetic field, but not until a much higher Hartmann number is reached. Comparisons at equivalent

Hartmann numbers, $Ha = 0$ or $Ha = 200$ for example, show the lower Prandtl number produces larger plume structures (again a direct consequence of increased thermal diffusivity) and thus these require higher magnetic field strengths to reduce plumes sizes to those seen at the moderate Prandtl number. Interestingly, at $Ha = 400$ these figures indicate some connectivity between adjacent plume structures of similar temperature, where long, thin structures have formed. By $Ha = 800$, the flow has reorganised significantly and the long weak structures joining the main plumes at $Ha = 400$ have transformed into long, thin, main sections that align with each other in an orderly alternating fashion. This is a somewhat surprising result since, though the sudden change in temperature profiles between $Ha = 400$ and $Ha = 800$ provided some indication of a significant change, overall changes to the flow structures seemed initially consistent with that seen at the moderate Prandtl number (albeit in a much more gradual fashion).

Figure 7.21, which presents instantaneous streamlines, highlights the very ordered nature of the plumes. The most striking representations of these structures, however, can be found in the isosurface plots of the Q-criterion and the non-dimensional vertical velocity in Figure 7.22. At $Ha = 400$, the isosurface of W^* clearly shows some coherent connectivity between the plume structures which was absent at lower Hartmann numbers, and at $Ha = 800$ the Q-criterion shows very clear vortical structures aligned with each other. Towards the corners of the domain, these structures change orientation and appear to be more curved. This may suggest some influence of the symmetric boundary conditions which, for structures considerably larger than what the domain was originally designed for, may no longer be entirely appropriate.[1]

Leaving this discrepancy with the boundary conditions aside, one possible explanation for the observed flow structures is as follows. In the moderate Prandtl number cases, the highest magnetic field strength produced structures with significantly reduced lateral dimensions. A look back at the temperature contours in Figure 7.9, for the vertical magnetic field at $Ha = 800$, shows that some communication can be seen between plume structures of similar temperature. If one was to assume the magnetic field would afford at least a reduction in lateral lengthscale of similar order in the lower Prandtl number case, then the increased thermal diffusivity of the fluid would tend to homogenize the small temperature differences between adjacent plumes. Once joined, the plumes form much larger coherent structures. If one aligned plume rises, then a plume of equal form would sink adjacent to it leading to the formation of larger scale patterns such as that seen here.

It is important to note that animations from the time-series data collected in this case showed that the pattern was not stationary, exhibiting slow changes in orientation as the

[1] That is, in the absence of magnetic fields and any other external influences, one would expect the height of the domain to characterize the size of a typical plume in Rayleigh-Bènard convection. Then, an 8:8:1 aspect ratio domain allows several of these to be captured whilst ensuring the symmetry conditions at the sides are far away enough so as to not significantly influence their development. Clearly, with structures now which span nearly the width of the domain, symmetry conditions might not be entirely appropriate.

long plumes occasionally split and rejoined with other plumes. The timescale of this motion, though, was much larger than that observed at lower Hartmann numbers. From Figure 7.20 it can be seen that although the structures at $Ha = 800$ are quite large, the intensity of the vertical motions is dramatically reduced. The specific mechanism behind the transformation seen here warrants suggestion for further work, which is made later in Chapter 8.

Finally, Figure 7.23 provides a side view of the Q-criterion isosurface seen in Figure 7.22. Clearly the vertical dimensions associated with the plume structures follow a similar trend to that observed at the more moderate Prandtl number, though the extension towards the walls occurs at the higher Hartmann number of $Ha = 200$. At $Ha = 800$, the magnetic field confines the structures to the core region, allowing the thermal boundary layers to thicken.

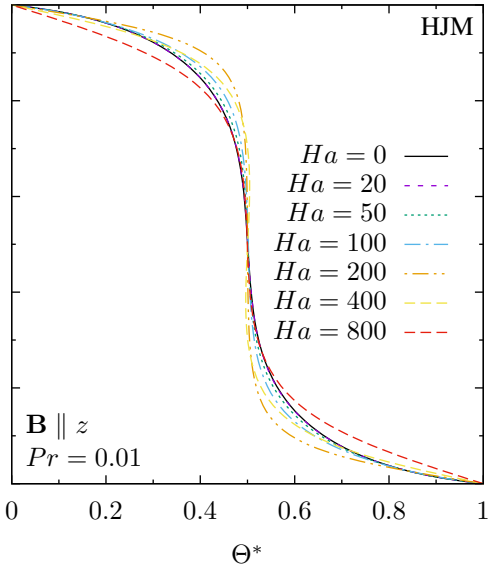

Figure 7.16: Long-term time averaged profiles of the non-dimensional temperature, Θ^* in magnetic Rayleigh-Bènard convection. HJM model over a range of Hartmann numbers; $Ra = 10^7$, $Pr = 0.01$, $\mathbf{B} \parallel z$.

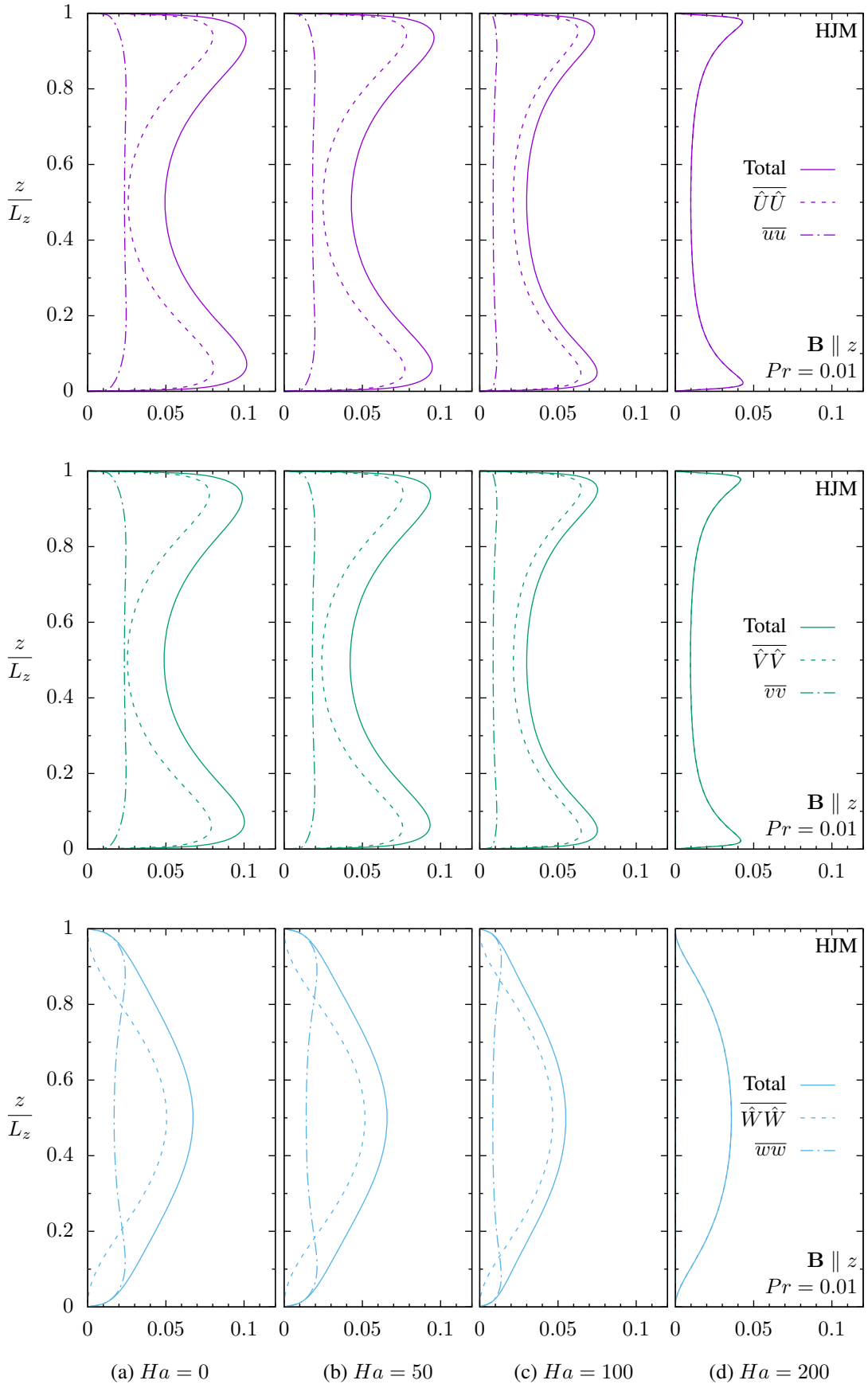

(a) $Ha = 0$ (b) $Ha = 50$ (c) $Ha = 100$ (d) $Ha = 200$

Figure 7.17: Long-term time averaged profiles of the contributions to the non-dimensional normal stresses, $\overline{uu}^*$ (top), $\overline{vv}^*$ (middle) and $\overline{ww}^*$ (bottom), in magnetic Rayleigh-Bènard convection at selected Hartmann numbers; $Ra = 10^7$, $Pr = 0.01$, $\mathbf{B} \parallel z$.

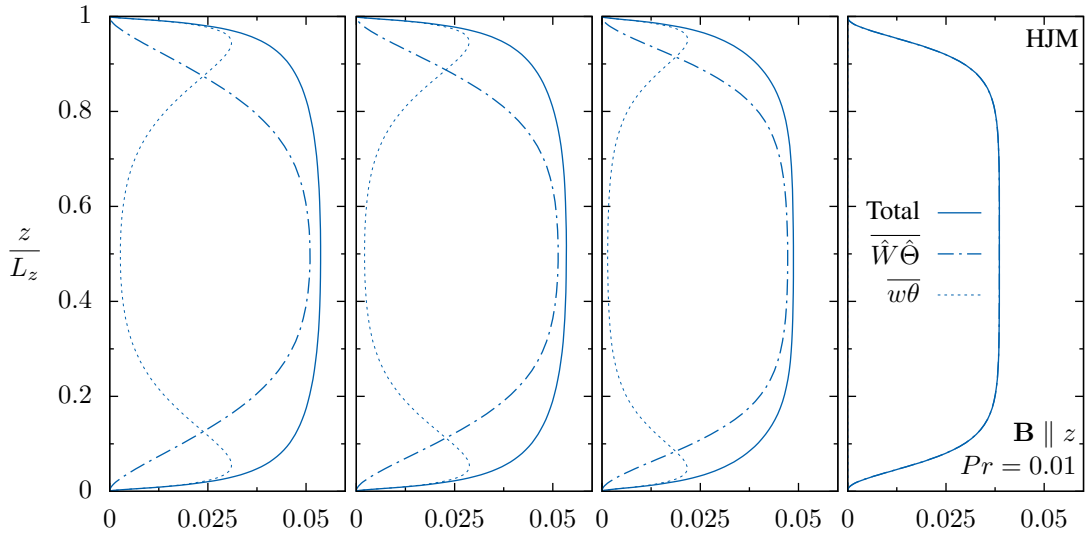

(a) $Ha = 0$ (b) $Ha = 50$ (c) $Ha = 100$ (d) $Ha = 200$

Figure 7.18: Long-term time averaged profiles of the contributions to the wall-normal heat flux in magnetic Rayleigh-Bènard convection at selected Hartmann numbers; $Ra = 10^7$, $Pr = 0.01$, $\mathbf{B} \parallel z$.

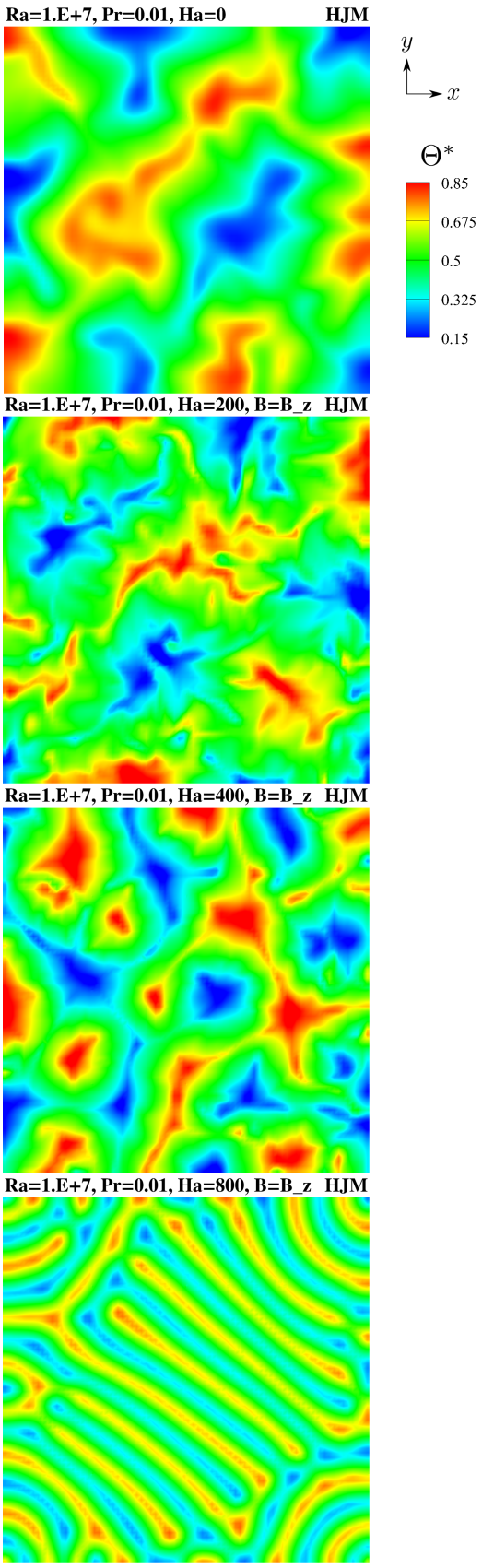

Figure 7.19: Effect of magnetic field strength and orientation on the instantaneous temperature distribution in the central $x-y$ plane $(z/L_z = 0.5)$. HJM model; $Ra = 10^7$, $Pr = 0.01$, $\mathbf{B} \parallel z$.

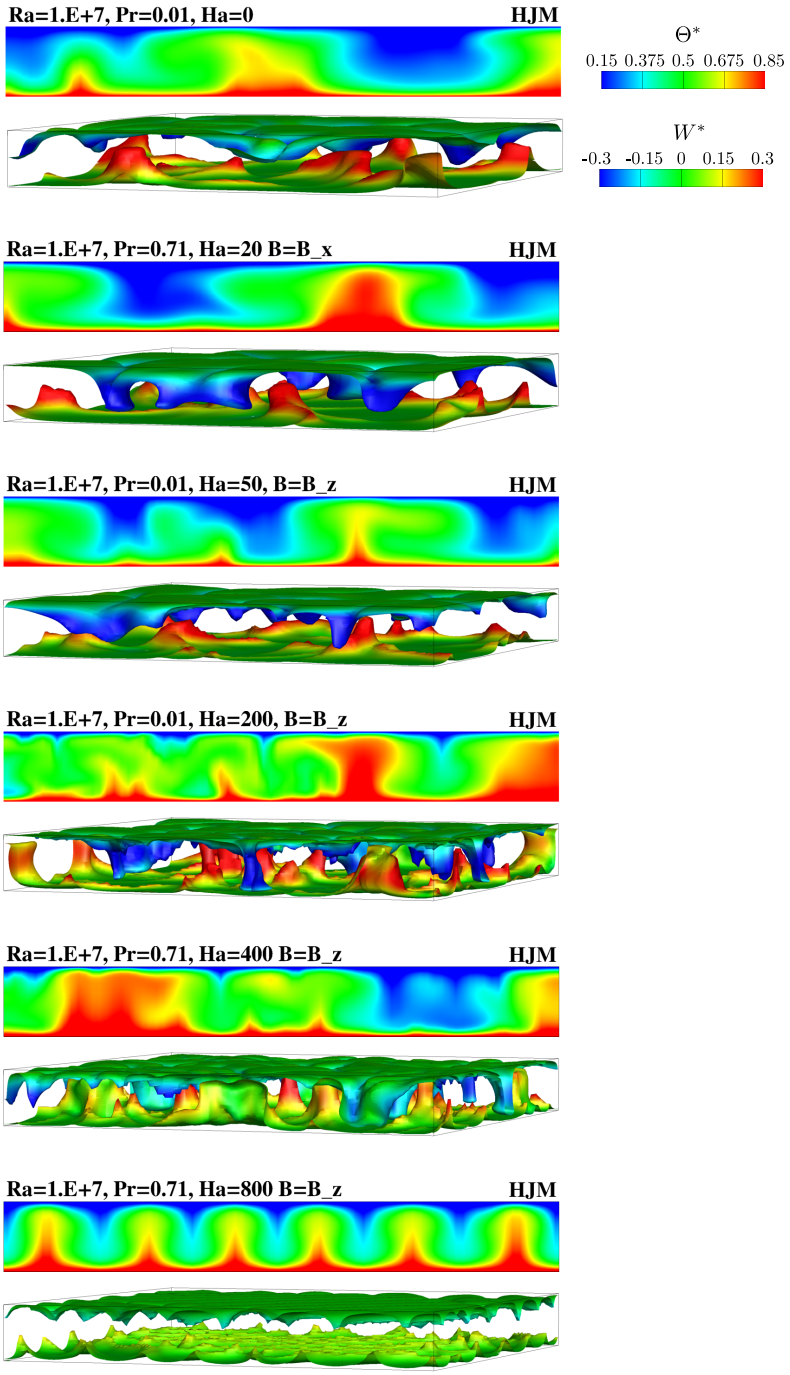

Figure 7.20: Effect of magnetic field strength and orientation on the instantaneous temperature distribution in the central $y - z$ plane $(x/L_x = 0.5)$ and isosurfaces of temperature $(\Theta^* = 0.15, 0.85)$ coloured by the non-dimensional vertical velocity $(-0.3 < W^* < 0.3)$. HJM model; $Ra = 10^7$, $Pr = 0.01$ $\mathbf{B} \parallel z$.

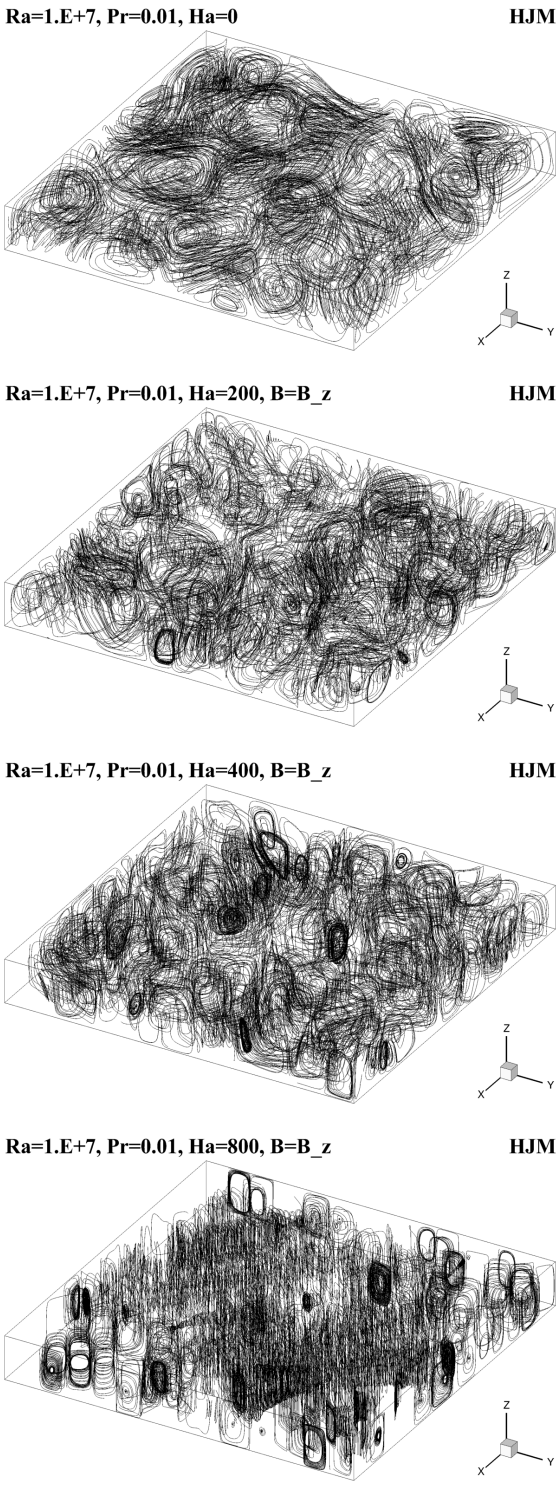

Figure 7.21: Instantaneous streamlines showing the changes in flow structure brought about by the application of a vertical magnetic field to Rayleigh-Bènard convection for increasing Ha; $Ra = 10^7$, $Pr = 0.01$.

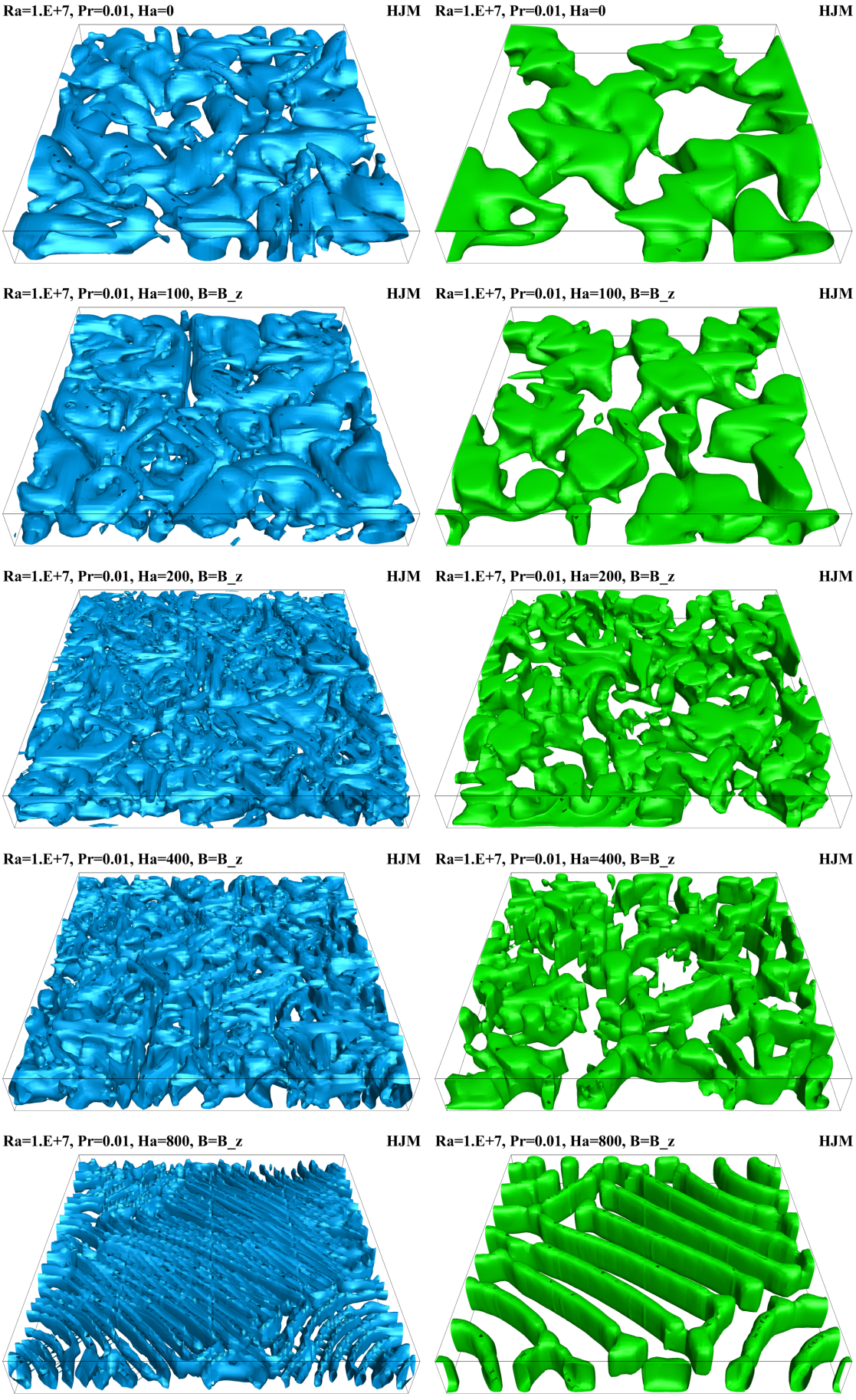

Figure 7.22: Isosurface of Q-criterion ($Q = 0.015$) (left) and non-dimensional vertical velocity ($W^* = 0.025$) (right) showing the changes in flow structure brought about by the application of a vertical magnetic field for increasing Ha. HJM model; $Ra = 10^7$, $Pr = 0.01$.

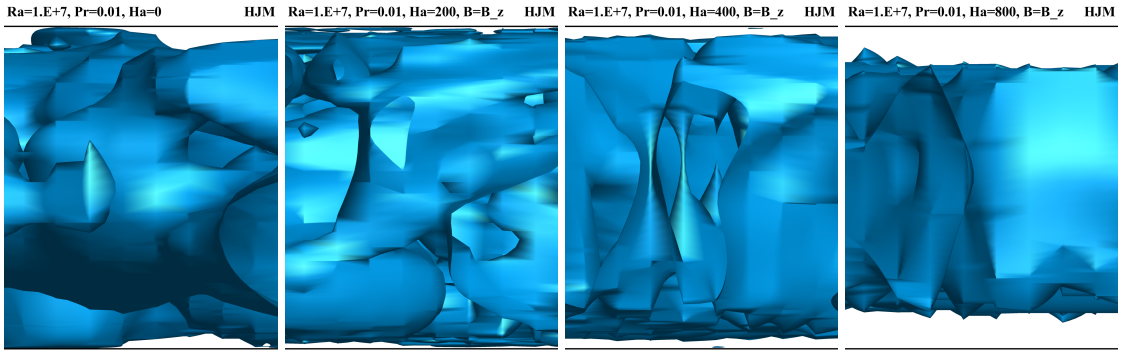

Figure 7.23: Side view, normal to the $x-z$ plane, of the isosurface of Q-criterion $(Q = 0.015)$ from Figure 7.22. Showing the effect of a vertical (top) and horizontal (bottom) magnetic field on the degree to which the flow structures penetrate the upper and lower boundary layers. HJM model; $Ra = 10^7$, $Pr = 0.01$.

7.7 Conclusion

The objective of this chapter was, having provided a fairly detailed assessment of the different electromagnetically modified turbulence models in the simple shear flows considered in Chapter 6, to apply and test the models in the more challenging case of three-dimensional turbulent Rayleigh-Bènard convection.

First, to validate the time-dependant aspects and buoyant implementation within the numerical solver STREAM, results were computed for non-magnetic Rayleigh-Bènard convection at a Rayleigh number of $Ra = 6.3 \times 10^5$ and Prandtl number of $Pr = 0.71$. Despite both models returning no contribution to the modelled turbulence, the unsteady RANS approach was able to resolve the large scale fluctuations and results were both in excellent agreement with DNS data by Wörner (1994) and displayed behavior characteristic of Rayleigh-Bènard convection.

Results were then presented for a higher Rayleigh number of $Ra = 10^7$, with a moderate Prandtl number of $Pr = 0.71$, where horizontal and vertical magnetic fields were imposed over a wide range of magnetic field strengths $(0 \leq Ha \leq 800)$. Both orientations of the magnetic field caused noticeable changes in the long-term time averaged wall-normal temperature profiles across the domain, initially causing an extension of the uniform core region (with associated thinning of the thermal boundary layers) before then producing inversions in the temperature profiles at $Ha > 200$ with thermal boundary layers thicker than those at $Ha = 0$. This was attributed to structural changes in the roll cells, which reduced the extent to which they penetrate the thermal boundary layers. Though no DNS data was available for comparisons, the HJM model was able to predict a more gradual change in the temperature profile as the Hartmann increases when compared with the LSM model.

The effect of the magnetic fields on the turbulence was to almost universally suppress both modelled and resolved contributions across the channel. By $Ha = 50$, the vertical magnetic field had suppressed modelled contributions to the turbulence from both the HJM and LSM models. With a horizontal magnetic field, the modelled contribution offered by the HJM model was non-zero, but small. At large magnetic field strengths $(Ha > 200)$, this orientation of the magnetic field was seen in generate a substantial increase in the resolved contribution to the horizontal normal stress component perpendicular to the magnetic field. This was attributed to changes in the flow structure which, for large Hartmann numbers, were significant.

It was noted that both forms of the turbulent heat flux model employed would, in the case of Rayleigh-Bènard convection, only return non-zero mean values when the mean temperature gradient in the vertical direction was non-zero. This was due to the absence of any long-term time averaged shear stress or gradients of temperature in the horizontal

direction. Despite this, results were in agreement with those presented by Hanjalić and Kenjereš (2000, 2001). Further investigations surrounding the influence of the magnetic field on the thermal field are proposed in Chapter 8.

The most significant observations from the above cases were the striking reorganizations of flow structure predicted and this was substantially dependant on the orientation of the magnetic field. For a weak ($Ha = 50$) vertical magnetic field, and to some extent with a horizontal magnetic field, lateral squeezing of the coherent structures and a general reduction in turbulent mixing, both by the horizontally active Lorentz force, was seen to cause the thermal plumes to break down into a larger number of thinner, more cylindrical, plumes which more densely populated the domain. At higher Hartmann numbers the lateral squeezing, and associated vertical stretching, of the plumes continued with the vertical magnetic field but the horizontal magnetic field caused the roll cells to realign themselves along the direction of the magnetic field lines. This alignment results from a requirement for the flow to conserve the component of angular momentum parallel to the magnetic field despite a continual removal of energy through Joule dissipation. Notably, simulations performed with the LS model, without the additional electromagnetic terms, did not predict any significant change in flow structure.

Results for the lower Prandtl number of $Pr = 0.01$, for which only the vertical magnetic field was considered, largely demonstrated similar behaviour to the moderate Prandtl number case albeit with the presence of noticeably thicker thermal boundary layers. These were seen to generate much larger plume structures in the non-magnetic case, and thus higher magnetic field strengths were required to reduce them to sizes similar to those seen at equivalent field strengths in the moderate Prandtl number case. A surprising result was that at the highest magnetic field strength considered, the randomly distributed plume structures present at lower magnetic field strengths appear to 'join' together and form long coherent structures, aligned parallel to each other, which were seen to span nearly the entire width of the domain.

In summary, the results presented here demonstrate the potential of the unsteady RANS approach, and specifically the stress-transport approach, in reproducing flows affected by complex interactions from both buoyant and Lorentz forces. The changes in flow structure brought about by different magnetic field orientations have implications for controlling both turbulence levels and the formation of coherent structures.

CHAPTER

EIGHT

CONCLUSION AND FUTURE WORK

This chapter details the main conclusions and findings from the research carried out and presented as part of this thesis. It begins in Section 8.1 with a reminder of the objectives of the thesis and provides a brief synopsis of how the objectives were achieved. Then, Section 8.2 and Section 8.3 summarise the main conclusions from the two major results chapters in the thesis, Chapter 6 and Chapter 7 respectively. Finally, Section 8.4 identifies several areas in which further work would help to advance this research further.

8.1 Synopsis of research

The fundamental aim of this research, as stated in Section 1.4, was to explore the extent to which modelling approaches within the Reynolds-averaged Navier-Stokes (RANS) framework can reproduce the reported effects of flows influenced by electromagnetic forces. To achieve this fundamental aim, several objectives were set out. The first was to identify and implement electromagnetic modifications to existing engineering type RANS based turbulence models, as identified in the literature, within the numerical solver STREAM. The second, was to apply these models to two main classes of flow, simple channel flow and Rayleigh-Bènard convection, and provide an assessment of their performance. Finally, the third was to identify the strengths and weaknesses of the models and identify further areas for model development. What follows is a synopsis of how these objectives were achieved in the thesis.

To identify existing electromagnetic modifications to RANS based turbulence models, an extensive literature survey was carried out and presented in Chapter 2. The survey identified a number of fundamental, and more engineering application based, studies which served to fulfil several roles within the research. First, they helped elucidate the main physical phenomena associated with magnetohydrodynamic interactions across a range of different electromagnetically influenced flows, which included flows through simple channels, Rayleigh-Bènard type convective flows and some other, less explored flows, such as those surrounding targeted drug delivery and materials processing. Second, they identified two electromagnetically extended RANS turbulence models, the low-Re Launder-Sharma $k-\varepsilon$ linear eddy viscosity model (LEVM) and the low-Re Hanjalić and Jakirlić Reynolds stress model (RSM) with additional electromagnetic terms by Kenjereš and Hanjalić (2000) and Kenjereš et al. (2004) respectively, which were suitable for implementation and testing with the numerical solver STREAM. Finally, they provided sets of Direct Numerical Simulation (DNS) data, primarily for simple channel flows subjected to magnetic fields of varying strength and direction, through which the models could be tested and assessed.

Chapter 3 and Chapter 4 then developed the necessary theoretical background concerning magnetohydrodynamics and detailed how the identified electromagnetically extended models fit within the context of both the eddy-viscosity and stress-transport approaches. The implementation of these models, which included an additional equation for the electrostatic potential and the specification of various source terms, within the STREAM solver was then documented in Chapter 5.

To apply these models to the two main classes of flow identified within the literature survey, a number of cases were numerically simulated, covering a wide range of hydrodynamic and magnetic flow parameters. With the simple channel flows, two main configurations were investigated. The first was a one-dimensional, fully-developed, channel

flow where a magnetic field was applied in either the wall-normal or streamwise direction. Both laminar and turbulent flows were considered, where the former provided the means to validate the implementation within the STREAM solver and the latter provided the means to assess the performance of the models tested against existing DNS data. The second was a two-dimensional, fully-developed, duct flow where the effect of changing the wall conductivity was investigated. The main findings and conclusions drawn from these results are summarised in Section 8.2.

In the second, more complex, class of flow, time-dependent Rayleigh-Bènard convection was simulated within a three-dimensional rectangular cavity. Two magnetic field directions and two Prandtl numbers were considered where, in addition to the electromagnetic effects, buoyant effects were also influential. The results and conclusions drawn from these cases are summarised in Section 8.4.

Identification of the strengths and weaknesses of the models was carried out through the analysis and discussion of the results obtained in the above two main test cases. These are provided in detail within the conclusions at the end of their respective chapters and are further summarised in Section 8.2 and Section 8.4 below. From this, and the discussion throughout the thesis in general, several areas for further work have been identified that would be helping in bringing improvements to not just the models considered in this thesis, but to the modelling of complex multiphysics flows in general.

8.2 Fully developed channel flows

In Chapter 6, a series of one-dimensional and two-dimensional, laminar and fully turbulent, electromagnetically influenced fully-developed channel flows were investigated. The objective was to both provide confidence in the implementation of the electromagnetic modifications within the numerical solver STREAM, and to contribute towards a major objective of the thesis by providing a detailed assessment of how the employed electromagnetically modified turbulence models respond to imposed magnetic fields of varying direction and intensity.

The implementation of the electromagnetic modifications was validated, in the laminar regime, through a series of one-dimensional and two-dimensional fully-developed channel flow calculations. Results in the former case demonstrated excellent agreement with the developed analytical solution, and in the latter verified the code could predict a number of MHD phenomena discussed as part of Chapter 2, including the development of near-wall jets at sufficient Hartmann numbers.

The implementation of the existing turbulence models in STREAM was validated in the non-magnetic case with computations of one-dimensional fully-developed channel flows over a range of Reynolds numbers $(150 \leq Re_\tau \leq 2000)$. A slight overprediction of the near-wall turbulent shear stress by the Hanjalić and Jakirlić RSM, which led to reduced mass flow rates when compared to DNS data, was attributed to an unknown discrepancy between the form of the model implemented in STREAM and that presented by Kenjereš et al. (2004). Both models did, however, correctly reproduce the salient features of fully-developed channel flow and showed generally good quantitative agreement with available DNS data.

A detailed assessment of the performance of the electromagnetically modified Launder-Sharma $k - \varepsilon$ and Hanjalić and Jakirlić stress-transport models was presented through a series of one-dimensional, turbulent, fully-developed channel flow calculations. In the case with a wall-normal magnetic field, the modified Launder-Sharma model was seen to consistently overestimate the direct suppression of turbulence afforded by the magnetic field, leading to premature laminarization at the higher Hartmann numbers considered. The response of the Hanjalić and Jakirlić RSM was much better, providing quantitative changes in the velocity and Reynolds stress profiles which were more in line with the DNS data than those of the Launder-Sharma model. The contributions from the additional electromagnetic terms in the Hanjalić and Jakirlić model, however, were shown to be quite modest and the improved performance of the RSM was thus attributed to its ability to better represent changes to the production of the Reynolds stresses, and hence to levels of turbulent kinetic energy. An analysis of the budgets of the $\overline{u_i u_j}$ and k equations,

as provided by the DNS data, confirmed this assessment and revealed that the primary turbulence suppression mechanism of the wall-normal magnetic field was to reduce turbulent production by reducing mean strain.

In the case with a streamwise magnetic field, the mean flow was not subjected to a mean Lorentz force and the effects of the magnetic field were thus only felt through changes to the turbulence. Increases to the near-wall peak values of k and $\overline{uu}$ as the Hartmann number increased were correctly represented by the modified RSM, whilst the modified EVM predicted a decrease. Both models predicted laminar flow at the highest Hartmann number considered, contrary to the DNS data. With the EVM, comparisons of the computed additional source terms with budgets from DNS data showed that they grossly over predict the magnitudes of both sinks and this was attributed to the ad-hoc nature of the terms, which are unable to directly take account of the directionality associated with the magnetic field. With the RSM, an inadequate model for the modelled part of the additional source terms in the $\overline{u_i u_j}$ equations led to the prediction of a sink term in the $\overline{uv}$ budget, when DNS data indicated the opposite.

8.3 Magnetic Rayleigh-Bènard convection

In Chapter 7, results from a series of three-dimensional, time-dependent, Rayleigh-Bènard convection flows were presented over a range of Hartmann numbers ($0 \leq Ha \leq 800$), for two different Prandtl numbers ($Pr = 0.71$, $Pr = 0.01$) and for two different magnetic field directions (horizontal, vertical). The objective was to assess the performance of the two electromagnetically extended models in some more challenging flows, which also included interactions from buoyant forces. Most attention was devoted to the RSM since it proved superior in the previously computed fully-developed channel flow cases.

The implementation of the buoyant and time-dependent components of STREAM were validated through computations of non-magnetic three-dimensional Rayleigh-Bènard convection between two infinite horizontal flat plates. Both turbulence models could not sustain the low level of turbulence predicted by the DNS data (at a relative low $Ra = 6.3 \times 10^5$), but long-term time averaged temperature profiles showed excellent agreement and displayed behaviour characteristic of time-dependent Rayleigh-Bènard convection.

Results at the higher Rayleigh number of $Ra = 10^7$ showed that the application of sufficiently strong magnetic fields, in both horizontal and vertical directions, led to substantially different changes in the predicted flow structure, and caused noticeable changes to the long-term time averaged statistics. In the moderate Prandtl number case, a vertical magnetic field fully suppressed the modelled contribution to the turbulence by $Ha = 50$. The subsequent reduction in mixing that this brought, together with a horizontally active mean Lorentz force, laterally squeezed the thermal thermal plumes, breaking them down into a larger number of thinner, more cylindrical, plumes which more densely populated the domain and extended further into the thermal boundary layers. With a horizontally orientated magnetic field, higher Hartmann numbers ($Ha \geq 400$) were seen to cause the roll cells to realign themselves along the direction of the magnetic field lines. This realignment was attributed to a requirement for the flow to conserve the component of angular momentum parallel to the magnetic field despite a continual removal of energy through Joule dissipation. Notably, simulations with the standard Launder-Sharma model did not predict any significant changes in flow structure. Thus, whilst the additional terms were generally not required in the simple channel flows, they were instrumental in reproducing the effects of the magnetic field in the more complex Rayleigh-Bènard cases.

In the lower Prandtl number cases, for which only a vertical magnetic field was considered, the results largely demonstrated similar behaviour to that seen at the moderate Prandtl number case, with the notable exception that much higher magnetic field strengths were required. This was attributed to the thicker thermal boundary layers (a direct consequence of the lower Prandtl number) which generated much larger plume sizes in the non-magnetic case. An unexpected observation was seen at the highest magnetic field

strength considered, where the initially smaller plume structures (generated by the lateral squeezing of the Lorentz force) appeared to organize into long parallel rolls which spanned nearly the entire width of the domain.

The observed changes in the flow structure, brought about by the application of different magnetic fields, was seen to be in agreement with existing numerical simulations and physical reasoning. This demonstrated the potential of the unsteady RANS stress-transport approach in reproducing flows affected by complex interactions from both buoyant and Lorentz forces.

8.4 Suggestions for further work

Although a significant number of investigations have been performed as part of the research undertaken in this thesis, there are a number of areas which have arisen as being suitable for further investigation. These are discussed in the next few subsections.

8.4.1 Further explorations of cases studied

In the Rayleigh-Bènard convection cases explored as part of Chapter 7, one of the more unexpected results was the prediction that, at the lower Prandtl number, a strong magnetic field caused the initially small plume structures to reorganize into a series of long adjacent parallel structures which spanned almost the entire width of the domain. This raised several points which would be suitable for further investigation.

Firstly, it was noted that once the lengthscale of the structures becomes a significant fraction of the width of the domain (as is the case here), the boundary conditions employed for this particular case, which are symmetry conditions, might no longer be appropriate. Secondly, the physical mechanism behind the transformation (assuming it is not entirely an artefact of the symmetry boundary conditions, which seems unlikely) was not entirely obvious.

To address the above points, several further explorations, at some intermediate and higher magnetic field strengths and using, for example, periodic boundary conditions, would be useful in helping to determine why that particular flow pattern, if realistic, is occurring.

8.4.2 Improvements within the eddy-viscosity framework

It was concluded in Section 8.3 that whilst additional electromagnetic modifications to the Launder-Sharma $k-\varepsilon$ EVM were generally unhelpful in simple magnetic channel flows, they appeared instrumental in bringing about changes in flow structure that were predicted to occur by the more advanced RSM in Rayleigh-Bènard convection (and that which were more in line with physical intuition).

Whilst there may be some specific areas which could be addressed, such as the prescription of a correction to the modelled form of the electromagnetic source term in the ε equation ($\mathcal{F}_\varepsilon$), which was seen to be heavily underestimated in the Hartmann flow cases, the analysis of the fully-developed channel flow results revealed the reason for the poor performance of the electromagnetically extended Launder-Sharma model was more its inability to correctly capture the anisotropic effects of the magnetic field on the Reynolds

stresses themselves. Without this additional information, it is difficult to see what wholesale improvements to the form of the terms proposed by Kenjereš and Hanjalić (2000) one could suggest.

One possible route for improvement would be to employ a non-linear stress-strain relationship. These have been shown to offer better predictions of the stress anisotropy over a range of different flows, including plane channel flows, transitional flows and impinging jets (Craft et al., 1997). With better predictions of normal stresses, use of the more exact form of the electromagnetic source term in the k equation, $\mathcal{F}_k^L$, would be worthwhile, and would hopefully allow the model to better capture the directional effects of the magnetic field on the Reynolds stresses.

8.4.3 Improvements within the stress-transport framework

It was seen in Chapter 4 that the only unknown in the exact expression for $\mathcal{F}_{ij}^L$, the direct contribution from the magnetic field to the Reynolds stress transport equation, was the correlation between the fluctuating velocity and the fluctuating electric potential. The model for this, proposed by Kenjereš et al. (2004), implied that the two constituent terms were proportional to each other and of opposite sign. This was seen to be generally the case with the wall-normal magnetic field, but the application of a streamwise magnetic field, detailed in Subsection 6.4.3, revealed that the model returned values of $\mathcal{F}_{uv}^L$ with an incorrect sign.

Unfortunately, little is known about the correlation discussed above, and information on its distribution in the low-Re channel flow cases was not readily presented by the group who computed the DNS data (Noguchi et al., 2004). If the unprocessed data for these cases, or other suitably identified cases, were to be obtained, then it would enable the behaviour of that term to be properly assessed. This would hopefully reveal avenues which could potentially bring improvements to the modelled form currently employed.

A further area for additional exploration within the stress-transport approach was discussed during the analysis of the Rayleigh-Bènard convection results in Section 7.5. It was noted there that the use of the GGDH may under predict the turbulent contribution to the heat flux since it does not fully take account of all the generation processes which are present in the parent transport equation (see Subsection 4.3.3). These would also contain contributions from the fluctuating Lorentz force. These could be included through either full solution of the parent transport equation for $\overline{u_i\theta}$, or use of a more advanced algebraic closure such as that proposed by Kenjereš and Hanjalić (1999b) and may bring improvements in those flows affected by buoyancy in addition to the Lorentz force.

8.4.4 Production of experimental or DNS data

One major area which, if developed, would bring improvements to the modelling of flows considered in this thesis (and is always welcomed by the turbulence modelling community), is the production of reliable experimental or DNS data. The literature survey presented in Chapter 2, whilst clearly identifying a number of interesting electromagnetically influenced flows, served to highlight the lack of detailed DNS or experimental data, especially in more complex flows, which could be used to develop and tune models.

Obviously, DNS of magnetic Rayleigh-Bènard cases would be immediately useful in validating the results presented in this thesis, but DNS in which magnetic fields are applied to other well-studied flows, such as backwards facing steps or impinging jets, would provide an array of results sufficient in depth to both further develop the electromagnetically modified turbulence models discussed in this thesis and instigate the development of new models.

REFERENCES

Abbassi, H. and Ben Nassrallah, S. (2007). "MHD flow and heat transfer in a backward-facing step". *International Communications in Heat and Mass Transfer* 34.2, pp. 231–237.

Ahlers, G., Grossmann, S., and Lohse, D. (2009). "Heat transfer and large scale dynamics in turbulent Rayleigh-Bénard convection". *Reviews of Modern Physics* 81.2, pp. 503–537.

Álamo, J. C. del, Jiménez, J., Zandonade, P., and Moser, R. D. (2004). "Scaling of the energy spectra of turbulent channels". *Journal of Fluid Mechanics* 500, pp. 135–144.

Alemany, A., Moreau, R., Sulem, P. L., and Frisch, U. (1979). "Influence of an external magnetic field on homogeneous MHD turbulence". *Journal de Mecanique* 18, pp. 277–313.

Alexiou, C., Jurgons, R., Schmid, R., Erhardt, W., Parak, F., Bergemann, C., and Iro, H. (2005). "Magnetisches Drug Targeting—ein neuer Ansatz in der lokoregionären Tumortherapie mit Chemotherapeutika". *HNO* 53, pp. 618–622.

Alexiou, C., Schmid, R., Jurgons, R., Kremer, M., Wanner, G., Bergemann, C., Huenges, E., Nawroth, T., Arnold, W., and Parak, F. (2006). "Targeting cancer cells: magnetic nanoparticles as drug carriers". *European Biophysics Journal* 35.5, pp. 446–450.

Alfvén, H. (1942). "Existence of Electromagnetic-Hydrodynamic Waves". *Nature* 150, pp. 405–406.

Ammour, D., Craft, T., and Iacovides, H. (2013). "Highly Resolved LES and URANS of Turbulent Buoyancy-Driven Flow Within Inclined Differentially-Heated Enclosures". en. *Flow, Turbulence and Combustion* 91.3, pp. 669–696.

Andreev, O., Kolesnikov, Y., and Thess, A. (2007). "Corrected Article: "Experimental study of liquid metal channel flow under the influence of a nonuniform magnetic field" (Phys. Fluids 18, 065108 (2006))". *Physics of Fluids* 19, p. 039902.

Andreev, O., Thess, A., and Haberstroh, Ch (2003). "Visualization of magnetoconvection". *Physics of Fluids* 15.12, pp. 3886–3889.

Arruebo, M., Fernández-Pacheco, R., Ibarra, M. R., and Santamaría, J. (2007). "Magnetic nanoparticles for drug delivery". *Nano Today* 2.3, pp. 22–32.

Aurnou, J. M. and Olson, P. L. (2001). "Experiments on Rayleigh–Bénard Convection, Magnetoconvection and Rotating Magnetoconvection in Liquid Gallium". *Journal of Fluid Mechanics* 430, pp. 283–307.

Battira, M. and Bessaïh, R. (2008). "Three-Dimensional Natural Convection in the Horizontal Bridgman Configuration Under Various Wall Electrical Conductivity and Magnetic Field". *Numerical Heat Transfer, Part A: Applications* 55.1, pp. 58–76.

Berger, T. W., Kim, J., Lee, C., and Lim, J. (2000). "Turbulent boundary layer control utilizing the Lorentz force". *Physics of Fluids* 12.3, pp. 631–649.

Bocheninskii, V. P., Branover, G. G., Tananaev, A. V., and Chernyaev, Yu P. (1971). "Experimental investigation of the resistance to the flow of a conducting fluid in flat insulated ducts in the presence of a transverse magnetic field with allowance for fringe effects and wall roughness". *Fluid Dynamics* 6.4, pp. 559–569.

Bodenschatz, E., Pesch, W., and Ahlers, G. (2000). "Recent Developments in Rayleigh-Bénard Convection". *Annual Review of Fluid Mechanics* 32.1, pp. 709–778.

Boussinesq, J. (1877). "Essai sur la théorie des eaux courantes". *Essai sur la théorie des eaux courantes* 23.1, pp. 1–680.

Branover, H. (1978). *Magnetohydrodynamic Flow in Ducts*. 1st. John Wiley & Sons.

Breuer, K. S., Park, J., and Henoch, C. (2004). "Actuation and control of a turbulent channel flow using Lorentz forces". *Physics of Fluids* 16.4, pp. 897–907.

Burr, U. and Müller, U. (2001). "Rayleigh–Bénard convection in liquid metal layers under the influence of a vertical magnetic field". *Physics of Fluids* 13.11, p. 3247.

Burr, U. and Müller, U. (2002). "Rayleigh–Bénard Convection in Liquid Metal Layers Under the Influence of a Horizontal Magnetic Field". *Journal of Fluid Mechanics* 453, pp. 345–369.

Chandrasekhar, S. (1952). "XLVI. On the inhibition of convection by a magnetic field". *Philosophical Magazine Series 7* 43.340, pp. 501–532.

Chandrasekhar, S. (1954a). "CXXXI. On the inhibition of convection by a magnetic field : II". *Philosophical Magazine Series 7* 45.370, pp. 1177–1191.

Chandrasekhar, S. (1954b). "The Instability of a Layer of Fluid Heated below and Subject to the Simultaneous Action of a Magnetic Field and Rotation". *Proceedings of the Royal Society of London. Series A. Mathematical and Physical Sciences* 225.1161, pp. 173–184.

Chandrasekhar, S. (1956). "The Instability of a Layer of Fluid Heated below and Subject to the Simultaneous Action of a Magnetic Field and Rotation. II". *Proceedings of the Royal Society of London. Series A. Mathematical and Physical Sciences* 237.1211, pp. 476–484.

Chandrasekhar, S. (1961). *Hydrodynamic and hydromagnetic stability*. English. Oxford: Clarendon Press.

Chang, C. C. and Lundgren, T. S. (1961). "Duct flow in magnetohydrodynamics". *Zeitschrift für Angewandte Mathematik und Physik* 12.2, pp. 100–114.

Chaudhary, R., Thomas, B., and Vanka, S. (2012). "Effect of Electromagnetic Ruler Braking (EMBr) on Transient Turbulent Flow in Continuous Slab Casting using Large Eddy Simulations". *Metallurgical and Materials Transactions B* 43.3, pp. 532–553.

Chaudhary, R., Vanka, S. P, and Thomas, B. G (2010). "Direct numerical simulations of magnetic field effects on turbulent flow in a square duct". *Physics of Fluids* 22.7, p. 075102.

Chien, K. (1982). "Predictions of Channel and Boundary-Layer Flows with a Low-Reynolds-Number Turbulence Model". *AIAA Journal* 20.1, pp. 33–38.

Choi, H., Moin, P., and Kim, J. (1994). "Active turbulence control for drag reduction in wall-bounded flows". *Journal of Fluid Mechanics* 262, pp. 75–110.

Chu, T. Y. and Goldstein, R. J. (1973). "Turbulent convection in a horizontal layer of water". *Journal of Fluid Mechanics* 60.01, pp. 141–159.

Cioni, S., Chaumat, S., and Sommeria, J. (2000). "Effect of a vertical magnetic field on turbulent Rayleigh-Bénard convection". *Physical Review E* 62.4, R4520–R4523.

Craft, T. J., Iacovides, H., and Uapipatanakul, S. (2010). "Towards the development of RANS models for conjugate heat transfer". *Journal of Turbulence* 11, N26.

Craft, T. J., Launder, B. E., and Suga, K. (1997). "Prediction of turbulent transitional phenomena with a nonlinear eddy-viscosity model". *International Journal of Heat and Fluid Flow*. Selected Papers from the Engineering Foundation Turbulent Heat Transfer Conference 18.1, pp. 15–28.

Cuevas, S., Smolentsev, S., and Abdou, M. (2006a). "Vorticity generation in creeping flow past a magnetic obstacle". *Physical Review E* 74.5, p. 056301.

Cuevas, S., Smolentsev, S., and Abdou, M.A. (2006b). "On the flow past a magnetic obstacle". *Journal of Fluid Mechanics* 553, pp. 227–252.

Daly, B. J. and Harlow, F. H. (1970). "Transport Equations in Turbulence". *Physics of Fluids* 13.11, pp. 2634–2649.

Davidson, P. A. (1995). "Magnetic Damping of Jets and Vortices". *Journal of Fluid Mechanics* 299, pp. 153–186.

Davidson, P. A. (1997). "The Role of Angular Momentum in the Magnetic Damping of Turbulence". *Journal of Fluid Mechanics* 336, pp. 123–150.

Davidson, P. A. (1999). "Magnetohydrodynamics in Materials Processing". *Annual Review of Fluid Mechanics* 31, pp. 273–300.

Davidson, P. A. (2001). *An Introduction to Magnetohydrodynamics*. Cambridge: Cambridge University Press.

Dey, Prasanta K. and Zikanov, Oleg (2012). "Turbulence and transport of passive scalar in magnetohydrodynamic channel flows with different orientations of magnetic field". *International Journal of Heat and Fluid Flow* 36, pp. 101–117.

Dobson, J. (2006). "Magnetic nanoparticles for drug delivery". *Drug Development Research* 67.1, 55–60.

Faraday, M. (1832). “Experimental Researches in Electricity”. *Philosophical Transactions of The Royal Society* 122, pp. 125–162.

Fauve, S., Laroche, C., and Libchaber, A. (1981). “Effect of a horizontal magnetic field on convective instabilities in mercury”. *Journal de Physique Lettres* 42.21, p. 3.

Fauve, S., Laroche, C., Libchaber, A., and Perrin, B. (1984). “Chaotic Phases and Magnetic Order in a Convective Fluid”. *Physical Review Letters* 52.20, pp. 1774–1777.

Gailitis, A., Gerbeth, G., Gundrum, T., Lielausis, O., Platacis, E., and Stefani, F. (2008). “History and results of the Riga dynamo experiments”. *Comptes Rendus Physique* 9.7, pp. 721–728.

Gailitis, A., Lielausis, O., Dement’ev, S., Platacis, E., Cifersons, A., Gerbeth, G., Gundrum, T., Stefani, F., Christen, M., Hänel, H., and Will, G. (2000). “Detection of a Flow Induced Magnetic Field Eigenmode in the Riga Dynamo Facility”. *Physical Review Letters* 84.19, pp. 4365–4368.

Gailitis, A., Lielausis, O., Platacis, E., Dement’ev, S., Cifersons, A., Gerbeth, G., Gundrum, T., Stefani, F., Christen, M., and Will, G. (2001a). “Magnetic Field Saturation in the Riga Dynamo Experiment”. *Physical Review Letters* 86.14, pp. 3024–3027.

Gailitis, A., Lielausis, O., Platacis, E., Dement’ev, S., Cifersons, A., Gerbeth, G., Gundrum, T., Stefani, F., Christen, M., and Will, G. (2002a). “Dynamo experiments at the Riga sodium facility”. *Magnetohydrodynamics* 38, pp. 5–14.

Gailitis, A., Lielausis, O., Platacis, E., Gerbeth, G., and Stefani, F. (2001b). “On the results of the Riga dynamo experiments”. *Magnetohydrodynamics* 37.1-2, pp. 71–79.

Gailitis, A., Lielausis, O., Platacis, E., Gerbeth, G., and Stefani, F. (2002b). “Colloquium: Laboratory experiments on hydromagnetic dynamos”. *Reviews of Modern Physics* 74.4, pp. 973–990.

Gailitis, A., Lielausis, O., Platacis, E., Gerbeth, G., and Stefani, F. (2002c). “On back-reaction effects in the Riga dynamo experiment”. *Magnetohydrodynamics* 38, pp. 15–26.

Gailitis, A., Lielausis, O., Platacis, E., Gerbeth, G., and Stefani, F. (2003). “The Riga Dynamo Experiment”. *Surveys in Geophysics* 24.3, pp. 247–267.

Gailitis, A., Lielausis, O., Platacis, E., Gerbeth, G., and Stefani, F. (2004). “Riga dynamo experiment and its theoretical background”. *Physics of Plasmas* 11.5, pp. 2838–2843.

Gardner, R. A. and Lykoudis, P. S. (1971). “Magneto-fluid-mechanic pipe flow in a transverse magnetic field. Part 1. Isothermal flow”. *Journal of Fluid Mechanics* 47.04, pp. 737–764.

Getling, A. V. (1998). *Rayleigh-Bénard Convection: Structures and Dynamics*. en. World Scientific.

Gibson, M. and Launder, B. (1978). “Ground Effects on Pressure Fluctuations in the Atmospheric Boundary Layer”. *Journal of Fluid Mechanics* 86.03, pp. 491–511.

Gillon, P. (2000). “Uses of intense d.c. magnetic fields in materials processing”. *Materials Science and Engineering: A* 287.2, pp. 146–152.

Grief, A. D. and Richardson, G. (2005). "Mathematical modelling of magnetically targeted drug delivery". *Journal of Magnetism and Magnetic Materials* 293.1, pp. 455–463.

Griffiths, David J (1999). *Introduction to electrodynamics*. English. Upper Saddle River, N.J.: Prentice Hall.

Grötzbach, G. (1982). "Direct Numerical Simulation of Laminar and Turbulent Bénard Convection". *Journal of Fluid Mechanics* 119, pp. 27–53.

Ha, M. Y., Lee, H. G., and Seong, S. H. (2003). "Numerical simulation of three-dimensional flow, heat transfer, and solidification of steel in continuous casting mold with electromagnetic brake". *Journal of Materials Processing Technology* 133.3, pp. 322–339.

Haik, Y., Pai, V., and Chen, C-J. (2001). "Apparent viscosity of human blood in a high static magnetic field". *Journal of Magnetism and Magnetic Materials* 225.1–2, pp. 180–186.

Hanjalić, K. and Jakirlić, S. (1993). "A model of stress dissipation in second-moment closures". en. *Applied Scientific Research* 51.1-2, pp. 513–518.

Hanjalić, K., Jakirlić, S., and Durst, F. (1994). "A computational study of joint effects of transverse shear and streamwise acceleration on three-dimensional boundary layers". *International Journal of Heat and Fluid Flow* 15.4, pp. 269–282.

Hanjalić, K, Jakirlić, S, and Hadžić, I (1997). "Expanding the limits of "equilibrium" second-moment turbulence closures". *Fluid Dynamics Research* 20.1-6, pp. 25–41.

Hanjalić, K. and Kenjereš, S. (2000). "Reorganization of turbulence structure in magnetic Rayleigh–Bénard convection: a T-RANS study". *Journal of Turbulence* 1, N8.

Hanjalić, K. and Kenjereš, S. (2001). "'T-RANS' Simulation of Deterministic Eddy Structure in Flows Driven by Thermal Buoyancy and Lorentz Force". *Flow, Turbulence and Combustion* 66.4, pp. 427–451.

Hanjalić, K. and Kenjereš, S. (2006). "RANS-Based Very Large Eddy Simulation of Thermal and Magnetic Convection at Extreme Conditions". *Journal of Applied Mechanics* 73.3, pp. 430–440.

Hanjalic, K. and Launder, B. (2011). *Modelling Turbulence in Engineering and the Environment: Second-Moment Routes to Closure*. Cambridge University Press.

Hartmann, J. (1937). "Theory of the Laminar Flow of an Electrically Conducive Liquid in a Homogenous Magnetic Field". *Matematisk-fysiske meddelelser* 15.6, p. 1.

Hartmann, J. and Lazarus, F. (1937). "Experimental Investigations on the Flow of Mercury in a Homogenous Magnetic Field". *Matematisk-fysiske meddelelser* 15.7, p. 1.

Hof, B., Juel, A., and Mullin, T. (2003). "Magnetohydrodynamic Damping of Convective Flows in Molten Gallium". *Journal of Fluid Mechanics* 482, pp. 163–179.

Hof, B., Juel, A., and Mullin, T. (2005). "Magnetohydrodynamic Damping of Oscillations in Low-Prandtl-Number Convection". *Journal of Fluid Mechanics* 545, pp. 193–201.

Hossain, M. (1991). "Inverse energy cascades in three-dimensional turbulence". *Physics of Fluids B: Plasma Physics (1989-1993)* 3.3, pp. 511–514.

Hunt, J. C. R. (1965). "Magnetohydrodynamic flow in rectangular ducts". *Journal of Fluid Mechanics* 21.04, pp. 577–590.

Hunt, J. C. R. and Stewartson, K. (1965). "Magnetohydrodynamic flow in rectangular ducts. II". *Journal of Fluid Mechanics* 23.03, pp. 563–581.

Hunt, J. C. R., Wray, A. A., and Moin, P. (1988). "Eddies, streams, and convergence zones in turbulent flows". In: pp. 193–208.

Hurle, D. T. J. (1966). "Temperature oscillations in molten metals and their relationship to growth striae in melt-grown crystals". *Philosophical Magazine* 13.122, pp. 305–310.

Idogawa, A., Sugizawa, M., Takeuchi, S., Sorimachi, K., and Fujii, T. (1993). "Control of molten steel flow in continuous casting mold by two static magnetic fields imposed on whole width". *Materials Science and Engineering: A* 173.1–2, pp. 293–297.

Ikbal, Md. A., Chakravarty, S., Wong, K., Mazumdar, J., and Mandal, P. K. (2009). "Unsteady response of non-Newtonian blood flow through a stenosed artery in magnetic field". *Journal of Computational and Applied Mathematics* 230.1, pp. 243–259.

Ince, N. Z. and Launder, B. E. (1989). "On the computation of buoyancy-driven turbulent flows in rectangular enclosures". *International Journal of Heat and Fluid Flow* 10.2, pp. 110–117.

Jakirlić, S. and Hanjalić, K. (1995). "A second-moment closure for non-equilibrium and separating high- and low-Re-number flows". In: *10th Symposium on Turbulent Shear Flows*. Pennsylvania State University, pp. 23–30.

Ji, H.-C and Gardner, R.A (1997). "Numerical analysis of turbulent pipe flow in a transverse magnetic field". *International Journal of Heat and Mass Transfer* 40.8, pp. 1839–1851.

Jones, W.P and Launder, B.E (1972). "The prediction of laminarization with a two-equation model of turbulence". *International Journal of Heat and Mass Transfer* 15.2, pp. 301–314.

Jurgons, R., Seliger, C., Hilpert, A., Trahms, L., Odenbach, S., and Alexiou, C. (2006). "Drug loaded magnetic nanoparticles for cancer therapy". *Journal of Physics: Condensed Matter* 18.38, S2893–S2902.

Kenjereš, S. (2008). "Numerical analysis of blood flow in realistic arteries subjected to strong non-uniform magnetic fields". *International Journal of Heat and Fluid Flow* 29.3, pp. 752–764.

Kenjereš, S., Cate, S. ten, and Voesenek, C.J. (2011). "Vortical structures and turbulent bursts behind magnetic obstacles in transitional flow regimes". *International Journal of Heat and Fluid Flow* 32.3, pp. 510–528.

Kenjereš, S. and Hanjalić, K. (1999a). "Identification and visualization of coherent structures in rayleigh-bénard convection with a time-dependent RANS". en. *Journal of Visualization* 2.2, pp. 169–176.

Kenjereš, S. and Hanjalić, K. (1999b). "Transient analysis of Rayleigh–Bénard convection with a RANS model". *International Journal of Heat and Fluid Flow* 20.3, pp. 329–340.

Kenjereš, S. and Hanjalić, K. (2000). "On the implementation of effects of Lorentz force in turbulence closure models". *International Journal of Heat and Fluid Flow* 21.3, pp. 329–337.

Kenjereš, S. and Hanjalić, K. (2004). "Numerical simulation of magnetic control of heat transfer in thermal convection". *International Journal of Heat and Fluid Flow* 25.3, pp. 559–568.

Kenjereš, S. and Hanjalić, K. (2007). "Numerical insights into magnetic dynamo action in a turbulent regime". *New Journal of Physics* 9, pp. 306–306.

Kenjereš, S., Hanjalić, K., and Bal, D. (2004). "A direct-numerical-simulation-based second-moment closure for turbulent magnetohydrodynamic flows". *Physics of Fluids* 16.5, p. 1229.

Kenjereš, S., Hanjalić, K., Renaudier, S., Stefani, F., Gerbeth, G., and Gailitis, A. (2006). "Coupled fluid-flow and magnetic-field simulation of the Riga dynamo experiment". *Physics of Plasmas* 13.12, p. 122308.

Kerr, R. and Herring, J. (2000). "Prandtl number dependence of Nusselt number in direct numerical simulations". *Journal of Fluid Mechanics* 419, pp. 325–344.

Kim, J., Moin, P., and Moser, R. (1987). "Turbulence statistics in fully developed channel flow at low Reynolds number". *Journal of Fluid Mechanics* 177, pp. 133–166.

Kim, S.-J. and Lee, C. M. (2000). "Investigation of the flow around a circular cylinder under the influence of an electromagnetic force". *Experiments in Fluids* 28.3, pp. 252–260.

Kobayashi, H. (2008). "Large eddy simulation of magnetohydrodynamic turbulent duct flows". *Physics of Fluids* 20.1, pp. 015102–015102.

Kolesnikov, Yu B. and Tsinober, A. B. (1974). "Experimental investigation of two-dimensional turbulence behind a grid". en. *Fluid Dynamics* 9.4, pp. 621–624.

Kolmogorov, A. (1941). "The Local Structure of Turbulence in Incompressible Viscous Fluid for Very Large Reynolds' Numbers". *Akademiia Nauk SSSR Doklady* 30, pp. 301–305.

Kolsi, L., Abidi, A., Borjini, M. N., Daous, N., and Ben Aïssia, H. (2007). "Effect of an External Magnetic Field on the 3-D Unsteady Natural Convection in a Cubical Enclosure". *Numerical Heat Transfer, Part A: Applications* 51.10, pp. 1003–1021.

Krasnov, D. S., Zienicke, E., Zikanov, O., Boeck, T., and Thess, A. (2004). "Numerical Study of the Instability of the Hartmann Layer". *Journal of Fluid Mechanics* 504, pp. 183–211.

Krasnov, D., Zikanov, O., and Boeck, T. (2012). "Numerical study of magnetohydrodynamic duct flow at high Reynolds and Hartmann numbers". *Journal of Fluid Mechanics* 704, pp. 421–446.

Krasnov, D., Zikanov, O., Schumacher, J., and Boeck, T. (2008). "Magnetohydrodynamic turbulence in a channel with spanwise magnetic field". *Physics of Fluids* 20.9, pp. 095105–095105.

Krishnamurti, R. (1973). "Some further studies on the transition to turbulent convection". *Journal of Fluid Mechanics* 60.02, pp. 285–303.

Ku, D. N. (1997). "Blood Flow in Arteries". *Annual Review of Fluid Mechanics* 29, pp. 399–434.

Lan, C.-W. "Convection and Control in Melt Growth of Bulk Crystals". In: *Springer Handbook of Crystal Growth*. Springer Berlin Heidelberg.

Launder, B. (1975). "On the effects of a gravitational field on the turbulent transport of heat and momentum". *Journal of Fluid Mechanics* 67.03, pp. 569–581.

Launder, B., Reece, G. J., and Rodi, W. (1975). "Progress in the development of a Reynolds-stress turbulence closure". *Journal of Fluid Mechanics* 68.03, pp. 537–566.

Launder, B. and Sharma, B. (1974). "Application of the energy-dissipation model of turbulence to the calculation of flow near a spinning disc". *Letters in Heat and Mass Transfer* 1.2, pp. 131–137.

Launder, B. and Spalding, D. (1974). "The numerical computation of turbulent flows". *Computer Methods in Applied Mechanics and Engineering* 3.2, pp. 269–289.

Lee, D. and Choi, H. (2001). "Magnetohydrodynamic Turbulent Flow in a Channel at Low Magnetic Reynolds Number". *Journal of Fluid Mechanics* 439, pp. 367–394.

Lee, H.G., Ha, M.Y., and Yoon, H.S. (2005). "A numerical study on the fluid flow and heat transfer in the confined jet flow in the presence of magnetic field". *International Journal of Heat and Mass Transfer* 48.25–26, pp. 5297–5309.

Lehnert, B. and Little, N. C (1957). "Experiments on the Effect of Inhomogeneity and Obliquity of a Magnetic Field in Inhibiting Convection". *Tellus* 9.1, pp. 97–103.

Leonard, B.P. (1979). "A stable and accurate convective modelling procedure based on quadratic upstream interpolation". *Computer Methods in Applied Mechanics and Engineering* 19.1, pp. 59–98.

Lien, F. and Leschziner, M. (1994a). "A general non-orthogonal collocated finite volume algorithm for turbulent flow at all speeds incorporating second-moment turbulence-transport closure, Part 1: Computational implementation". *Computer Methods in Applied Mechanics and Engineering* 114.1–2, pp. 123–148.

Lien, F. and Leschziner, M. (1994b). "Upstream monotonic interpolation for scalar transport with application to complex turbulent flows". *International Journal for Numerical Methods in Fluids* 19.6, pp. 527–548.

Lingwood, R. J. and Alboussière, T. (1999). "On the stability of the Hartmann layer". *Physics of Fluids* 11.8, p. 2058.

Lowes, F. J. and Wilkinson, I. (1963). "Geomagnetic Dynamo: A Laboratory Model". en. *Nature* 198.4886, pp. 1158–1160.

Lowes, F. J. and Wilkinson, I. (1968). "Geomagnetic Dynamo: An Improved Laboratory Model". *Nature* 219.5155, pp. 717–718.

Lundgren, T. S., Atabek, B. H., and Chang, C. C. (1961). "Transient Magnetohydrodynamic Duct Flow". *Physics of Fluids (1958-1988)* 4.8, pp. 1006–1011.

Manneville, P. (2006). "Rayleigh-Bénard Convection: Thirty Years of Experimental, Theoretical, and Modeling Work". In: *Dynamics of Spatio-Temporal Cellular Structures*. Ed. by I. Mutabazi, J. E. Wesfreid, and E. Guyon. Vol. 207. New York, NY: Springer New York, pp. 41–65.

Maxwell, J. C. (1873). *A treatise on electricity and magnetism*. Vol. 1. Clarendon Press.

Merrill, R. T., McElhinny, M. W., and McFadden, P. L. (1998). *The Magnetic Field of the Earth: Paleomagnetism, the Core, and the Deep Mantle*. en. Academic Press.

Milton, Kimball A. (2006). "Theoretical and experimental status of magnetic monopoles". en. *Reports on Progress in Physics* 69.6, p. 1637.

Moffatt, H. K. (1967). "On the Suppression of Turbulence by a Uniform Magnetic Field". *Journal of Fluid Mechanics* 28.03, pp. 571–592.

Mohanty, S., Das, B., and Mishra, B.K. (2011). "A preliminary investigation into magnetic separation process using CFD". *Minerals Engineering* 24.15, pp. 1651–1657.

Moreau, R., Moreau, R., and Molokov, S. (2007). "Julius Hartmann and His Followers: A Review on the Properties of the Hartmann Layer". In: *Magnetohydrodynamics*. Vol. 80. Fluid Mechanics and Its Applications. Dordrecht: Springer Netherlands, pp. 155–170.

Moroz, P., Jones, S. K., and Gray, B. N. (2002). "Magnetically mediated hyperthermia: current status and future directions". *International Journal of Hyperthermia* 18.4, pp. 267–284.

Moser, R. D., Kim, J., and Mansour, N. N. (1999). "Direct numerical simulation of turbulent channel flow up to Reτ=590". *Physics of Fluids* 11.4, p. 943.

Müller, U. and Stieglitz, R. (2002). "The Karlsruhe Dynamo Experiment". *Nonlinear Processes in Geophysics* 9.3/4, pp. 165–170.

Müller, U., Stieglitz, R., and Horanyi, S. (2004). "A Two-Scale Hydromagnetic Dynamo Experiment". *Journal of Fluid Mechanics* 498, pp. 31–71.

Müller, U., Stieglitz, R., and Horanyi, S. (2006). "Experiments at a Two-Scale Dynamo Test Facility". *Journal of Fluid Mechanics* 552, pp. 419–440.

Murgatroyd, W. (1953). "CXLII. Experiments on magneto-hydrodynamic channel flow". *The London, Edinburgh, and Dublin Philosophical Magazine and Journal of Science* 44.359, pp. 1348–1354.

Mutschke, G., Gerbeth, G., Albrecht, T., and Grundmann, R. (2006). "Separation control at hydrofoils using Lorentz forces". *European Journal of Mechanics - B/Fluids* 25.2, pp. 137–152.

Nakagawa, Y. (1955). "An Experiment on the Inhibition of Thermal Convection by a Magnetic Field". *Nature* 175.4453, pp. 417–419.

Naot, D., Shavit, A., and Wolfshtein, M. (1970). "Interactions between components of the turbulent velocity correlation tensor due to pressure fluctuations". *Israel Journal of Technology* 8.3, pp. 259–269.

Noguchi, H., Ohtsubo, Y., and Kasagi, N. (2004). *DNS Database of Turbulence and Heat Transfer*. http://www.thtlab.t.u-tokyo.ac.jp/DNS/dns_database.html.

Okada, K. and Ozoe, H. (1992). "Experimental Heat Transfer Rates of Natural Convection of Molten Gallium Suppressed Under an External Magnetic Field in Either the X, Y, or Z Direction". *Journal of Heat Transfer* 114.1, pp. 107–114.

O'Sullivan, P. L. and Biringen, S. (1998). "Direct numerical simulations of low Reynolds number turbulent channel flow with EMHD control". *Physics of Fluids* 10.5, pp. 1169–1181.

Ozoe, H. and Okada, K. (1989). "The effect of the direction of the external magnetic field on the three-dimensional natural convection in a cubical enclosure". *International Journal of Heat and Mass Transfer* 32.10, pp. 1939–1954.

Pankhurst, Q. A., Connolly, J., Jones, S. K., and Dobson, J. (2003). "Applications of magnetic nanoparticles in biomedicine". *Journal of Physics D: Applied Physics* 36.13, R167–R181.

Patankar, S. (1980). *Numerical Heat Transfer and Fluid Flow*. 1st ed. Taylor & Francis.

Pope, S. B (2000). *Turbulent flows*. English. Cambridge; New York: Cambridge University Press.

Posdziech, O. and Grundmann, R. (2001). "Electromagnetic control of seawater flow around circular cylinders". *European Journal of Mechanics - B/Fluids* 20.2, pp. 255–274.

Rayleigh, Lord (1916). "LIX. On convection currents in a horizontal layer of fluid, when the higher temperature is on the under side". *Philosophical Magazine Series 6* 32.192, pp. 529–546.

Reed, Claude B. and Lykoudis, Paul S. (1978). "The effect of a transverse magnetic field on shear turbulence". *Journal of Fluid Mechanics* 89.01, pp. 147–171.

Rhie, C. M. and Chow, W. L. (1983). "Numerical study of the turbulent flow past an airfoil with trailing edge separation". *AIAA Journal* 21.11, pp. 1525–1532.

Richardson, Lewis F. (1922). *Weather prediction by numerical process*. eng. Cambridge.

Roberts, P. H. (1967a). *An introduction to magnetohydrodynamics*. English. London: Longmans.

Roberts, P. H. (1967b). "Singularities of Hartmann Layers". *Proceedings of the Royal Society of London. Series A. Mathematical and Physical Sciences* 300.1460, pp. 94–107.

Rotta, J. (1951). "Statistische Theorie nichthomogener Turbulenz". *Zeitschrift fur Physik* 129, pp. 547–572.

Sankar, D. S., Jaffar, N. A., Ismail, A. I. M., and Nagar, A. K. (2011). "Mathematical Modeling of a Complex System for MHD Flow in Hemodynamics". In: *2011 Sixth Interna-*

tional Conference on Bio-Inspired Computing: Theories and Applications (BIC-TA), pp. 324–328.

Sarkar, A. and Tilgner, A. (2005). "Magnetic field oscillation in simulations of the Karlsruhe Dynamo". *Astronomische Nachrichten* 326.3-4, pp. 250–253.

Satake, S., Kunugi, T., Takase, K., and Ose, Y. (2006). "Direct numerical simulation of turbulent channel flow under a uniform magnetic field for large-scale structures at high Reynolds number". *Physics of Fluids* 18.12, pp. 125106–125106-8.

Satake, Shin-ichi, Kunugi, Tomoaki, and Smolentsev, Sergey (2002). "Direct numerical simulations of turbulent pipe flow in a transverse magnetic field". *Journal of Turbulence* 3, N20.

Satake, Shin-ichi, Yoshida, Naoshi, Kunugi, Tomoaki, Takase, Kazuyuki, Ose, Yasuo, and Kano, Takuma (2008). "DNS of turbulent heat transfer under a uniform magnetic field at high Reynolds number". *Fusion Engineering and Design* 83.7–9, pp. 1092–1096.

Schumann, U. (1976). "Numerical Simulation of the Transition from Three- to Two-Dimensional Turbulence Under a Uniform Magnetic Field". *Journal of Fluid Mechanics* 74.01, pp. 31–58.

Shercliff, J. A. (1953). "Steady motion of conducting fluids in pipes under transverse magnetic fields". *Mathematical Proceedings of the Cambridge Philosophical Society* 49.01, pp. 136–144.

Shercliff, J. A. (1965). *A Textbook of Magnetohydrodynamics*. 1st. Pergamon Press.

Shir, C. C. (1973). "A Preliminary Numerical Study of Atmospheric Turbulent Flows in the Idealized Planetary Boundary Layer". *Journal of the Atmospheric Sciences* 30.7, pp. 1327–1339.

Sillero, J. A., Jiménez, J., and Moser, R. D. (2013). "One-point statistics for turbulent wall-bounded flows at Reynolds numbers up to $\delta \approx 2000$". *Physics of Fluids* 25.10, p. 105102.

Sommeria, JoëL and Moreau, René (1982). "Why, How, and When, MHD Turbulence Becomes Two-Dimensional". *Journal of Fluid Mechanics* 118, pp. 507–518.

Spong, E., Reizes, J. A., and Leonardi, E. (2005). "Efficiency improvements of electromagnetic flow control". *International Journal of Heat and Fluid Flow* 26.4, pp. 635–655.

Sterl, A. (1990). "Numerical Simulation of Liquid-Metal MHD Flows in Rectangular Ducts". *Journal of Fluid Mechanics* 216, pp. 161–191.

Stieglitz, R. and Müller, U. (2001). "Experimental demonstration of a homogeneous two-scale dynamo". *Physics of Fluids* 13.3, pp. 561–564.

Sukoriansky, S., Zilberman, I., and Branover, H. (1986). "Experimental studies of turbulence in mercury flows with transverse magnetic fields". *Experiments in Fluids* 4.1, pp. 11–16.

Sutton, G. W. and Sherman, A. (2006). *Engineering magnetohydrodynamics*. Mineola, NY: Dover Publications.

Svoboda, J. and Fujita, T. (2003). "Recent developments in magnetic methods of material separation". *Minerals Engineering* 16.9, pp. 785–792.

Theerthan, S. A. and Arakeri, J. H. (1994). "Planform structure of turbulent Rayleigh-Bénard convection". *International Communications in Heat and Mass Transfer* 21.4, pp. 561–572.

Toh, T. and Takeuchi, E. (2002). "Electromagnetic Phenomena in Steel Continuous Casting". In: *Mechanics for a New Mellennium*. Ed. by Hassan Aref and James W. Phillips. Springer Netherlands, pp. 99–112.

Tournier, R.F, Beaugnon, E, Noudem, J, and Rakotoarison, S (2001). "Materials processing in a magnetic force opposed to the gravity". *Journal of Magnetism and Magnetic Materials* 226–230, Part 2, pp. 2094–2100.

Utech, H. P. and Flemings, M. C. (1966). "Elimination of Solute Banding in Indium Antimonide Crystals by Growth in a Magnetic Field". *Journal of Applied Physics* 37.5, pp. 2021–2024.

Varshney, H. and Baig, M. F. (2008a). "Rotating magneto-convection: Influence of vertical magnetic field". *Journal of Turbulence* 9.

Varshney, H. and Baig, M. F. (2008b). "Rotating Rayleigh–Bénard convection under the influence of transverse magnetic field". *International Journal of Heat and Mass Transfer* 51.15-16, pp. 4095–4108.

Versteeg, H. and Malalasekra, W. (1996). *An Introduction to Computational Fluid Dynamics: The Finite Volume Method Approach*. 1st ed. Prentice Hall.

Votyakov, E. V. and Kassinos, S. C. (2009). "On the analogy between streamlined magnetic and solid obstacles". *Physics of Fluids* 21.9, p. 097102.

Votyakov, E. V. and Kassinos, S. C. (2010). "Core of the magnetic obstacle". *Journal of Turbulence* 11, N49.

Votyakov, E. V., Kolesnikov, Yu., Andreev, O., Zienicke, E., and Thess, A. (2007). "Structure of the Wake of a Magnetic Obstacle". *Physical Review Letters* 98.14, p. 144504.

Votyakov, E. V. and Zienicke, E. (2007). "Numerical study of liquid metal flow in a rectangular duct under the influence of a heterogenous magnetic field". *Fluid Dynamics & Materials Processing* 3.2, pp. 97–114.

Votyakov, E. V., Zienicke, E., and Kolesnikov, Y. (2008). "Constrained Flow Around a Magnetic Obstacle". *Journal of Fluid Mechanics* 610, pp. 131–156.

Walker, J. S., Ludford, G. S. S., and Hunt, J. C. R. (1971). "Three-dimensional MHD duct flows with strong transverse magnetic fields. Part 2. Variable-area rectangular ducts with conducting sides". *Journal of Fluid Mechanics* 46.04, pp. 657–684.

Walker, J. S., Ludford, G. S. S., and Hunt, J. C. R. (1972). "Three-dimensional MHD duct flows with strong transverse magnetic fields. Part 3. Variable-area rectangular ducts with insulating walls". *Journal of Fluid Mechanics* 56.01, pp. 121–141.

Walker, J.S. and Ludford, G.S.S. (1974a). "MHD flow in conducting circular expansions with strong transverse magnetic fields". *International Journal of Engineering Science* 12.3, pp. 193–204.

Walker, J.S. and Ludford, G.S.S. (1974b). "MHD flow in insulated circular expansions with strong transverse magnetic fields". *International Journal of Engineering Science* 12.12, pp. 1045–1061.

Walker, J.S. and Ludford, G.S.S. (1975). "MHD flow in circular expansions with thin conducting walls". *International Journal of Engineering Science* 13.3, pp. 261–269.

Wang, S., Liu, H., and Xu, W. (2008). "Hydrodynamic modelling and CFD simulation of ferrofluids flow in magnetic targeting drug delivery". *International Journal of Computational Fluid Dynamics* 22, pp. 659–667.

Widlund, O., Zahrai, S., and Bark, F. H. (1998). "Development of a Reynolds stress closure for modeling of homogeneous MHD turbulence". *Physics of Fluids* 10.8, p. 1987.

Wilcox, David C (1998). *Turbulence modeling for CFD*. English. La Cãnada, Calif.: DCW Industries.

Wilkinson, I. (1984). "The contribution of laboratory dynamo experiments to our understanding of the mechanism of generation of planetary magnetic fields". *Surveys in Geophysics* 7.1, pp. 107–122.

Williamson, C. H. K. (1996). "Vortex Dynamics in the Cylinder Wake". *Annual Review of Fluid Mechanics* 28.1, pp. 477–539.

Wilson, D. R., Craft, T. J., and Iacovides, H. (2014). "Application of RANS turbulence closure models to flows subjected to electromagnetic and buoyancy forces". *International Journal of Heat and Fluid Flow*. 8th Symposium on Turbulence & Shear Flow Phenomena (TSFP8) 49, pp. 80–90.

Wilson, D. R., Craft, T. J., and Iacovides, H. (2015). "Application of Reynolds stress transport turbulence closure models to flows affected by Lorentz and buoyancy forces". *International Journal of Heat and Fluid Flow*. Special Issue devoted to the 10th Int. Symposium on Engineering Turbulence Modelling and Measurements (ETMM10) held in Marbella, Spain on September 17-19, 2014 55, pp. 180–197.

Wollaston, C. (1881). "Tidally induced emf s in cables". *J. Soc. Tel. Engrs* 10, p. 50.

Wörner, M. (1994). "Direkte Simulation turbulenter Rayleigh-Bénard-Konvektion in flüssigem Natrium". de. Ph.D. Thesis. Kernforschungszentrum Karlsruhe: University of Karlsruhe.

Xu, B., Li, B.Q., and Stock, D.E. (2006). "An experimental study of thermally induced convection of molten gallium in magnetic fields". *International Journal of Heat and Mass Transfer* 49.13-14, pp. 2009–2019.

Yamamoto, Y., Kunugi, T., Satake, S., and Smolentsev, S. (2008). "DNS and k–ε model simulation of MHD turbulent channel flows with heat transfer". *Fusion Engineering and Design* 83.7–9, pp. 1309–1312.

Yanagisawa, T., Hamano, Y., and Sakuraba, A. (2015). “Flow reversals in low-Prandtl-number Rayleigh-Bénard convection controlled by horizontal circulations”. *Physical Review E* 92.2, p. 023018.

Yanagisawa, T., Yamagishi, Y., Hamano, Y., Tasaka, Y., Yano, K., Takahashi, J., and Takeda, Y. (2010). “Detailed investigation of thermal convection in a liquid metal under a horizontal magnetic field: Suppression of oscillatory flow observed by velocity profiles”. *Physical Review E* 82.5, p. 056306.

Zhi-Hua, Chen, Bao-Chun, Fan, Aubry, Nadine, and Ben-Mou, Zhou (2006). “Electro-Magnetic Control of Vortex Shedding Behind a Circular Cylinder”. *Chinese Physics Letters* 23.1, pp. 154–157.

Zikanov, O. and Thess, A. (1998). “Direct Numerical Simulation of Forced MHD Turbulence at Low Magnetic Reynolds Number”. *Journal of Fluid Mechanics* 358, pp. 299–333.